5.66% C_2H_6- air mixture
p_0=100 kPa; T_w= 487 K

diffusion control

kinetic to diffusion transition

induction period

kinetic control

CHEMIA

S T U D I A

UNIVERSITATIS BABEŞ-BOLYAI

CHEMIA

3

CUPRINS – CONTENT – SOMMAIRE – INHALT

Studia Universitatis Babes-Bolyai Chemia has been selected for coverage in Thomson Reuters products and custom information services. Beginning with V. 53 (1) 2008, this publication is indexed and abstracted in the following:

- Science Citation Index Expanded (also known as SciSearch®)
- Chemistry Citation Index®
- Journal Citation Reports/Science Edition

Professor Ioan Bâldea at his 70's Anniversary

Brilliant teacher and warm colleague, Professor Ioan Bâldea was born on the 21st of October 1939. Still active, he dedicates himself to science and teaching after graduating Babeş-Bolyai University as a chemist in 1962. Well-known in the academic community as one of the top kineticists of the country, his 70's anniversary finds him with unaltered optimism and creativeness.

Beginning immediately after graduation as a teaching assistant, his academic carrier unfolded rigorously step by step, while obtaining his PhD in 1969. As an appointed lecturer (1971), associated professor (1990) and full professor (1993), his work continuously contributed to the development and growth of the Department of Physical Chemistry.

Besides over 120 various scientific papers, Professor Ioan Bâldea also published 4 books as a single author and contributed to 2 others. These summarize his prodigious experience in chemical kinetics of homogeneous redox and organic reactions, characterization of short-life chemical complexes, modeling of complex processes, design and reactor engineering as well as kinetic methods of analysis. This valuable and diverse knowledge was shared with the young scientists he tutored during their PhD scholarships. It also contributed both to solving of over 50 contracts and putting forward of 4 patents for the Romanian chemical industry. A production line for ethyl acetate was based on his designs and functioned till the early 90's at the plant in Craiova. The 12 research Grants he coordinated (among these, one financed by the World Bank) substantially contributed to the development of Chemical Kinetics and General Physical Chemistry at the Babeş-Bolyai University.

While always endeavoring on sharing and passing over his knowledge to the young generations, Professor Bâldea wrote or collaborated to the publication of 8 manuals of Physical as well as General Chemistry. The students highly appreciated the funny and nonconformist explanations; the examples illustrating daily life made his lectures colorful and easy to understand. The approximately 100 graduate and postgraduate thesis coordinated by the Professor stand proof for this fact.

Also beloved and highly regarded by his colleagues, Professor Ioan Bâldea was elected for nearly 10 years as Head of the Department of Physical Chemistry and represented for 23 years the same Department in the Faculty's Council. He was also the local coordinator of the CEEPUS academic exchange Program for 8 years. The vast experience allowed the Professor to manage the Program of didactic personnel improvement for 8 years and to be a referee for various scientific publications, grants and events.

This issue of Studia Universitas Babeş-Bolyai, Seria Chemia reflects the tight professional relationships Professor Ioan Bâldea has build within the academic community of Romania. Teachers and researchers from the University of Bucharest, Baia-Mare or Iuliu Haţieganu University of Medicine from Cluj-Napoca also contributed to this volume.

Now, at his 70's anniversary, we – the colleagues of the Department of Physical Chemistry – as well as all the colleagues and researchers of the Faculty of Chemistry of the Babeş-Bolyai University, along with the Editorial Board, wish Professor Ioan Bâldea health in the many years to come, as well as the spice of current valuable scientific activity.

Volum Editors

Liana Mureşan
Alexandra Csavdári

NEW LC/MS/MS METHOD FOR THE QUANTIFICATION OF PHENYTOIN IN HUMAN PLASMA

MARCELA ACHIM[a], DANA MUNTEAN[a], LAURIAN VLASE[a], IOAN BÂLDEA[b], DAN MIHU[c], SORIN E. LEUCUȚA[a]

ABSTRACT. A simple, reversed-phase high performance liquid chromatography method with mass spectrometric detection (HPLC-MS/MS) was developed for determination of an antiepileptic drug, phenytoin, in human plasma. The procedure involves a simple extraction step by mixing 0.2 ml plasma with 0.6 ml methanol. After centrifugation, 1 μl of the supernatant was injected onto a Zorbax SB-C18 100 mm x 3 mm, 3.5 μm column, and eluted with a mobile phase consisting in a mixture of water containing 2 mM ammonium acetate and methanol 50:50 (v/v). Detection was in MRM mode, using an electrospray positive ionization. The ion transition monitored was 253.1→(182.1+225.1). The method was evaluated in terms of linearity (between 2.0 μg/ml to 80.0 μg/ml), accuracy, precision, recovery, sensitivity. The lower limit of quantification was established at 2.0 μg/ml. The simple extraction procedure and short chromatographic runtime make the method suitable for therapeutic drug monitoring studies.

Keywords: phenytoin, HPLC-MS/MS, human plasma

INTRODUCTION

Phenytoin (Figure 1) is widely used in the treatment of epilepsy and is effective against all types of seisures. No drug has greater need for therapeutic drug concentration monitoring and individualized dosing than phenytoin. A good correlation usually is observed between the total concentration of phanytoin in plasma and the clinical effect. Therapeutic concentration of phenytoin is above 10 μg/ml [1]. Enzyme induction by phenytoin is well documented, even auto-induction by phenytoin should be considered during the treatment with phenytoin [2].

[a] *University of Medicine and Pharmacy "Iuliu Hațieganu", Faculty of Pharmacy, Emil Isac 13, RO-400023 Cluj-Napoca, Romania, dana@tbs.ubbcluj.ro*
[b] *Babeş-Bolyai" University, Faculty of Chemistry and Chemical Engineering, Arany Janos 11, RO-400028 Cluj-Napoca, Romania*
[c] *University of Medicine and Pharmacy "Iuliu Hațieganu", Faculty of Medicine, Emil Isac 13, RO-400023 Cluj-Napoca, Romania*

Plasma concentration monitoring is widely used for the clinical management of epileptic patients receiving phenytoin [3]. To minimize toxicity, monitoring of plasma anticonvulsant levels is a part of the routine management of patients in many clinics. To the best of our knowledge, almost all of the methods that were applied for determination of antieplileptic drugs in biological media are often chromatography, electrophoresis and immunoassay techniques [4,5].

The aim of the present study was to develop a fast LC-MS/MS method, able to quantify phenytoin in human plasma after a simple sample preparation by protein precipitation. The proposed method proved to be accurate and despite of very simple sample preparation, showed high sensitivity.
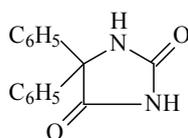
Figure 1. Molecular structure of phenytoin

RESULTS AND DISCUSSION

Figure 2 shows representative chromatograms of drug-free (blank) human plasma and a sample containing 2.0 µg/ml phenytoin (LOQ). No significant interference at the retention time of phenytoin (1.6 min) was observed, due to the specificity of the selected signal (Figure 3).
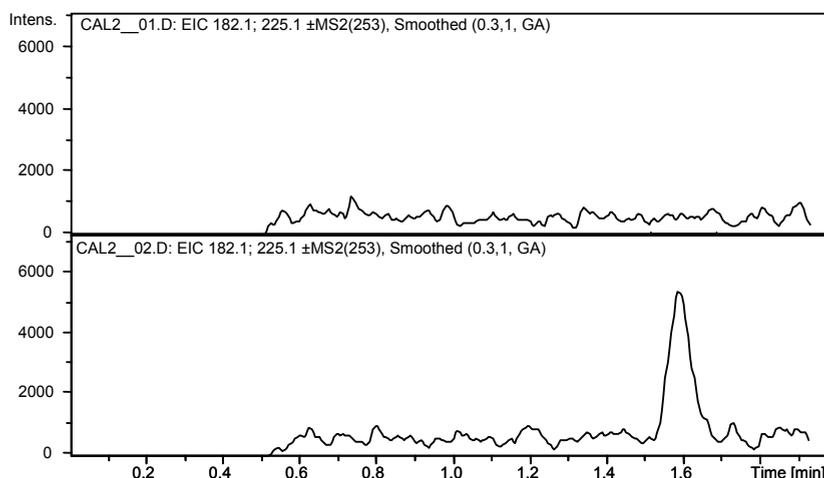
Figure 2. Chromatograms of a drug-free plasma sample (up) and LOQ plasma standard with 2.0 µg/ml phenytoin (down)
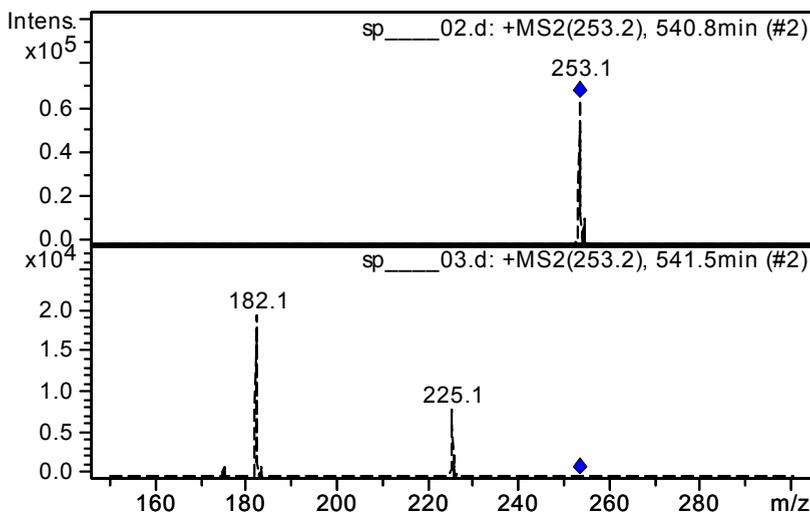
Figure 3. Mass spectra of phenytoin. Full-scan spectrum (up) and MS/MS spectrum (down). The sum of ions with *m/z* 182.1 and 225.1 was used for quantification

The analyte detection was made in MRM mode, the ion transition monitored was *m/z* 253.1→(*m/z* 182.1 + *m/z* 225.1). This way, the detection is more sensitive than in case based only on ion *m/z* 253.1 (Figure 3).

The analyte carryover was verified using a blank injection made right after an injection of the most elevated concentration level from calibration curve. No interference at retention time of analyte due to carryover was observed.

The mean calibration curve y = a(±S.D.)x + b(±S.D.), with S.D. standard deviation, was: y = (59590.4±1971.9)x – (10490.5±2501.6), N = 8 calibration points, n = 5 determinations for each calibration point. The residuals had no tendency of variation with concentration. The applied calibration curve model proved to be accurate over the concentration range 2 – 80 µg/ml, with a correlation coefficient grater than 0.998 (Figure 4).

The intra-day precision was determined from replicate analysis of samples containing phanytoin at four different concentrations covering the low, medium and higher ranges of calibration curve (Table 1), in good agreement to international regulations regarding bioanalytical methods validation [6-8]. The intra-day precision and accuracy ranged from 1.9% to 9.5% and 3.7% to 10% respectively.
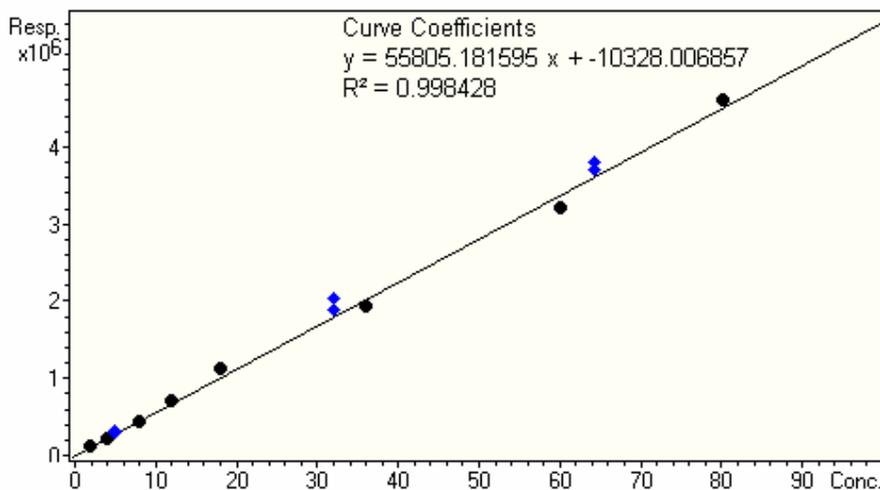
Figure 4. Calibration curve for phenytoin

Table 1. Intra-day precision, accuracy and recovery for phenytoin (n = 5)

$c_{nominal}$ (µg/ml)	Mean c_{found} (µg/ml) (± S.D.)	C.V. %	Bias %	Recovery % (± S.D.)
2.0	2.07 (0.2)	9.5	3.7	106.5 (10.5)
5.0	5.50 (0.10)	1.9	10.0	100.3 (1.9)
32.0	34.87 (1.94)	5.6	9.0	102.4 (5.7)
64.0	67.60 (3.74)	5.5	5.6	101.1 (5.6)

The intra-day precision and accuracy were determined by analyzing in five different days samples that have the same concentration, at lower, medium and higher levels from calibration curve. The precision ranged from 3.5% to 10.1% and accuracy from 1.5% to 7.2 % (Table 2):

Table 2. Inter-day precision, accuracy and recovery for phenytoin (n = 5)

$c_{nominal}$ (µg/ml)	Mean c_{found} (µg/ml) (± S.D.)	C.V. %	Bias %	Recovery % (± S.D.)
2.0	2.03 (0.20)	10.1	1.5	121.1 (35.3)
5.0	5.36 (0.21)	4.0	7.2	97.3 (9.1)
32.0	33.10 (1.16)	3.5	3.4	101.4 (5.6)
64.0	66.32 (2.87)	4.3	3.6	99.1 (4.6)

Under the experimental conditions used, the lower limit of quantification (LOQ) was of 2 µg/ml phenytoin. LOQ is the lowest amount of analyte which can be measured with accuracy and precision less than 20%.

CONCLUSIONS

A simple, sensitive, accurate and precise HPLC/MS/MS method for determination of phenytoin in human plasma using a simple single-step extraction procedure is reported. Another advantage of the method is the short chromatographic runtime of only 2.1 min. The method is suitable for therapeutic drug monitoring studies and can also be used for pharmacokinetic studies conducted on healthy volunteers [9-13].

EXPERIMENTAL SECTION

Reagents

Phenytoin, methanol, ammonium acetate, were purchased from Merck (Merck KgaA, Darmstadt, Germany). Solvents used were HPLC grade and all other chemicals were of analytical grade. Distilled, deionised water was produced by a Direct Q-5 Millipore (Millipore SA, Molsheim, France) water system. The drug-free human plasma was supplied by the Local Bleeding Centre Cluj-Napoca, Romania.

Preparation of standard solutions

A stock solution containing 10 mg/ml phenytoin was prepared in methanol. A working solution of 200 µg/ml was prepared by diluting the appropriate volume of stock solution with plasma. Than this was used to spike different volumes of drug-free plasma, providing finally eight plasma standards with concentration between 2.0 and 80.0 µg/ml. Quality control samples (QC) of 5.0, 32.0, and 64.0 µg/ml were prepared by diluting specific volumes of working solution with plasma and were used to evaluate precision and accuracy of the method.

Chromatographic and mass spectrometry systems and conditions

The HPLC system was an 1100 series model (Agilent Technologies) consisted in a binary pump, an in-line degasser, an autosampler, a column thermostat and an Ion Trap VL mass spectrometer detector (Bruckner Daltonics GmbH, Germany). Chromatograms were processed using QuantAnalysis Software. The detection of phenytoin was in MRM (MS/MS) mode, using an electrospray positive ionization (ESI positive). The ion transitions monitored was: m/z 253.1→(m/z 182.1 + m/z 225.1). Chromatographic separation was performed at 45ºC on a Zorbax SB-C18 100 mm x 3 mm, 3.5 µm column (Agilent Technologies), protected by an inline filter.

Mobile phase

The mobile phase consisted in a mixture of water containing 2 mM ammonium acetate and methanol (50:50 v/v). It was always freshly prepared and was degassed before elution for 10 min in am Elma Transsonic 700/H (Singen, Germany) ultrasonic bath. The pump delivered the mobile phase at a flow rate of 1 ml/min.

Sample preparation

Plasma samples were prepared as follows in order to be chromatographically analyzed: in an Eppendorf tube (max 1.5 ml), 0.2 ml plasma and 0.6 ml methanol were added. The tube was vortex-mixed for 10 s (Vortex Genie 2, Scientific Industries) and centrifuged for 6 min at 5000 rpm (2-16 Sartorius centrifuge, Osterode am Harz, Germany). The supernatant was transferred to an autosampler vial and 1 μl was injected into the HPLC system.

Validation

As a first step of method validation [6-8], specificity was verified using six different plasma blanks obtained from healthy volunteers who had not previously taken any medication.

The concentration of the analyte was determined automatically by the instrument data system. The calibration curve model was $y = ax + b$, weight $1/y$ linear response, where y-peak area and x-concentration. Distribution of the residuals (% difference of the back-calculated concentration from the nominal concentration) was investigated. The calibration model was accepted, if the residuals were within ±20% at the lower limit of quantification (LOQ) and within ±15% at all other calibration levels and at least 2/3 of the standards meet this criterion, including highest and lowest calibration levels.

The intra-day and inter-day precision (expressed as coefficient of variation, CV%) and accuracy (expressed as relative difference between obtained and theoretical concentration, bias%) of the assay procedure were determined by analysing on the same day five different samples at each of the lower (5.0 μg/ml), medium (32.0 μg/ml) and higher (64.0 μg/ml) levels of the considered concentration range and one different sample of each at five different occasions, respectively.

The recovery of phenytoin was analyzed at each of the three concentration levels mentioned above, e.g. lower, medium and higher level, and also at the quantification limit, by comparing the peack area response of spiked plasma samples with the response of standards prepared in water with the same concentration of ivabradine as the plasma samples, all these prepared as stated in section "Sample preparation".

ACKNOWLEDGMENTS

REFERENCES

1. Z. Rezaei, B. Hemmateenejab, S. Khabnadideh, M. Gorgin, *Talanta*, **2005**, *65*, 21.
2. M. Cheety, R. Miller, M. A. Seymour, *Ther. Drug Monit.*, **1998**, *20*, 60.
3. K. M. Patil, S. L. Bodhankar, *J. Pharm. Biomed. Analysis*, **2005**, *39*, 181.
4. D. J. Speed, S. J. Dickson, E. R. Cairus, N. D. Kim, *J. Anal. Toxicol.*, **2000**, *24*, 685.
5. M. E. Queiroz, S. M. Silvia, D. Carralho, F. M. Lancas, *J. Chroma. Sci.*, **2002**, *40*, 219.
6. The European Agency for the Evaluation of Medicinal Products. Note for Guidance on the Investigation of Bioavailability and Bioequivalence, London, UK, **2001** (CPMP/EWP/QWP/1401/98).
7. U. S. Department of Health and Human Services, Food and Drug Administration, Center for Drug Evaluation and Research. Guidance for Industry. Bioavailability and Bioequivalence Studies for Orally Administrated Drug Products – General Considerations, Rockville, USA, **2003**, *http://www.fda.gov/cder/guidance/index.htm*.
8. U. S. Department of Health and Human Services, Food and Drug Administration, Guidance for Industry – Bioanalytical Method Validation, **2001**.
9. L. Vlase L, S. E. Leucuta, S. Imre, *Talanta*, **2008**, *75*, 1104.
10. L. Vlase, A. Leucuta, D. Farcau D, M. Nanulescu, *Biopharma. Drug Dispos.*, **2006**, *27*, 285.
11. L. Vlase, S. Imre, D. Muntean, S. E. Leucuta, *J. Pharma. Biomed. Analysis*, **2007**, *44(3)*, 652.
12. L. Vlase, D. Muntean, S. E. Leucuta, I. Baldea, *Studia Univ. Babes-Bolyai Chemia*, **2009**, *54*, 43.
13. A. Butnariu, D. S. Popa, L. Vlase, M. Andreica, D. Muntean, S. E. Leucuta, *Revista Romana De Medicina De Laborator*, **2009**, *15*, 7.

STUDIES ON WO$_3$ THIN FILMS PREPARED BY DIP-COATING METHOD

ECATERINA BICA[a,b]**, LAURA ELENA MUREŞAN**[a]**, LUCIAN BARBU-TUDORAN**[c]**, EMIL INDREA**[d]**, IONEL CĂTĂLIN POPESCU**[b] **AND ELISABETH-JEANNE POPOVICI**[a]

ABSTRACT. WO$_3$ films obtained by dip-coating technique were investigated to evidence the properties of tungsten trioxide films for water splitting applications. The deposition solution containing peroxo-tungstic acid was prepared by sol-gel method. The films were deposited on conductive glass substrates and were annealed at 250-550^{0}C. The properties of WO$_3$ films were investigated by UV-Vis Spectroscopy, X-Ray diffraction (XRD) and Scanning Electron Microscopy (SEM).

Keywords: Tungsten trioxide films; ITO support; Dip-coating.

INTRODUCTION

Tungsten oxide (WO$_3$) is a wide – band gap semiconductor of great interest because of its applications in optoelectronics, catalysis and environmental engineering [1-3]. On the other hand, it was demonstrated that WO$_3$ thin films exhibits chemical sensing properties such as H$_2$S, NO$_x$, [4-7]. Moreover, WO$_3$ thin films electrodes are reversible and have fast electrochromic properties [8].

Tungsten oxide films can be synthesized by several physical and chemical routes such as sputtering [9], acid precipitation method [10] and sol-gel processing [11-14].

Application of tungsten trioxide (WO$_3$) thin films strongly depends on morpho-structural characteristics that are regulated during the synthesis.

The aim of this study is to obtain high quality WO$_3$ thin films for photo-catalysis and water splitting applications. The performed study presents the influence of some preparative conditions on the morpho-structural characteristics

[a] *Babeş-Bolyai University, "Raluca Ripan" Institute for Research in Chemistry, Fantanele 30, Cluj-Napoca, Romania, ebica@chem.ubbcluj.ro*
[b] *Babeş-Bolyai University, Faculty of Chemistry and Chemical Engineering, Arany Janos 11, Cluj-Napoca, Romania*
[c] *Babeş-Bolyai University, Electronic Microscopy Centre, Clinicilor 5-7, Cluj-Napoca, Romania*
[d] *National Institute for R&D of Isotopic and Molecular Technologies, Donath 30, Cluj-Napoca, Romania*

of WO$_3$ films, and put in evidence that the quality of the dip-coating solution and the thermal treatment play an important role on the properties of conductive glass supported WO$_3$ films.

RESULTS AND DISCUSSIONS

WO$_3$/ITO/Glass/WO$_3$ heterostructures containing tungsten oxide thin films were obtained using the dip-coating method, from peroxo-tungstic acid sol. The multilayer technique was used to prepare films with variable thickness whereas the thermal treatment was performed at 250 - 550°C (Table 1). Film thickness varies between 35 and 135 nm, in parallel with the number of dip coating deposition cycles; it seems that the thickness is not influenced by the annealing regime.

Table 1. Synthesis conditions of WO$_3$ thin films prepared from peroxo-tungstic acid sol (dip-coating method)

Sample code	Thermal treatment (°C)	Number of layers	WO$_3$ weight (g)	Film thickness (nm)
R4 I1	350	1	0.55 x 10^{-3}	35
R4 I2	350	2	0.94 x 10^{-3}	60
R4 I3	350	3	1.62 x 10^{-3}	95
R4 I4	350	4	1.97 x 10^{-3}	125
R4 I5	350	5	2.20x 10^{-3}	135
R3.1 I2	250	1	0.30 x 10^{-3}	20
R3.1 I3	350	1	0.56 x 10^{-3}	35
R3.1 I4	550	1	0.50 x 10^{-3}	35

In order to establish the optimal thermal treatment regime for WO$_3$ thin films, the peroxo-tungstic acid (PTA) precursor was investigated by thermal analysis.
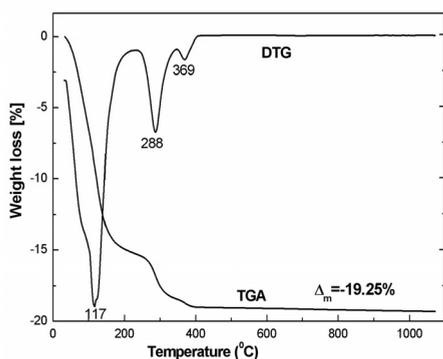
Figure 1. TGA and DTG curves of PTA precursor.
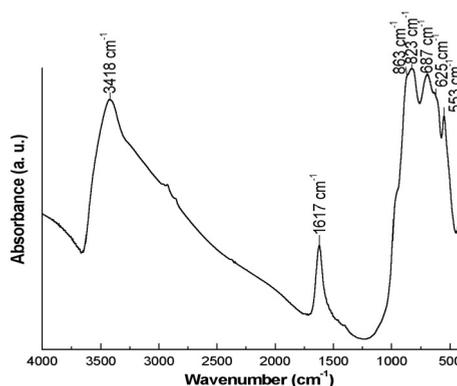
Figure 2. FT-IR spectrum of PTA precursor.

16

The TGA and DTG curves of PTA precursor indicate three most important weight loss steps i.e. (1) -14.92% at 20-200°C (removal of physical adsorbed water and alcohol); (2) -3.35% at 235-345 °C (removal of H$_2$O$_2$, i.e. peroxo-tungstic acid decomposition) and (3) -1.05% at 345-405 °C (removal of chemically bonded water i.e. tungstic acid decomposition) (Fig.1).The weight loss steps are accompanied by weak endo- and exo- thermal effects.

The FT-IR spectrum of the precursor powder (that corresponds to the as- deposited WO$_3$ film), illustrates the hydrated and the hydroxilated nature of the WO$_3$ deposit (Figure 2). Water presence is signalled by the 3418 cm^{-1} {ν(OH)} and 1617 cm^{-1} {δ(HOH)} bands. Because the ν(OH) appears as a single featureless band, it is difficult to isolate the independent contributions from structural water, hydroxyl groups, hydrogen bonded and adsorbed species. Despite the complexity of the W-O stretching bands region (400-1000cm^{-1}), it gives important information about the precursor. Besides the specific ν(W-O$_{intra}$-W) and ν(W-O$_{inter}$-W) bridging stretches (863-823 cm^{-1} and 687 -625 cm^{-1}), the stretching vibrations of W(O$_2$) and W-O could be noticed (959 cm^{-1} and 553 cm^{-1}), thus indicating the formation of [(O$_2$)$_2$W(O).O.W(O)(O$_2$)2]$^{2-}$ complex associated with the peroxo-tungstic acid [15-17].

The optical properties of WO$_3$ films were evaluated from UV-Vis transmission (Figure 3) and reflection (Figure 4) spectra.
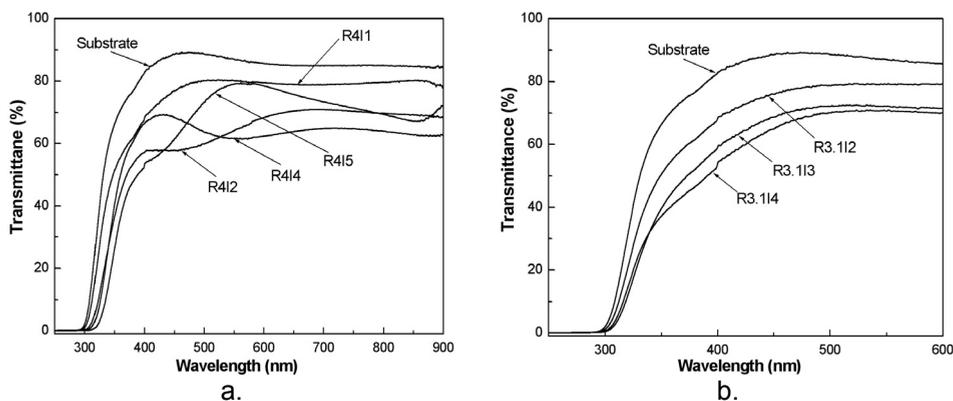
Figure 3. Transmission spectra of WO$_3$ films obtained in different conditions: a) multilayer films treated at 350°C; b) monolayer films annealed at 250 – 550°C.

The monolayer WO$_3$ film (R4I1) shows an almost constant transmittance of about 80% on the entire visible domain. As expected, the multilayer films R4I2, R4I3, R4I4 and R4I5 have a lower transmittance (50 -80 %) as compared with the monolayer heterostructures. The absorption edge shifts from 300 nm to 315 nm as the film thickness increases (Figure 3a).

The thermal treatment determines the decreases of the transmittance, in parallel with the temperature increase (Figure 3b). The thermal treatment also produces the color change of transparent films from colorless to yellow-pale, thus suggesting some morpho-structural variation.
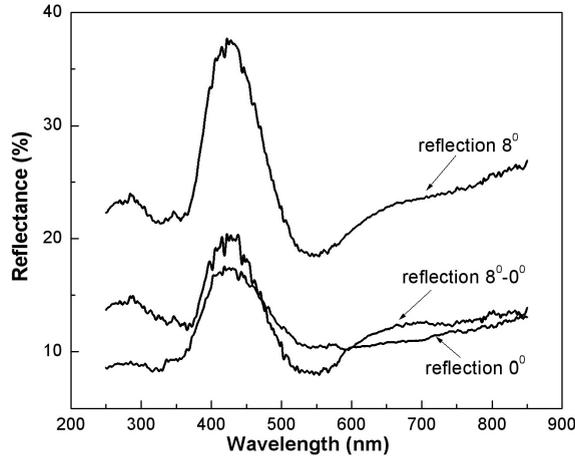
Figure 4. Reflectance spectra for the multilayer WO_3 film (R4I5) measured on ITO face.

The specular reflectance (8^0-0^0) spectrum is obtained by the difference between the total reflectance (8^0) and diffuse reflectance (0^0) spectra. The reflection maximum is situated in the blue range of the spectral domain.

In order to determine the optical energy band gap of WO_3 films, the Bardeen equation [18] was used:

$$(\alpha h v)^r = A(h v - E_g) \tag{1}$$

where: α is the absorption coefficient, E_g is the energy band gap of the semiconductor, h is the Plank's constant, A is a parameter that depends on the transition probability and r is a number that characterises the transition process. Depending on the semiconductor type, r values could be: r =2 and 2/3 for direct allowed and forbidden transitions, respectively, and r=1/2 and 1/3 for indirect allowed and forbidden transitions, respectively [18]. The absorption coefficient α was calculated using the formula (2):

$$\exp(-\alpha d) = T \tag{2}$$

where:
d is the film thickness (see table 1), and T is the measured transmittance [19].

From the transmittance spectra of WO$_3$ films (calculated without substrate), the band gap energy (E$_g$) was evaluated using the Tauc plot's, by extrapolation of the straight line in the plot $(\alpha h\nu)^{1/2}$ *vs* hν (Figure 5).

The determined band gap of dip-coated WO$_3$ films varies between 2.9 and 3.2eV, in agreement with the literature data [20, 21]. The plot feature illustrates that the as obtained WO$_3$ films behaves as an indirect semiconductor between about 3.3 and 4.0 eV [20].
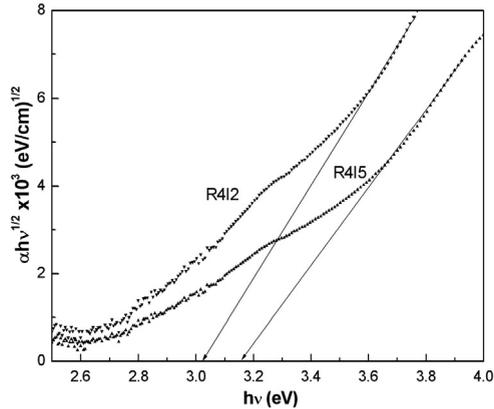
Figure 5. Plot of $(\alpha h\nu)^{1/2}$ *vs* hν for WO$_3$ films.

The X-ray diffraction indicates that peroxotungstic acid precursor is amorphous, whereas the WO$_3$ films deposited on conductive glass are crystallized (Figure 6).
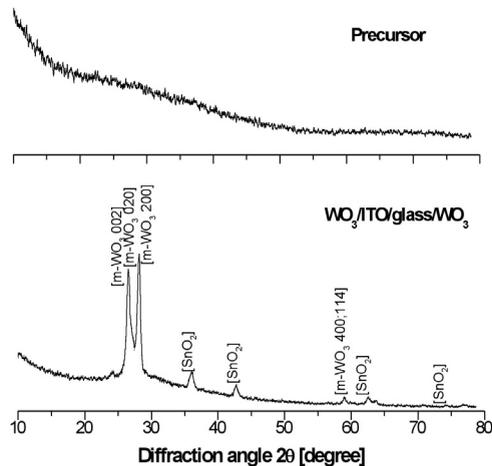
Figure 6. XRD patterns for PTA precursor and the corresponding heterostructure WO$_3$/ITO/Glass/WO$_3$ (film R4I5).

The XRD pattern contains the characteristic diffraction lines of the conductive substrate identified as being cubic SnO_2 (JCPDS 33-1374) and the diffraction lines of monoclinic WO_3 (JCPDS 72-0677). One can be noted that, due to the crystalline structure of the substrate, the growth of WO_3 films seams to be oriented alongside the (200) reflection plane.

The SEM images illustrate that WO_3 film consists on nano-metric particles that creates a homogeneous surface (Figure 7). A small tendency toward the increase of cracks number with the number of layers could be noticed. More than that, the increase of the annealing temperature from 350^0C to 550^0C, leads to the formation of larger crakes in the WO_3 film.

a

b

c
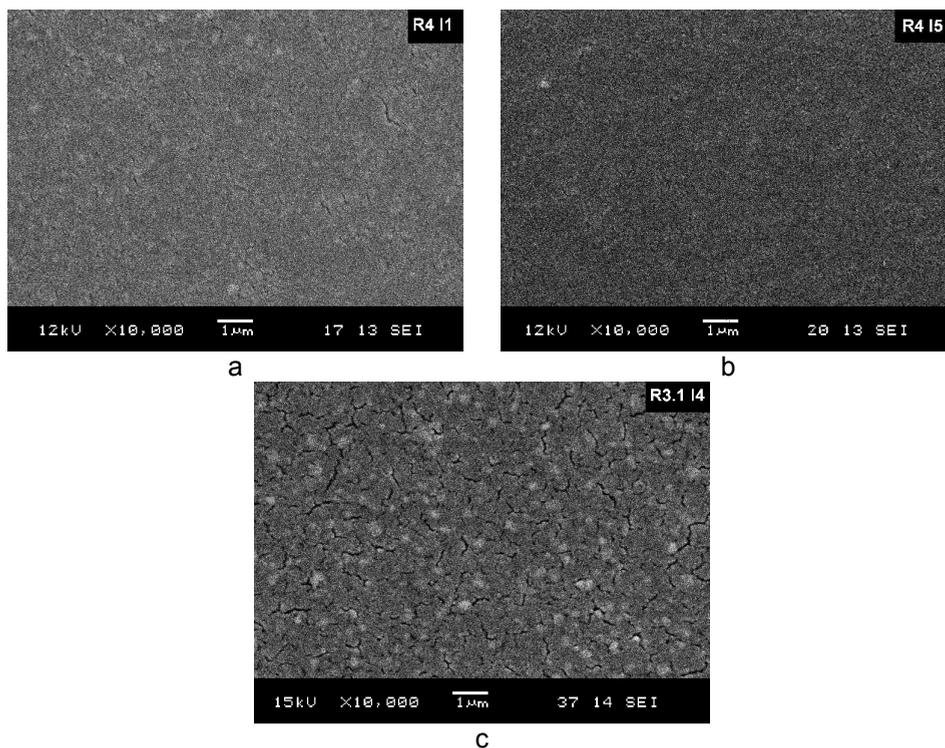
Figure 7. SEM images of WO_3 film surface: (a) one layer ($350°C$)
(b) five layers (350^0C) and (c) one layer (550^0C).

CONCLUSIONS

Homogeneous and adherent WO_3 thin films were obtained by dip coating technique, on conductive glass substrates from aqueous solution of peroxotungstic acid obtained by dissolving fresh prepared tungstic acid into hydrogen peroxide solution. Film thickness increases from ~35 to 135 nm as the number of dip coating deposition cycles increases.

Thermal analysis and FT-IR spectroscopy suggest that the precursor isolated from the colloidal dip-coating solution, corresponds to peroxotungstic acid.

The optical transmittance of WO$_3$ films is influenced by the number of layers. In this respect, the WO$_3$/ITO/Glass/WO$_3$ monolayer has a good transmittance between 450-1000 nm and it decreases as the film thickness increases. The thermal treatment deteriorates the transmission of WO$_3$ films. The calculated values of the optical band gap energy (Eg) vary between 2.9 and 3.2eV, in accordance with the literature data. The reflectance of the as obtained WO$_3$ films is dominant in the blue domain of visible spectra.

SEM images put in evidence that WO$_3$ film morphology depends on the layer number as well as the thermal treatment that both determine the number of cracks and their size.

EXPERIMENTAL SECTION

Preparation. In order to obtain WO$_3$ thin films, the sol-gel solution was prepared starting from an 0.5M aqueous solution of sodium tungstate (Na$_2$WO$_4 \cdot$ 2H$_2$O – Aldrich), which was passed through a cationic exchange resin (~2 ml/min) to yield a yellow pale solution of H$_2$WO$_4$. The freshly prepared tungstic acid was dissolved in hydrogen peroxide (H$_2$O$_2$, Merck) and the as obtained peroxo-tungstic acid (PTA) was stabilized with ethanol addition. In the meantime, the conductive glass substrates (30x30x1mm, Optical Filters Ltd.) were cleaned in acidic bath and alcohol, and dried. From this peroxo-tungstic acid sol, WO$_3$ films were deposited on the conductive support (notated ITO), by dip-coating method, using an withdrawal speed of 4cm/min. The films were dried at 110^{0}C, and annealed at 350-550^{0}C for 30 minutes, in air. Several dipping-drying cycles were used to consolidate the WO$_3$ structure.

Sample characterization. The PTA precursor (dried at ~70°C) was investigated by thermal analysis (Mettler Toledo TGA/SDTA851; heating rate 5^{0}C/min; nitrogen atmosphere) and FT-IR Spectroscopy (JASCO 610 Spectrometer; KBr pellets technique).

UV-Vis spectroscopy (UNICAM Spectrometer UV4, with RSA-UC-40 integrating sphere accessory), X-ray diffraction (DRON 3M Diffractometer, CoKα radiation) and scanning electronic microscopy (JEOL-JSM 5510LV Microscope Au coated samples) were used to characterize the WO$_3$ thin films. The films thickness was estimated by micro-weighing method (Saltec Balance).

ACKNOWLEDGEMENTS

REFERENCES

1. J. Luo, M. Hepel, *Electrochim. Acta*, **2001**, *46*, 2913.
2. S. Wang, X. Shi, G. Shao, S. Duan, H. Yang, T. Wang, *J. Phys. Chem. Solid.*, **2008**, *69*, 2396.
3. J.-C. Yang, P. K. Dutta, *Sensors and Actuators*, **2008**, *136*, 523.
4. A. K. Chawla, S. Singhal, H. O. Gupta, R. Chandra, *Thin Solid Films*, **2008**, *517*, 1042
5. C. Santato, M. Odziemkowski, M. Ullman, J. Augustinski, *J. Am. Chem. Soc.*, **2001**, *123*, 10639.
6. A. I. Gavrilyuk, *Electrochim. Acta*, **1999**, *44*, 3027.
7. P. M. S. Monk, R. D. Partridge, R. Janes, C. G. Granqvist, *Solar Energ. Mater. Solar Cell.*, **2000**, *60*, 201-262.
8. G. Leftheriotis, P. Yianoulis, *Solid State Ionics*, **2008**, *179*, 2192.
9. S. Supothina, P. Seeharaj, S.Yoriya, M. Sriyudthsak, *Ceramics International*, **2007**, *33*, 931.
10. M. Deepa, R. Sharma, A. Basu, S. A. Agnihotry, *Electrochim. Acta*, **2005**, *50*, 3545.
11. Y. Suda, H. Kawasaki, T. Ohshima, Y. Yagyuu, *Thin Solid Films*, **2008**, *516*, 4397.
12. B. Yang, P. R. F. Barnes, W. Bertram, V. Luca, *J. Mater. Chem.*, **2007**, *17*, 2722.
13. L. Muresan, E. J. Popovici, A. R. Tomsa, L. Silaghi-Dumitrescu, L. Barbu-Tudoran, E. Indrea, *J. Optoelec. Adv. Mater.*, **2008**, *10*, 2261.
14. K. Huang, J. Jia, Q. Pan, F. Yang, D. He, *Physica B*, **2007**, *396*, 164.
15. B. Pecquenard, H. Lecacheux, J. Livage, C. Julien, *J. Solid State Chem.*, **1998**, *135*, 159.
16. A. Novinrooz, M. Sharbatdaran, H. Noorkojouri, *Central European J. Phys*, **2005**, 3, 456.
17. M. F. Daniel, B. Desbat, *J. Solid State Chem.*, **1992**, *67*, 235.
18. M. G. Hutchins, O. Abu-Alkhair, M. M. El-Nahass, K. Abd El-Hady, *Mater.Chem. Phys*, **2006**, *98*, 401.
19. P. Sharma, V. Sharma, S. C. Katyal, *Chalcogenide Letters*, **2006**, *3*, 73.
20. K. J. Lethy, D. Beena, R. V. Kumar, V. P. Mahadevan Pillai, V. Ganesan, V. Sathe, *Applied Surface Sci.*, **2008**, *254*, 2369.
21. M. Deepa, A. K. Srivastava, M. Kar, S. A. Agnitory, *J. Phys. D: Applied Phys.*, **2006**, *39*, 1885.

PREPARATION AND CHARACTERIZATION OF MANGANESE DOPED ZINC SULPHIDE NANOCRYSTALLINE POWDERS WITH LUMINESCENT PROPERTIES

ADRIAN-IONUŢ CADIŞ[a,b], **ADRIAN RAUL TOMŞA**[a], **ECATERINA BICA**[a], **LUCIAN BARBU-TUDORAN**[c], **LUMINIŢA SILAGHI-DUMITRESCU**[b], **ELISABETH-JEANNE POPOVICI**[a]

ABSTRACT. Manganese-doped zinc sulphide nanocrystalline powders have been synthesized from zinc-manganese acetate and sodium sulphide, in aqueous solution containing methacrylic acid. Precipitation was performed at low temperature, using the sequential reagent addition technique. Different Mn^{2+} concentrations have been used to control the optical properties of $ZnS:Mn^{2+}$ nanoparticles. All samples were characterized by thermal analysis (TGA), infrared absorption spectroscopy (FT-IR), photoluminescence spectroscopy (PL), scanning (SEM) and transmission electron microscopy (TEM). A correlation between the preparation conditions and optical and morphological characteristics of $ZnS:Mn^{2+}$ powders was established.

Keywords: Zinc sulphide, Mn-doped nanoparticles, Photoluminescence

INTRODUCTION

Nanocrystalline materials have been of interest for more than 25 years [1-3]. The main cause is in their unusual properties based on the high concentration of atoms at interfacial structure and the relative simple ways of their preparation. Recently, nanoparticles of zinc sulphide have become the subject of intense investigations due to their potential applications in catalysis, sensors, nonlinear optics and molecular electronics [4-5]. At the same time, the synthesis of zinc sulphide (ZnS) particles with uniform morphology and narrow size distribution is still in the future and need to be further studied.

[a] *"Raluca Ripan" Institute for Research in Chemistry, "Babes- Bolyai" University, 30 Fântânele, RO-400294 Cluj-Napoca, Romania, cadisadi@chem.ubbcluj.ro*
[b] *Faculty of Chemistry and Chemical Engineering, "Babes-Bolyai" University, 11 Arany Janos, RO-400028 Cluj-Napoca, Romania*
[c] *Electronic Microscopy Centre, "Babes-Bolyai" University, 5-7 Clinicilor, RO-400006 Cluj-Napoca, Romania*

The increasing interest in these materials has lead to the development of a variety of chemical routes to prepare nanoparticles, including sputtering [6], ultrasound irradiation [7], co-evaporation [8], sol–gel method [9], solid-state reaction [10], gas-phase condensation [11], liquid-phase chemical precipitation [12], ion complex transformation [13], microwave irradiation [14] and biological synthesis [15]. From all these works, it has been found that particle size and luminescent properties of ZnS powders depend strongly on the specific preparation method and the applied experimental conditions.

This paper is the first in the series dedicated to the comparative investigation of luminescent and morphostructural properties of nanocrystalline ZnS:Mn powders obtained by different synthesis routes. In this respect, attempts to obtain manganese doped ZnS nanoparticles are performed by precipitation, using the sequential reagent addition technique (SeqAdd). In order to control the particle morphology and size, methacrylic acid is used as passivating agent. A systematic investigation on the influence of Mn-concentration on the photo-luminescence properties of nanocrystalline ZnS:Mn^{2+} is reported. A variety of methods including scanning electron microscopy (SEM), Fourier transform infrared spectroscopy (FTIR), and photoluminescence spectroscopy (PL) were used to characterise the ZnS:Mn nanoparticles.

RESULTS AND DISCUSSION

The goal of our study was to obtain luminescent manganese doped zinc sulphide ZnS:Mn^{2+} nanoparticles with controlled particle dimensions. In this purpose, attempts were made to prepare ZnS:Mn^{2+} powders, starting from Zn-Mn acetate mixture and sodium sulphide, in presence of methacrylic acid as particle size regulating agent. Precipitation was performed at low temperature, using SeqAdd technique. Zn-Mn acetate mixtures with variable compositions were used to obtain ZnS nanoparticles with variable Mn-doping level. The as obtained precipitation product can be considered as Zn-Mn double sulphide and the chemical process can be described by the overall equation:

$$(1\text{-}x)Zn(CH_3COO)_2 + xMn(CH_3COO)_2 + Na_2S \longrightarrow (1\text{-}x)ZnS \cdot xMnS + 2CH_3COONa$$

In this manner, a series of 6 samples was prepared from mixture containing the following Mn/(Zn+Mn) ratios: 0 mol% (CAI17), 5.6 mol% (CAI19), 11.0 mol% (CAI73), 16.4 mol% (CAI21), 21.8 mol% (CAI20) and 25.0 mol% (CAI77). Mention has to be made that, the amount of incorporated Mn is about 0.1% of its concentration, as illustrated by the ICP measurements.

The as prepared ZnS powders show a high capacity to absorb anionic impurities from the precipitation medium, as exemplified by thermal analysis and FTIR spectroscopy.

The thermal behaviour of ZnS:Mn^{2+} powders was investigated in the 25-1100°C range, under N$_2$ flow. Thermogravimetric (TGA) and differential thermogravimetric (DTG) curves of ZnS powder are depicted in Figure 1. There are four major weight loss steps i.e. (1) - 7.2% at 20-188°C; (2) -9.9% at 188-300°C; (3) - 9.9 % at 300-850°C and (4) over 850°C that could be associated with: (1) removal of physically adsorbed water; (2) thermal dissociation of the acetate species adsorbed on the particle surface; (3) thermal dissociation and removal of organic compound and (4) sublimation of zinc sulphide, facilitated by the N2 flow.
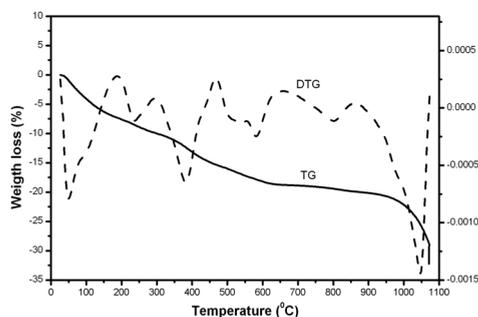
Figure 1. TGA and DTG curves for ZnS:Mn powder (CAI21)
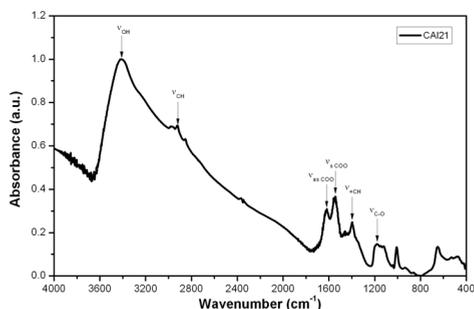
Figure 2. FT-IR spectrum of ZnS:Mn^{2+} sample (CAI21)

The FT-IR spectrum of ZnS:Mn^{2+} powder show the characteristic vibration bands for metal acetate, water and methacrylic acid, ionic or molecular compounds adsorbed from the precipitation medium (Fig.2.). The most important absorption bands are assigned as follows: hydroxyl groups (O-H) (between 3000 and 3600 cm^{-1}), CH$_3$ bending modes (950-1100 and 2800-3000 cm^{-1}), H$_2$O and COO group (between1300 and 1600 cm^{-1}) and C=C and =CH groups (1000-1200 cm^{-1}) [16].

Mention has to be made of the large surface area of powders determines a high amount of anionic species to be adsorbed from the precipitation medium. In spite of the fact that all samples were carefully washed and centrifuged, the contaminants removal can not be completely done, due to the ZnS hydrolysis.

The as prepared manganese doped zinc sulphide powders show photoluminescence properties under ultraviolet excitation. Figure 3 shows the emission spectra (λ_{exc} = 335 nm) for samples synthesised from acetate

mixtures with different Mn^{2+} concentrations. Nanocrystalline $ZnS:Mn^{2+}$ shows a weak blue emission (430 nm) and an orange emission (600 nm) under 335 nm excitation. The blue emission can be assigned to a defect-related emission of the ZnS host-lattice whereas the orange emission can be attributed to the $^4T_1$-$^6A_1$ transition of the Mn^{2+} ion.

The sample without Mn^{2+} shows only the ZnS-related blue emission. As soon as Mn^{2+} is incorporated in the ZnS nanoparticles, the intensity of the blue emission decreases and the Mn^{2+} emission comes up, since the energy transfer between ZnS host and Mn^{2+} impurity is very efficient. With an increasing Mn^{2+} concentration, the characteristic 600 nm emission becomes stronger.
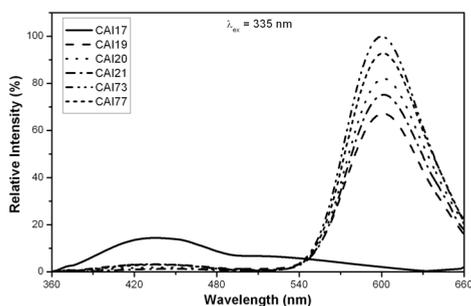
Figure 3. Emission spectra of $ZnS:Mn^{2+}$ powders obtained from acetate mixtures with various Mn^{2+} concentration.
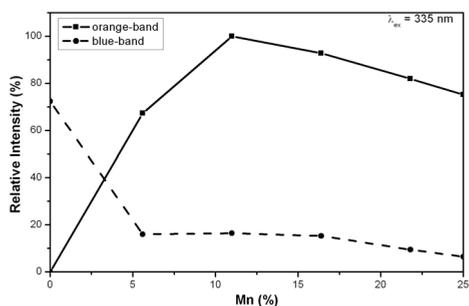
Figure 4. Relative intensity of the orange and blue bands *versus* Mn concentration (blue band is 5 times multiplied)

In figure 4, the luminescence intensity of the orange and blue bands is plotted as a function of the Mn/(Zn+Mn) ratio from acetate solution. The orange band intensity increases with Mn^{2+} concentration, in parallel with the increase of the emission centres numbers. At higher Mn-amounts, the luminescence intensity starts to decrease due to the mutual interaction between the doping (activator) ions (concentration quenching). The maximum intensity is reached at about 11% Mn^{2+} and corresponds to the optimum ratio between the number of the emission centres and the quenching ones. The blue band intensity decreases continuously with increasing Mn^{2+} amount, due to the decrease of the numbers of self activated centres related with the lattice defects of the zinc sulphide.

Usually the PL properties of ZnS powders are connected with a high temperature firing stage. In this case, the nanostructure state of ZnS powders determines the unexpected intense luminescence.

The morphology and particle dimensions were put in evidence by scanning (SEM) and transmission (TEM) electron microscopy investigations. The SEM image of CAI21 sample shows that ZnS:Mn^{2+} powder consists of 1-3 µm aggregates of tightly packed particles with sizes under 20 nm (Fig. 5). The TEM image of the same sample illustrates that in fact, the ZnS:Mn^{2+} powder consists from very small particles (quantum dots) with diameters less than 3 nm. Due to the high surface area, these nanoparticles show a strong tendency toward agglomeration to much larger particles.
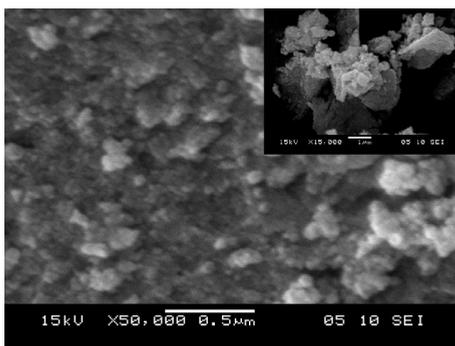
Figure 5. SEM image of ZnS:Mn^{2+} sample (inset scale bar = 1 µm)
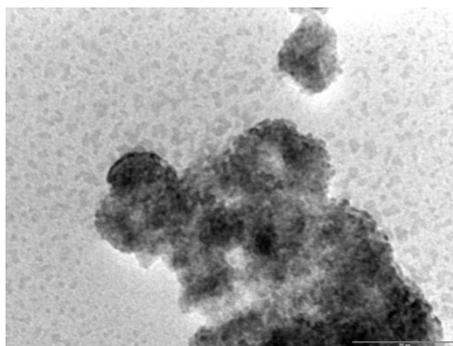
Figure 6. TEM image of ZnS:Mn^{2+} (scale bar=50 nm)

CONCLUSIONS

Manganese doped ZnS nanoparticles were obtained by precipitation, using the sequential reagent addition technique (SeqAdd). In order to control the particle morphology and size, methacrylic acid was used as particle regulating agent. The influence of Mn concentration on the luminescence properties of ZnS:Mn^{2+} nanocrystals was investigated. Photoluminescence measurements show that the as obtained ZnS:Mn nanopowders exhibit a strong orange emission centred at 600 nm that is related with the Mn emission centres. The maximum intensity is reached at about 11% Mn^{2+} in the Zn-Mn acetate mixture and corresponds to the optimum ratio between the number of the emission centres and the quenching ones. The strong PL of the un-annealed ZnS:Mn^{2+} powder could be associated with the particle nano-dimension.

Although ZnS:Mn^{2+} powders are formed from nano-sized crystallites (about 3 nm), they are tightly packed into larger and irregular shaped particles. The large surface area explains the high absorption capacity of the ZnS powder, as illustrated by TGA and FTIR investigations.

Supplementary work has to be done in order to improve the ZnS:Mn^{2+} powder dispersability.

EXPERIMENTAL SECTION

ZnS powders were prepared by precipitation, using SeqAdd technique, from Zn-Mn acetate and sodium sulphide in aqueous medium, at low temperatures (5°C). For this purpose, Zn-Mn acetate mixture containing 5.6, 11.0, 16.4, 21.8 and 25.0 mol Mn/100 mol (Zn+Mn) was prepared from 1M $Zn(CH_3COO)_2$ and 1M $Mn(CH_3COO)_2$ solutions and it was diluted with deionised water containing α-methacrylic acid (MA). The aqueous solution of Na_2S was added to the above mixture solution and vigorously stirred for 30 min. The resulting powder was washed and centrifuged, and finally dried at 80°C under vacuum. The wash process was performed with deionised water and isopropyl alcohol. As a comparison, pure ZnS nanoparticles were also prepared using the above method.

A METTLER-TOLEDO TGA/SDTA851 thermogravimeter was used for thermal and differential thermal gravimetry (TGA-DTG). The measurements were performed in alumina crucibles, in nitrogen flow (20 mL/min), with a heating rate of 5°C/min. Infrared absorption spectra (FTIR) of the samples prepared in KBr pellets were registered on a NICOLET 6700 FT-IR Spectrometer. Photoluminescence (PL) spectra were registered with JASCO FP-6500 Spectro-fluorimeter Wavel equiped with photomultiplier PMT R928 (Farbglasfilter WG 320-ReichmannFeinoptik) and were normalized to the maximum intensity of the best sample (CAI73). The scanning electron microscopy (SEM) images were obtained with a JEOL–JSM 5510LV electron microscope using Au-coated powders. The accelerating voltage was 20 kV. The transmission electron microscopy (TEM) was performed with JEM JEOL 1010 microscope. The accelerating voltage was 20 kV.

ACKNOWLEDGMENTS

REFERENCES

1. A. Henglein, *Berichte der Bunsengesellschaft für Physikalische Chemie*, **1982**, *86*, 301.
2. H. Gleiter, *Progress in Materials Science*, **1989**, *33*, 223.
3. L. F. Chen, Y. H. Shang, J. Xu, H. L. Liu, Y. Hu, *Journal of Dispersion Science and Technology*, **2006**, *27*, 839.

4. J. Wen, G. L. Wilkes, *Chemistry of Materials*, **1996**, *8*, 1667.

5. M. Miyake, T. Torimoto, M. Nishizawa, T. Sakata, H. Mori, H. Yoneyama, *Langmuir*, **1999**, *15*, 2714.

6. S. K. Mandal, S. Chaudhuri, A. K. Pal, *Thin Solid Films*, **1992**, *350*, 209.

7. A. R. Tomsa, E. J. Popovici, A. I. Cadis, M. Stefan, L. Barbu-Tudoran, S. Astilean, *Journal of Optoelectronics and Advanced Materials*, **2008**, *10*, 2342.

8. R. Thielsch, T. Bohme, H. Bottcher, *Physica Status Solidi A*, **1996**, *155*, 157.

9. B. Bhattacharjee, D. Ganguli, S. Chaudhuri, A. K. Pal, *Thin Solid Films*, **2002**, *422*, 98.

10. P. Balaz, E. Boldizarova, E. Godocıkova, J. Briancin, *Materials Letters*, **2003**, *57*, 1585.

11. J. C. Sanchez-Lopez, A. Fernandez, *Thin Solid Films*, **1998**, *317*, 497.

12. J. F. Suyver, S. F. Wuister, J. J. Kelly, A. Meijerink, *Nano Letters*, **2001**, *8*, 429.

13. W. B. Sang, Y. B. Qian, J. H. Min, M. D. Li, L. L. Wang, W. M. Shi, Y. F. Liu, *Solid State Communications*, **2002**, *121*, 475.

14. Y. Jiang, Y. J. Zhu, *Chemistry Letters*, **2004**, *33*, 1390.

15. H. J. Bai, Z. M. Zhang, J. Gong, *Biotechnology Letters*, **2006**, *28*, 1135.

16. N. B. Colthup, L. H. Daly, S. E. Wiberley, "Introduction to Infrared and Raman Spectroscopy", Academic Press, New York, **1964**.

ELECTRICAL CHARACTERISTICS OF A BIOBATTERY WITH STAPHYLOCOCCUS AUREUS

COSMIN CĂȚĂNAȘ[a], **MIHAI MOGOȘ**[a], **DANIEL HORVAT**[a], **JAKAB ENDRE**[b], **ELEONORA MARIA RUS**[a], **IULIU OVIDIU MARIAN**[a]

ABSTRACT. A homemade biobattery was studied from electrical point of view. The open circuit voltage for a 0.2 mA short circuit current was of 0.6 V. The maximum power for an internal resistance of 1.1 kΩ and a concentration of 10^9 cells/cm^3 of *Staphylococcus aureus* was of 17.57 µW.

Keywords: biobattery, electrical power, bacteria, Staphylococcus aureus.

INTRODUCTION

In the last years, microbial fuel cells (MFCs) have received a great deal of attention as a promising solution for renewable energy generation and waste disposal [1-6]. A MFC converts energy, available in a bio-convertible substrate, directly into electricity through the catalytic activities of microorganisms.

It can be said that the MFCs are a hybrid of biological and electro-chemical reactors. By this dualistic nature, MFCs offer the advantage of utilizing a wide range of organic compounds as fuel, and exploit the value of electro-chemical cells by direct generation of electricity [7].

In a MFC, electricity is being generated in a direct way from biowastes and organic matter. This implies that the overall conversion efficiencies that can be reached are potentially higher for MFCs compared to other biofuel processes.

Parameters influencing the overpotentials at the anode are the electrode surface, the electrochemical characteristics of the electrode, the electrode potential, and the kinetics together with the mechanism of the electron transfer and the current of the MFC.

Mediators are important in MFC cells that use microorganisms such as *Escherichia coli*, *Pseudomonas*, *Proteus*, and *Bacillus* species that are unable to effectively transfer electrons derived from central metabolism to the

[a] *Babeş-Bolyai University, Faculty of Chemistry and Chemical Engineering, Romania, Cluj-Napoca, Arany Ianos, 11 iomar@chem.ubbcluj.ro*
[b] *Babeş-Bolyai University, Center for Molecular Biology, Romania, Cluj-Napoca, Treboniu Laurian, 42*

outside of the cell. Common electron shuttles include thionine, benzylviologen, 2,6-dichlorophenolindophenol, 2-hydroxy-1,4-naphtho-quinone and various phenazines, phenothiazines, phenoxoazines, iron chelates and neutral red [8]. These electron shuttles are typically capable to cross the cell membranes, accepting electrons from one or more electron carriers within the cell, exiting the cell in the reduced form and then transferring electrons onto the electrode surface. The critical issue with mediated electron transfer is the diffusion of the shuttle out of the biofilm or the bacterial environment [9].

There is a report on the bacteria, *Rhodoferax ferrireducens* that can be used in microbial fuel cells effectively without a mediator [10].

Oxygen is generally used as the electron acceptor for the cathodic reaction in MFCs. Graphite is a commonly used electrode material. To improve catalytic activity, graphite can be modified with platinum [11].

Various metals (copper, gold, palladium/cobalt, molybdenum, tungsten, and manganese) and their complexes have been investigated as replacements for expensive platinum in the cathode [11-13].

Because the power output of MFCs is low relative to other types of fuel cells, reducing their cost is essential, if power generation using this technology is to be an economical method of energy production. Further research is required to enhance the power production.

In this study, we investigate the performance of a biobattery with *Staphylococcus aureus* bacteria without mediator in the original arrangement of electrode materials at anode compartment because the biobatteries are less investigated at this moment.

RESULTS AND DISCUSSION

The purpose of the experiments was to measure the open circuit voltage, the short circuit current and to plot the power curve of the biobattery. The bacteria used in the experiment were *Staphylococcus aureus* and the substrate was the sodium acetate.

$FeCl_3$ was used as a cathode mediator in order to improve oxygen reduction kinetics [14-15] and acetate was used as substrate in the anodic compartment. The purpose of the experiment was to measure the voltage between the two compartments at 2 different concentrations of acetate in the absence and presence of the bacteria. The activation of the biobattery has been achieved by adding the bacterial solution. After a few seconds it was observed the bubbling process on the anode rods electrode material due to the carbon dioxide gas resulted from the bacterial activity.

The pH of first solution was 8.6 and for the second solution 8.9.
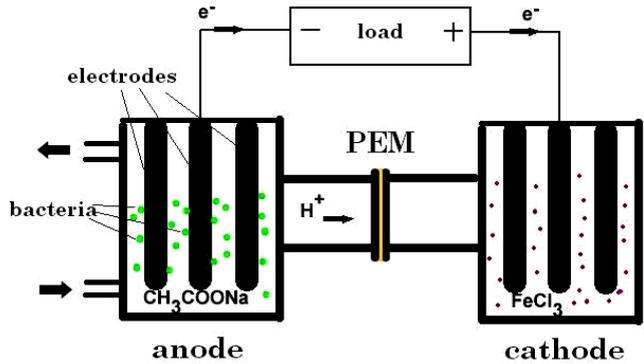
Figure 1. Biobattery representation

In the first experiment by monitoring the cell voltage for 5 hours, a drift of OCV (open circuit voltage) appears from 0.46V to 0.42 V before activation. A maximum peak of 0.6 V was measured after biobattery activation. The short circuit current was of 0.2 mA. (Figure.2a).
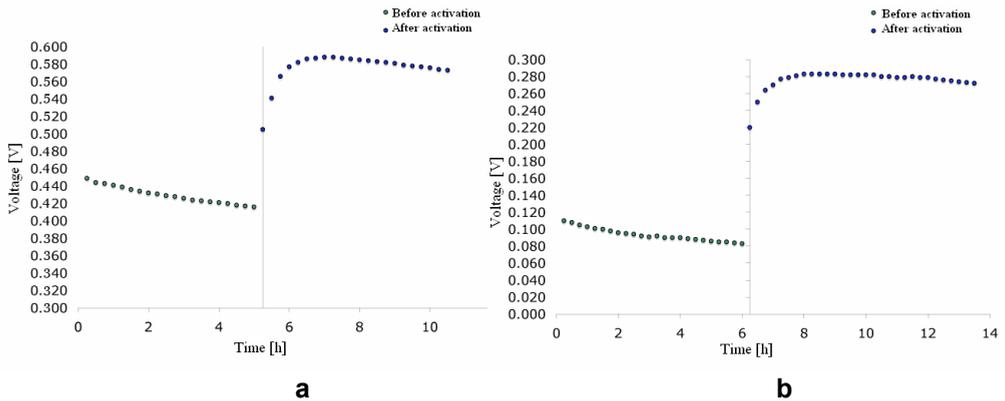
Figure 2. Voltage-time dependency.
a) for 0.05M sodium acetate solution b) for 0.1M sodium acetate solution

In the second experiment before activation the same drift appear (about 40mV) and after activation we measured a maximum cell voltage of 0.3 V and the short circuit current of 0.2mA (Figure 2b). In both cases the open circuit voltage remains at the constant values of 0.56V respectively 0.26 V for one month. Current-time curve and power curve, was recorded for the biobattery with increased OCV.
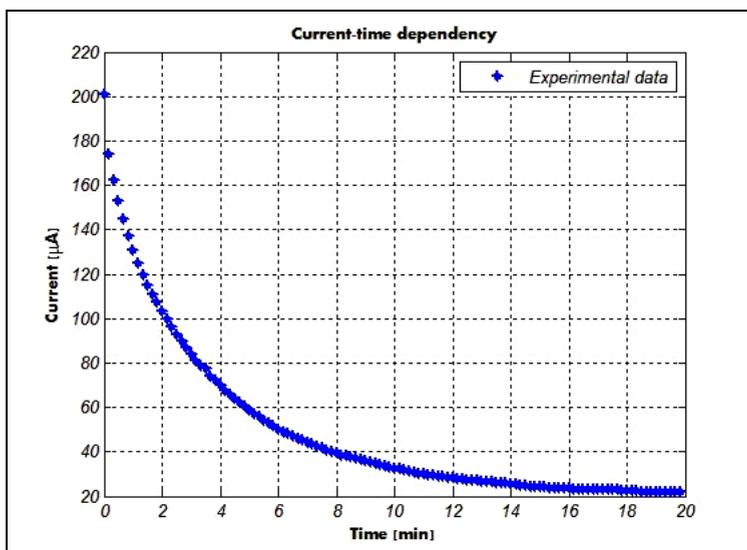
Figure 3. Short circuit current-time dependency
0.05M sodium acetate solution

Initially, after the biobattery activation, a peak current of about 200 µA was registered. After 20 minutes, the limit current of about 20 µA was reached in agreement with the last point of the power curve (Figure 4).
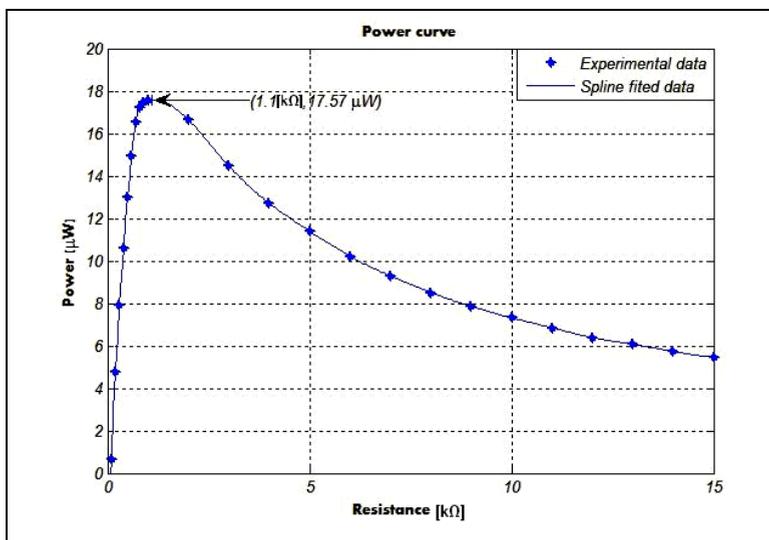
Figure 4. Power curve 0.05M sodium acetate solution

As we reduce the external resistance, a decrease of the voltage was recorded. In this way, we looked for having the smallest possible drop in voltage as the current is increased in order to attain the maximum power production over the investigated range of interest.

The internal resistance of the battery and the maximum power generated were calculated by using the Mathworks MATLAB® environment for processing the experimental data. Spline functions have been used to approximate the power curve. (Figure 4).

All of the equipment used was sterilized with hydrogen peroxide after the experiments.

CONCLUSIONS

The maximum power of the biobattery was of 17.57 µW, achieved at the internal resistance of 1.1 kΩ and for the external resistance of about 15 kΩ the minimum power reached was 5.45 µW, in the case of 0.05M substrate concentration in anode compartment.

The value of the OCV remained at the constant value of about 0.56 V for a month. The difference which appears in OCV in both experiments can be explained by decreasing of the bacterial activity whit pH increase.

The biobatteries represent a viable method of generating electricity from chemical energy. Further research must be done with the purpose of reducing the dimensions of the biobattery for possible applications in medicine and other fields.

EXPERIMENTAL SECTION

An electrochemical cell has been built with two chambers separated by a Nafion proton exchange membrane (Figure 1). Nine graphite rod electrodes of 6 mm in diameter and10 cm in length have been used for each chamber. For the anode compartment a 300 ml sodium acetate solution 0.05 M and 0.1 M respectively, has been combined with 2 ml of *Staphylococcus aureus* (10^9 cell/ml concentration). For the cathode compartment, 300 ml of 1 M $FeCl_3$ solution was used.

The circuits which contain a biobattery and multimeters were connected to a computer with continuous data acquisition software.

The used bacteria were *Staphylococcus aureus*. The bacteria posed no threat to the working environment because they were non sporogenous.

Bacterial strains. Both used bacterial strains, the UCLA 8076 (University of California, Los Angeles, USA) [16] and the 1190R (Semmelweis University, Budapest, Hungary) [17], were heterogeneous MRSA (methicillin-resistant Staphylococcus aureus)strains. These strains are preserved in glycerol (25% final concentration) at -80°C and prepared as follows: 5ml of overnight bacteria culture at 37°C in LB broth (Gibco BRL, Life Technologies, Paisley, Scotland)

were centrifuged in 15ml centrifuge tubes in a Sigma 1-18K centrifuge (Sigma Laborzentrifugen, Osterode am Harz, Germany –5,500 rpm, 10 min., room temperature) and the pellet was resuspended in 500µl sterile 50% glycerol.

The thawed bacteria were cultured overnight in 5ml of Mueller Hinton broth (Fluka, Buchs, Switzerland) into a Certomat BS-T incubation shaker (Sartorius Stedim Biotech, Aubagne, France) at 37°C, 150 rpm until the culture reached an OD_{600} of 0.8-1.0 (Spekol UV VIS 3.02, Analytic Jena, Jena, Germany). A loop of bacterial suspension was passed on Mueller Hinton agar (Fluka, Buchs, Switzerland) to maintain the culture for further analysis. The bacteria were cultured also on blood agar plates (Fluka, Buchs, Switzerland) and confirmed using colony morphology method.

REFERENCES

1. K.J. Chae, M. Choi, F.F. Ajayi, W. Park, I.S. Chang and I.S. Kim, *Energy & Fuels*, **2008**, *22,* 169.

2. B.H. Kim, I.S. Chang, G.M. Gadd**,** *Appl. Microbiol. Biotechnol.,* **2007**, *76,* 485.

3. B.E. Logan, *Water Science & Technology*, **2005**, *52*, 31.

4. B.E. Rittmann et all., *Environ. Sci. Tech.*, **2006,** *15*, 1097.

5. D.R. Lovley, *Microbiology*, **2006**, *4*, 497.

6. A.K. Shukla, P. Suresh, S. Berchmans, A. Rajendran, *Current Science*, **2004**, *87*, 455.

7. A.K. Marcus, C.I. Torres, B.E. Rittmann, *Biotechnology and Bioengineering,* **2007,** *98*, 1171.

8. K. Rabaey, W. Verstraete, *TRENDS in Biotechnology*, **2005**, *23,* 291.

9. S.E. Childers, S. Ciufo, D.R. Lovley, *Nature,* **2002**, *416*, 767.

10. A.K. Shukla, P. Suresh, S. Berchmans and A. Rajendran, *Current Science,* **2004**, *87*, 455.

11. T.H. Pham, J.K. Jang, I.S. Chang, and B.H. Kim, *J. Microbiol. Biotechnol.,* **2004**, *14*, 324.

12. K.H. Kang, J.K. Jang, T.H. Pham, H.I. Moon, S.B. Chang, H. Kim, *Biotechnol. Lett.,* **2003**, *25,* 1357.

13. I.S. Chang, J.K. Jang, G.C. Gil, M. Kim, H.J. Kim, B.W. Cho, *Biosens. Bioelectron.,* **2004**, *19*, 607.

14. S. Cheng, H. Liu, B.E. Logan, *Environ. Sci.Technol.,* **2006**, *40*, 364.

15. B.H. Kim, H.J. Kim, M.S. Hyun, D.H. Park, *J. Microbiol.Biotechnol.,* **1999**, *9*, 127.

16. J.M. Swenson, F.C. Tenover, *J. Clinical Microbiology*, Cefoxitin Disk Study Group, **2005**, *43(8)*, 3818.

17. L. Majoros, E. Papp Falusi, I. Andriko, F. Rozgonyi, *Acta Microbiologica et Immunologica Hungarica*, (**1996**) 43(2-3):160.

MODELING AND SIMULATION OF CARBON DIOXIDE ABSORPTION IN MONOETHANOLAMINE IN PACKED ABSORPTION COLUMNS

ANA-MARIA CORMOS[a], JOZSEF GASPAR[a], ANAMARIA PADUREAN[a]

ABSTRACT. Computer-based process simulations are today recognized as an essential tool to be applied in chemical process industries. For this paper a mathematical model is needed to describe closer the real physical – chemical processes that take place in a reactor (packed absorption column) used for carbon dioxide absorption in mono-ethanolamine aqueous solution.

The mathematical model was developed for analyzing absorption rate and understanding of micro level interaction of various processes taking place inside de absorption column. The modeling includes transfer processes: mass and heat to study the coupled effect of temperature and concentration on the rate of absorption. The reaction kinetics and the vapor-liquid equilibrium (VLE) are other important parts of the mathematical model. The developed equations include both ordinary differential equations and partial differential equation. The discretization was used to transform partial differential equations in ordinary ones.

The evolutions (in time and space) of the processes parameters (liquid and gaseous flows, composition of the streams, temperatures etc.) were studied for carbon dioxide absorption process.

Keywords: Chemical absorption, Packed column, Stationary-dynamic model

INTRODUCTION

The protection of the environment is a significant problem of modern human society for a sustainable development. For environmental protection and climate change mitigation, the reports of Intergovernmental Panel on Climate Change established on scientific basis that climate change and rising of global temperature levels noticed in the past 50 years are undoubteful linked with human activity and greenhouse gas emissions (mainly carbon dioxide) [1]. At the same time with realizing the danger there had been adopted strict laws to control the emission of polluting substances. From different greenhouse gases, the most important from the volume of emissions is carbon dioxide.

---

[a] *Babes-Bolyai University, Faculty of Chemistry and Chemical Engineering, Kogalniceanu Street, No. 1, RO-400084 Cluj-Napoca, Romania, cani@chem.ubbcluj.ro*

For the limitation of climate changes, the goal is to reduce the emission of carbon dioxide by capture and storage techniques. For carbon dioxide capture there are multiple technological options: capture from combusted gases resulted after the burning of fuels (post-combustion capture), capture before the burning of fuels (pre-combustion capture), or the oxy-combustion technique where the fuels are burned in oxygen, not in air, and after the condensation of the water from the burnt gases carbon dioxide can be captured and stored because it is the main component. Once carbon dioxide captured, has to be stored in safety under special conditions for a long period of time [2,3].

Nowadays the absorption of carbon dioxide in alkanolamines is the most common technology and one of the few technological options viable for large CO_2 removal process (to be applied for instance in power generation sector). Economic studies show that this method will be competitive also in the future. To extensive laboratory work, modeling and simulation of absorption process are needed in order to evaluate the process.

This paper aims to develop a dynamic mathematical model for carbon dioxide absorption in aqueous solution of mono-ethanolamine in packed absorption columns. The main purpose of the paper is to develop and than to validate a model which can be then used in various operation condition for optimization of techno indicators of carbon dioxide absorption process.

RESULTS AND DISCUSSION

Mathematical model of absorption column

Carbon dioxide absorption using alkanolamines falls in the general category of chemical gas – liquid absorption [4,5]. In Figure 1, a simplified flowsheet of a carbon dioxide capture using mono-ethanolamine (MEA) is presented. The setup consist of 3 major sections [5]: (1) reactor-absorption section (tower column called), (2) the liquid low section consisting the peristaltic pump and (3) gas collection section with the gas flow composition and pressure measurement apparatus. In absorption column with stuffing, the liquid and a gas flowing in opposite directions, enable a chemical component to be transferred from the gas phase to the liquid phase. The gas enters at the base of the absorption column, it flow rates being determined by variable area flow meters. The liquid to the top of the column is similarly metered and falls through the packing where it is contacted with the rising gas.

A mathematical model has been developed for prediction the rate absorption of carbon dioxide into aqueous solution of mono-ethanolamine (MEA). The basic assumption considered for the CO_2 absorption by mono-ethanolamine solution in an absorption column with Raschig rings are presented below:

- Model parameters are constant in the radial cross section of the column (piston-type flow);
- Both gas and solids velocities are considered constant;

- Heat transfer by conduction and radiation are negligible in the axial direction;
- Carbon dioxide solubility in liquid phase is in accordance with the Henry's law;
- Phase liquid is not volatile in the process temperature;
- Chemical reaction takes place only in the film of liquid;
- The absorption columns is operated adiabatic;
- Both phases (liquid and gas) are considered ideal mixtures.
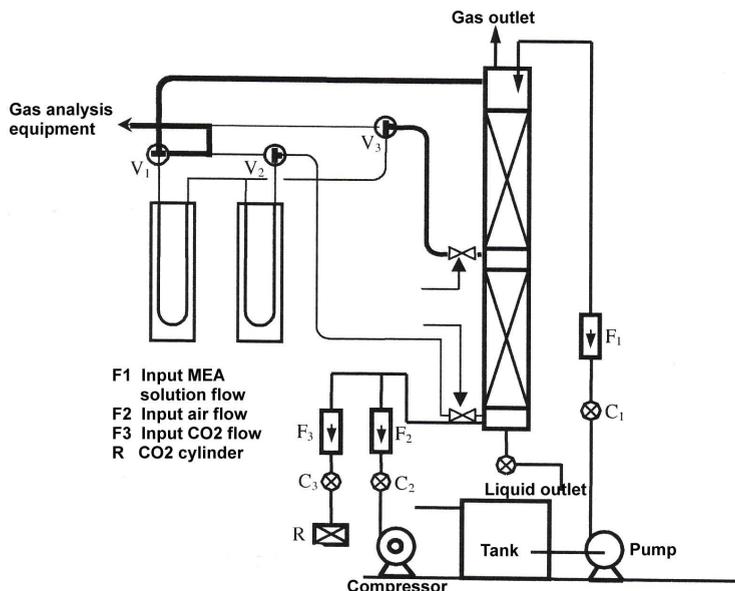
Figure 1. Gas – liquid packed absorption column

Chemical absorption of carbon dioxide can be done using base chemicals like alkaline hydroxides, ammonia or organic compounds (e.g. alkanolamine). The absorption of CO_2 into alkanolamine solution involves a chemical reaction of a weak base (alkanolamine) with a weak acid (CO_2). The chemical equilibrium takes place in the liquid phase, when carbon dioxide is absorbed in an aqueous solution of alkanolamines.

The overall chemical reaction occurring in the liquid phase between CO_2 and mono-ethanolamine (MEA) may be expresses as follow:

$$CO_2 + 2\ RNH_2 \leftrightarrow RNH_3^+ + RNHCOO^-$$

where R indicates $HOCH_2CH_2$-. This chemical reaction is second order, respectively is first order with respect to CO_2 and MEA separately [5], and

the reaction rate (r), can be defined in function of the molar concentration of reactants, as follows: r=k*C_A*C_B [5], where k is the reaction rate constant The temperature dependence of the reaction rate constant is presented bellow [3]:

$$k = 4.4 \cdot 10^8 \cdot e^{\left(\frac{5400}{T}\right)} m^3/mol \cdot s \tag{1}$$

The model equations include both partial differential equations and algebraic equations. The model contains basically mass and heat conservation equations presented below [3,6,7]. A list of abbreviations used is presented at the end of the paper.

The mass balance for liquid phase is described by the equations of consuming both reactants (mono-ethanolamine and carbon dioxide):

$$\frac{\partial C_A}{\partial t} = -v_L \cdot \frac{\partial C_A}{\partial z} - k \cdot C_A \cdot C_B + E \cdot K_G \cdot a_u \cdot \left(C_{AG} - H_{CO_2} \cdot C_A\right)$$

$$\frac{\partial C_B}{\partial t} = -v_G \cdot \frac{\partial C_B}{\partial z} - b \cdot k \cdot C_A \cdot C_B \tag{2, 3}$$

The effect of a chemical reaction is given by the enhancement factor, E, defined as the ratio of the absorption rate of a gas into a reacting liquid to that if there was no reaction [7]. The enhancement factor can be approximated [6,7]:

$$E = \sqrt{k \cdot D_{CO_2,G} \cdot C_B} \Big/ k_L \tag{4}$$

The heat balance equation for the liquid phase is presented in the following equation (the chemical reaction between carbon dioxide and mono-ethanolamine is exothermic):

$$\frac{\partial T_L}{\partial t} = -v_L \cdot \frac{\partial T_L}{\partial z} - \frac{\Delta_R H \cdot k \cdot C_A \cdot C_B}{\rho_{sol} \cdot c_{p_{sol}}} + \frac{h \cdot a_u}{\rho_{sol} \cdot c_{p_{sol}}} \cdot (T_G - T_L) \tag{5}$$

The heat transfer coefficient in the gas phase was found by using the Chilton-Colburn analogy. The value of the heat transfer coefficient depends of the gas density, diffusivity, heat capacity and thermal conductivity.

The mass balance for gas phase is described by the equation of consuming carbon dioxide:

$$\frac{\partial C_{AG}}{\partial t} = -v_G \cdot \frac{\partial C_{AG}}{\partial z} - E \cdot K_G \cdot a_u \cdot \left(C_{AG} - H_{CO_2} \cdot C_A\right) \tag{6}$$

The heat balance equation for the gas phase is presented in the following equation:

$$\frac{\partial T_G}{\partial t} = -v_G \cdot \frac{\partial T_G}{\partial z} - \frac{h \cdot a_u}{c_{p_G} \cdot \rho_G} \cdot (T_G - T_L)$$ (7)

Table 1. Parameters of the model

Absorption column parameters:
  Height
  Diameter
  Specific area
	$H = 1.4\ m$
	$D = 0.075\ m$
	$a_u = 440\ m^2/m^3$

Input flows:
  Gas flow
  Liquid flow
	$F_G = 2*10^{-3}\ m^3/s$
	$F_L = 3.42*10^{-6}\ m^3/s$

Feed composition:
  Gas
  MEA solution
	$Y_A = 0.11$ (molar);
	$C_B = 30\ wt.\ \%$

Input feed temperatures	$T_L = 293\ K$; $T_G = 298\ K$

Density:
  CO2 (at 0 °C and 1 atm) [8]
  Gas mixture [9]
 	
  Aqueous alkanolamine solution [10]
	$\rho_{CO2} = 1.963\ kg/m^3$
	$\rho_{gas} = \Sigma(y_i \cdot \rho_i)\ kg/m^3$
	
	$\rho = 2.45 \cdot C_{BO} + 919.13 \cdot e^{24.23/T_L}\quad kg/m^3$

CO_2 solubility according with Henry's law [10]	$H_{CO_2} = 10^{(5.3 - 0.035 \cdot C_{B0} - \frac{1140}{T_L})}\quad atm \cdot m^3/kmol$
Diffusion coefficient of CO_2 in water [10]	$D_{CO_2,w} = 2.35 \cdot 10^{-6} \cdot e^{\left(-\frac{2119}{T_L}\right)}\ m^2/s$
Diffusion coefficient of CO_2 in amine solution [10,11]	$D_{CO_2,Am.sol} = D_{CO_2,w} \cdot \left(\frac{\mu_{H_2O}}{\mu_{MEA}}\right)^{\gamma}\ m^2/s$
Diffusion coefficient of CO_2 in gas [9]	$D_{CO_2} = 1.38 \cdot 10^{-5} \cdot \left(\frac{p_o \cdot T}{p \cdot T_o}\right)^{3/2}\ m^2/s$
Viscosity: MEA solution [9]	$\ln(\mu_{MEA}) = 0.16 \cdot C_{MEA} - 19.1 \cdot e^{\frac{298.3}{T_L}}\ Pa \cdot s$

Thermal conductivity:
  CO_2 [8,9]*
  Air [8,9]*
	$\lambda_{CO2} = 8 \cdot 10^{-5} \cdot T_G - 0.0071\ W/m \cdot K$
	$\lambda_{air} = 7 \cdot 10^{-5} \cdot T_G + 0.005\ W/m \cdot K$

Specific heat capacity *(J/kgK): $C_p = b \cdot T + cT^2 + a$*	a	b	c
MEA [8]	1411.264	4.7151	0
H_2O [9]	4185	0	0
CO_2 [8]	983.24	0.2605	$-1.86 \cdot 10^{-7}$

***the equation has been obtained via regression of data taken from literature**

The partial differential equations of the mathematical model were transformed in ordinary ones, by discretization. The mathematical model was solved using MATLAB software package (version 2006) to evaluate the rate of CO_2 absorption changes with respect to the MEA concentration decrease in the aqueous solution.

For modeling and simulation of the carbon dioxide absorption in packed columns, the parameters presented in the Table 1 were used.

Model simulation results

The simulation of the mathematical model of CO_2 absorption into aqueous mono-ethanolamine solution show the evolutions (both in time and space) of temperature, and concentration in the liquid and gas phase, in the gas – liquid absorption column. Some of the most representative simulation results are presented in the figures below.
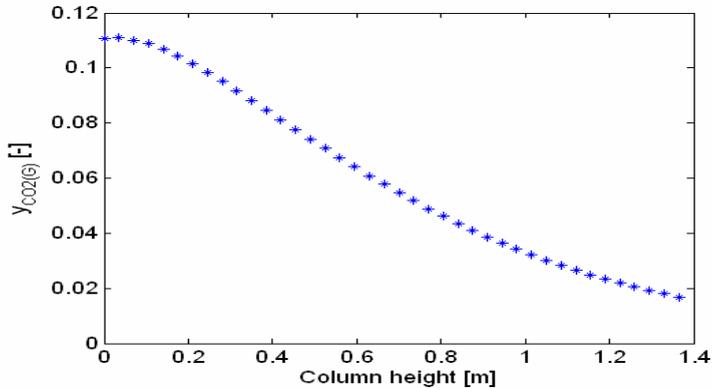
Figure 2. CO_2 concentration (in gas phase) along the column height
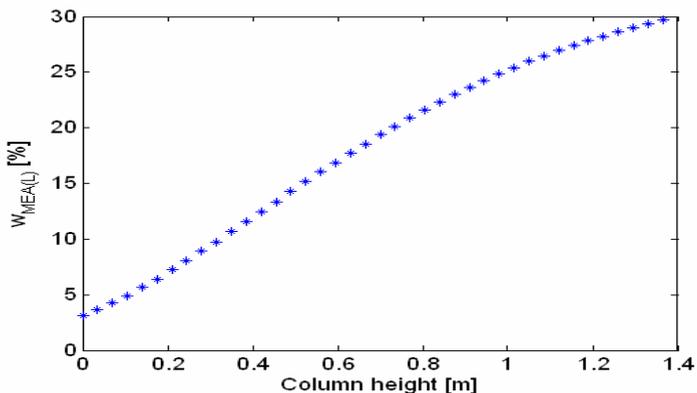
Figure 3. MEA concentration profile along the column height
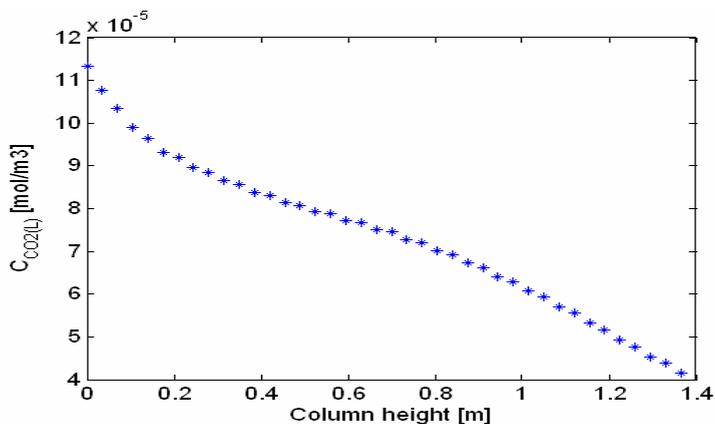
Figure 4. CO_2 concentration (in liquid phase) profile along the column height

In Figure 3 an increasing in the concentration of MEA in liquid phase respectively a decrease of CO_2 in gas and liquid phase against column height is observed. Because the rate of reaction is directly proportional to carbon dioxide concentration in the liquid phase and the concentration of MEA, the rate of reaction increases versus the column height. Figure 2 shows the decreasing of the CO_2 concentration in the gas phase due to the chemical absorption [12, 13].

The temperature profile along the column is presented in Figure 5 (chemical absorption of carbon dioxide is an exothermic process).
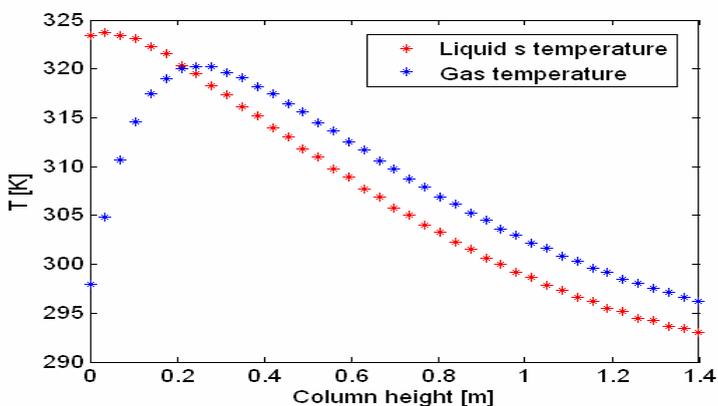
Figure 5. Temperature profile along the column height

The simulation results were compared with data collected from literature [3,12,14] and data obtained (by authors) from simulation of the CO_2 absorption process using ChemCAD, in the same operational conditions, in order to validate the application developed for modeling and simulation of the absorption process.

Table 2. Comparison of data obtained with developed model and ChemCAD software, F_L=3,42·10^{-6} m^3/s, F_G=2·10^{-3} m^3/s.

Parameter	MATLAB	CHEMCAD
Input Concentration of MEA in liquid phase [wt%]	30.00	30.00
Output Concentration of MEA in liquid phase [wt%]	3.11	2.64
Input molar fraction of CO_2 in gas phase [-]	0.110	0.110
Output molar fraction of CO_2 in gas phase [-]	0.0168	0.0100
Input temperature of the liquid flow [K]	293.00	293.00
Output temperature of the liquid flow [K]	323.40	324.78
Input temperature of the gas flow [K]	298	298
Output temperature of the gas flow [K]	296.20	296.76

The good correlation between the results of developed model and ChemCAD model data indicates the accuracy of developed chemical absorption model described above in predicting actual gas-absorption performance of absorption packed column.

The dynamic behavior of the absorption column was also investigated in the presence of the typical process disturbances (e.g. gas and liquid flow variation). Knowledge of the behavior in time to the occurrence of disturbance is important for the process control design and process optimization [9]. Some of the most representative results are presented in the Figures 6 to 8.

Figure 6 shows the effect of the liquid flow increasing on liquid flow's temperature when appear a perturbation. The temperature of the liquid flow at input, at the top of the column, is 293 K and it is increasing to 319.9 K at output, at the bottom, because of exothermic reaction (reaction heat is 65000 kJ/kmole).
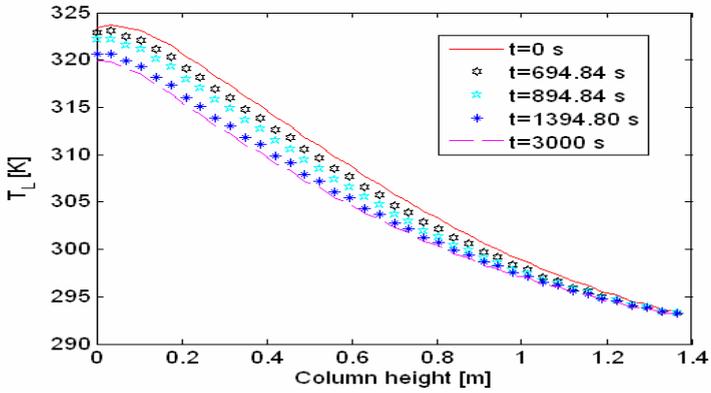
Figure 6. Variation of liquid's temperature ($F_L = F_L + 20$ %)
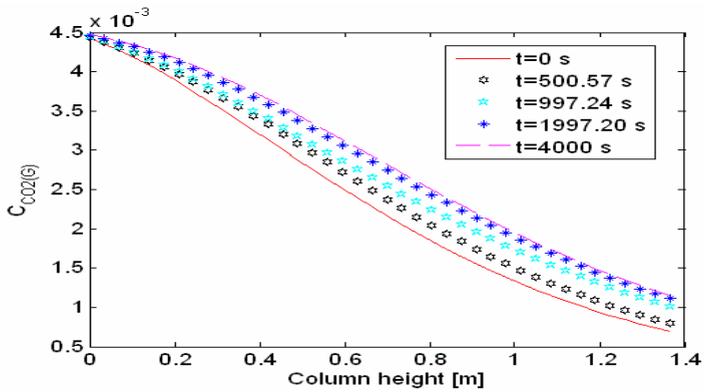
Figure 7. Variation of CO_2 molar fraction in gas phase ($F_G = F_G + 20$ %)
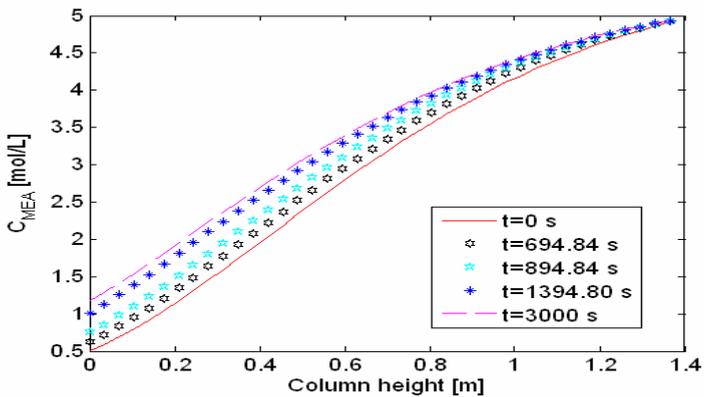
Figure 8. Variation of MEA height concentration ($F_L = F_L + 20$ %)

Figure 7 shows the effect of the gas flow increasing on CO_2 concentration in gas phase. The presence of process perturbations determine a significant increasing of CO_2 output concentration. Figure 8 shows the MEA concentration evolution in time and column's height if the liquid flow increasing. All these stationary and dynamic parameters profiles along the packed absorption column are valuable information for process optimization and to develop a control strategy for the process.

The developed mathematical model will be tuned against experimental data for adjusting the parameters and then it can be used for pre-screening and designing practical CO_2 absorption process in various conditions (laboratory, pilot and industrial size, different solvents and column internals, various operational conditions etc.).

CONCLUSION

A mathematical model was developed for analyzing carbon dioxide absorption rate and understanding of micro level interaction of various processes going inside de reactor (packed absorption column). Simulation of carbon dioxide gas – liquid absorption process in mono-ethanolamine (MEA) was done using Matlab software.

The evolutions of the process parameters (liquid and gaseous flows, composition of the streams, temperatures) were studied during the carbon dioxide absorption process. For verification of the developed model, the simulation results were compared with ChemCAD model simulation.

The mathematical model and the simulation results proved to be a reliable tool for process analyzing and are useful for making preliminary calculations of experimental parameters for the column absorption. Also, the developed model can be used to determine optimal operation conditions and to design the control system.

NOTATION

a_u specific area (m^2/m^3)
A gaseous reactant (CO_2)
b stoichiometric coefficient of B
B liquid reactant (MEA)
C_A concentration of dissolved gas A ($kmol/m^3$)
C_{AG} concentration of A in gas ($kmol/m^3$)
C_B concentration of reactant B ($kmol/m^3$)
C_{B0} initial concentration of reactant B ($kmol/m^3$)
$c_{p,CO2}$ specific heat capacity of CO_2 (J/mol*K)
$c_{p,G}$ specific heat capacity of gas (J/mol*K)
c_{psol} specific heat capacity of solution (J/mol*K)

D column's diameter (m)

$D_{CO2,i}$ diffusion coefficient of CO_2 in substance i (m2/s)

E enhancment factor (-)

F_G flow rate of gas (m^3/s)

F_L flow rate of solution (m^3/s)

h heat transfer coefficient in gas phase (J/s*m^2*K)

H column's height (m)

H_{CO2} Henry's constant [-]

k reaction rate constant (m^3/mol·s)

k_L liquid film mass transfer coefficient (m/s)

K_G overall mass transfer coefficient (m/s)

p_o normal pressure (1 atm)

t time (s)

T_G gas phase temperature (K)

T_L liquid phase temperature (K)

T_o normal temperature (273 K)

v_L axial velocity of liquid film (m/s)

v_G velocity of gas film (m/s)

y_{CO2} molar fraction of CO_2 in gas (-)

z axial coordinate (m)

$\Delta_r H$ heat of reaction (J/kmol)

ρ_g density of gas (kg/m^3)

ρ_{sol} density of solution (kg/m^3)

μ_i viscosity of component i (Pa·s)

ACKNOWLEDGMENTS

REFERENCES

1. Intergovernmental Panel on Climate Change (IPCC), 4-th Assessments Report, Climate Change, **2007**, www.ipcc.ch.

2. International Energy Agency (IEA), Greenhouse Gas Program (GHG), "Oxy-combustion process for CO_2 capture from power plants", Report 2005/9, **2005**.

3. F.A. Tobiesen, "Modeling and Experimental study of Carbon Dioxide Absorption and Desorption", Ph. Thesis, **2007**, chapter 1, 3 and 8.

4. G. Bozga, O. Muntean, "Reactoare chimice – Reactoare eterogene", vol. II, Editura Tehnică, Bucureşti, **2000**.

5. Akanksha, K.K. Pant, V.K. Srivastava, *Chemical Engineering Journal*, **2007**, *133*, 229.

6. J. Gabrielsen, *"CO$_2$ Capture from Coal Fired Power Plants*", Ph. Thesis, **2007**, chapter 3.

7. H. Dang, G.T. Rochelle, *National Conference on Carbon Sequestration*, Washington DC, May 14-17, **2001**.

8. R.H. Perry, D.W. Green, *"Perry's Chemical Engineers' Handbook"*, **1999.**

9. C.F. Pavlov, P.G. Romankov, "*Procese şi aparate în ingineria chimică"*, Editura Tehnică, Bucureşti, **1981**.

10. R. Maceiras, E. Alvarez, M.A. Cancela, *Chemical Engineering Journal*, **2008**, *137*, 422.

11. G.F. Verstege, L.A.J. Van Dijck, W.P.M. Van Swaaij, *Chemical Engineering Journal*, **1996**, 144, 113.

12. A. Aboudheir, P. Tontiwachwuthikul, R. Idem, *Chemindix,* **2007**, *CCU/09.*

13. D.R. Olander, *A.I.Ch.E. Journal*, **1960**, *6*, 223.

14. F. A. Tobiesen, H. F. Svendsen, *A.I.Ch.E. Journal*, **2007**, *53* (4), 846.

RED PEPPER POWDER COLOR MEASUREMENT BY USING AN INTEGRATING SPHERE AND DIGITAL IMAGE PROCESSING

EUGEN DARVASI AND LADISLAU KÉKEDY-NAGY[a]

ABSTRACT. A home made integrating sphere and a commercial digital camera were used to calculate the color characteristics of 16 pepper powder samples. Similar data for the samples were calculated from reflectance spectrum data measurements too, as reference ones. The color parameters calculated with the two methods agree within the experimental errors.

Keywords: red pepper, color, integrating sphere, CIELa*b*, RGB, digital image

INTRODUCTION

Different varieties of pepper (*Capsicum annuum* L.) are largely grown plants for human alimentary consumption. The fruit of the plant is consumed as fine grounded powder, called paprika, added to different foods. The young fruits are green, during the ripening their color gets red due to the deterioration of the chlorophyll and formation of red, orange and yellow colored pigments. About thirty different pigments contribute to the paprika color, mainly from the class of carotenes (β-carotene, α-carotene, lycopin) and oxygenated carotenes, also known as xanthophylls (capsanthin, capsorubin, zeaxanthin, violaxanthin, β-cryptoxanthin). The predominant carotenoid in paprika is capsanthin, exclusive to *Capsicum* species [1,2]. Paprika powder as well as the concentrated paprika extract, called oleoresin, is used mainly as natural colorants added to the foodstuffs, in cosmetics and less as spice or vegetable [3,12]. Since paprika is used as a coloring agent, its market value depends partly on the red color, the color being considered the main quality factor of it. More intensive the red color more valuable the powder.

The paprika red color and tone depend on many factors such as: the pepper brand [4], the growing conditions (soil, temperature, light and humidity), the processing and storage conditions (harvest, milling, dehydration, heat, light, packing etc.)[5,6,10]. On the other hand, during processing and storage, carotenoids are susceptible to degradation, oxidation and isomerization, due to the influence of light, temperature, heat, oxygen, enzymes, metals, etc. fact, which led to the color change, mainly to the redness loss of the powder [7-9,11,12].

---

[a] *Babeş-Bolyai University, Faculty of Chemistry and Chemical Engineering, Department of Analytical Chemistry, Str. Arany János 11, 400028 Cluj-Napoca, Romania*

The color of the peppers can be evaluated from three different aspects: surface color, extractable color and carotenoids profiles, the first two being the standard quality evaluation in the spice industry. The surface color measurements are used to specify colors perceived by the human eye. The visual evaluation of the color depends to a great extent on the individual's eye color perception and training level, the evaluator momentary state of mind, the physical conditions of the observation (light source, illumination and background conditions, etc.). So, each person for the same sample and observation condition will interpret the described color a little differently, the verbal descriptions could be difficult, imprecise and sometimes confusing. In order to avoid the subjective, peculiar color assessment several optical instruments, systems and techniques were developed for objective color determinations of different objects, including pepper, either fruit or grinded powder. The early instruments measured the reflectance of the uniformly illuminated samples (at three different wavelengths or in the whole visible spectral domain) and the RGB and CIELa*b* values were calculated from the reflectance data [13-15]. The data allow the precise calculation of the color parameters of the sample, but only the average ones. Meanwhile many attempts were made in order to replace the classic illumination and detection system. These consists in the replacement of the integrating sphere with a light source which allows diffuse, uniform illumination (as new type of discharge tubes, halogen tungsten lamps with diffuser and multidirectional illumination etc.) as well as the replacement of the vacuum photo detectors with calibrated CCD cameras [16-21]. The use of such camera has several advantages over the vacuum tube detectors, as: eliminate the use of the monochromators or filters, allows the determination of color parameters of each individual point of the surface, the digital image could be easily saved and processed by proper PC software programs.

In principle other digital optical devices, as webcams or still cameras, could be used as photo detectors, their use are not come yet into general use. To our best knowledge the use of commercially available digital camera for determination of the color parameters of foods, including pepper powder, was not reported. The aim of our work is to evaluate the features of an integrating sphere and digital camera as photo detector system for the determination of color characteristics of grounded pepper powder.

INSTRUMENTATION

The experiments were carried out with a home-made integrating sphere by casting of gypsum cubic block, with a spherical inner hole having a diameter of 26 cm (Fig. 1).
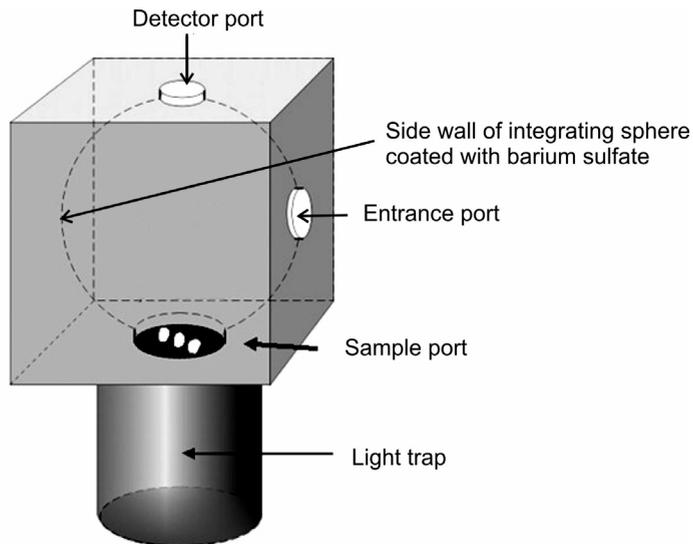
Figure 1. The schematic drawing of the integrating sphere

The inner wall was covered with $BaSO_4$ powder (used as white reference material for reflectance measurement). The sphere was provided with 3 ports, of diameter of 5. 9 cm, each perpendicular to other. The port on the upper side served as observation hole for camera. In the horizontally disposed entrance port was fixed the box of the light source with a 20 W / 12V halogen tungsten lamp provided from a Specol 20 spectrophotometer (Carl Zeiss, Germany), used as stabilized power source too. The third port, on the lower side, and face to face with the first, served for sample introduction. The samples were put on a plastic tray, and lifted upwards till they reach a tangential position to the sphere. Below the tray a light trap was mounted (a black painted plastic pipe, its lower end covered with black velvet). The tray has three vertical holes, which communicate with the light trap disposed beneath the block, serving as the black reference. The photo detector was a commercially available digital camera SONY DSC-H1. The shots were carried out in the automatic adjustment mode of the shutter speed and aperture. The digital image, of 5. 3 megapixels, was saved as . jpg file and transferred to the Pentium III PC for processing. As white reference surface a $BaSO_4$ tablet was photographed together with each pepper sample.

The SFA-01 VIS spectrophotometric module (ICIA, Bucharest, Romania) with a concave diffraction grating and a CCD detector was used for the plot of reflectance spectra of the samples in the spectral domain of 400-700 nm, and 45/0° geometry. The spectrum was recorded in 512 points and saved as a . txt file. The color parameters were calculated from these data and served as reference values for comparison.

CONVERSION OF COLOR SPACES

From the reflectance (R) data the CIE XYZ tristimulus value, the CIELa*b* color coordinates and C, h* color attributes have been calculated [22]. The RGB values of each camera pixel were converted into device-independent CIE XYZ tristimulus values, using a conversion matrix as shown in Equation1.

$$
\begin{bmatrix} X \\ Y \\ Z \end{bmatrix} = \begin{bmatrix} p_1 & p_2 & p_3 \\ q_1 & q_2 & q_3 \\ r_1 & r_2 & r_3 \end{bmatrix} \begin{bmatrix} R \\ G \\ B \end{bmatrix}
$$

(1)

Using a set of paired RGB and CIE XYZ values obtained with the digital camera and reflectance measurements, a cost function was defined and then minimized to obtain an optimized conversion matrix for our system (Fig. 2) [23].
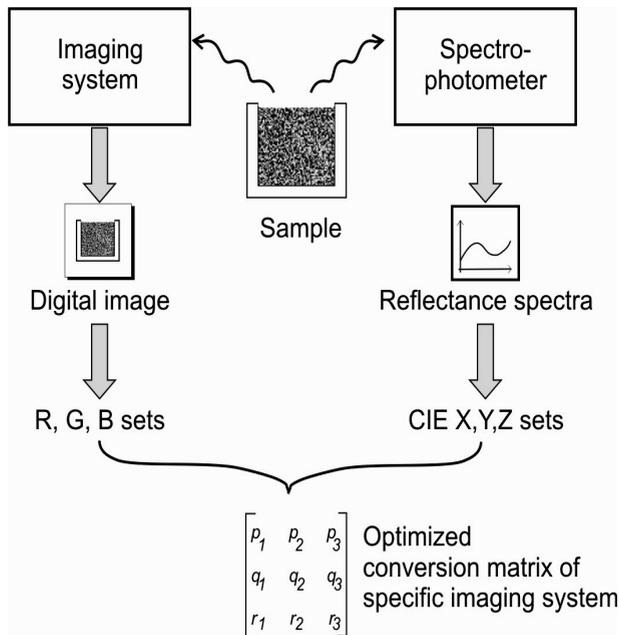
Figure 2. The optimization scheme of the conversion matrix

The cost function for **p** :

$$
(\boldsymbol{p}) = \sum_{i=1}^{n} ((RGB)_i (p_1 \ p_2 \ p_3)^T - X_i)^2
$$

(2)

The solution, which minimizes this function, is:

$$(p_1 \ p_2 \ p_3)^T = K^{-1}\gamma \qquad (3)$$

Where:

$$K = \sum_{i=1}^{n} (RGB)_i^T (RGB)_i$$

$$\gamma = \sum_{i=1}^{n} X_i (RGB)_i^T$$

Similarly, we calculated the optimized second and third row vectors, $(q_1 \ q_2 \ q_3)$ and $(r_1 \ r_2 \ r_3)$, respectively.

SAMPLING AND SAMPLE HANDLING

Thirteen different blend and origin of packed red pepper powders were purchased from the commerce and three samples from individual farmers. The powders were used as purchased, about 0. 5 g was introduced into a small plastic cup, gently pressed in order to obtain a compact smooth surface. The sample cups were introduced in the spectrophotometer and the spectrum has been drown, than it was placed in the integrating sphere and the digital photo was taken. The brand (as indicates the label on the original package) and the appropriate code used in this paper are presented in the Table 1.

Table 1. The pepper samples brand and codes

Nr.	Brand / origin	Code
1	Kalocsai - Csemege	PS1
2	Szegedi - Rózsa	PS2
3	Házi arany - Édesnemes	PS3
4	Fuchs – Édesnemes	PS4
5	Fuchs – Boia de ardei iute	PS5
6	Fuchs – Boia de ardei dulce	PS6
7	Galeo - Boia de ardei iute	PS7
8	Kotányi – Boia de ardei dulce	PS8
9	Cosmin – Boia de ardei dulce	PS9
10	Clever – Boia ardei dulce	PS10
11	Apahida – Boia de ardei dulce	PS11
12	Echom – Boia de ardei dulce	PS12
13	Home made-1 – Boia de ardei dulce (Gheorgheni-area)	PS13
14	Home made-2 – Boia de ardei dulce (Războieni- area)	PS14
15	Home made-3 – Boia de ardei dulce (Cluj-Napoca area)	PS15
16	Kamis Chili – Boia de ardei iute	PS16
17	Idem 1	PS17
18	Idem 1	PS18

53

PROCEDURE

First the white, the black and the color values of the digital image was corrected by using the ColorPilot 4. 80. 01v software package (Two Pilots™, USA, Germany, Russia). The corrected image was then processed with the ImageJ 1. 37v software program (Wayne Rasband, National Institute of Health, USA), the RGB parameters of the selected area were determined. Then the tristimulus values of XYZ and the CIELa*b* chromatic coordinates and of C, h* color attributes have been calculated.

RESULTS AND DISCUSSION

DETERMINATION OF THE PEPPER POWDER COLOR PARAMETERS BASED ON THE REFLECTANCE SPECTRA

The typical reflectance spectra of five selected pepper samples are represented in the Figure 3.
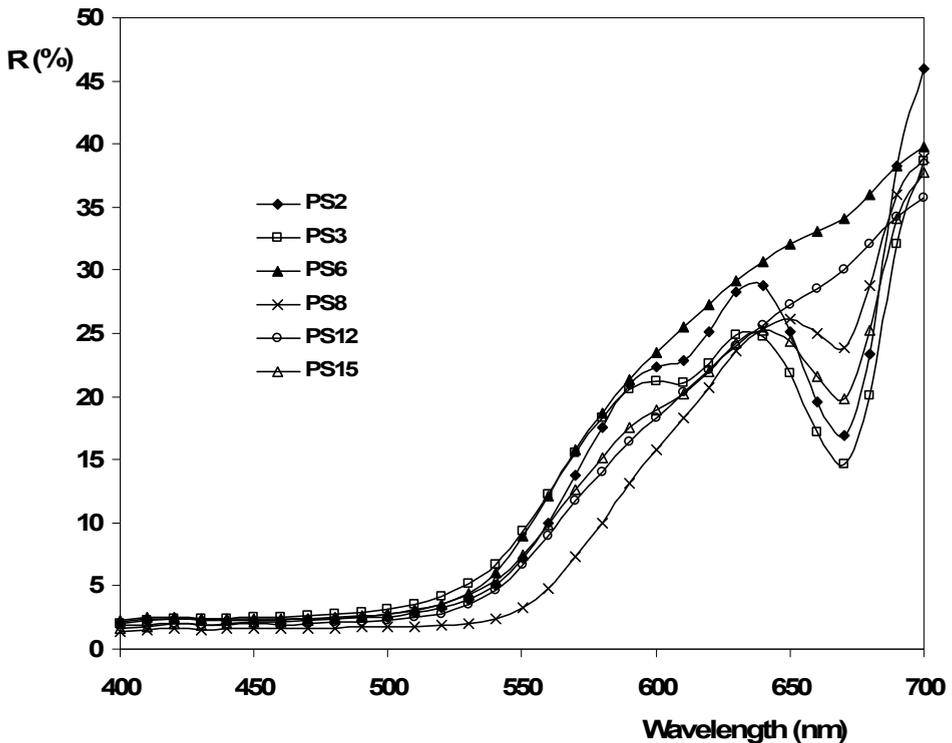
Figure 3. The reflectance spectra of five selected pepper samples

The samples reflect the light only over 500 nm. A group of spectrum (samples PS3 and PS6) exhibits a continuous, monotone increase of reflectance versus the wavelengths. For the other group of spectra (PS2, PS8, PS12 and PS15) the presence of local maxima and minimum are the characteristic feature of the increasing reflectance values versus the wavelength.

The local maxima appear at ~ 600 nm and at ~ 640 nm, respectively, the minimum appears at the 670 nm, despite of the pepper brand. In the later cases, the spectra look like a superposed molecular spectrum of three different colorants in the 530 – 700 nm spectral domain. This fact suggests the presence of three, yellow and red, colorants in the pepper powder in higher concentrations.

Based on the reflectance data the calculated color characteristics of the samples are summarized in the Table 2.

Table 2. The CIE color attributes based on the reflectance data

Sample	Color characteristics							
	X	Y	Z	L	a	b	C	h
PS1	11. 665	9. 401	2. 442	36. 74	21. 36	34. 27	40. 38	58. 07
PS2	14. 440	10. 738	2. 515	39. 14	29. 39	37. 84	47. 91	52. 16
PS3	14. 137	11. 309	2. 767	40. 10	23. 36	37. 64	44. 30	58. 17
PS4	7. 357	4. 998	1. 509	26. 73	29. 11	25. 41	38. 64	41. 11
PS5	8. 210	5. 874	1. 554	29. 09	26. 87	29. 01	39. 54	47. 19
PS6	15. 929	11. 953	2. 635	41. 14	29. 62	40. 40	50. 10	53. 75
PS7	12. 665	9. 326	2. 039	36. 60	28. 88	37. 33	47. 20	52. 27
PS8	10. 462	7. 041	1. 732	31. 90	33. 39	32. 05	46. 28	43. 83
PS9	8. 608	6. 095	1. 751	29. 65	27. 98	27. 99	39. 58	45. 01
PS10	14. 911	11. 032	2. 564	39. 63	30. 11	38. 32	48. 74	51. 84
PS11	14. 660	11. 020	3. 660	39. 61	28. 68	31. 04	42. 26	47. 26
PS12	12. 586	9. 300	2. 135	36. 56	28. 55	36. 43	46. 28	51. 91
PS13	16. 938	11. 932	2. 288	41. 11	35. 48	43. 01	55. 75	50. 48
PS14	17. 550	11. 921	2. 310	41. 09	38. 90	42. 81	57. 84	47. 74
PS15	12. 839	9. 859	2. 305	37. 59	25. 80	36. 81	44. 95	54. 97
PS16	15. 970	12. 397	2. 861	41. 84	26. 85	39. 99	48. 17	56. 12
PS17	13. 322	10. 801	2. 893	39. 24	21. 85	35. 29	41. 50	58. 23
PS18	12. 480	10. 078	2. 628	37. 98	21. 69	35. 00	41. 18	58. 21

DETERMINATION OF THE PEPPER POWDER COLOR PARAMETERS BASED ON THE DIGITAL IMAGE

In this case, only the color corrected pictures were taken into the consideration, the pixels representing the sample surface points on each photo was processed further. RGB values of each camera pixel were converted into device-independent CIE XYZ tristimulus values using a conversion matrix as shown in Equation1. The calculated color characteristics of the samples based on the digital image are summarized in the Table 3.

Table 3

The CIE color attributes calculated based on the digital image

Sample	R	G	B	X	Y	Z	L	a	b	C	h
						Color characteristics					
PS1	116.80	36.68	16.90	12.223	9.822	2.748	37.52	21.89	33.33	39.87	56.70
PS2	135.58	35.77	15.18	14.184	10.842	2.773	39.31	27.01	36.24	45.20	53.30
PS3	125.79	42.44	14.74	14.229	11.539	2.944	40.47	22.29	37.05	43.24	58.97
PS4	89.89	13.24	13.17	7.432	4.998	1.559	26.73	29.81	24.87	38.82	39.84
PS5	89.71	17.39	13.03	7.981	5.711	1.708	28.67	26.58	26.71	37.68	45.14
PS6	144.85	40.36	15.70	15.534	12.016	3.025	41.24	26.87	37.82	46.39	54.61
PS7	121.81	27.42	9.78	12.895	9.458	2.175	36.85	29.32	36.59	46.89	51.29
PS8	114.91	15.28	9.69	10.701	7.067	1.672	31.96	34.91	32.73	47.86	43.15
PS9	95.85	15.63	9.32	9.055	6.218	1.548	29.96	30.46	30.55	43.14	45.08
PS10	140.32	34.01	11.34	15.154	11.296	2.599	40.07	29.65	38.81	48.84	52.63
PS11	136.72	32.72	14.82	13.965	10.431	2.654	38.61	28.69	35.87	45.94	51.35
PS12	122.63	28.19	9.88	13.051	9.616	2.213	37.14	29.10	36.78	46.90	51.65
PS13	162.40	33.69	8.98	17.624	12.667	2.645	42.26	34.25	42.24	54.38	50.96
PS14	164.13	26.97	9.48	16.814	11.549	2.423	40.49	37.42	40.87	55.41	47.52
PS15	119.67	30.58	9.88	13.087	9.872	2.283	37.61	27.32	37.01	46.00	53.57
PS16	134.97	36.37	10.16	15.198	11.584	2.61	40.55	27.87	39.55	48.38	54.82
PS17	117.59	36.29	11.33	13.348	10.541	2.536	38.80	23.92	37.08	44.13	57.18
PS18	113.23	32.57	10.56	12.614	9.795	2.34	37.47	24.77	36.32	43.96	55.71

The CIELa*b* characteristics and C, h* color attributes (Fig. 4) show that the data are close to that obtained from the reflectance spectrum, as reference data. The differences are within the error of determinations. We can conclude, that the use of integrating sphere and digital still camera is suitable system for the precise determination of the color characteristics, and based on it, the quality assessment of different pepper powder brands.
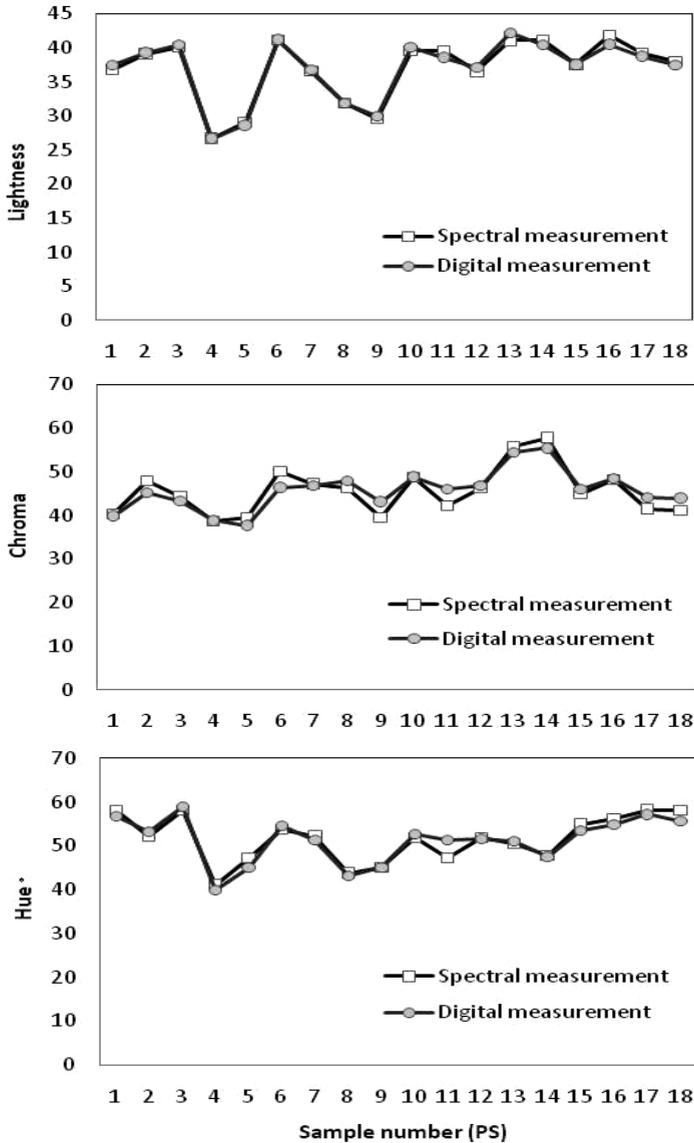
Figure 4. The calculated Lightness, Chroma and Hue values of the pepper samples based on the reflectance spectra and the digital image

CONCLUSIONS

The pepper samples exhibit different color and tone which could be emphasize by measuring the color characteristics. The reflectance spectra reveal the presence of there different colorants in some pepper powders. The differences in the reflectance spectrum appear as a tone change on the digital photo, which appears clearly as a difference in color characteristics. The color parameters calculated with the two methods agree within the experimental errors. As final conclusion, we can reveal, that the use of integrating sphere and digital still camera is suitable system for the precise determination of the color characteristics, and based on it, the quality assessment of different pepper powder brands.

REFERENCES

1. J. Deli, Gy. Tóth, *Z. Lebensm. Unters. Forsch*., **1997**, *205*, 388.
2. M. Jarén-Galán, M. I. Mínguez-M., *J. Agric. Food Chem.,* **1999**, *47*, 4379.
3. Z. Niu, J. Fu, Y. Gao, F. Liu, *Intern. J. Poultry Sci.,* **2008**, 7, 887.
4. R. Gomez, J. E. Pardo, F. Navarro, R. Varon*, J. Sci. Food Agric*., **1998**, *77*, 268.
5. L. O. Vračar, A. N. Tepić, B. L. Vujičić, S. Šolaja, *Acta Periodica Technologica*, **2007**, *38*, 53.
6. M. Krajayklang, A. Klieber, P. R. Dry, *Postharvest Biology and Technology* **2000**, *20*, 269.
7. A. N. Tepić, B. L. Vujičić, *Acta Periodica Technologica*, **2004**, *35*, 59.
8. B. Dobrzański, jr., R. Rybczyński, *Int. Agrophys.,* **2002**,*16*, 261.
9. M. Alvarez-Ortí, R. Gómez, J. E. Pardo, *J. Food Agric. Environ.,* **2009**, *7*, 16.
10. N. Staack, L. Ahrné, E. Borch, D. Knorr**, *Proceedings-RELPOWFLO IV*, **2008**, 68.
11. B. Dobrzański, jr., R. Rybczyński, *Res. Agr. Eng.,* **2008**, *54*, 97.
12. R. Gómez-Ladrón de Guevara, J. E. Pardo-González, R. Varón-Castellanos, F. Navarro-Albaladejo, *J. Agric. Food Chem*., **1996**, *44*, 2049.
13. T. Huszka, M. Halász-F., Gy. Lukács, *Hungarian Sci. Instruments*,**1985**, *60*, 43.
14. M. Drdak, G. Greif, P. Kusy, *Nahrung*, **1989**, *33,* 737.
15. M. Drdak, L. Sorman, M. Zemkova, A. Schaller, *Confructa*, **1990**, *25*, 141.
16. A. Szepes, *PhD Thesis*, **2004**, Budapesti Közgazdaságtudományi és Államigazgatási Egyetem.
17. L. Baranyai, *PhD Thesis*, **2001**, Szent István Egyetem, Budapest.
18. Zs. H. Horváth, C. Hodúr, *Int. Agrophys.,* **2007**, *21*, 67.
19. *Zs. H. HORVATH ; Acta alimentaria*, **2007**, *36*, 75.
20. K. León, D. Mery, F. Pedreschi, *Food Res. Int.,* **2006**, *39*, 1084.

21. D. Bicanic, E. Westra, J. Seters, S. van Houten, D. Huberts, I. Colic-Baric, J. Cozijnsen and H. Boshoven, *J. Phys. IV* France, **2005**, *125*, 807.

22. Gy. Lukács, *Szinmérés*, Műszaki Könyvkiadó, Budapest, **1982.**

23. Chang-Seok Kim, Moon Ki Kim, Byungjo Jung, Bernard Choi, Wim Verkruysse, Myung-Yung Jeong, J. Stuart Nelson, *Lasers in Surgery and Medicine* **2005**, *37*, 138.

MATHEMATICAL MODELING FOR THE CRYSTALLIZATION PROCESS OF HYDROXYAPATITE OBTAINED BY PRECIPITATION IN AQUEOUS SOLUTION

VALENTINA R. DEJEU[a], BARABÁS RÉKA[a], POP ALEXANDRU[a], BOGYA ERZSÉBET SÁRA[a], PAUL-ŞERBAN AGACHI[a]

ABSTRACT. In the paper are presented the theoretical and experimental results concerning the influence of pH and temperature over the rate of the transformation: beta-whitlockite (beta-tricalcium phosphate) in hydroxyapatite (HAP). From the data of the kinetic studies were calculated the values of the rate constants and activation energies at pH = 8.5 – 12. Based on the obtained values for the activation energies it has been established that the process of transformation of beta-whitlockite in HAP could be described using a combined macrokinetic mechanism: transfer – mass transformation. The mathematical of the process has been elaborated and the numerical values of the constants from the mathematical model were determined. Based on the proposed model process simulations were made and the results show that the obtained values fit well with the experimental data, which confirms the model validation.

Keywords: hydroxyapatite, macrokinetic mechanism, mathematical model

INTRODUCTION

Due to its excellent properties like high biocompatibility, atoxicity and bone integration, HAP was accepted as biomaterial for biomedical purposes since 1920 and nowadays has many applications in medicine [1, 2, 3, 4].

Factors that affect the rate of adsorption of HAP in the human body are mostly determined by its chemical reactivity which depends on many different factors like: composition, particle size, defects, porosity, surface area and crystallinity [5]. On the other hand, these properties are greatly influenced on the route and conditions under which HAP is produced [6, 7].

HAP powder can be prepared in a variety of ways. The reactions could be classified in two categories:

a - solid phase reaction

b – precipitation

---

[a] *Universitatea Babeş-Bolyai, Facultatea de Chimie şi Inginerie Chimică, Str. Kogălniceanu Nr. 1, RO-400084 Cluj-Napoca, Romania, vdejeu@chem.ubbcluj.ro*

Although many methods have been developed to synthesize apatites, the most prevalent method in preparation is still *precipitation* because of its ease in operation and tailoring composition, as well as in scaling up for mass production [8].

Among the precipitation methods, one of the most widely used is the precipitated method, uses as reactants calcium nitrate, bi - ammonium phosphate and ammonia solution.

The chemical reaction, which describes the process, is:

$$10\,Ca(NO_3)_2 \cdot 4H_2O + 6\,(NH_4)_2HPO_4 + 8NH_4OH \rightarrow$$
$$\rightarrow Ca_{10}(PO_4)_6(OH)_2 + 20NH_4NO_3 + 6H_2O \tag{1}$$
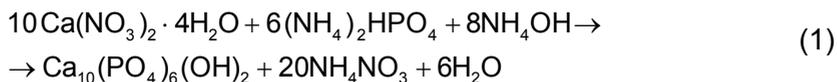
In the literature are no quantitative data concerning how the main parameters of the synthesis (pH of the reaction environment and temperature) influence the rate of transformation of beta-whitlokite in hydroxyapatite. In this paper are presented the experimental results regarding the influence of the reaction environment, pH and temperature on the rate of transformation of beta-whitlokite in hydroxyapatite. These results obtained from the kinetic studies are the base for the mathematical model of the transformation of beta-whitlokite in hydroxyapatite.

MATHEMATICAL MODELING OF THE PREPARATION PROCESS OF HYDROXYAPATITE

The duration of the HAP obtaining procedure doesn't identify with the duration of the chemical reaction (1), because the chemical reaction between the calcium nitrate and bi - ammonia phosphate is an ionic reaction with a high rate. On the other hand, because the solubility of the reaction product is very low, the critical supersaturation will be quickly achieved which makes the separated solid phase (beta-whitlockite) be a metastabile one and in time will be converted in HAP.

In the second stage, after the chemical reaction is finished, the forming process of the new phase nuclei (HAP) will take place. That means that the obtaining process of HAP takes place in two stages, the total duration of the process being the sum of each stage.

The scheme for the obtaining process of HAP by precipitation can be presented as in Figure 1.
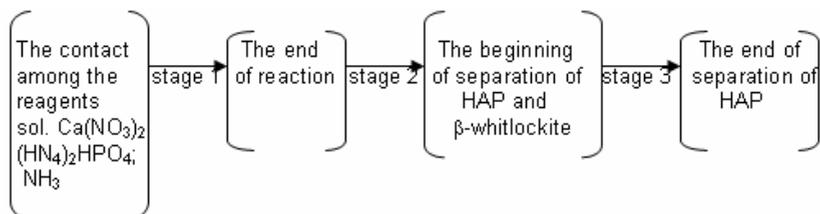
Figure 1. The scheme for the forming process of hydroxyapatite

This scheme suggests that the process of obtaining HAP could be realized after one of the following macrokinetic mechanisms:

a. mass transformation (chemical reaction – nuclei formation and growing)
b. mass transfer
c. combined model (mass transfer - mass transformation)

Because the rate of the chemical reaction is very high, the most probable macrokinetic mechanism for the obtaining process of HAP is a combined one, which includes not only processes of mass transformation but also processes of mass transfer (a, b). This combined mechanism could be presented directly using the balance equation (2) of the final reaction product (HAP):

$$n_{A_1'} = n_{A_1'\,[\,]l} + n_{A_1'}^p \cdot N_p \tag{2}$$

In the first stage of the reaction beta-whitlockite will be formed with metastable character, which will be transformed in time in HAP, in constant conditions of supersaturation.

In these conditions the balance equation (2) becomes:

$$n_{A_1'} = n_{A_1'}^p \cdot N_p \tag{3}$$

$$dn_{A_1'} = n_{A_1'}^p \cdot dN_p + N_p dn_{A_1'}^p \tag{4}$$

$$\frac{dn_{A_1'}}{V_T \cdot d\tau} = n_{A_1'}^p \cdot \frac{dN_p}{V_T \cdot d\tau} + N_p \cdot \frac{dn_{A_1'}^p}{V_T \cdot d\tau} \tag{5}$$

Using the relationships which express the number of moles of HAP from one particle $n_{A_1'}^p$ and the total number of moles of HAP ($n_{A_1'}$) from the total volume of the new formed phase ($V_{[\,]n}$):

$$n_{A_1'}^p = \frac{m_{A_1'}}{M_{A_1'}} = \overline{\rho_{A_1'}} \cdot v_p \; ; \quad n_{A_1'} = \overline{\rho_{A_1'}} \cdot V_{[\,]n} \tag{6}$$

equation (5) will be:

$$\overline{\rho_{A_1'}} \cdot \frac{dV_{[\,]n}}{V_T \cdot d\tau} = \overline{\rho_{A_1'}} \cdot \frac{dN_p}{V_T \cdot d\tau} + N_p \cdot \overline{\rho_{A_1'}} \cdot \frac{dv_p}{V_T \cdot d\tau} \tag{7}$$

If we note the volume of the new phase with $V_{[\,]n}$ and we considered that the total volume V_T is the sum of the two phase volumes:

$$V_T = V_{[\,]m} + V_{[\,]n} = V_{[\,]m} + v_{[\,]n} \cdot V_T \text{ and } v_{[\,]n} = \frac{V_{[\,]n}}{V_T} :$$

$$V_T = \frac{V_{[]m}}{1 - v_{[]n}} \tag{8}$$

we obtain:

$$\frac{dv_{[]n}}{d\tau} = (1 - v_{[]n}) \cdot v_p \cdot \frac{dN_p}{V_{[]m} \cdot d\tau} + (1 - v_{[]n}) \cdot N_p \cdot \frac{dv_p}{V_{[]m} \cdot d\tau} \tag{9}$$

Equation (9) represents the nuclei forming and growing combined macrokinetic model, where the first right term expresses the rate of the nuclei formation and the second one the growing rate.

When the process is developing after this macrokinetic model and because the reaction rate is higher than the germs formation rate, solutions with high supersaturation will be formed.

MATHEMATICAL DESCRIPTION OF THE PROCESS

For the mathematical description of the process according to the macrokinetic model presented in equation (9) we must refer to the geometrical shape of the macro particles and to the τ signification (τ - the time to reach the final value of the volume fraction $v_{[]n}$ in case of the new phase).

Considering that the macroparticles are spherical, equation (9) can be written as follows [9]:

$$\frac{dv_{[]n}}{(1 - v_{[]n}) \cdot d\tau} = \frac{4}{3} \pi r^3 \cdot \frac{dN_p}{V_{[]n} \cdot d\tau} + \frac{N_p}{V_{[]m}} \cdot 4\pi r^2 \cdot \frac{dr}{d\tau} \tag{10}$$

where: $w_3 = \dfrac{dN_p}{V_{[]n} \cdot d\tau}$ and $w_2 = \dfrac{dr}{d\tau}$.

Because the process is developing at constant supersaturating, it is proposed that not only the rate of the germs formation but also the rate of transformation-growing are constant. Based on this hypothesis results that:

$$N_p = w_3 \cdot V_{[]n} \cdot \tau ; \; (w_2 = \frac{r}{\tau}) \tag{11}$$

and equation (10) becomes:

$$\frac{dv_{[]n}}{(1 - v_{[]n}) \cdot d\tau} = \frac{16}{3} \pi \cdot w_2^3 \cdot w_3 \cdot \tau^3 \tag{12}$$

where w_3 expresses the germs forming rate and w_2 is their linear growing. When w_3 and w_2 are constant, equation (12) can be written as:

$$\frac{dv_{[]n}}{(1 - v_{[]n}) \cdot d\tau} = K_3 \cdot \tau^3 \tag{13}$$

The integration of equation (13) in the limits:

$$\tau = 0 ; \quad V_{[]n} = 0 ; \quad \tau = \tau ; \quad V_{[]n} = V_{[]n}$$

Leads to the equation (14):

$$\eta = 1 - e^{-K_3 \cdot \tau^4} \tag{14}$$

In conditions of forming and growing needle like HAP macroparticles:

$$v_p = l ; \quad w_2 = \frac{l}{\tau} ,$$ equation (10) becomes:

$$\frac{dv_{[]n}}{(1 - v_{[]n}) \cdot d\tau} = 2 \cdot w_2 \cdot w_3 \cdot \tau \tag{15}$$

which by integration:

$$\eta = 1 - e^{-K_2 \cdot \tau^2} \tag{16}$$

In the case that the particles don't grow any more, $w_2 = 0$, equation (10) becomes:

$$\frac{dv_{[]n}}{\left(1 - v_{[]n}\right) \cdot d\tau} = v_g \cdot w_3 \tag{17}$$

Integration of equation (17) leads to:

$$\eta = 1 - e^{-K_1 \cdot \tau} \tag{18}$$

Equations (13), (15) and (17) allow the calculation of the time for the fraction $v_{[]n} \equiv \eta$ of the new formed phase (HAP) to reach a certain value (within $0 \div 1$). To use these equations experimental measurements are needed, which allow the validation of the kinetic mechanism and also the numerical values for K_1, K_2 and K_3.

RESULTS AND DISCUSSION

The results presented in Table 1 describe the evolution in time of the transformation of beta-whitlockite in hydroxyapatite. Data form Table 1 were used for the determination of K_1, K_2 and K_3 constants from the (14), (16) and (18) equations. For this purpose these three equations were plotted: $-\ln(1 - \eta) = f(\tau)$, Figure 2 (a – c).
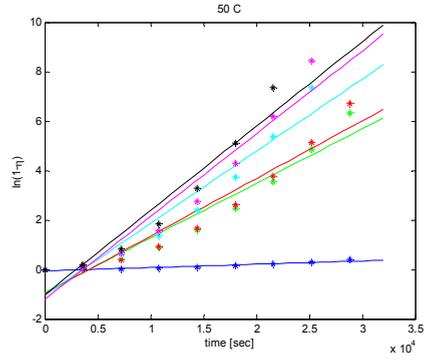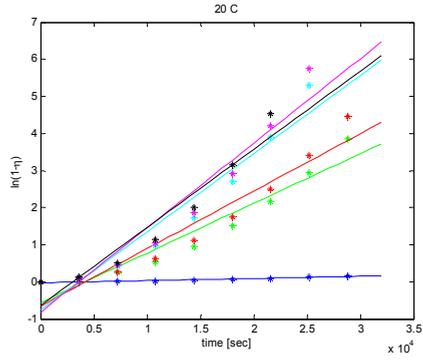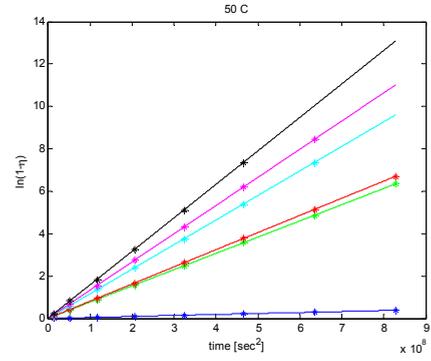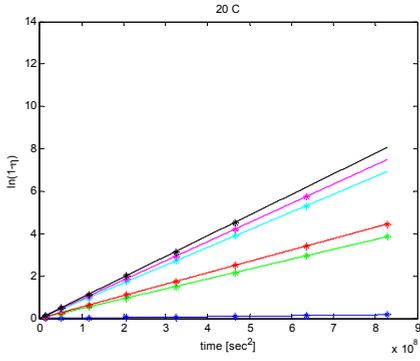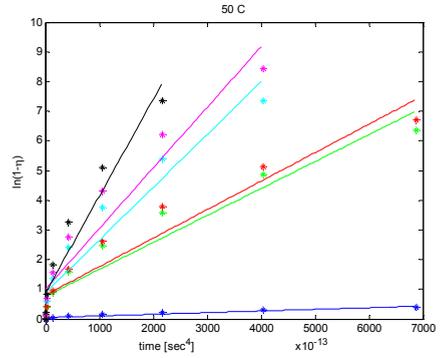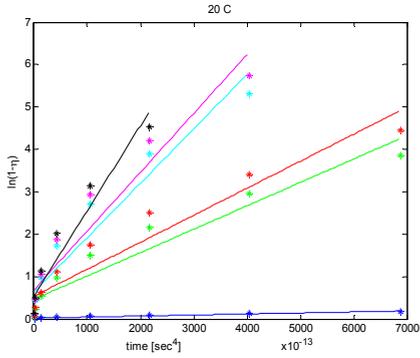
Figure 2. a: $-\ln(1-\eta) - \tau$; b: $-\ln(1-\eta) - \tau^2$; c: $-\ln(1-\eta) - \tau^4$

Table 1. The experimental results of the transformation grade of beta-whitlockite in time and at 20 ^{0}C and 50 ^{0}C for different pH values

pH	Time [s] η	0	3600	7200	10800	14400	18000	21600	25200	28800	32400
8.5	20ºC	0	0.003	0.009	0.021	0.042	0.063	0.092	0.120	0.158	0.191
	50ºC	0	0.005	0.025	0.052	0.090	0.142	0.190	0.250	0.328	0.390
9.1	20ºC	0	0.055	0.215	0.415	0.620	0.775	0.880	0.945	0.981	0.991
	50ºC	0	0.092	0.330	0.590	0.800	0.910	0.971	0.990	1.000	-
9.7	20ºC	0	0.068	0.240	0.470	0.670	0.820	0.920	0.962	0.980	1.000
	50ºC	0	0.102	0.340	0.610	0.815	0.920	0.977	0.990	1.000	-
10.2	20ºC	0	0.101	0.350	0.620	0.820	0.940	0.981	0.996	1.000	-
	50ºC	0	0.136	0.450	0.740	0.910	0.978	0.996	1.000	-	-
11.3	20ºC	0	0.110	0.370	0.650	0.840	0.950	0.986	0.996	1.000	-
	50ºC	0	0.157	0.490	0.790	0.931	0.982	0.997	1.000	-	-
12	20ºC	0	0.119	0.400	0.680	0.860	0.960	0.989	1.000	-	-
	50ºC	0	0.187	0.560	0.840	0.960	0.995	1.000	-	-	-

From the slope were determined the numerical values of the K constants, presented in Table 2.

Tablel 2. The values of K constant

pH	20 ^{0}C			50 ^{0}C		
	K_1	K_2	K_3	K_1	K_2	K_3
8.5	6.583E-06	2.032E-10	1.920E-19	1.513E-05	4.671E-10	4.412E-19
9.1	1.510E-04	4.649E-09	4.392E-18	2.480E-04	7.655E-09	7.232E-18
9.7	1.740E-04	5.372E-09	5.075E-18	2.620E-04	8.089E-09	7.641E-18
10.2	2.410E-04	8.356E-09	9.915E-18	3.340E-04	1.158E-08	1.374E-17
11.3	2.600E-04	9.036E-09	1.072E-17	3.830E-04	1.329E-08	1.577E-17
12	2.450E-04	9.728E-09	1.494E-17	3.980E-04	1.579E-08	2.425E-17

In order to identify the mathematical model which describes the process the process simulation was needed. For this purpose the numerical values of the K_1, K_2 and K_3 from Table 2 were used and different times were calculated relating to the transformation grade of beta-whitlockite in HAP and compared with the experimental results. The results obtained at 20 ^{0}C and 50 ^{0}C for pH=9.7 are presented in Figure 3 (the simulations were made for all pH values, but in this article are presented only the relevant simulation results).

The analysis of the results show a very good fit of the experimental results with those calculated for equation (16), where the errors for the majority of the results don't exceed 2%. In the mathematical models expressed by equations (14) and (18) the deviations from the experimental values are high.

At pH = 8.5 the proposed model fits well with experimental data only until 20 % conversion (at 20 ^{0}C) and until 40 % (at 50 ^{0}C).
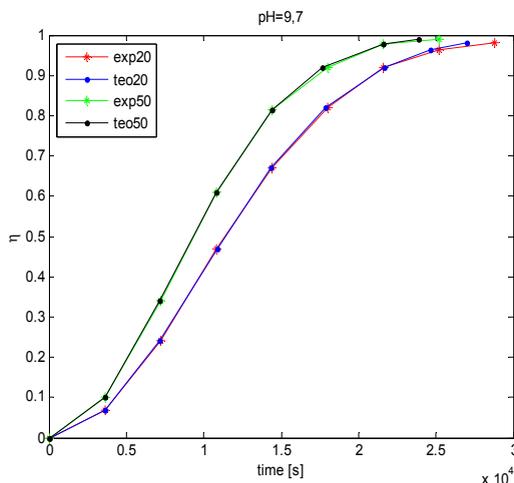
Figure 3. The variation of conversion in time at 20 ^{0}C and 50 ^{0}C at pH = 9.7

CONCLUSIONS

Based on the kinetic study regarding the transformation process of beta-whitlockite in HAP the mathematical model of this process was established. The implementation of the model for three particular cases led to equations, which were used to calculate the numerical values of K_1, K_2 and K_3 constants, based on experimental data. The process simulation using the mathematical model indicate that this could be described using the equation: $\eta = 1 - e^{-K_2 \cdot \tau^2}$, which corresponds to a combined macrokinetic mechanism: transfer (transfer of Ca^{2+} and PO_4^{3-} ions towards the HAP crystal surface) – mass transformation (formation and growing of HAP nuclei)

EXPERIMENTAL SECTION

For the synthesis of HAP and the kinetic study for the transformation of beta-whitlockite in hydroxyapatite, reactants of analytical purity were used: calcium nitrate tetra hydrate, bi-ammonia phosphate and ammonia solution 28 %.The concentration of the calcium nitrate solution was 0.5 mol/L and by adding ammonia solution the pH was turned to the value of 8.5. The concentration of the bi-ammonia phosphate solution was 0.3 mol/L and to this solution was added the necessary amount of ammonia to reach the pH values presented in Table 1. In all the experiments the phosphate solution

was added in drops over the calcium nitrate solution. The ammonia losses were avoided by fixing a closed ascending refrigerator and a hydraulic closing to the reaction vessel. The temperature was measured and maintained constant with a thermostat. From time to time, during the reaction, samples were taken, filtered, washed with distillated water and dried at 105 ^{0}C until constant weight. The dried samples were crushed into fine powders with $d_p < 50\mu m$ and were heated for 2 hours at 1000 ^{0}C.

Determination of the phase composition using XRD
The quantitative analysis of the phases was made using DRON-3 by measuring the integrated intensity of the peaks. Knowing the absorption mass coefficients in a bi-phase system, the amount of HAP was determined using the equation:

$$\frac{I_1}{I_1^0} = \frac{w_1 \cdot \mu_1}{w_1(\mu_1 - \mu_2) + \mu_2} \tag{18}$$

The evolution in time of the process was followed up using the transformation grade of the beta-whitlockite in HAP.

REFERENCES

1. M. Vallet-Regi, *J. Chem. Soc., Dalton Trans*., **2001**, 97.
2. K E. Sovaleval, A. G. Veresovl, A. V. Soinl, V. I. Putlyaev, Yu. D. Tret'yakovl, *J. Surf. Investig –X –RA,* **2007**, *1(6)*, 683.
3. Z. Bako, I. Kotsis, *Ceram. Int.,* **1992**, *18*, 373.
4. R. Z. LeGeros, *Clin. Orthop. Relat. Res.,* **2002**, *395*, 81.
5. S. Zhang, K. E. Gonsalves, *J. Mater. Sci-Mater. M.,* **1997**, *8*, 25.
6. K. Cheng, W. Weng, H. Wang, S. Zhang, *Biomat.,* **2005**, *26*, 6288.
7. M. Jarcho, C. H. Bolen, M. B. Thoma, J. Bobick, J. F. Kay and R. H. Doremus, *J. Mater. Sci.,* **1976**, *11*, 2027.
8. E. C. Moreno, T. M. Gregory, W. E. Brown, *J. Res. NBS. A. Phys. Ch.,* **1968**, *72A*, 6.
9. C. Calistru, C. Leonte: "Tehnologia substantelor anorganice", *Ed. Didactica si Pedagogica*, Bucuresti, **1972**, 179.

NOMENCLATURE

I_1 integrated intensity of pure phase in mixture

I_1^0 integrated intensity of pure phase

$m_{A_1'}$ mass of HAP (kg)

μ_1, μ_2 mass absorption coefficients

w_1 mass fraction of phase

n_{A_1} mols of HAP formed in reaction (mol)

$n_{A_{1[l]}}$ mols of HAP formed in the liquid phase (mol)

$n_{A_1}^p$ mols of HAP in one macroparticle (mol)

N_p number of macroparticles (-)

r^2 particle radius (m)
l particle length (m)

w_3 rate of germs forming (m/s)

w_2 rate of germs growing (m/s)

K rate constant (-)

$V_{[]n}$ the volume fraction of the new phase (m^3)

$V_{[]m}$ the volume fraction of the new phase (m^3)

V_T total volume of the new formed phase (m^3)

Greek symbols

$\overline{\rho_{A_1'}}$ molar density (kmol/ m^3)

τ time (s)

v_p stoechiometric coefficient of macroparticles (-)

$v_{[]n}$ stoechiometric coefficient of the new phase (-)

STUDY OF THE CHROMATOGRAPHIC RETENTION OF SOME NEW ORGANOSELENIUM AND ORGANOTELLURIUM COMPOUNDS CONTAINING INTRAMOLECULAR INTERACTIONS BY HPTLC

SILVIA LENUŢA DUNCA[a]**, MONICA KULCSAR**[a]**, ANCA SILVESTRU**[a]**, CRISTIAN SILVESTRU**[a]**, COSTEL SÂRBU**[a]

ABSTRACT. The chromatographic behaviour of some new metal complexes of organoselenium and organotellurium compounds containing intramolecular interactions, were investigated by means of different HPTLC systems with polyamide, cellulose, normal and modified silica gel thin-layers and various organic solvents of relatively high polarity. Recommendable phase system for the separation of metal-complexes is a combination of fluorescent polyamide thin-layer with a methanol-water (8:2 v/v) mixture when well-defined compact spots come out and migrate. Dark zones appeared on fluorescent green background under UV lamp (λ = 254 nm). R_F values were determined by using the one-dimensional ascending technique and modelling by using different molecular descriptors calculated by using efficient software. It has been concluded that a successful analysis will be executable for the compounds studied with the possibility of modelling the chromatographic retention.

Keywords: *organoselenium and organotellurium compounds, lipophilicity, TLC, QSRR, MLR, PCA, PCR*

INTRODUCTION

Quantitative structure-activity relationships (QSAR) describe how the molecular structure, in terms of descriptors – lipophilic, electronic and steric – affects the biological activity of a compound [1-4]. Similarly, quantitative structure-retention relationships (QSRR) relate these descriptors to chromatographic retention. Finally, the quantitative retention-activity relationships (QRAR) imply that conclusions concerning biological activity can be based on chromatographic experiments [5-11]. In this regard of QRAR it is considering that the same basic intermolecular interactions determine the behaviour of chemical compounds in both biological and chromatographic environments. As a consequence, the

[a] *Babeş-Bolyai University, Faculty of Chemistry and Chemical Engineering, Arany Janos 11, 400028 Cluj-Napoca, Romania; E-mail: costelsrb@yahoo.co.uk*

chromatographic approach has been quite successful, for example, in duplicating Log P data derived by traditional "shake-flask" technique or other procedures. The relationships themselves are usually based on correlation analysis.

Another form of computational analysis used for the correlation of chemical or biological activity and chromatographic retention with different molecular descriptors are Multiple Linear Regression (MLR) [11-13], Principal Component Analysis (PCA) [14-16], Partial Least Squares (PLS) [17-19], or Artificial Neural Networks (ANN) [20-22]. In the case of PCA and PLS, for example, starting from a multidimensional space described by different variables, a quantitative model is derived that transforms the axes of the hypersystem. The first principal component (PC1) defines as much of the variation in the data as possible. The second principal component (PC2) describes the maximum amount of residual variation after the first PC has been taken into consideration, and so on. By using only a limited number of PCs, the dimensionality of the data space is reduced, thereby simplifying further analysis.

In this paper we discuss and apply three multivariate regression methods to develop comparative studies and to provide a QSAR-QSRR model for the characterization and classification of some new organo-selenium and organotellurium compounds with potential applications for asymmetric synthesis in organic and organometallic chemistry, catalytic antioxidant activity, enzyme mimics and chemotherapeutic agents.

PRINCIPAL COMPONENT ANALYSIS

Principal components analysis (PCA) is also known as *eigenvector* analysis, *eigenvector* decomposition or Karhunen-Loéve expansion. Many problems from chemistry and other scientific fields are strongly related to PCA. The main purpose of PCA is to represent in an economic way the location of the samples in a reduced coordinate system where instead of m-axes (corresponding to m characteristics) only p ($p < m$) can usually be used to describe the data set with maximum possible information.

Principal component analysis practically transforms the original data matrix (X_{nxm}) into a product of two matrices, one of which contains the information about the objects (S_{nxm}) and the other about the variables (V_{mxm}). The S matrix contains the scores of the n objects on m principal components (the scores are the projection of the objects on principal components). The V matrix is a square matrix and contains the loadings of the original variables on the principal components (the loadings are the weights of the original variables in each principal component).

Moreover, it may well turn out that usually two or three principal components provide a good summary of all the original variables. Loading and respectively score plots are very useful as a display tool for examining the relationships between characteristics and between compounds, looking for trends, grouping or outliers.

MULTIPLE LINEAR REGRESSION

Multiple linear regression (MLR) is an extension of simple linear regression consisting of two or more independent variables (*e.g.* chemical descriptors or properties) and a numeric dependent variable (*e.g.* chromatographic retention index). MLR attempts to model the relationship between the independent variables and a response variable (*R*) by fitting a linear equation to observed data in the following equation:

$$R = a_o + \sum_{i=1}^{k} a_i x_i \, , \tag{1}$$

where a_o, a_i are the estimated regression parameters.

PRINCIPAL COMPONENT REGRESSION

Principal component regression (PCR) is a two-step multivariate calibration method: in the first step, a principal component analysis of the data matrix **X** is performed. The measured or calculated variables (*e.g.* descriptors) are converted into new ones (scores on latent variables). This is followed by a multiple linear regression step, MLR, between the scores obtained in the PCA step and the characteristic *R* to be modelled.

RESULTS AND DISCUSSION

By reducing the number of features from 9 original descriptors (including retention indices R_f and R_m) to three principal components (latent variables), the information preserved is enough to permit a primary examination of the similarities and differences between descriptors and organoselenium and organotellurium compounds. The contribution of the first component represents 42.81% of the total variance and a two components model accounts for 68.52% of the total variance. The first three components reproduce approximately 81% of the total variance and the first six even 99.31%, and the *eigenvalues* become negligible after the seventh component.

All the statements above are well supported by the 2D- and 3D-representations of the loadings (Figures 1 and 2). The projection of the 3D-representation gives a more complete pattern: it is clear, for example, that the majority of the descriptors considered in this study form two close clusters: the first one includes *M, MW, V* and *MR*, the second one encompasses *CLogP, H* and *GS*; $R_f/(R_m)$ and *GS* appear more or less as outliers.

The scatter plot of scores onto the plane defined by PC1 and PC2 (Figure 3) and in the space described by PC1, PC2 and PC3 (Figure 4) shows interesting results. Two clusters appear to be well defined and in a good agreement to the structure of compounds: one of them corresponds to the

compounds **3**, **4**, **5**, **6**, **8**, **12**, **13**, **14**, **17**, **18** and **19** (the largest molecules in the series) in the above right part of the graph, the second include the group of fluorine derivatives (**9**, **10**, **15**, **16**), with the exception of compound **1**, **2**, **7** and **11**, is located in the middle-bottom of the graph.
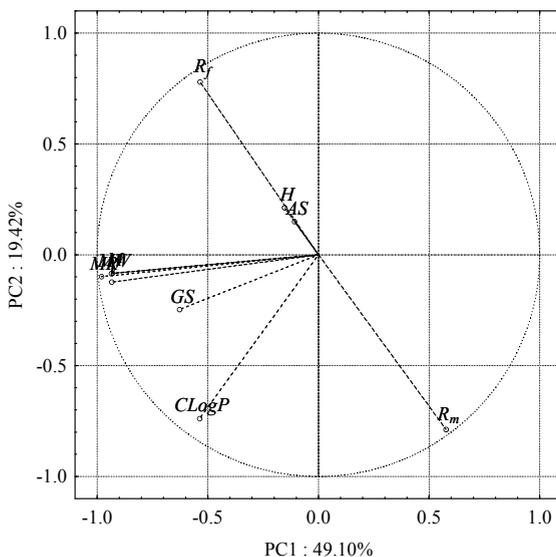
Figure 1. PC1 and PC2 loading plot of the autoscaled data in Table 2
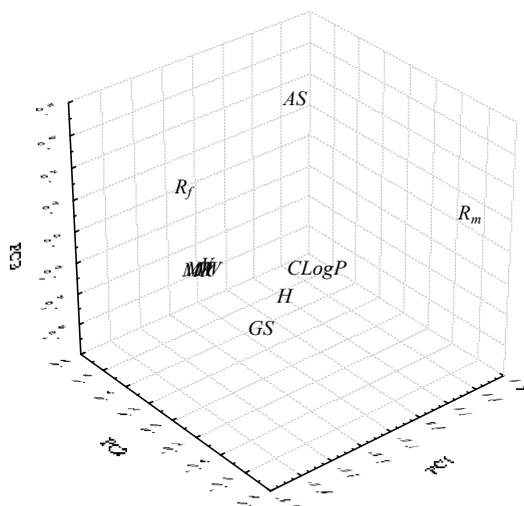
Figure 2. PC1, PC2 and PC3 loading plot of the autoscaled data in Table 2

74
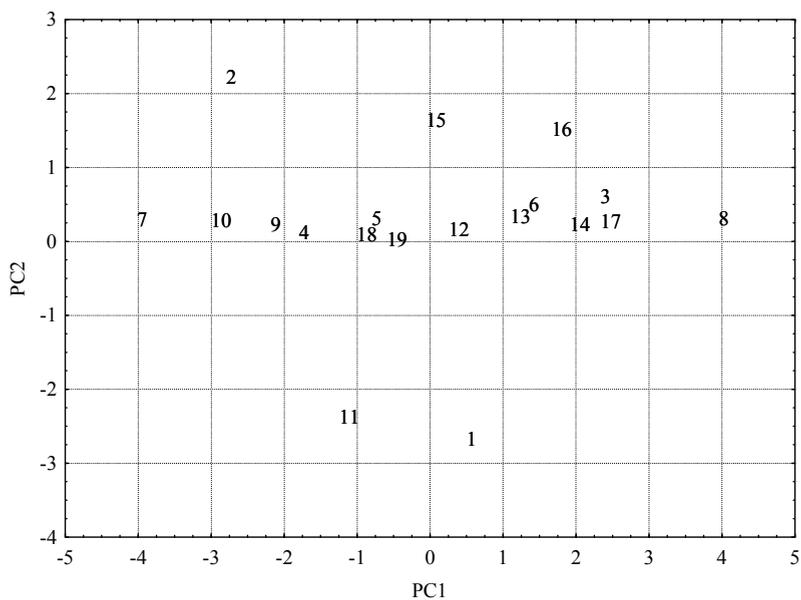
Figure 3. PC1and PC2 score plot of the autoscaled data in Table 2
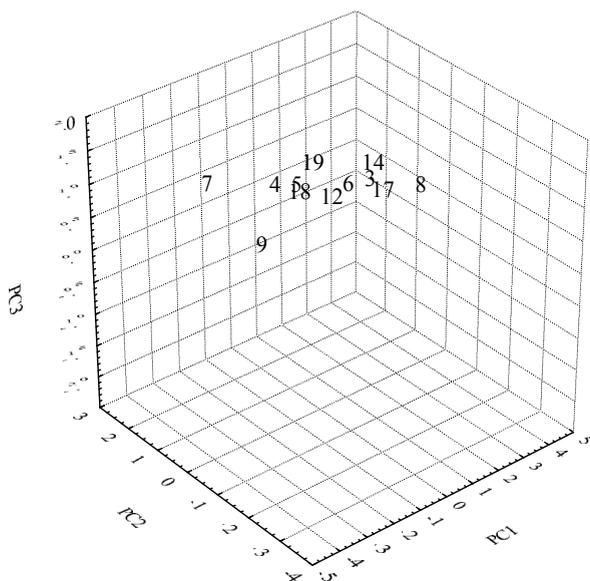
Figure 4. PC1, PC2 and PC3 score plot of the autoscaled data in Table 2

In order to describe the relationship between the chromatographic retention indices of the tested compounds (R_{Mo} and b, intercept and slope values, in equation 7) and the calculated structural descriptors, a multivariate regression analysis was performed. By forward stepwise multiple regression analysis, the following high-quality regression equations were obtained:

$$R_{Mo} = 0.119 - 0.404MR + 0.264CLogP + 0.006M \qquad (2)$$
$$(r = 0.9153, n = 19, F = 26, p < 0.0000, s = 0.225)$$

$$R_f = 0.500 + 0.173RM - 0.105CLogP - 0.003M \qquad (3)$$
$$(r = 0.8894, n = 19, F = 19, p < 0.0000, s = 0.105)$$

where n is the number of compounds, r the correlation coefficient, F the F-test value, p is the significance level of the all equation and s is standard error of estimates. The F and p values of equation (2) and (3) show that the multiple regression equations are very significant having high correlation coefficient and relatively small s values.

The results suggest also that the molecular refractivity and partition coefficient seem to be dominant in the retention mechanism and, as a consequence, control the lipophilicity of the investigated compounds.

For the PCR method, the original 7 descriptors were used for the selection of the optimum number of factors (principal components) by using also the statistics discussed above. The obtained multiple regression equations are also highly significant:

$$R_m = -0.247 - 0.774PC6 + 0.091PC1 + 0.184PC3 + 0.226PC4 + 0.857PC7 + 40.179PC8 - 0.111PC5 \qquad (4)$$
$$(r = 0.9360, n = 19, F = 11, p < 0.0003, s = 0.229)$$

$$R_f = 0.599 + 0.353PC6 - 0.103PC4 - 0.033PC1 - 0.337PC7 - 0.054PC3 - 23.392PC8 + 0.038PC5 \qquad (5)$$
$$(r = 0.9557, n = 19, F = 17, p < 0.0000, s = 0.079)$$

CONCLUSIONS

Correlation obtained between chromatographic retention indices and structure descriptors for organoselenium and organotellurium compounds are high significant and might be used to predict the retention behaviour and, as a consequence, the lipophilicity of other members of the series. By comparing the multivariate regression methods used in this study, the forward stepwise MLR appeared to be the most effective in predicting retention indices for the investigated compounds. The molecular refractivity and the partition coefficient seem to be dominant in the retention mechanism and hence these descriptors control the lipophilicity.

EXPERIMENTAL SECTION

The chromatographic behaviour of the compounds were investigated by means of different HPTLC systems with polyamide, cellulose, normal and modified silica gel thin-layers and various organic solvents of relatively high polarity. Recommendable phase system for the separation of metal complexes is a combination of fluorescent polyamide thin-layer with a methanol-water (8:2 v/v) mixture when well-defined compact spots come out and migrate. Dark zones appeared on fluorescent green background under UV lamp (λ = 254 nm). Glass HPTLC plates (20 x 20 cm) were obtained from Macherey-Nagel (Düren, Germany) and methanol for chromatography was supplied from Reactivul (Bucharest, Romania). Solutions in chloroform of each compound (Table 1)

Table 1. Chemical structure of the investigated organometallic compounds

were prepared at a concentration of approximative 1 mg mL^{-1}. Chromatograms were developed by ascending technique at room temperature ($\sim$20 ^{0}C); the developing distance being 10 cm. After being developed, the dried plates were examined under UV lamp (λ = 254 nm). The R_M values of each compound were obtained by using the following well-known equation

$$R_M = \log (1/R_f -1) \qquad (6)$$

The R_M values are measured at several compositions of binary mobile phase systems and linearly extrapolated (interpolated) on the basis of the relationship between the R_M and the mobile phase organic modifier as was described by the TLC adapted Soczewiński-Wachtmeister equation:

$$R_M = R_{M0} + bC \qquad (7)$$

where R_{M0} indicates the extrapolated value to the pure water as mobile phase and it is the HPTLC descriptor most frequently used into QSAR analysis. b is frequently associated to the specific surface area of the stationary phase, while C represents the volume fraction of the organic modifier in the mobile phase. The specific surface area is considered an alternative descriptor of lipophilicity.

Table 2. The descriptors and retention indices computed for the organo-selenium and organotellurium compounds investigated in this paper

Nr.	M	H	CLogP	MR	AS	GS	V	R_f	R_m
1	428.03	0.97	4.71	10.93	69046	160.38	584.13	0.726	-0.423
2	542.14	1.44	4.38	14.45	3680	377.84	650.25	0.973	-1.562
3	287.08	0.97	2.36	7.563	155	324.16	486.52	0.873	-0.839
4	463.01	0.97	8	12.95	21	353.86	603.18	0.455	0.079
5	427.03	0.97	6.38	11.02	3281	362.82	573.15	0.647	-0.264
6	334.01	0.97	3.51	9.013	187	330.52	506.56	0.652	-0.273
7	538.03	0.97	9.51	15.19	186	415.57	712.31	0.729	-0.430
8	248.98	0.97	1.76	6.046	164	261.12	381.15	0.737	-0.447
9	538.11	0.97	5.54	14.1	129	352.33	588.69	0.799	-0.598
10	638.09	0.97	3.68	14.84	685	353.81	591.81	0.925	-1.089
11	477.02	0.97	5.45	11.39	115180	353.89	556.98	0.650	-0.269
12	419.96	0.97	5.61	9.628	2918	320.02	487.19	0.554	-0.094
13	413.89	0.97	3.19	8.154	123	307.05	471.81	0.390	0.194
14	313.91	0.97	5.04	7.412	125	299.23	462.66	0.436	0.112
15	441.92	1.28	4.18	9.081	164	335.87	526.59	0.316	0.335
16	345.93	1.28	3.94	7.93	224	298.46	447.89	0.334	0.300
17	331.91	0.97	3.44	7.466	119	284.98	414.53	0.403	0.171
18	455.94	0.97	7.24	11.56	4	331.76	544.93	0.392	0.191
19	405.95	0.97	8.16	11.19	1	326.12	541.16	0.385	0.203

DESCRIPTION OF ORGANOSELENIUM AND ORGANOTELLURIUM COMPOUNDS

The investigated organoselenium and organotellurium compounds were synthesized by procedures described earlier [24-26]. The molecular structure of the organoselenium and organotellurium compounds studied in this paper is depicted in Table 1.

In order to define the character of the compound structure, the following descriptors available in the ChemDraw Pro program were taken into consideration and used as independent variables: exact mass (M), partition coefficient ($CLogP$), molar refractivity (MR), Henry's law constant (H), surface area (AS), surface area (Grind)(GS), volume (V), molecular polarizability (MP). The obtained values are presented in Table 2. We have been computing only so few descriptors because the conventional software does not recognize Se and Te. Also, in the case of polarizability, the software does not have the ability to calculate the dithiophosphinates ligands.

ACKNOWLEDGEMENTS

REFERENCES

1. A. Leo, C. Hansch, D. Elkins, *Chem. Rev*., **1971**, *71*, 525.
2. R. F. Rekker, R. Mannhold, *Calculation of Drug Lipophilicity*, VCH, Weinheim,**1992**.
3. M. Karelson, *Molecular Descriptors in QSAR/QSPR*, Wiley & Sons, New York, **2000**.
4. A. Chiriac, D. Ciubotariu, Z. Simon, *QSAR-Quantitative Relationships*, Mirton Publishing House, Timişoara, **1995**.
5. R. Kaliszan, *Anal. Chem*., **1992**, *64*, 619A.
6. A. Pyka, M. Miszczyk, *Chromatographia*, **2005**, *61*, 37.
7. R. Kaliszan, *Trends Anal. Chem*., **1999**, *18*, 401.
8. Q. S. Wang, L. Zhang, *J. Liq. Chrom. & Rel. Technol*., **1999**, *22*, 1.
9. M. C. Garcia Alvarez-Coque, J. R. Torres Lapasio, *Trends Anal. Chem*., **1999**, *18*, 533.
10. T. L. J. Djaković-Sekulić, C. Sârbu, N. U. Perišić-Janjić, *J. Planar Chromatogr*., **2005**, *18*, 432.
11. J. Dai, L. Jin, S. Yao, L. Wang, *Chemosphere*, **2001**, *42*, 899.

12. A. Detroyer, Y. V. Heyden, S. Carda-Broch, M. C. Garcia-Alvarez-Coque, D. L. Massart, *J. Chromatogr. A*, **2001**, *912*, 211.

13. C. Sârbu, D. Casoni, M. Dărăbanțu, C. Maiereanu, J*. Pharm. Biomed. Anal*., **2004**, 35, 213.

14. C. Sârbu, S. Todor, *J. Chromatogr. A*, **1998**, 822, 263.

15. C. Sârbu, K. Kuhajda, S. Kevresan, *J. Chromatogr. A*, **2001**, 917, 361.

16. A. Detroyer, V. F. Schoonjans, F. Questier, Y. V. Heyden, A. P. Borosy, Q. Guo, D. L. Massart, *J. Chromatogr. A*, **2000**, 897, 23.

17. H. Martens, T. Naes, *Multivariate Calibration*, Wiley, Chichester, **1991**.

18. Y. Zhou, L. Xu, Y. Wu, B. Liu, *Chemometr. Intell. Lab. Syst*., **1999**, 45, 95.

19. T. Li, H. Mei, P. Cong, *Chemometr. Intell. Lab. Syst*., **1999**, 45, 177.

20. R. Zhang, A. Yan, M. Liu, H. Liu, Z. Hu, *Chemometr. Intell. Lab. Syst*., **1999**, 45, 113.

21. R. H. Zhao, B. F. Yue, J. Y. Ni, H. F. Zhou, Y. K. Zhang, *Chemometr. Intell. Lab. Syst*., **1999**, 45, 163.

22. Y. Chen, D. Chen, C. He, S. Hu, *Chemometr. Intell. Lab. Syst*., **1999**, 45, 267.

23. C. Sârbu, H. F. Pop, *Fuzzy Soft-Computing Methods and Their Applications in Chemistry*. In *Reviews in Computational Chemistry*. K. B. Lipkowitz, D. B. Boyd, T. R. Cundari, Eds., Wiley-VCH, **2004**, 249-332.

24. M. Kulcsar, A. Silvestru, C. Silvestru, J. E. Drake, C. L. B. Macdonald, M. B. Hursthouse, M. E. Light, *J. Organomet. Chem*., **2005,** 690, 3217.

25. J. E. Drake, M. B. Hursthouse, M. Kulcsar, M. E. Light, A. Silvestru, *J. Organomet. Chem*., **2001**, 623, 153.

26. C. Deleanu, J. E. Drake, M. B. Hursthouse, M. Kulcsar, M. E. Light, A. Silvestru, *Appl. Organometal. Chem*., **2002**, 16, 727.

LOWER RIM SILYL SUBSTITUTED CALIX[8]ARENES

NATHAN FLEURET[a,b], SEBASTIAN PAIC[a], GABRIELA NEMES[a], RALUCA SEPTELEAN[a], PETRONELA PETRAR[a], IOAN SILAGHI-DUMITRESCU[*a]

ABSTRACT. New lower rim silyl substituted calix[8]arenes have been synthesized by reaction of the parent *p-tert*-butylcalix[8]arene with *n*-BuLi at low temperature followed by addition of trimethylchlorosilane/(3-chloropropyl)-trimethoxysilane when octakis-(trimethylsilyl)calix[8]arene (**3**)/octakis-(*n*-propyl-trimetoxisilan)calix[8]arene (**4**) is obtained. The new calixarene derivative **4** has been characterized by NMR and IR spectroscopy.

Keywords: *calix[8]arene, octakis-(n-propyl-trimetoxisilan)calix[8]arene.*

INTRODUCTION

Functionalization of calix[n]arenes is an important way in getting useful products for many areas of research and applications [1, 2, 3].

The most accessed positions for functionalizations of the parent calixarenes are the phenolic -OH groups of the lower rim or the *p-* position of the aromatic rings (upper rim) [4,5]. *Tert*-butylcalix[n]arenes (n = 4,6,8) can be functionalized at the upper rim either by removal of the *tert*-butyl groups thus forming calix[n]arenes which can be then halogenated (see references [6] and [7] for bromination), or directly by reactions of nitration or sulfonation [6,7]. The first step in all the processes is however the protection of -OH groups by *o*-methylation or acetylation [8,9].

Larger calixarenes have been successfully modified at the lower rim with ethers or esters formation leading to new host molecules by the introduction of additional functional groups [10]. These functionalizations allow a degree of control on the calixarene conformations and also on the hindrance of ring inversion since voluminous groups attached to the oxygen atoms increase the barrier to conformational inversion in calix[8]arenes compared with calix[4]arenes [11].

[a] *Faculty of Chemistry, "Babes-Bolyai" University, Cluj-Napoca, RO-400028, Romania*
[b] *IUT de Rouen, Universite de Rouen, 76821 Rouen, France*

In view of their potential to bind to inorganic substrates, calixarenes functionalized with organosilyl groups are promising precursors for new hybrid organic/inorganic materials.

Literature data show that trimethylsilylated-*tert*-butylcalix[n]arenes are obtained from the brominated derivative of the corresponding calixarene, by lithiation with an excess of *tert*-butyllithium followed by silylation with excess chlorotrimethylsilane [12]. In case of calix[4]arenes, a *tetra*-trimethylsilylated product was obtained by this method, however only tri-trimethylsilylated and di-trimethylsilylated derivatives were reported for calix[6]arene and calix[8]arene respectively [12]. A fully substituted *tert*-octylcalix[8]arene octakis-(trimethylsilyl) ether was obtained by reaction of *p-tert*-octyl-calix[8]arene with N-O-bis[(trimethylsilyl)oxy]acetamide in solution of acetonitrile [12].

Herein we present a new method based on the lithiation of calix[8]arenes for the synthesis of octakis-(trimethylsilyl) ether of *tert*-butylcalix[8]arene. This protocol has been also applied for obtaining the new silyl substituted octakis(*n*-propyl-trimethoxisilan)calix[8]arene.

RESULTS AND DISCUSSIONS

The parent *p-tert*-butylcalix[8]arene has been obtained by the method described in literature [13] (Scheme 1).
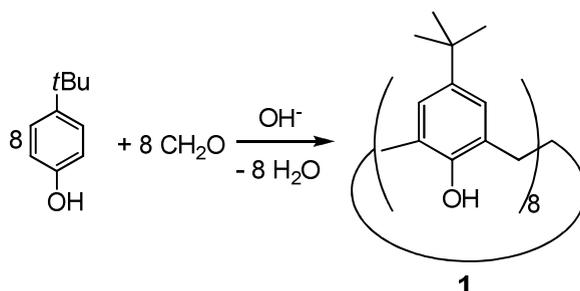
Scheme 1

^{1}H NMR spectrum of **1** shows a specific signal at 9.66 ppm due to the presence of the –OH groups. Two nonequivalent doublet signals in the 3 – 4,5 ppm range are assigned to the two nonequivalent (*endo* and *exo*) protons of the methylene bridges [14,15].

The new silyls substituted derivatives **3** and **4** were obtained via the lithium intermediate **2** which is stable under inert atmosphere until 0 $^{\circ}$C (Scheme 2). The reaction is complete after 2 hours of stirring at a temperature ranging from -50 to -20 $^{\circ}$C.
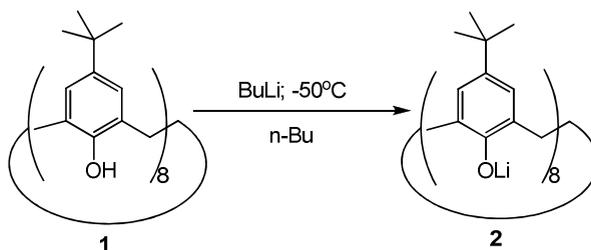
Scheme 2

Lithium derivative **2** is added at -50 ^{o}C to a solution (THF) containing excess trimethylchlorosilane or (3-chloropropyl)trimethoxysilane and the corresponding **3** or **4** lower rim silyl substituted calix[8]arenes are formed (**Scheme 3**).
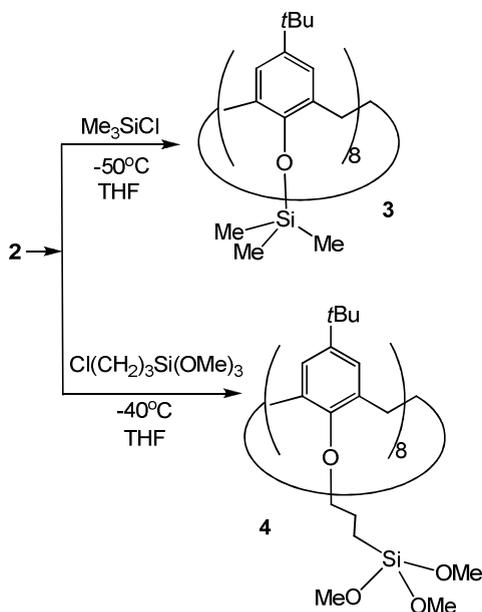
Scheme 3

Calix[8]arenes **3** and **4** were characterized by multinuclear NMR, and IR spectroscopy.

In the ^{1}H NMR spectra of **3** and **4,** the singlet signal corresponding to -OH groups of the parent calixarene is missing, proving the full substitution at the oxygen atoms. Furthermore, in the aliphatic range of spectrum, the characteristic signals for O-SiMe_3 (2.19 ppm) and -O-(CH_2)$_3$-Si(OMe)$_3$ (1.30 ppm for -C$\underline{H}_2$-Si(OMe)$_3$,1.90 ppm for -CH$_2$-C$\underline{H}_2$-CH$_2$-, 3.53 ppm for -O-C$\underline{H}_2$-, and 3.57 ppm for Si-(O-C$\underline{H}_3$)$_3$) protons were observed. **3** and **4** derivatives show a

broadened signal for the bridge methylene protons, as opposed to the sharp AB system observed for the parent compound. This has been evidenced in the case of other similar substituted compounds as well [12] and it is no doubt due to a greater flexibility of the substituted calixarene basket. A PM3 energy profile calculation with Spartan06 [16] for a monosubstituted calixarene[8]arene (Figure 1) shows a barrier for the inversion of the methylene group, accompanied by a corresponding rotation of the arene ring, of less then 15 kcal/mol, comparable with the experimentally determined barriers of interconversion of various calix[4,8] arenes [10]. The calculated overall barrier is even smaller when two vicinal oxygen atoms are substituted with $SiMe_3$ groups (Figure 2), so the observed pattern of the bridging methylene groups in the NMR spectra of **3** and **4** has also some theoretical support.
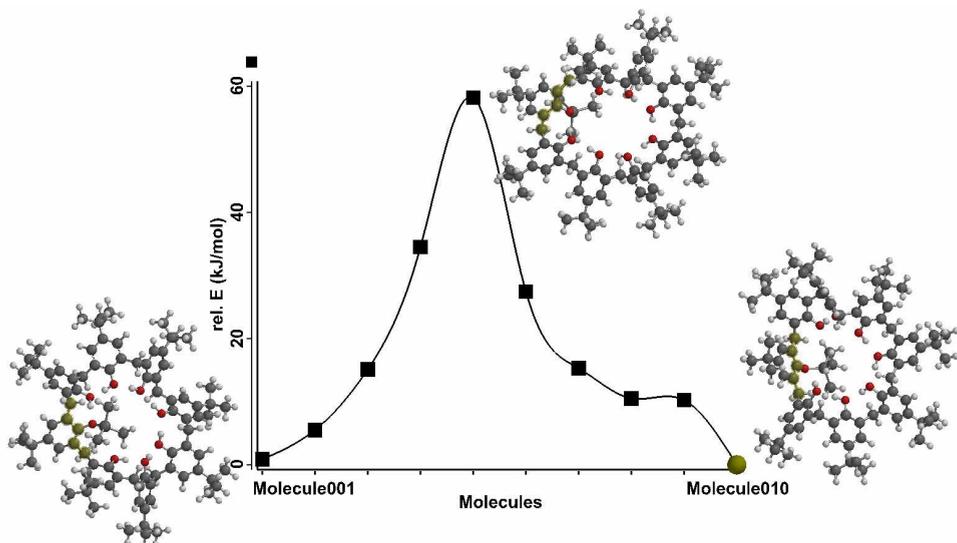
Figure 1. A plot of the PM3 calculated energies against the HC…CH (marked) dihedral angle for the monosubstituted calix[8]arene.

The complete substitution at the lower rim has also been evidenced by the IR spectra of **3** and **4** where the band corresponding to the –OH stretching vibration at 3280 cm^{-1} [17, 18] is no longer present.

Furthermore, in the 3000-2800 cm^{-1} range, the characteristic C-H stretching vibrations for the -Me groups of the -$SiMe_3$ fragment appear as sharp bands. In addition, an intense band corresponding to the -O-Si-stretching vibration evidenced at 1148 cm^{-1} for **3** and 1013 cm^{-1} for **4** [18]. Most probably the substituents in **3** are oriented alternatively up and down relative to the mean plane of **1**, (Figure 3) an arrangement which minimizes the repusions between the $SiMe_3$ groups and also maximizes the π...HC interactions between the arene fragments and the silyl substituents.
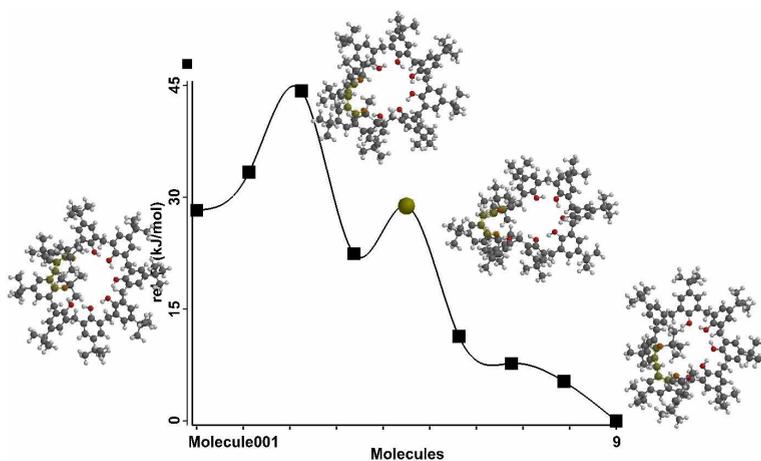
Figure 2. A plot of the PM3 calculated energies against the HC…CH (marked) dihedral angle for a vicinal disubstituted calix[8]arene.

Figure 3 shows also a linear dependence of enthalpy of formation with the number of SiMe$_3$ substituents.
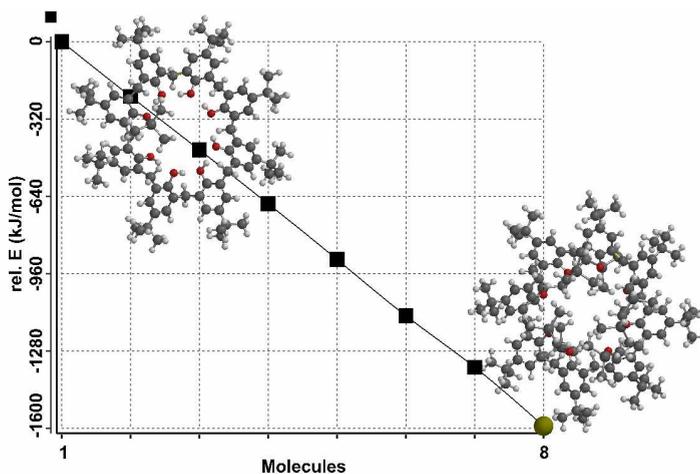
Figure 3. Variation of the PM3 calculated enthalpy of formation of SiMe$_3$ substituted calix[8]arenes. Only structures of the monosubstituted and fully substituted calixarenes are displayed.

CONCLUSIONS

Lithiation of the parent calix[8]arene followed by addition of the appropriate halogeno-alkoxisilane proves to be a convenient way to prepare lower rim fully substituted calix[8]arenes.

EXPERIMENTAL SECTION

All experiments were carried out in flame-dried glassware under argon atmosphere by using high-vacuum-line techniques. Solvents were dried and freshly purified with SPS-5MB system. NMR spectra were recorded (with $CDCl_3$ as solvent) with a Bruker Avance 300 spectrometer at the following frequencies: [1]H, 300.13 MHz; ^{13}C, 75.47 MHz (reference TMS). IR spectra were recorded with a Vector 22 Bruker spectrometer by direct introduction method and a Jasco FT/IR Specord 600 spectometer in KBr pills. Melting points were determined with a Wild Leitz-Biomed apparatus. Me_3SiCl, $Cl\text{-}(CH_2)_3\text{-}Si(OMe_3)_3$, and BuLi were purchased from Merck.

p-tert-butyl-calix[8]arene 1

p-tert-butylcalix[8]arene was obtained according to the literature data [13]. *p-tert*-butylphenol (50 g; 0,33 mol), *para*formaldehyde (17.5 g, 0,58 mol), sodium hydroxide (2,5 ml, 10 N) were dissolved in a mixture of xylenes (300 ml) at room temperature. This suspension was stirred for 4 h at reflux temperature and the water was eliminated through a Dean Stark trap. Solvents and volatile products were removed in vacuo, and the white precipitate formed was filtered and washed with water and acetone. Recrystallization from chloroform (100 ml) afforded pure **1**.

Yield: 46.1 g (85 %). M.p. 405–410 ℃.

^{1}H NMR: δ = 9.66 ppm (s, 1H, <u>OH</u>), 7.17 ppm (s, 2H, H-5, <u>ArH</u>), 3.53 ppm (d, 2H, <u>CH_2</u>), 1.25 ppm (s, 9H, <u>C(CH_3)_3</u>).

Octakis-(trimethylsilyl)-*p-tert*-butyl-calix[8]arene 3

4.24 ml of a solution of *n*BuLi (1.6 M in hexane, 6.78 mmol) mmol) was added dropwise, at –80 ℃, to a solution of *p-tert*-butyl-calix[8]arene (1 g, 0.77 mmol) in THF (40 ml). The solution turned yellow and was stirred at this temperature for an additional hour. The lithium compound was then transferred to Me_3SiCl (0.9 ml, 7.04 mmol, d = 0.85 g/ml) in THF (20 ml) cooled at –80 ℃. After 2 hours of stirring the mixture was allowed to warm to room temperature. Solvents and volatile products were removed in vacuo, and the residue was dissolved in pentane (20 ml) to filter out the lithium salts. Recrystallization from chloroform (100 ml) afforded pure **3**

Yield: 0.81 g (62 %). M.p. 316 - 322 ℃.

^{1}H NMR: δ = 1.10, 1.27 ppm (m, 9H, <u>C(CH_3)_3</u>), 2.19 ppm (s, 9H -O-Si<u>Me_3</u>) 3.85 ppm (broad m, $^2J_{HH}$ = 12,85 Hz, 2H, CH_2), 6.92 ppm (broad s, 2H, H arom.).

IR: 2904-2869 cm^{-1} (ν_a SiMe_3), 1148 cm^{-1} (ν_a -O-Si-)

Octakis-(*n*-propyl-trimethoxysilane)-*p-tert*-butyl-calix[8]arene 4

4.5 ml of a solution of *n*BuLi (1.6 M in hexane, 7.2 mmol) was added dropwise, at –80 ℃, to a solution of *p-tert*-butyl-calix[8]arene (1 g, 0.77 mmol) in THF (40 ml). The solution turned yellow and was stirred at this temperature

for an additional hour. The lithium compound was then transferred to a solution of 3-chloropropyl-trimetoxysilane (1.30 ml, 7.09 mmol, d = 1.09 g/ml) in THF (20 ml) cooled at −40 °C. The orange solution was allowed to warm to room temperature. Solvents and volatile products were removed in vacuo, and the residue was dissolved into pentane (20 ml). Lithium salts were filtered out; compound **4** crystallized as a brick-colored solid after 4 − 5 h at − 4 °C under argon atmosphere.

Yield: 1.13 g (56 %). M.p. 422 °C (decomposition).

^{1}H NMR: δ = 0.80 ppm (dd, 2H, -C$\underline{H}_2$-Si(OMe)$_3$), 1.30 ppm (m, 9H, *t*-Bu), 1.90 ppm (q, 2H, -CH$_2$-C$\underline{H}_2$-CH$_2$-), 3.53 ppm (t, 2H, -O-C$\underline{H}_2$-), 3.57 ppm (s, 9H, -Si-(O-C$\underline{H}_3$)$_3$), 7.15 ppm (m, 2H, H arom).

^{13}C RMN: δ = 6.63 ppm (s, -$\underline{C}$H$_2$-Si(OMe)$_3$), 8.03 ppm (s, -CH$_2$-$\underline{C}$H$_2$-CH$_2$-), 26.21 ppm (s, -$\underline{C}$-(CH$_3$)$_3$), 31.66 ppm (s, -C-($\underline{C}$H$_3$)$_3$), 33.77 ppm (s, -Ph-$\underline{C}$H$_2$-Ph-), 47.14 ppm (s, -Ar-O-$\underline{C}$H$_2$-) 50.44 ppm (s, -(O-$\underline{C}$H$_3$)$_3$), 122-126 ppm (m, *meta* $\underline{C}$), 126-132 ppm (m, ipso $\underline{C}$), 135-145 ppm (m, *para* $\underline{C}$).

IR: 1013 cm^{-1} (ν_a *Si-O*Me)

ACKNOWLEDGMENTS

REFERENCES

1. C. D. Gutsche, J. A. Levine, *J.Am.Chem.Soc.*, **1982**, *104*, 2652.

2. Z. Asfari, V. Bohmer, J. Harrowfield, J. Vicens, *Calixarenes 2001*, Kluwer Academic Publishers, **2001**, chapter 5.

3. P. Jose, S. Menon, *Bioinorg. Chem. Appl.*, **2007**, ID 65815, 1.

4. J. W. Cornforth, E. D. Morgan, K. T. Potts, R. J. W. Rees, *Tetrahedron*, **1973**, *29*, 1659.

5. D. Gutsche, *Calixarenes: An introduction, 2nd edition,* RSC, Thomas Graham House, Science Park, Milton Road, Cambridge, UK, **2008**, chapter 2.

6. S. Seiji, K. Hirosuke, A. Takashi, M. Tsutomu, S. Hirosi, M. Osamu, *J. Chem. Soc. Perkin Trans. 1*, **1989**, *5*, 1073.

7. A. Arduini, A. Casnati, *Macrocycle Synth.*, **1996**, 145.

8. C. D. Gutsche, L. G. Lin, *Tetrahedron*, **1986**, *42*, 1633.

9. C. D. Gutsche, B. Dhawan, K. H. No, R. Muthukrishnam, *J. Am. Chem. Soc.*, **1981**, *103*, 3782.

10. C.D.Gutsche, L. J. Bauer, *J. Am. Chem. Soc.*, **1985**, *107*, 6052.

11. C. D. Gutsche, L. J. Bauer, *J. Am. Chem. Soc.*,**1985**, *107*, 6059.

12. F. Billo, R. M. Musau, A. Whiting, *ARKIVOC*, **2006**, *10*, 199.

13. J. H. Munch, C. D. Gutsche, *Org. Synth.*, **1990**, *68*, 243.

14. G. Ferguson, J. F. Gallagher, M. A. McKervey, E. Madigan, *J. Chem. Soc. Perkin Trans 1*, **1996**, 599.

15. C. D. Gutsche, *Calixarenes Revisited*, The Royal Society of Chemistry, Thomas Graham House, UK, **1998**, chapter 3.

16. Spartan'06 Wavefunction, Inc. Irvine, CA, Except for molecular mechanics and semi-empirical models, the calculation methods used in Spartan have been documented in: Y. Shao, L.F. Molnar, Y. Jung, J. Kussmann, C. Ochsenfeld, S.T. Brown, A.T.B. Gilbert, L.V. Slipchenko, S.V. Levchenko, D.P. O'Neill, R.A. DiStasio Jr., R.C. Lochan, T. Wang, G.J.O. Beran, N.A. Besley, J.M. Herbert, C.Y. Lin, T. Van Voorhis, S.H. Chien, A. Sodt, R.P. Steele, V.A. Rassolov, P.E. Maslen, P.P. Korambath, R.D. Adamson, B. Austin, J. Baker, E.F.C. Byrd, H. Dachsel, R.J. Doerksen, A. Dreuw, B.D. Dunietz, A.D. Dutoi, T.R. Furlani, S.R. Gwaltney, A. Heyden, S. Hirata, C-P. Hsu, G. Kedziora, R.Z. Khalliulin, P. Klunzinger, A.M. Lee, M.S. Lee, W.Z. Liang, I. Lotan, N. Nair, B. Peters, E.I. Proynov, P.A. Pieniazek, Y.M. Rhee, J. Ritchie, E. Rosta, C.D. Sherrill, A.C. Simmonett, J.E. Subotnik, H.L. Woodcock III, W. Zhang, A.T. Bell, A.K. Chakraborty, D.M. Chipman, F.J. Keil, A.Warshel, W.J. Hehre, H.F. Schaefer, J. Kong, A.I. Krylov, P.M.W. Gill and M. Head-Gordon, *Phys. Chem. Chem. Phys.*, **2006**, *8*, 3172.

17. G. Ferguson, J. F. Gallagher, M. A. Mckervey, E.Madigan, *J. Chem. Soc. Perkin Trans 1*, **1996,** *599*.

18. P. J. Launer, *Infrared Analysis of Organosilicon Compounds: Spectra-Structure Correlation*, B. Arkles, G. L. Larson (eds), Petrarch Systems (section 8), **1987**.

THE INTERACTION OF SILVER NANOPARTICLES WITH LIPOIC ACID

OSSI HOROVITZ[a], **MARIA TOMOAIA-COTIŞEL**[a], **CSABA RACZ**[a], **GHEORGHE TOMOAIA**[b], **LIVIU-DOREL BOBOŞ**[a], **AURORA MOCANU**[a]

ABSTRACT. Silver nanoparticles of about 6 nm average size were prepared by reduction of an aqueous silver nitrate solution with sodium citrate and characterized by UV-Vis spectroscopy and transmission electron microscopy (TEM). The interaction of this aqueous colloidal silver solution with the α-lipoic acid solution in ethanol was investigated. The changes in the optical spectra and the TEM images suggest the adsorption of lipoic acid molecules onto the silver nanoparticles and the self assembly of the particles in three dimensional aggregates.

Keywords: *silver nanoparticles, α-lipoic acid, UV-Vis spectra, TEM, self aggregation*

INTRODUCTION

Silver is well known for its special optical properties, conferring him its role in photography, and for its bactericidal properties. Silver nanoparticles are of great interest for their various applications in surface enhanced Raman scattering (SERS) [1, 2], photonics [3] and photocatalysis [4], microelectronics [5-6], optics [7] and as antibacterial and antimicrobial agent [8, 9].

Thus it is not surprising that a great number of methods were devised for the synthesis of silver nanoparticles, both in aqueous and in biphasic systems. The silver source was mostly silver nitrate and the reducing agents were sodium citrate [10-12], sodium borohydride [13, 14], ethanol or methanol [15], polyols such as ethylene glycol, in the presence of poly(vinylpyrrolidone) as a polymeric capping reagent [16,17], or glycerol in the presence of o-phenylenediamine [18], formamide [13] and *N,N*-dimethylformamide [19-21], *N*-hexadecylethylenediamine [22], sodium acrylate [23] and even a cell filtrate from a fungus [24].

[a] *Babeş-Bolyai University of Cluj-Napoca, Faculty of Chemistry and Chemical Engineering, Department of Physical Chemistry, 11 Arany J. Str., 400028 Cluj-Napoca*
[b] *Iuliu Haţieganu University of Medicine and Pharmacy, Department of Orthopedic Surgery, 47 Moşoiu T. Str., 400132 Cluj-Napoca, mcotisel.chem.ubbcluj.ro@gmail.com*

Since colloidal silver presents a high sensitivity toward oxygen, at times synthesis was achieved in an inert atmosphere [23]. The formation of silver nanoparticles was also favored by γ radiation [12], laser irradiation [25] or UV illumination [26].

Bioconjugates of the hemoproteins, myoglobin, and hemoglobin have been synthesized by their adsorption on spherical silver nanoparticles [27]. Silver nanoparticle-oligonucleotide conjugates were prepared, based upon DNA with cyclic disulfide-anchoring groups [28]. When silver nanoparticles functionalized with complementary DNA sequences are combined, they assemble to form DNA-linked nanoparticles networks. The interaction between silver nanoparticles and various DNA bases (adenine, guanine, cytosine, and thymine) was described [13]. Silver nanoparticles were adsorbed on the surface of natural wool, as a result of the interaction of silver with sulfur moieties related to the cysteine group [29]. The adsorption of aliphatic-nonpolar amino acids represented by L-methionine on silver nanoparticles was studied by the FT-SERS method [30] and a physical and chemical adsorption by $-NH_3^+$, COO^-, S, was identified

In previous works, we synthesized gold nanoparticles in aqueous solutions and investigated their functionalization and self aggregation with various biomolecules, such as proteins [31] and amino acids [32-35].

The goal of the present investigation is to obtain silver nanoparticles in colloidal aqueous solution and to study their interaction with α-lipoic acid.

RESULTS AND DISCUSSION

The colloidal aqueous solution containing silver nanoparticles is yellow. The UV-visible absorption spectrum of this solution presents a well-defined absorption band with a maximum at the wavelength λ_{max} = 399 nm (Fig. 1). This value is characteristic for plasmon absorbance for nanometric Ag particles. The colloidal solution is rather stable; after one month, only slight modifications in the spectrum were observed.

As reported in literature, the position of λ_{max} for silver nanoparticles is highly dependent on particle shape and can range from around 400 nm for spherical particles to near 800 nm for sharp-edged triangles. For aggregated particles, a red shift is observed [36]. Wavelength and shape of this band are also affected by various adsorbed solutes [27].

The size of the colloidal silver particles has been measured by TEM imaging (for example, Fig. 2). The particles present mostly spherical or ovoid shape. From the sizes of a great number of particles, measured on the TEM images, the following characteristics were calculated: average size (diameter): 5.9 nm; standard deviation: 2.7 nm (extreme values 1.4 and 13.7 nm); average mass of a particle (considered spherical): $1.1 \cdot 10^{-18}$ g; average number of silver atoms in a particle: $6 \cdot 10^3$.
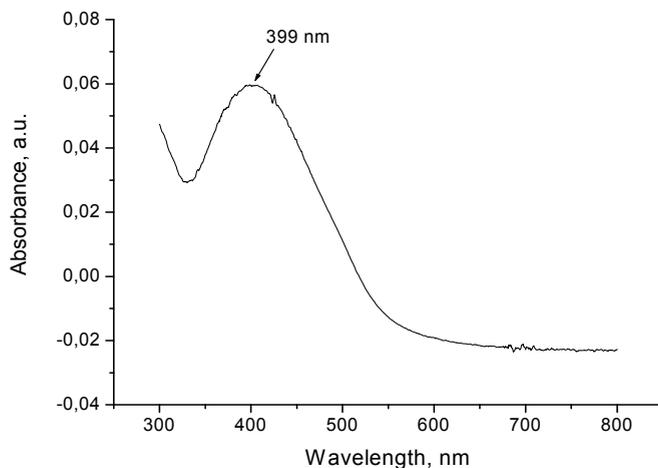
Figure 1. Optical spectrum of the colloidal silver solution
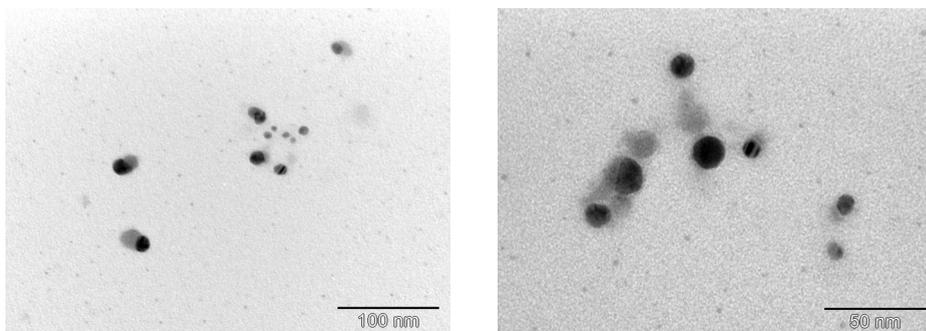
Figure 2. TEM images for silver nanoparticles
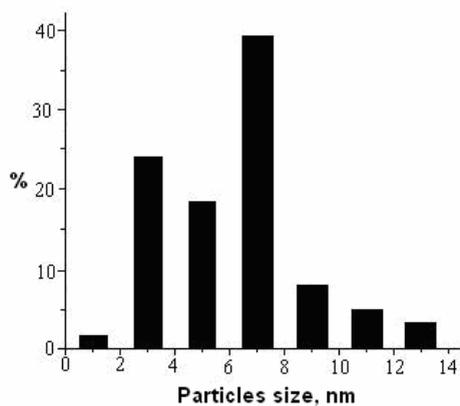
Figure 3. Histogram of size distribution for Ag particles

A histogram providing the size distribution of silver nanoparticles, obtained from TEM pictures, is given in Fig. 3. The predominant fraction is that of particles with about 7 nm diameter, but there are also important contributions from the particles of about 3 and 5 nm size.

The α-lipoic acid or thioctic acid, IUPAC name: 5-(dithiolan-3-yl)pentanoic acid (Scheme 1) is an important biomolecule, known for its antioxidant properties, and is used in the treatment of various diseases [37-39]. The presence of the disulfide group (the ditholane ring) suggests a potential strong interaction with silver nanoparticles. Lipoic acid is practically insoluble in water, so its ethanol solution had to be used to investigate its interaction with the colloidal silver solution.
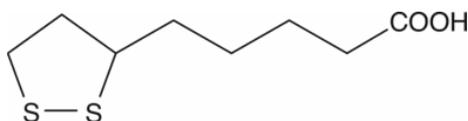
Scheme 1.

In the UV-Vis spectrum of α-lipoic acid, an absorption band with the maximum at 336 nm is observed (Fig. 4). Adding a small amount of the α-lipoic acid 0.01 M solution in ethanol to the aqueous silver colloidal solution (volume ratio 1/7.5) strongly modifies the spectra of both solutions. The absorption peak of α-lipoic acid disappears, being replaced by a shoulder at low wavelength, and the absorption peak of the silver nanoparticles vanishes
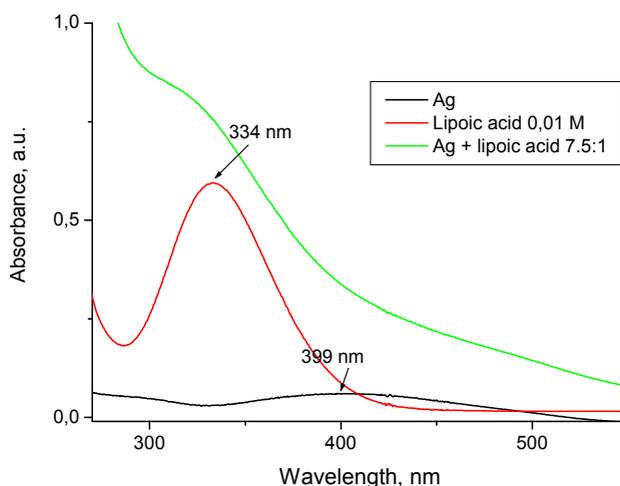
Figure 4. Optical spectra of the aqueous colloidal silver solution, of the α-lipoic acid solution in ethanol and of the mixture of the two solutions in the volume ratio 7.5/1

also (Fig. 4). The yellow color of the solutions fades away. These changes in the spectra suggest a strong interaction between silver nanoparticles and α-lipoic acid.

The TEM images of the mixtures of silver nanoparticles and α-lipoic acid, given in Fig. 5 for different magnifications, confirm this interaction. Large aggregates of silver nanoparticles are seen, resulted by their self assembly mediated by the α-lipoic acid molecules. The adsorption of the biomolecules proceeds probably by means of the sulfur containing groups. The process should be analogous to the adsorption of *n*-octadecyl disulfide onto colloidal silver nanoparticles [40], where the formation of three-dimensional self-assembled monolayers was observed.

On the other part, by introducing the lipoic acid solution in ethanol in the aqueous colloidal solution, an emulsion of lipoic acid is generated, and the silver nanoparticles seem to be trapped in the nanodrops of the organic phase (Fig. 5d).
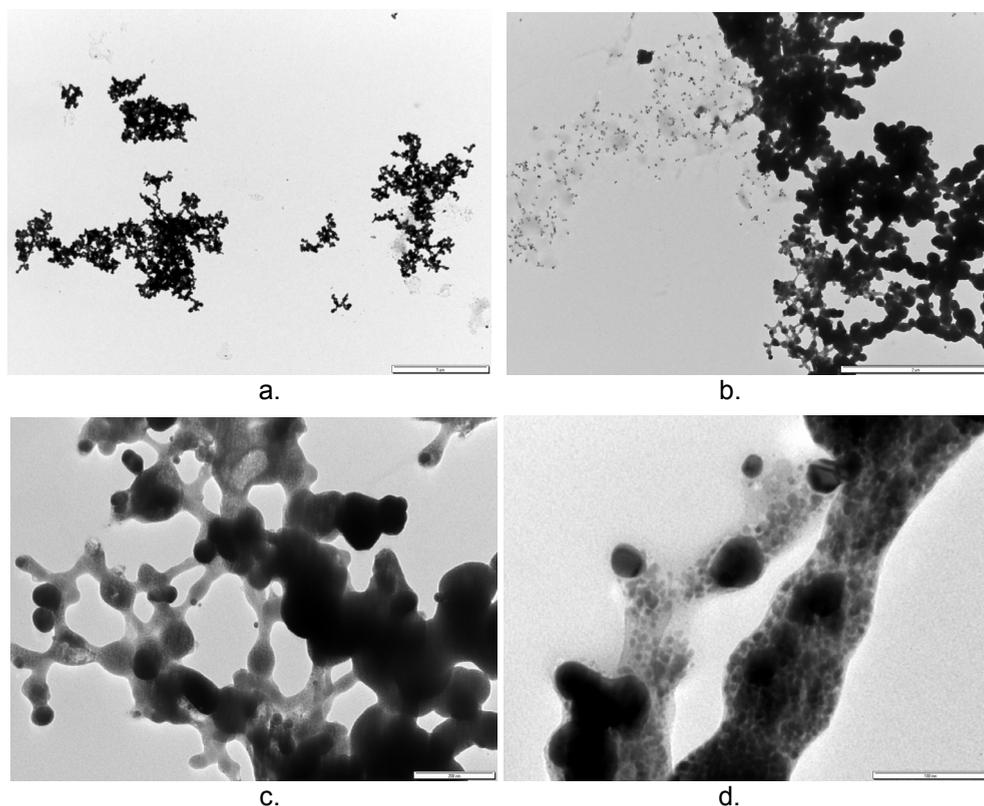
Figure 5. TEM images of silver nanoparticles with α-lipoic acid. The images bars correspond respectively to 5 µm (a), 2 µm (b), 200 nm (c), and 100 nm (d)

CONCLUSIONS

A stable silver colloidal solution was prepared and characterized by UV-Vis spectroscopy and TEM imaging. By means of these techniques the self-aggregation of silver nanoparticles is evidenced, the process being induced by α-lipoic acid. Functionalization of silver nanoparticles through biomolecules is important for the development of new biomaterials with implications in nanoscience and nanotechnology.

EXPERIMENTAL SECTION

The colloidal silver solution was prepared by a method adapted from [11]. 125 mL of 0.001 M solution of silver nitrate in water was heated until boiling under continuous magnetic stirring. Then 5 mL of 1% sodium citrate solution was added and the heating continued until the color was pale yellow. The solution was then rapidly cooled on ice to room temperature. The solution of colloidal silver particles was stored in brown bottles and kept at 4 ^{o}C. The silver content of the solution is 104 mg/L.

$AgNO_3$ was purchased from Merck (high purity above 99.5 %). The trisodium citrate dihydrate was obtained from Sigma Aldrich (high purity above 99%). α-Lipoic acid (extrapure) was purchased from Jiangsu Chemical Company – China, and its 0.01 M solution in ethanol was prepared. All aqueous solutions were prepared using deionized water with resistivity of 18 MΩ·cm, obtained from an Elgastat water purification system.

The UV/Vis absorption spectrum of the solutions was studied using a Jasco UV/Vis V-530 spectrophotometer, with 10 mm path length quartz cuvettes in the 190 – 900 nm wavelengths range.

The silver nanoparticles suspension (7 μL), in the absence and in the presence of lipoic acid, was deposited for 30 s on the carbon coated specimen grid and observed with a transmission electron microscope (TEM: JEOL – JEM 1010). TEM images have been recorded with a JEOL standard software

ACKNOWLEDGMENTS

REFERENCES

1. Z. Wang, S. Pan, T.D. Krauss, H. Du, L. J. Rothberg, *Proceedings of the National Academy of Sciences of the USA*, **2003**, *100*, 8638.

2. P. Matejka, B. Vlckova, J. Vohidal, P. Pancoska, V.J. Baumrunk, *Journal of Physical Chemistry,* **1992**, *96*,1361.

3. M. P. Plieni, A. Taleb, C. J. Petit, *Journal of Dispersion Science and Technology,* **1998**, *19* (2 and 3), 185.

4. Z. Zhang, R. C. Patel, R. Kothari, C. P. Johnson, S. E. Friberg, P. A. Aikens, *Journal of Physical Chemistry B,* **2000**, *104*, 1176.

5. R. B. Bright, M. D. Musick, M. J. Natan, *Langmuir*, **1998**, *14*, 5695.

6. R. C. Doty, H. Yu, C. K. Shih, B. A. Korgel, *Journal of Physical Chemistry B*, **2001**, *105*, 8291.

7. M. Kerker, *Journal of Colloid and Interface Science*, **1985**, *105*, 297.

8. Q. L. Feng, J. Wu, G. Q. Chen, F. Z. Cui, T. N. Kim, J. Kim, *Journal of Biomedical Materials Research,* **2000**, *52*, 662.

9. I. Sondi, B. Salopek-Sondi, *Journal of Colloid and Interface Science*, **2004**, *275*, 177.

10. Z. S. Pillai, P. V. Kamat, *Journal of Physical Chemistry B*, **2004**, *108*, 945.

11. P. V. Kamat, M. Flumiani, G. V. Hartland, *Journal of Physical Chemistry B*, **1998**, *102*, 3123.

12. A. Henglein, M. Giersig, *Journal of Physical Chemistry B,* **1999**, *103*, 9533.

13. S. Basu, S. Jana, S. Pande, T. Pal, *Journal of Colloid and Interface Science*, **2008**, *321*, 288.

14. Y.-H. Wang, J. Zhou, T. Wang, *Chinese Journal of Inorganic Chemistry*, **2007**, *23*, 1485.

15. P.-Y. Silvert, R. Herrera-Urbina, N. Duvauchelle, V. Vijayakrishnan, K. J. Tekaia-Elhissen, *Journal of Materials Chemistry*, **1996**, *6*, 573.

16. Y. Sun, Y. Xia, *Science*, **2002**, *298*, 2176.

17. C. Chen, L. Wang, G. Jiang, H. Yu, *Reviews on Advanced Materials Science*, **2006**, *11*, 1.

18. M. H. Ullah, I. Kim, C.-S. Ha, *Journal of Nanoscience and Nanotechnology*, **2006**, *6*, 777.

19. I. Pastoriza-Santos, L. M. Liz-Marzán, *Langmuir*, **1999**, *15*, 948.

20. I. Pastoriza-Santos, C. Serra-Rodríguez, L. M. Liz-Marzán, *Journal of Colloid and Interface Science*, **2000**, *221*, 236.

21. I. Pastoriza-Santos, L. M. Liz-Marzán, *Pure and Applied Chemistry*, **2000**, 72, 83.

22. A. Manna, T. Imae, M. Iida, N, Hisamatsu, *Langmuir*, **2001**, *17*, 6000.

23. I. Hussain, M. Brust, A .J. Papworth, A. I. Cooper, *Langmuir*, **2003**, *19,* 4831.

24. K. C. Bhainsa, S. F. D'Souza, *Colloids and Surfaces B: Biointerfaces*, **2006**, *47*, 160.

25. J. P. Abid, A. W. Wark, P .F. Breevt, H. H. Girault, *Chemical Communications (Cambridge)*, **2002** (7), 792.

26. A. Henglein, *Chemistry of Materials,* **1998**, *10*, 444.

27. R. T. Tom, A. K. Samal, T. S. Sreeprasad, T. Pradeep, *Langmuir*, **2007**, *23*, 1320.

28. J.-S. Lee, A. K. R. Lytton-Jean, S. J. Hurst, C. A. Mirkin, *Nano Letters*, **2007**, *7*, 2112.

29. L. Hadad, N. Perkas, Y. Gofer, J. Calderon-Moreno, A. Hule, A. Gedanken, *Journal of Applied Polymer Science*, **2007**, *104*, 1732.

30. S. Li, G.-M. Zhou, D.-C. Yang, D.-N. H.-J. Yu,. X.-J. Peng, N. W. Wu, *Spectroscopy and Spectral Analysis*, **2007**, *27*, 711.

31. O. Horovitz, Gh. Tomoaia, A. Mocanu, T. Yupsanis, M. Tomoaia-Cotisel, *Gold Bulletin*, **2007**, *40* (3), 213.

32. O. Horovitz, A. Mocanu, Gh. Tomoaia, L. Boboş, D. Dubert, I. Dăian, T. Yupsanis, M. Tomoaia-Cotisel, *Studia Universitatis Babes-Bolyai, Chemia*, **2007**, *52* (1), 97.

33. I. Petean, Gh. Tomoaia, O. Horovitz, A. Mocanu, M. Tomoaia-Cotisel, *Journal of Optoelectronics and Advanced Materials*, **2008**, *10*, 2289.

34. L. Barbu-Tudoran, Gh. Tomoaia, O. Horovitz, A. Mocanu, M. Tomoaia-Cotisel, *Journal of Optoelectronics and Advanced Materials*, **2008**, *10*, 2293.

35. A. Mocanu, I. Cernica, Gh. Tomoaia, L. D. Bobos, O. Horovitz, M. Tomoaia-Cotisel, *Colloids and Surfaces A, Physical and Engineering Aspects*, **2009**, *338*, 93.

36. W. P. Hall, G. Hartland, R. Van Duyne, H. Petrova, *Nanoscape*, **2005**, *2*, 35.

37. G. P. Biewenga, G. R. M. M. Haenen, A. Bast, *General Pharmacology: The Vascular System*, **1997**, *29*(3), 315.

38. P. J. Randle, *Diabetes / Metabolism Reviews*, **1998**, *14*(4) 263.

39. G. P. Biewenga, G. R. M. M. Haenen, A. Bast, *Drug Metabolism Reviews*, **1997**, *29*(4) 1025.

40. L. A. Porter, Jr., D. Ji, S. L. Westcott, M. Graupe, R. S. Czernuszewicz, N. J. Halas, T. R. Lee, *Langmuir*, **1998**, *14*, 7378.

OPTIMISATION OF COPPER REMOVAL FROM DILUTED SOLUTIONS

FLORICA IMRE-LUCACI[a], SORIN-AUREL DORNEANU, PETRU ILEA

ABSTRACT. An experimental study concerning the copper removal from a simulated wastewater containing 10 ppm of Cu^{2+} ions was performed in a continuous flow electrochemical reactor equipped with a rectangular three-dimensional (3D) cathode made of reticulated vitreous carbon (RVC) with 100 ppi porosity. The influence of low supporting electrolyte concentrations and of the electrode polarisation potential was investigated. The reactor performance was evaluated considering the residual copper concentration and the specific energy consumption. After 90 min of electrolysis, the copper ion concentration was reduced to less than 0.1 ppm, permitting the discharge of the treated solutions to the drain system. With an operating cell voltage around 1.8 V, specific energy consumptions close to 0.18 kWh per cubic meter of treated wastewater was calculated.

Keywords: *removal, copper, reticulated vitreous carbon electrode, waste waters*

INTRODUCTION

Wastewaters containing heavy metal ions (HMI), such as cadmium, chromium, copper, gold, lead, nickel, silver, tin and zinc, are generated in large quantities during electroplating, manufacturing of microelectronic parts, mining and processing of photographic materials. For environmental and economic reasons, these toxic metals should be removed from wastewater before discharge [1, 2].

The maximum admitted concentrations (MAC) of heavy metals is strictly regulated in EU, imposing a rigorous control and treatment of wastewaters. These limits are in the domain 0.05 – 1 ppm for HMI [3]. In order to respect the MAC, the removal by cathodic deposition presents a clear, versatile and efficient method.

Depending on the heavy metals concentrations, the removal process can be done in different manners. For high concentration (grams per litre), two-dimensional cathodes can be used and the content of heavy metals can be reduced with one order magnitude. The resulting effluent can be reused in the process or it can be introduced in a new stage of chemical or electrochemical decontamination [2].

---

[a] *Department of Physical Chemistry, "Babes-Bolyai" University, 11 Arany Janos, 400028 Cluj-Napoca, Romania;* *fimre@chem.ubbcluj.ro*

For low concentrations, under hundreds milligrams per litre, three-dimensional (3D) electrodes must be used and the content of heavy metals can be reduced to levels that allow the discharge of the effluents in environment [4-11].

Preliminary tests concerning the removal of Cu (RCu) from diluted solutions of nitric acid lead to very low current efficiencies due to a very intense hydrogen evolution reaction (HER) but also due to the cathodic reduction of the nitrate and dissolved oxygen. In this context, an alternative method of RCu, able to minimize the specific energy consumption, was searched.

In this work, we present our results concerning the optimization of the copper removal and recovery process from synthetic diluted solutions containing ~ 10 mg/L (ppm) of Cu^{2+} and Na_2SO_4 or NaCl at low concentrations (< 15 mM) as supporting electrolyte. The prepared solutions were electrolyzed, potentiostatically and galvanostatically, in a continuous flow electrochemical reactor (ER), equipped with a 3D RVC electrode. The reactor performance was evaluated based on the final residual copper concentration (C_R) and the global specific energy consumption (W_S) for metric cube (m^3) of treated solution. The concentrations of HMI were measured by atomic adsorption spectroscopy (AAS).

RESULTS AND DISCUSSIONS

Removal studies

The studies concerning the electrochemical copper elimination from dilute solutions were performed using electrolyte volumes of 250 mL. During the whole period of the electrolysis experiments (90 minutes), electrolyte samples of ~ 5 mL were taken out every 5 minutes for copper concentration evaluation. The working electrode current ($I_{W.E.}$) and the mean cell voltage (E_C) were used to estimate W_S and the current efficiency (C_E) for cooper recovery.

Potentiostatic removal of Cu from diluted chloride solutions
The influence of cathodic potential

The measurements' results concerning the influence of the cathodic potential ($\varepsilon_{W.E.}$) on E_C, W_S, C_E and C_R are presented in Table 1. These experiments were completed using 10 mM NaCl as supporting electrolyte and a volume flow rate (V_F) of 50 mL/min.

For a working electrode potential of –100 mV/RE, the system is swinging and it has a poor performance (low C_E and high W_S, respectively). Moreover, the oxygen evolved at the anode is reduced on the cathode, generating a significant parasitic current even in the absence of an intense copper electrodeposition process.

The increase of the cathodic polarization potential to –200 mV/RE induces the enhancement of C_E and, obviously, a decrease of W_S. Furthermore, the formation of a compact cathodic deposit of Cu inhibits the oxygen reduction reaction (RRO) and allows achieving the desired MAC level (< 0.1 ppm Cu^{2+}).

Table 1. Global electrolysis parameters obtained at different cathodic polarization potential (t = 90 min, C_{NaCl} = 10 mM; V_F = 50 mL/min).

$\varepsilon_{W.E.}$ [V/ER]	E_C [V]	W_S [kWh/m^3]	C_E [%]	C_R [ppm]
–0.100	2.17	0.81	2.57	0.626
–0.200	1.79	0.18	9.18	0.060
–0.300	2.16	0.52	3.81	0.059

A cathodic potential of –300 mV/RE is already excessive for RCu, producing a porous Cu deposit and a significant increase of W_S due to the RRO evolved on the anodes' surface.

In these conditions, it was decided to continue the experiments at a cathode polarization potential of –200 mV/RE.

Concerning the C_R, we observed that, after 90 min of electrolysis at $\varepsilon_{W.E.}$ of –100 mV, only 94 % of Cu is removed, without reaching concentrations below 0.1 ppm. Contrarily, at $\varepsilon_{W.E.}$ of –200 mV and –300 mV, around 99.4 % from the initial amount of Cu was removed, reaching C_R below 0.1 ppm.

The effect of the chloride concentration

Due to the low salinity of the used electrolyte solutions, the corresponding electric conductivities were very small and determine high values of W_S. In order to evaluate the influence of supporting electrolyte concentration, measurements have been made at different concentrations of NaCl, the corresponding results being presented in Table 2.

Table 2. Global electrolysis parameters at different C_{NaCl} values
(t = 90 min, $\varepsilon_{W.E.}$ = –200 mV/ER; V_F = 50 mL/min).

C_{NaCl} [mM]	E_C [V]	W_S [kWh/m^3]	C_E [%]	C_R [ppm]
5	2.55	0.73	4.24	0.050
10	1.79	0.18	9.18	0.060
15	1.53	0.12	11.37	0.138

The increase of the NaCl concentration in the electrolyte increases the C_E and decreases W_S. Unfortunately, C_R doesn't reach the desired level because, in the presence of high concentration of Cl$^-$ ions, the formation of Cu$^+$ ions complexes, $[CuCl_x]^{-(x-1)}$, and also the low solubility of CuCl compound inhibit RCu [12]. As a result, the presences of chloride ions have complex effects and a moderate concentration (~ 10 mM NaCl) represents an optimal compromise that includes a reasonable salinity value.

The influence of volume flow rate

In order to evaluate the positive effect of the mass transport intensification, several measurements were accomplished at different volume flow rates. In this context, the results concerning the influence of V_F on RCu are presented in Table 3. The evolutions in time of the copper concentration at different V_F values are also presented in Figure 1.

Table 3. Global electrolysis parameters at different volume flow rate
(t = 90 min, C_{NaCl} = 10 mM, $\varepsilon_{W.E.}$ = –200 mV/ER).

V_F [mL/min]	E_C [V]	W_S [kWh/m^3]	C_E [%]	C_R [ppm]
25	1.97	0.35	5.56	0.682
50	1.79	0.18	9.18	0.060
75	1.90	0.29	6.05	0.069
100	1.97	0.49	4.37	0.053
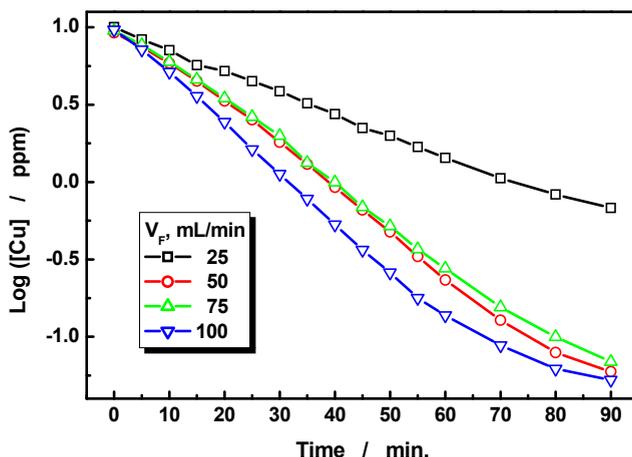
Figure 1. The evolution in time of the copper concentrations for different volume flow rates ($\varepsilon_{W.E.}$ = –200 mV/RE; C_{NaCl} = 10 mM).

At very low V_F values, the rate of RCu is also low and the Cu deposit is insufficient to inhibit RRO.

The increase of the volume flow rate intensifies Cu nucleation and a fast grows of the deposit, which inhibits RRO.

Anyway, the implicit increase of de oxygen quantity developed at the anode and its faster transport to the cathode produces a decrease of the C_E and an increase of W_S.

100

For volume flow rates higher than 25 mL/min, time values less than 90 min are required in order to attain 0.1 ppm Cu residual concentration (see Figure 1).

In these conditions, a flow rate of 50 mL/min is recommended.

Potentiostatic removal of copper from sulphate solutions
The influence of cathodic potential

The measurements' results concerning the influence of the cathodic potential on E_C, W_S, C_E and C_R are presented in Table 4. Based on preliminary tests (see next results), these experiments were completed using 7.5 mM Na_2SO_4 as supporting electrolyte and a volume flow rate of 50 mL/min.

Table 4. Global electrolysis parameters at different cathodic polarization (V_F = 50 mL/min; 7.5 mM Na_2SO_4).

$\varepsilon_{W.E.}$ [V/ER]	E_C [V]	W_S [kWh/m^3]	C_E [%]	C_R [ppm]
−0.100	1.51	0.15	8.84	0.858
−0.200	1.69	0.19	7.85	0.093
−0.300	2.05	0.33	5.37	0.079
−0.350	2.76	1.32	1.91	0.089

In sulphate solutions, the increase of the cathodic polarisation to more negative values induces an increase of the mean value of the recorded current and a decrease of C_E.

At $\varepsilon_{W.E.}$ values of −100 mV, −200 mV and −300 mV, the Cu deposit can inhibit RRO. For $\varepsilon_{W.E.}$ of −350 mV, the electrochemical system becomes lightly unstable (swinging) and a high amount of oxygen developed on anode is reduced at cathode, inducing the increase of the parasitic current and, consequently, the decrease of C_E.

In these conditions, we decided to continue the experiments at a cathodic polarization potential of −200 mV/RE because, at this value, the concentration of the Cu decrease bellow 0.1 ppm and reasonable energy consumption can be obtained.

The effect of Na_2SO_4 concentration

Because Na_2SO_4 is more toxic for environment that NaCl, we try to use the minimum amount of added sulphate. In order to evaluate the influence of Na_2SO_4 on RCu, several measurements have been made at low concentrations of supporting electrolyte, the corresponding results being presented in Table 5.

At low concentration of Na_2SO_4 (1.0 mM), the solution have a very low electric conductivity and, consequently, the W_s is very highly. The increase of Na_2SO_4 concentration induces a decrease of E_C, but the electrochemical system remains unstable due to the evolution of parasitic processes. Because,

in the 7.5 mM Na_2SO_4 solution, the C_R decrease under 0.1 ppm and W_s is low, we decide to use this concentration for further experiments.

Table 5. Global electrolysis parameters at different C_{Na2SO4} values
(t = 90 min; $\varepsilon_{W.E.}$ = −200 mV/RE; V_F = 50 mL/min)

C_{Na2SO4} [mM]	E_C [V]	W_S [kWh/m^3]	C_E [%]	C_R [ppm]
1.0	5.20	2.04	2.14	0.365
2.5	1.88	0.19	8.35	0.164
5.0	1.74	0.35	5.19	0.350
7.5	1,69	0.18	7.85	0.093
10.0	1.69	0.21	6.66	0.133

The influence of volume flow rate

In order to evaluate influence of electrolyte volume flow rate on RCu, measurements were accomplished at V_F values of 25, 50, 75, 100 mL/min, the obtained results being presented in Table 6. The evolutions in time of the copper concentration at different V_F values are also presented in Figure 2.

Table 6. Global electrolysis parameters at different volume flow rate
(t = 90 min, $\varepsilon_{W.E.}$ = −200 mV/ER; 7.5 mM Na_2SO_4).

V_F [mL/min]	E_C [V]	W_S [kWh/m^3]	C_E [%]	C_R [ppm]
25	1.42	0.11	11.78	0.727
50	1.69	0.19	7.85	0.093
75	1.72	0.19	7.82	0.264
100	1.87	0.29	5.79	0.062
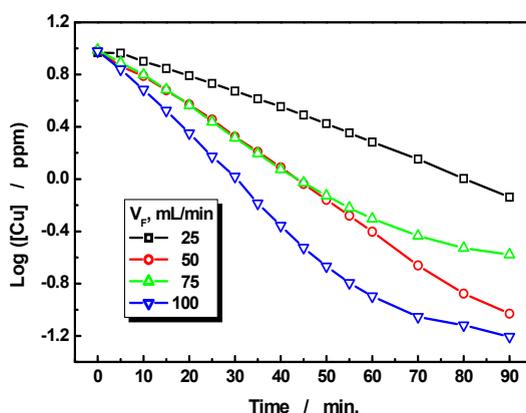
Figure 2. The evolution in time of the copper concentration for different volume flow rate ($\varepsilon_{W.E.}$ = −200 mV/RE; 7.5 mM Na_2SO_4)

At very low volume flow rates, RRO concurs with RCu and the Cu deposit is insufficient to inhibit RRO.

Based on the increase of V_F, the intensification of the mass transport allows Cu nucleation and a fast grow of the deposit, with positive effect on the RRO inhibition. Unfortunately, the implicit grow of de oxygen quantity evolved at the anode and its faster transport to the cathode induces a decrease of C_E and an increase of W_S.

Based on these observations, we concluded that a volume flow rate of 50 mL/min represents the optimal compromise for RCu.

Galvanostatic removal of copper from sulphate solutions

Based on the promising results obtained in potentiostatic conditions, we also decided to test RCu in galvanostatic mode.

The results concerning the influence of the imposed current on the RCu parameters are presented in Table 7. The measurements were done at current values of 25, 30 and 40 mA, at V_F = 50 mL/min and using 7.5 mM Na_2SO_4 as supporting electrolyte.

Table 7. Global electrolysis parameters evaluated for RCu in galvanostatic mode (V_F = 50 mL/min; 7.5 mM Na_2SO_4).

$I_{W.E.}$ [mA]	E_C [V]	W_S [kWh/m^3]	C_E [%]	C_R [ppm]
25	2.22	0.44	4.24	0.164
30	2.24	0.47	4.03	0.136
40	2.71	0.72	3.14	0.157

From the point of view of E_C, W_S and C_E, a current intensity of 25 mA is favourable to the RCu process but it isn't for C_R.

Using the same experiment time (90 min.), we observe that a volume flow rate of 50 mL/min is insufficient to reach the desired level of concentration (< 0.1 ppm).

CONCLUSIONS

The results of our researches concerning the removal of copper from diluted solutions allow us to take the following conclusions:

- For the potentiostatic RCu, a cathodic potential of –200 mV/ ER, a volume flow rate of 50 mL/minute and concentrations of 10 mM NaCl or 7.5 mM Na_2SO_4, respectively, represent the optimal values.
- Using the optimised parameters, MAC of Cu can be attained in the treated solutions.

- The evolution in time of the currents recorded in potentiostatic mode encouraged us to also test RCu in galvanostatic mode;
- The galvanostatic tests show us that increased volume flow rates and/or electrolyse time are required to attain the MAC. The optimisation of galvanostatic operating parameters involves additional experiments.

These promising obtained results prove the feasibility of copper removal from diluted solutions simulating wastewaters.

The validation of the obtained results requires additional measurements at scaling-up level, using pilot installation and real wastewaters samples.

EXPERIMENTAL SECTION

Reagents

The simulated solutions were prepared starting from analytical grade reagents ($CuSO_4$, NaCl and Na_2SO_4, all from Chimopar, Romania) and double-distilled water. The tested solution contained 10 mg/L Cu^{2+} and different concentrations of NaCl or Na_2SO_4.

Experimental setups

A Plexiglas home made electrochemical reactor (ER) previously described [2], a Reglo-Digital peristaltic pump (Ismatec, Switzerland) and a HP72 potentiostat (Wenking, Germany) were used for RCu tests.

A parallelepiped (L x W x H = 45 mm x 25mm x 25 mm) of 100 ppi RVC was used as working electrode. Four graphite cylindrical bars (Φ = 10 mm, L = 25 mm) were used as counter electrodes. Two Ag/AgCl/KCl$_{SAT}$ reference electrodes (RE) were used to record the cathode's and anode's potentials.

The LabView 6.1 software and a PCI 6024 E data acquisition board (National Instruments, USA) were used for process control.

The AAS measurements of Cu concentration in the electrolyte samples were performed with an Avanta PM Spectrometer (GBC, Australia).

ACKNOWLEDGEMENTS

<div align="center">

REFERENCES

</div>

1. A. Al.-Shammari, S.U. Rahman, D.-T. Chin, *J. Appl. Electrochem.*, **2004**, *34*, 447.

2. S.A. Dorneanu, F.-L. Beke, P. Ilea, *Studia Univ. Babes-Bolyai, Chemia*, **2008**, *53,* 97.

3. Romanian Government Decision no. 352 from 11.05.**2005**.
4. P. Ilea, S.A. Dorneanu, Tratarea apelor reziduale cu conţinut de ioni de metale grele, *A X Ediţie a Zilelor academice timişene*, **2007**.
5. C. Ponce de Leoon, D. Pletcher, *Electrochim. Acta,* **1996**, *41*, 533.
6. J.Y. Choi, D.S. Kim, *J. Hazard. Mater.,* **2003**, *B99*, 147.
7. A. Dutra, A. Espiinola, P. Borges, *Minerals Eng.*, **2000**, *13*, 1139.
8. E. Munoz, S. Palmero, M. A. Garcia-Garcia, *Electroanalysis*, **2000**, *10*, 12.
9. G.W. Reade, A.H. Nahle, P. Bond, J.M. Friedrich, F.C. Walsh, *J. Chem. Techn. Biotech.*, **2004**, *79*, 935.
10. G. W. Reade, P. Bond, C. Ponce de Leon, F.C. Walsh, *J. Chem. Techn. Biotech.,* **2004**, *79*, 946.
11. F.A. Lemos, L.G.S. Sobral, A.J.B. Dutra, *Minerals Eng.*, **2006**, *19*, 388.
12. S.C. Varvara, L.M. Muresan, Metode electrochimice de investigare a electrodepunerii metalelor, Casa Cărţii de Ştiinţă, Cluj-Napoca, **2008**, 31.

VOLATILE ORGANIC DISINFECTION BY PRODUCTS DETERMINATION IN DISTRIBUTION SYSTEM FROM CLUJ NAPOCA

MELINDA-HAYDEE KOVACS[a]**, DUMITRU RISTOIU**[a]**, SIDONIA VANCEA**[b]**, LUMINITA SILAGHI-DUMITRESCU**[c]

ABSTRACT. Chlorine is one of the most used water disinfectant agent used on the world. The use of chlorine in the treatment of drinking water has virtually eliminated waterborne diseases, because chlorine can kill or inactivate most microorganisms commonly found in water. The majority of drinking water treatment plants in Romania use some form of chlorine to disinfect drinking water: to treat the water directly in the treatment plant and/or to maintain a chlorine residual in the distribution system to prevent bacterial regrowth. Unfortunately it's used results in formation of some disinfection by products (DBPs) that are suspected from harmful effects on humans. Such of disinfection byproducts are trihalomethanes (THMs). Trihalomethanes are a group of volatile organic compounds that can form when the chlorine used to disinfect drinking water reacts with naturally occurring organic matter (e.g., decaying leaves and vegetation). The preliminary results presented in this paper shown that the THMs levels from Gilau Water treatment Plants and Cluj-Napoca distribution system. The results have higher values in the summer period relative to other seasons.

Keywords: *Volatile disinfection by-products, Trihalomethanes, Chlorine, Water Treatment Plant.*

INTRODUCTION

Chlorine is one of the most common disinfectant agents used in Water Treatment Plant (WTP) from Romania. The drinking water disinfection process with chlorine has been carried out since the dawn of the 20th century to eradicate and inactivate the pathogens from water. In addition to inactivating pathogens in the source water, chlorine are also used as oxidants in drinking water treatment to: remove taste and odors, oxidize iron and manganese,

[a] *Babes Bolyai University of Cluj-Napoca, Faculty of Environmental Science, Str. P-ta Stefan cel Mare, no. 4, 400084, Cluj-Napoca, email: dristoiu@enviro.ubbcluj.ro*

[b] *Garda de Mediu, Comisariatul Judetean Cluj, str. G-ral T. Mosoiu, nr. 49, Cluj-Napoca, Romania*

[c] *Universitatea Babeş-Bolyai, Facultatea de Chimie, str. Arany Janos, nr. 11, 400068, Cluj-Napoca, Cluj-Napoca.*

maintain a residual to prevent biological regrowth in the distribution system, improve coagulation and filtration efficiency and prevent algal growth in sedimentation basins and filters [1]. Chlorine's popularity is not only due to lower cost, but also to its higher oxidizing potential, which provides a minimum level of chlorine residual throughout the distribution system and protects against microbial recontamination [2, 3]. However, in 1974, it was discovered that the chlorination of water resulted in the production of trihalomethanes (THMs) due to reaction of chlorine with natural organic matter (NOM) present in all type of water, referred as precursor of THMs formation [4,5]. Since 1980' THMs have raised significant concern due to evidence of their adverse human health effects, in special cancer and reproductive disorders [6,7].

Because of this unwanted effects of chlorination process USEPA in November 29, 1978, has promulgated the first legislation (interim total THMs standard) to limit the concentration of total THMs (TTHMs) in drinking water.

In Romania the regulation and monitoring of THM has became a current issue in connection with Romania's entry to the UE and the fulfillment of the required drinking water standards. In order to minimize cancer risk, the Romanian has adopted the maximal permissible value fixed in the EU drinking water directive has been adopted by the Romanian legislation in 2002, granting the water companies a transition time of 10 years to meet the requested standards and accepting in the first 5 years a TTHM value of 150 μg/l. In terms of monitoring, the Romanian water law stipulates a minimal number of samples per year depending on the magnitude of the treatment plant. The local health authority carries out the monitoring.

Hence engineers are required to minimize the concentration of THMs in water in the distribution system.

Chlorine reacts with a wide variety of organics in water to give rise to haloform reaction and produce THMs. THMs are organohalogen compounds and they are named as derivates of the compound methane. THMs are formed when three of the four hydrogen atoms attached to the carbon atom in the methane compounds are replaced with atoms of chlorine, bromine and/or iodine [8]. THMs include chloroform – $CHCl_3$, dichlorobromomethane – $CHCl_2Br$, dibromochloromethane – $CHClBr_2$ and bromoform – $CHBr_3$. This complex reaction mechanism of THMs is controlled by parameters such as: concentration and type of precursors, concentration of chlorine, temperature, pH and time. The THMs formation process may be described by the following equation:

$$NOM \text{ (Precursors)} + HOCl \rightarrow \text{Chlorinated organic intermediates} + HOCl \rightarrow CHCl_3 \tag{1}$$

Natural bromide in water
$$(Br^-) + HOCl \rightarrow Br_2 + Cl^- \rightarrow CHCl_2Br/CHClBr_2/CHBr_3 \tag{2}$$

RESULTS AND DISCUSSIONS

THM measurements in Gilau WTP from Cluj: During the THMs analysis the main founded THMs species detected in the water sample was the $CHCl_3$. The $CHCl_3$ concentration differed from month to month during the years. Usually higher $CHCl_3$ concentration was found in the wormer season, than in the winter season. In Gilau WTP and distribution system the highest $CHCl_3$ concentration was detected in August 2007 – 81.1 μg/L. The measurement shows that the $CHCl_3$ concentration increased in the distribution system. The chloroform concentration range in the WTP at the exit of reservoir sampling point was in the range 8 μg/L (March 2007) and18.75 μg/L (November 2007). That could be explain by the fact in the winter season in the water are present lower concentration of NOM than in summer season due to low temperature and light. From that reason less chlorine concentration are required for water disinfection process. During the measurements was observed also that the chloroform concentration increased with distance. Started from the Exit of the reservoir from the WTP (considered 0 point) the chloroform concentration increased with 30 % at the enter of the city (located at 18 km from the Gilau WTP) and in the city center (located at 25 – 30 km from the Gilau WTP) the chloroform concentration was double or almost much with three times. That shows the THMs concentration increased with distance – see table 1.

Table 1. *CHCl3 concentration measured in 2006 – 2008 at the Gilau WTP and Cluj.* [*]Obs: Ex.R. – represent exit of reservoir, En.C. – enter of city, Cen. – center of city.

CHCl3 concentration (μg/L)			
	2007		
Month	Ex.R.	En.C.	Cen.
January	25.4	31.1	40.4
February	12.0	31.6	48.6
March	8.0	18.7	21.6
April	8.2	29.2	33.8
May	14.7	40.6	50.2
June	19.2	60.2	66.3
July	21.0	65.2	69.0
August	28.0	69.0	81.1
September	24.5	39.58	52.4
October	20.1	32.8	47.9
November	18.75	24.9	35.9
December	9.32	12.78	21.7

Factors affecting THM formation: Manny research showed that are several factors affecting the formation potential of THMs. Previous research studies have shown that the major variables that affect THM formation are: chlorine dose and residual, concentration and nature of NOM (mainly humic substances), contact time, pH, temperature of water, and the presence of inorganic ions like bromide [9-13]. In general, higher THM concentrations are expected at higher levels of the above mentioned parameters [2].

Increase of chlorine dose has been reported to have positive influence of DBPs yield. The same is true for increased concentrations of natural organic matter and increased temperature. The presence of bromide ion shifts the speciation of DBPs to more brominated analogues, while increased pH can enhance the formation of some categories of DBPs, e.g. THM, and inhibit the formation of some others, e.g. haloacetonitriles and haloketones [10-11].

The type of raw water also affects the THM levels. Generally, ground waters are naturally protected from runoff NOM, while the difference in occurrence of DBP precursors in river and lakes depends on geological, physical and environmental factors (trophic stage, watershed soil characteristics and land use, lake size, river flow rate, etc.) [2].

Chlorine dose: During the studies it was observed that one of the main important factor that affect the THMs formation in the distribution system in the four WTP studied was the chlorine dose that was applied in the WTP in water disinfection purposes.

In Gilau Water Treatment Plant was added different chlorine dose during the year, the chlorine dose could differed day-by-day as the water matrix was changed due to seasons, temperature, pH and the NOM concentration presented in the raw water. So in Gilau WTP the company has set 2 different chlorine dose range, as function of season: for summer season the chlorine dose range that was added to water for disinfection was set between 0.7 – 0.9 mg/ L and for winter season the chlorine dose set was in the range of 0.5 – 0.7 mg/L. After several measurement has shown that in the period when higher chlorine dose was used the $CHCl_3$ concentration increased – as shown in figure 1.

Nature and Concentration of NOM: Properties of NOM play an important role, since activated aromatic content of NOM increases THM formation [12, 13]. Singer (1999) in his researches shows that the THMs formation is relatively higher for the humic acid fraction, presumably because of the greater aromatic carbon content of the fraction [14]. Manny researcher works showed a linear relationship between chlorine consumption and the activated aromatic carbon content of the various humic and fulvic acid. In addition, NOM contains hydrophobic and hydrophilic materials, the nature and distribution of which may vary with different types of vegetation in the watershed and different species of algae in water. This results in varying influence of NOM on DBP formation [15].

110
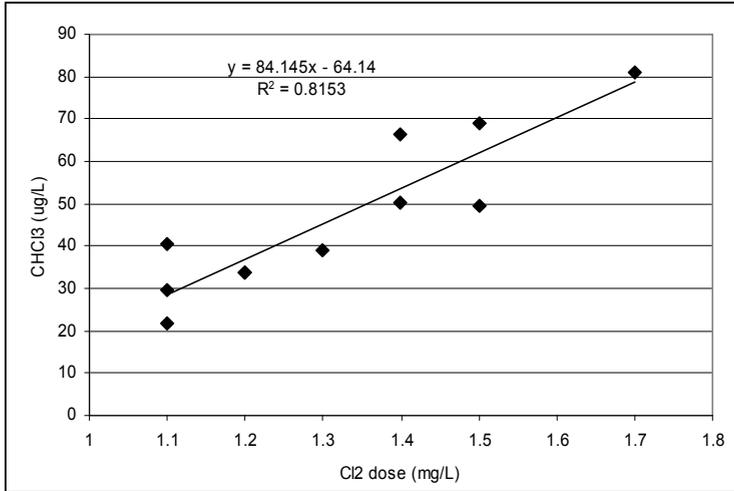
Figure 1. *Chlorine dose as function of CHCl$_3$ concentration in Gilau WTP*

In the WTP the presence of the natural organic matter was determinate with consumption of KMnO$_4$ mg/L – CCO Mn [mgKMnO4/L] – colorimetric method. The presence of the organic matter in the raw water is determinate once at the middle of day in every day in Gilau WTP. The results obtained showed that in the period when the NOM presence in water was higher also the CHCl$_3$ increases – see figure 2.
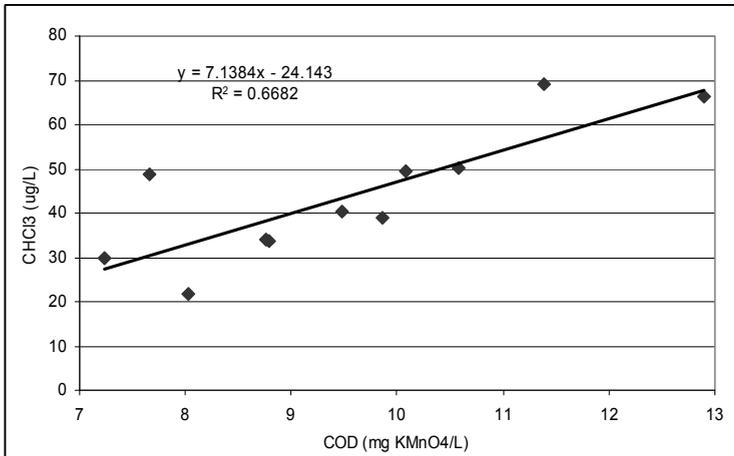
Figure 2. *Relationship between CHCl$_3$ (μg/L) and presence of natural organic mater in water*

Temperature/Season: When temperature increases, reactions are faster and a higher chlorine dose is required, leading to higher formation of THMs. Subsequently, THMs concentrations are expected to be higher in summer than in winter [11; 17; 18-21].

After THMs analysis in every month, the results show that in the winter season the THMs concentration were much lower that in the summer season, with almost 50 %. That could be explain by the fact that in some cases where the ice cover protects surface raw waters, the THM concentrations are lower due to lower water temperature and NOM. In these conditions, the chlorine demand is lower, therefore, the chlorine dose required to maintain adequate residual in the distribution system is also less.

In Gilau WTPs which used as disinfectant agent the chlorine the mean of total trihalomethanes (TTHM) levels for summer, fall, winter, and spring was: 72.17 μg/L, 40.716 μg/L, 30.606 μg/L and 35.23 μg/L respectively;

This study showed that the highest TTHM concentrations were found in the summer and fall seasons, and the lowest TTHM concentrations were present in the winter and spring. Since higher doses of chlorine were used in the warm summer and fall months to ensure prevention of microbiological problems, it was to be expected that this, in combination with warmer water temperatures, would lead to higher TTHMs concentration during the summer and fall seasons.

pH: Several studies have been made to investigate the effect of pH on THMs concentrations. The studies have shown that THM concentrations increases with increasing pH – as shown in figure 3, that could be explain by the fact that THMs formation is mainly attributed to the reactions of the chlorinated intermediates with hydroxide ion in the presence of a small amount of free chlorine.

Bromide: Recent studies have examined the relationship between bromide concentration in a drinking water supply and THMs formation. Based on the differences in bromide concentration, it is inferred that substantial variations in THM formation (and THM species) can be expected. Studies have shown that as the concentration of bromide increases, the concentration of TTHMs increases and more brominated THMs forms because there is more bromide present in the water source for the organics to react with. In the presence of bromide ion (Br-), more brominated and mixed chloro-bromo derivatives are formed [22-25]. When bromide is present, chlorine in the form of hypochlorous acid-hypochlorite ion (HOCl-OCl-) oxidizes bromide ion to hypobromous acid-hypobromite ion (HOBr-OBr-). A mixture of HOCl and HOBr can lead to the formation of both chlorinated and brominated by-products [26].

During the analysis of the THMs species in WTPs the brominated THMs species were very lower all the time, the total brominated THMs species never exceed 10 μg/L. So in the Gilau WTP the only brominated THMs species

that was found was $CHCl_2Br$ and its highest concentration was 9.69 μg/L. After that results we could concluded that in all WTPs the bromide concentration are almost inexistent or in very less concentration.
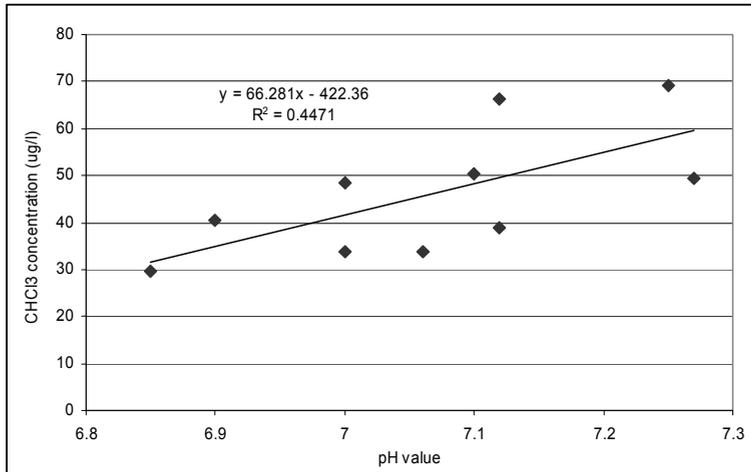
Figure 3. *Relationship between $CHCl_3$ (μg/L) and pH value of water.*

CONCLUSIONS

This study examined the trihalomethanes formation and they concentration in different sampling point take from different sampling points in Cluj-Napoca. Following conclusions were drawn based on the results of the measurements conducted with water samples of every month in 2007.

Chloroform was the determinate trihalomethanes species observed after the chlorination of reservoir water in all of the sampled months. Brominated compounds of trihalomethanes wasn't observed, just $CHCl_2Br$ but in very slow concentration. We can suppose for that reason, the bromine compounds in the raw water is very slow or almost inexistent.

The major factor that influences the trihalomethanes formation is the temperature that is clearly praise in chloroform concentration measured in different months of year. In the months like July, August, September and October when the temperature was highest (21 – 24 °C water temperature) also the chloroform concentration was high (66.3 – 81.1 μg/L) and when the water temperature wasn't high (2.8 – 3.7 °C) the chloroform concentration was between 21.7 – 40.4 μg/L. The major differences in temperature and pH value affect trihalomethanes potential formation (THMFP), with more volatile THM species being produced at the higher temperature and pH. Also we can concluded the season when the water matrix is change from the winter season to summer season also have a seriously influence on trihalomethanes formation.

MATERIALS AND METHODS

Sampling: Several samples were collected from different sampling point of the Gilau Water Treatment Plant (WTP) and distribution system from Cluj-Napoca – located in Cluj jurisdiction. Gilau WTP has as water sourced the Somesul Mic river basin and also Tarnita Storage Lake. All the samples were collected in every month of 2007. The sampling contains the following samples:

Gilau WTP:

-        raw water, filtrated water, chlorinated water, exit reservoir – sampling points that are located in the WTP;
-        Sapca Verde, Beer Factory, Chemistry Faculty, Environmental Faculty and Public Health Institute – sampling points that are located in the distribution system.

All water samples were collected and stored in 40 L vials and closed with Teflon lined screw cap and they were preserved with sodium thiosulfate ($Na_2S_2O_3$) at 4^0C until the analysis. All samples were measured between in 1 and 7 days after sampling.

THMs analysis: THMs were carried out by Thermo Finningan U.S.S. Trace GC Ultra gas chromatography with electron capture detector (GC-ECD) with TriPlus HS auto sampler. The analysis was made using headspace technique. 10 ml of sample was filled into 20 ml headspace vials and closed with Teflon lined screw cap. After that the samples were equilibrated in an oven at $60\,°C$ for 45 minutes, 1 ml of the headspace was then injected into the GC (Cyanopropylphenyl Polysiloxane column, 30 m x 53 μm, 3 μm film thickness, Thermo Finnigan, USA). The column program was $35\,°C$ (hold time 3 minutes), $15\,°C$/minutes to $200\,°C$ (hold time 3 minutes). The inlet was set at $200\,°C$.

The standard stock solution containing 2000 μg/l of each Trihalomethanes from Restek (Bellefont, U.S.) was used. THM working standard solutions (100 mg/l, 4mg/l) were prepared through dilution of the stock solution in 10 ml Methanol. The calibration standards were made using that THM stock solution and the calibration were prepared for the range 0 – 100 μg/L in mineral water Izvorul Alb.

REFERENCES

1. USEPA, 1999a, Microbial and Disinfection Byproduct Rules Simultaneous Compliance Guidance Manual, United States Environmental Protection Agency, EPA 815-R-99-015.
2. R. Sadiq, M. J. Rodriguez, *Science of the Total Environment*, **2004**, *321*, 21.
3. J. Huang, G. C. Smith, *J. of American Water Works Association*, **1984**, 76, 168.

4. J. J. Rook, *J. of American Water Works Association*, **1976**, *68*, 168.

5. T. A. Bellar, J. J. Lichtenberg, R. Krasner, *J. of American Water Works Association*, **1974**, *66*, 703.

6. K. P. Cantor, C. F. Lynch, M. E. Hildesheim, M. Dosemeci, J. Lubin, M. Alavanja, G. Craun, *Epidemiology*, **1988**, *9*, 21.

7. C. G. Graves, G. M. Matanoski, R. G. Tardiff, *Regul Toxicol Pharmacol*, **2002**, *34*, 103.

8. C. Vogt, S. Regli, *Journal of American Water Works Association*, **1981**, *73* (1), 33.

9. G. L. Amy, P. A. Chadik, Z. K. Chowdhury, *J. of American Water Works Association*, **1987**, *79,* 89 .

10. A. D. Nikolaou, S. K. Golfinopoulos, T. D. Lekkas, M. N. Kostopoulou, *Environmental Monitoring and Assessment*, **2004**, *93*, 301.

11. A. D. Nikolaou, T. D. Lekkas, S. K. Golfinopoulos, *Chemical Engineering Journal*, **2004**, *100*, 139.

12. W. E. Elshorbagy, H. Abu-Quadis, K. Elsheamy, *Water Research*, **2000**, *34*, 3431.

13. S. K. Golfinopoulos, G. B. Arhonditsis, *Chemosphere*, **2002**, *47*, 1007.

14. D. A. Reckhow, P. C. Singer, R. L. Malcolm, *Environmental Science & Technology*, **1990**, *24,* 1655.

15. G. Harrington, Characteristics of natural organic matter and their Influence on alum coagulation, Ph.D. Dissertation, **1997**, University of North Caroline.

16. P.C. Singer, *Water Science and Technology*, **1999**, *40*, 25.

17. P. C. Singer, *J. of Environmental Engineering*, **1994**, 120.

18. D. T. Williams, G. L. LeBel, F. M. Benoit, *Chemosphere*, **1997**, *34*, 299.

19. G. L. LeBel, F. M. Benoit, D. T. Williams, *Chemosphere*, **1997**, *34*, 2301.

20. W. J. Chen, C. P. Weisel, *J. of American Water Works Association*, **1998**, *90* 151.

21. H. Arora, M. W. LeChevallier, K. L. Dixon, *J. of American Water Works Association*, **1997**, *89,* 60.

22. M. J. Rodriguez, J. B. Serodes, *Water Research*, **2001**, *35,* 1572.

23. S. W. Krasner, W. H. Glaze, H. S. Weinberg, P. A. Daniel, I. N. Najm, *J. of American Water Works Association*, **1993**, *85*, 73.

24. L. Heller-Grossman, J. Manka, B. Limoni-Relis, M. Rebhun, *Water Research*, **1993**, *27*, 1323.

25. H. Pourmoghaddas, A. A. Stevens, *Water Research*, **1995**, *29*, 2059.

26. H. Pourmoghaddas, A. Stevens, R. N. Kinman, R. C. Dressman, L. A. Moore, J. C. Ireland, *J. of American Water Works Association*, **1993**, *85*, 82.

IRON DOPED CARBON AEROGEL AS CATALYST FOR PHENOL TOTAL OXIDATION

ANDRADA MĂICĂNEANU[a], COSMIN COTEŢ[a], VIRGINIA DANCIU[a], MARIA STANCA[a]

ABSTRACT. Two types of iron doped carbon aerogels were prepared by sol-gel polymerization of potassium salt of 2,4-dihydroxybenzoic acid with formaldehyde. This process was followed by an ion-exchange process between K^+ doped wet gel and Fe(II) or Fe(III) ion aqueous solutions. The resulted Fe(II) or Fe(III) doped gels were dried in supercritical conditions with liquid CO_2 and then pyrolyzed when two types of iron carbon aerogels were obtained. These aerogels were morpho-structural investigated by means of transmission electron microscopy (TEM), X-ray diffraction (XRD), specific surface area determination using nitrogen adsorption (BET and BJH methods) and elemental analysis. Iron doped carbon aerogels were tested as catalytic materials in phenol wet air oxidation process (total oxidation). Temperature, air flow, catalyst quantity and phenol concentration over the removal efficiency of the organic compound was studied.

Keywords: iron doped carbon aerogel, phenol, catalytic wet air oxidation

INTRODUCTION

Wastewaters containing organic compounds (pollutants) from chemical, petrochemical or pharmaceutical industries can create many problems in choosing an appropriate method to treat them. Many of them, (refractory organic pollutants), are difficult to remove by conventional methods (mechanical and biological treatment), therefore alternative methods have to be developed [1-3]. Because of their toxicity and frequency of their presence in industrial wastewaters, phenol and phenolic compounds have gained increased attention in the last two decades. Moreover, phenol is considered to be an intermediate in the oxidation route of higher molecular weight aromatics and so usually is taken as a model compound in research studies [4,5]. The choice of treatment, in case of wastewaters polluted with phenol and phenolic compounds, depends on the concentration, which can varies from 0.1 to 6800 mg/dm^3 depending on the wastewater source (pulp and paper industry, refineries, coking operations, coal processing) [5], economics, efficiency, easy control and reliability [6].

---

[a] *Universitatea Babeş-Bolyai, Facultatea de Chimie şi Inginerie Chimică, Str. Kogălniceanu Nr.1, RO-400084 Cluj-Napoca, România, andrada@chem.ubbcluj.ro*

Several processes for phenol abatement from wastewaters, which can be included in two large categories, recuperative methods (separation) and destructive methods, were studied.

In the first category, methods such as: steam distillation [5], liquid-liquid extraction (n-hexane, cyclohexane, benzene, toluene, etc.) [5], adsorption (activated carbon, activated bentonite, activated zeolites, perlite, resins, etc.) [5,7,8], adsorption-flocculation [9], membrane pervaporation [5], membrane-based solvent extraction [5,10,11] are included.

In the second category the following methods are included: (a) total oxidation by air or oxygen (non catalytic wet air oxidation – WAO, supercritical water oxidation – SCWO, catalytic wet air oxidation – CWAO, oxidative polymerization with oxygen in presence of enzymes), (b) wet oxidation with chemical oxidants (ozone and H_2O_2 – wet peroxide oxidation WPO – with its alternative, non catalytic oxidation, catalytic homogeneous and heterogeneous Fenton oxidation CWPO, catalytic non iron heterogeneous catalysis, and oxidative polymerization in presence of peroxidases) [5,12-16], (c) oxidation with chlorine, chlorine dioxide, potassium permanganate, ferrate (VI) ion [5], (d) electrochemical treatment (indirect electro-oxidation, direct anodic oxidation) [5,17,18], photocatalytic oxidation [5,19,20], supercritical water gasification – SCWG [5], electrical discharge (electro-hydraulic discharge, pulsed corona discharge, glow discharge electrolysis) [5], sonochemical processes [5,21], biodegradation (microbial or fungi species) [5,22,23].

Chemical oxidation with all its alternatives is widely used for treatment of wastewaters in order to remove organic pollutants, and has as final objective total oxidation (mineralization) of the organic contaminants to CO_2, H_2O and inorganics or, at least at their transformation into harmless products [13]. Also between the oxidation processes the catalytic ones become useful alternative due to the working conditions, which are milder [24]. As catalyst used to destroy organic pollutants, including phenol, we can mention: Ru, Rh, Pt, Ir, Ni, Ag supported on TiO_2, CeO_2, Al_2O_3 [24,25], metal oxides CuO, CoO, Cr_2O_3, NiO, MnO_2, Fe_2O_3, ZnO, CeO_2 [6,24,26,27], activated carbon [28], and iron and copper immobilised on synthetic zeolites [29,30] or pillared clays [31,32].

Due to their controllable and interesting nanostructural properties, such as high surface area, low mass density, high conductivity and continuous porosity, iron doped carbon aerogels [33-36], could be attractive materials for total oxidation of organic compounds.

In this paper two iron doped, Fe(II) and Fe(III) carbon aerogels were prepared, characterized and investigated as catalytic materials in phenol total oxidation process (catalytic wet air oxidation).

RESULTS AND DISCUSSION

Iron doped aerogel morpho-structural characterization

TEM images of the iron doped carbon aerogels presented in figure 1, show metal particles dispersed in the carbon aerogel matrix.

The XRD patterns of $Fe^{(2+)/(3+)}$-DCA shows two broad bands around $2\theta = 22^\circ$ and 43°, indicating an amorphous structure of the carbon matrix (figure 2). The thin peaks correspond to the iron/iron oxide phases of metal particles [35].

Specific surface area was determined to be 745 m^2/g for $Fe^{(3+)}$-DCA and 368 m^2/g for $Fe^{(2+)}$-DCA.

The iron content determined using elemental analysis is about 10% (wt) for $Fe^{(3+)}$-DCA and 18% (wt) for $Fe^{(2+)}$-DCA [35]. Because of its high metal content a smaller specific surface area and a higher content of graphitic structures are present in $Fe^{(2+)}$-DCA [35]. A part of these graphitic structures cloud the iron/iron oxide particles.
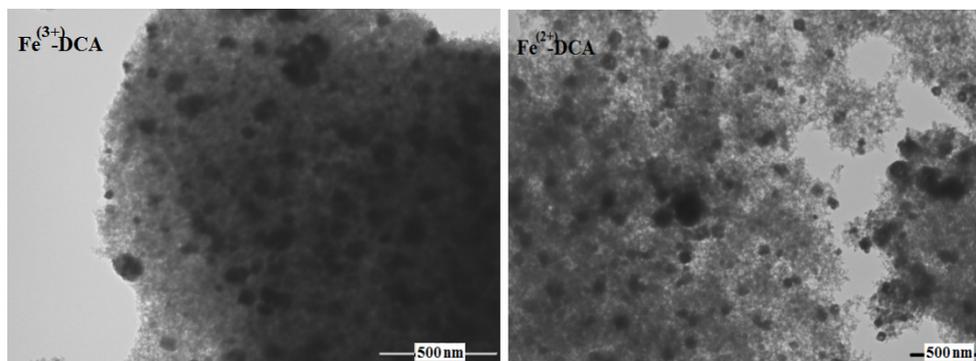
Figure 1. TEM images of iron doped carbon aerogels.
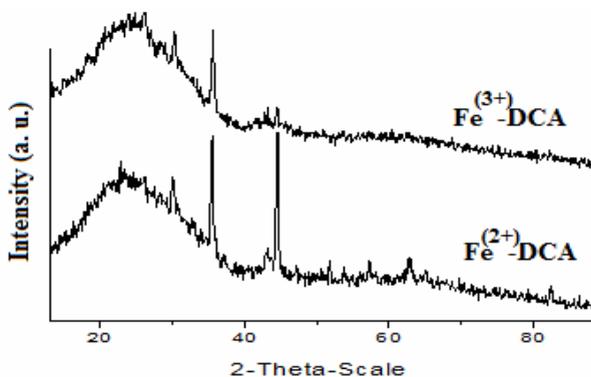
Figure 2. XRD patterns of iron doped carbon aerogels.

Phenol total oxidation results

The influence of operating temperature over the evolution of the overall efficiency, air flow 60 L/h, 0.1 g $Fe^{(3+)}$-DCA catalyst and C_i = 1000 mg phenol/dm^3, is presented in figure 3(a). As expected, overall efficiency increased with the

119

increasing of the temperature. In the first 30 minutes, the efficiency increased up to 50.65, 55.74 and 66.56% for an operating temperature of 20, 60 and 80°C respectively. Maximum values for overall efficiency are presented in figure 3(b). The highest value obtained was 68.85% at 80°C.

(a)   (b)
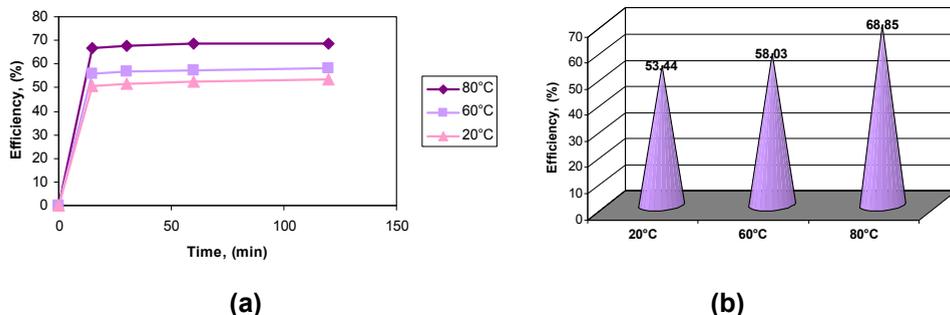
Figure 3. Variation (a) and maximum values (b) of overall efficiency in the phenol CWAO process, at different temperatures and constant air flow, 60 L/h, for Fe$^{(3+)}$-DCA catalyst (0.1 g catalyst and C_i = 1000 mg phenol/dm^3).

The influence of air flow over the overall efficiency variation in time, for Fe$^{(3+)}$-DCA catalyst, at constant temperature 80°C, 0.1 g catalyst and C_i = 1000 mg phenol/dm^3, is presented in figure 4(a). Maximum increase of the overall efficiency was observed in the first 15 minutes and varies from 36.07 to 66.56% for 20 and 60 l/h respectively. We observed also that the increase of overall efficiency is not as steep as in case of temperature variation, suggesting that oxygen diffusion process could be rate determining step in the catalytic wet air oxidation process. Maximum values obtained for all air flows are presented in figure 4(b).

a   b
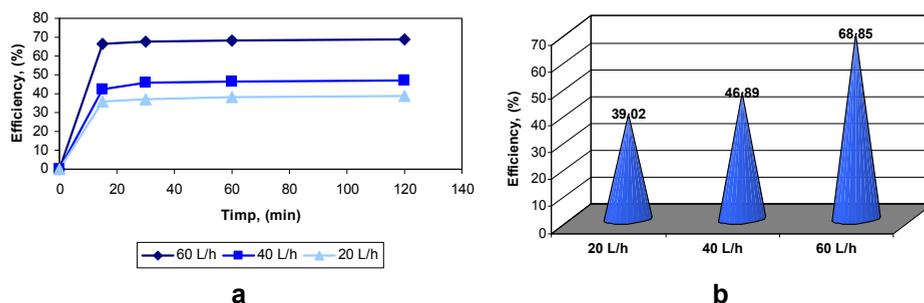
Figure 4. Variation (a) and maximum values (b) of overall efficiency in the phenol CWAO process, at different air flows and constant temperature, 80°C, for Fe$^{(3+)}$-DCA catalyst (0.1 g catalyst and C_i = 1000 mg phenol/dm^3).

We also studied the influence of the catalyst quantity and phenol initial concentration over the overall efficiency in the CWAO process. Results obtained in these cases are presented in figures 5 and 6. If we used a double catalyst quantity (0.2 g instead of 0.1 g) an increase with only 11% of the overall efficiency was observed, figure 5. Also a 10 times decrease of the phenol solution concentration led to an increase of 28% in overall efficiency value (figure 6).
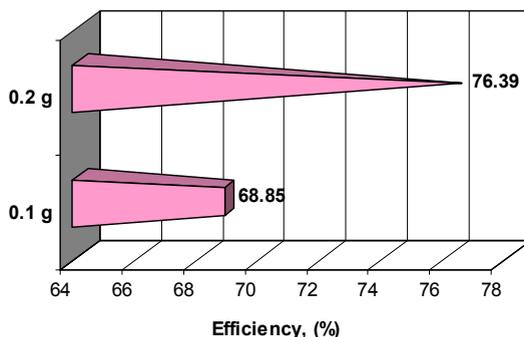
Figure 5. Catalyst quantity influence over the maximum overall efficiencies obtained in the phenol CWAO process, at constant air flow and constant temperature, 60 L/h, 80°C, for $Fe^{(3+)}$-DCA catalyst (C_i = 1000 mg phenol/dm^3).
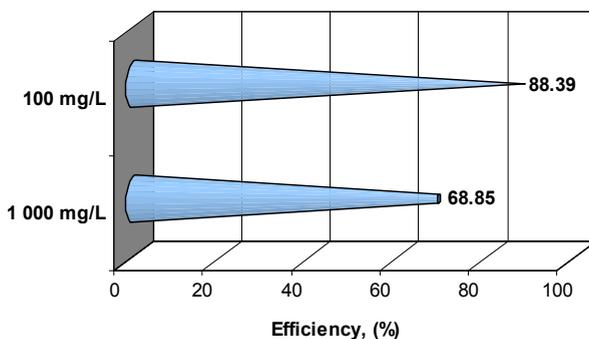
Figure 6. Phenol initial concentration influence over the overall efficiencies in the phenol CWAO process, at constant air flow and constant temperature, 60 L/h, 80°C, for $Fe^{(3+)}$-DCA catalyst (0.1 g catalyst).

In the same working conditions, on the $Fe^{(2+)}$-DCA catalyst we obtained overall efficiency values with 20% smaller than in case of $Fe^{(3+)}$-DCA, fact that can be explained by its smaller surface area and partial coverage of iron/iron oxide particles by graphitic clouds. The blank carbon aerogel sample had no activity in phenol oxidation process.

CONCLUSIONS

The influence of catalyst type and air flow rate over the overall process efficiency was studied. An increase of the temperature and air flow rate led to an increase of the overall efficiency. Total oxidation overall efficiencies up to 88.39% were reached for $Fe^{(3+)}$-DCA catalyst at 80°C and 60 l air/h for 0.1 g catalyst and C_i = 100 mg phenol/dm^3.

$Fe^{(3+)}$-DCA catalyst proved to be more efficient than $Fe^{(2+)}$-DCA catalyst, probably due to its superior morphological properties (higher surface area, iron particles on the DCA surface).

Further studies will be performed in order to establish the optimum working conditions for total oxidation of organic compounds, and catalyst reproducibility and lifetime

EXPERIMENTAL SECTION

Iron doped carbon aerogel preparation

Carbon aerogels doped with Fe were prepared by sol-gel polymerization of potassium salt of 2,4-dihydroxybenzoic acid with formaldehyde, followed by an ionic exchange process between K^+ doped wet gel and Fe(II) or Fe(III) ion aqueous solutions [35,37]. The resulted Fe(II) or Fe(III) doped gels were dried in supercritical conditions with liquid CO_2 and then pyrolyzed in high temperature and inert atmosphere.

K_2CO_3 was added under vigorous stirring to a 2,4-dihidroxybenzoic acid (DHBA) demineralised water suspension (DHBA/K_2CO_3 = 0.5; DHBA/H_2O = 0.0446 g/cm^3), a potassium salt solution resulting. After 30 min, when all the acid was neutralized, the solution became clear and after another 30 min, 37% formaldehyde (F) and then K_2CO_3 (C) (DHBA/F = 2; DHBA/C = 50) were added to the solution. The resulting mixture was placed into tightly closed glass moulds (7 cm – length × 1 cm – internal diameter) and cured in two time intervals: 1 day at room temperature and 4 days at 70°C. The resulting K^+-doped gel rods were cut into 0.5-1 cm pellets and washed with fresh acetone for 1 day. The K^+-loaded wet gels were then soaked for 3 days in 0.1M aqueous solutions of $Fe(NO_3)_3 \cdot 9H_2O$ or $Fe(OAc)_2$ [35]. Iron solutions were renewed daily. Finally, samples were washed once more with fresh acetone and then were subsequently dried with CO_2 in supercritical conditions. The resulting iron doped organic aerogels were pyrolysed at 750°C for 3h in an Ar atmosphere, obtaining iron and iron oxide particles-doped carbon aerogel. The iron doped carbon aerogels prepared using Fe (II) and Fe (III) salts were termed $Fe^{(2+)}$-DCA and $Fe^{(3+)}$-DCA, respectively. By drying and pyrolysis of K^+-doped gels the blank carbon aerogel sample (K-DCA) was obtained.

Iron doped aerogel morpho-structural investigations

Transmission electron microscopy (TEM) of the metal doped carbon aerogels was performed with a Hitachi H-7000 microscope operating at 125 keV.

X-ray diffraction patterns were recorded in a θ–2θ Bragg–Bretano geometry with a Siemens D5000 powder diffractometer with Cu-K$_\alpha$ incident radiation (λ = 1.5406 Å) and a graphite monochromator.

Specific surface area determinations were performed using Brunauer-Emmett-Teller (BET) and Barrett-Joyner-Halenda (BJH) methods using an ASAP 2000 surface area analyzer (Micrometrics Instruments Corp.). Prior to determination, samples of approximately 0.03 g were heated to 130°C under vacuum (10^{-5} Torr) for at least 18 h to remove all adsorbed species.

Elemental analyses were performed with an inductively coupled plasma-mass spectroscope (ICP-MS).

Phenol total oxidation – working conditions

Phenol total oxidation or catalytic wet air oxidation (CWAO), was carried out in a thermostated stirred batch reactor (magnetic stirrer) at atmospheric pressure, using different temperatures of 20, 40 and 60°C, air flows (20, 40 and 60 L/h), catalyst quantities (0.1 and 0.2 g) and phenol initial concentrations (100 and 1000 mg/dm^3). The Fe$^{(3+)}$-DCA catalyst, brought at a grain size of d < 250 μm using an appropriate sieve, was contacted with 100 cm^3 phenol solution. During the experiment, determination of the organic compounds in solution was carried out every 15 minutes, (first two determinations), and then every 30 minutes. Taking in account the fact that in this stage of the research we were interested to see how this type of material acts as catalyst for total oxidation of organic compounds we used KMnO$_4$ chemical oxygen demand, CCO-Mn, method in order to establish the final concentration of the organics in solution. This determination is currently used in environmental laboratories for wastewaters characterization (STAS 3002/85, SR ISO 6060/96) according to Romanian legislation [38]. The experiment was carried out for 120 minutes, until no modifications were observed in the organic compound final concentration. We also tested a Fe$^{(2+)}$-DCA catalyst and a blank carbon aerogel sample (K-DCA).

The evolution of phenol oxidation process was followed by means of overall efficiency (calculated using chemical oxygen demand values as CCO-Mn at a moment t and the initial CCO-Mn value), eq. (1).

$$X = \frac{C_i - C_t}{C_i} \cdot 100 \tag{1}$$

where,

C_i is the CCO-Mn initial value, in mg KMnO$_4$/dm^3

C_t is the CCO-Mn value at moment t, in mg KMnO$_4$/dm^3.

ACKNOWLEDGMENTS

REFERENCES

1. A. Santos, P. Yustos, B. Durban, F. Garcia-Ochoa, *Industrial Engineering Chemical Research*, **2001**, *40*, 2773.

2. A. Santos, P. Yustos, B. Durban, F. Garcia-Ochoa, *Catalysis Today*, **2001**, *66*, 511.

3. C. Catrinescu, C. Teodosiu, M. Macoveanu, J. Miehe-Brendle, R. Le Dred, *Water Research*, **2003**, *37*, 1154.

4. A. Santos, P. Yustos, A. Quintanilla, F. Garcia-Ochoa, J. A. Casas, J. J. Rodriguez, *Environmental Science and Technology*, **2004**, *38*, 133.

5. G. Busca, S. Berardinelli, C. Resini, L. Arrighi, *Journal of Hazardous Materials*, **2008**, *160*, 265.

6. A. Alejandre, F. Medina, A. Fortuny, P. Salagre, J. E. Sueiras, *Applied Catalysis B: Environmental*, **1998**, *16*, 53.

7. S. Al-Asheh, F. Banat, L. Abu-Aitah, *Separation and Purification Technology*, **2003**, *33*, 1.

8. E. Fernandez, D. Hugi-Cleary, M. V. Lopez-Ramon, F. Stoeckli, *Langmuir*, **2003**, *19*, 9719.

9. Y-H. Shen, *Water Research*, **2002**, *36*, 1107.

10. Z. Lazarova, S. Boyadzhieva, *Chemical Engineering Journal*, **2004**, *100*, 129.

11. W. Kujawski, A. Warszawski, W. Ratajczak, T. Porebski, W. Capala, I. Ostrowska, *Desalination*, **2004**, *163*, 287.

12. F. Luck, *Catalysis Today*, **1999**, *53*, 81.

13. R. Andreozzi, V. Caprio, A. Insola, R. Marrota, *Catalysis Today*, **1999**, *53*, 51.

14. B. Legube, N. Karpel Vel Leitner, *Catalysis Today*, **1999**, *53*, 61.

15. S. Zrncevic, Z. Gomzi, *Industrial Engineering Chemical Research*, **2005**, 44, 6110.

16. I. V. Perez, S. Rogak, R. Branion, *Journal of Supercritical Fluids*, **2004**, *30*, 71.

17. D. Fino, C. Carlasi Jara, G. Saracco, V. Specchia, P. Spinelli, *Journal of Applied Electrochemistry*, **2005**, *35*, 405.

18. A. M. Polcaro, A. Vacca, S. Palmas, M. Marcia, *Journal of Applied Electrochemistry*, **2003**, *33*, 885.

19. J-M. Herrmann, *Catalysi Today*, **1999**, *53*, 115.

20. U. Bali, E. C. Catalkaya, F. Sengul, *Journal of Environmental Science and Health*, **2003**, *A38*, 2259.

21. Y. G. Adewuyi, *Industrial Engineering Chemical Research*, **2001**, *40*, 4681.

22. G. Collins, C. Foy, S. McHugh, T. Mahony, V. O'Flaherty, *Water Reserach*, **2005**, *39*, 1614.

23. A. Nuhoglu, B. Yalciu, *Proceses in Biochemistry*, **2005**, *40*, 1233.

24. Y.I. Matattov-Meytal, M. Sheintuch, *Industrial Engineering Chemical Research*, **1999**, *37*, 309.

25. A. Cybulski, J. Trazynski, *Applied Catalysis B: Environmental*, **2004**, *47*, 1.

26. L. Chang, I-P. Chen, S-S. Lin, *Chemosphere*, **2005**, *58*, 485.

27. P. M. Alvarez, D. Mclurgh, P. Plucinski, *Industrial Engineering Chemical Research*, **2001**, *41*, 2153.

28. A. Santos, P. Yustos, S. Gomis, G. Ruiz, F. Garcia-Ochoa, *Industrial Engineering Chemical Research*, **2005**, *44*, 3869.

29. M. Noorjahan, V.D. Kumari, M. Subrahmanyam, L. Panda, *Applied Catalysis B: Environmental*, **2005**, *57*, 291.

30. N.H. Phu, T.T.K. Hoa, N.V. Tan, H.V. Thang, P.L. Ha, *Applied Catalysis B: Environmental*, **2001**, *34*, 267.

31. J. Barrault, J-M. Tatibouet, N. Papayannakos, *C. R. Academie des Science Paris, Serie IIc Chimie*, **2000**, *3*, 777.

32. J. Barrault, C. Bouchoule, K. Echachoui, N. Frini-Srasra, M. Trabelsi, F. Bergaya, *Applied Catalysis B: Environmental*, **1998**, *15*, 269.

33. C. Moreno-Castilla, F. J. Maldonado-Hodar, *Carbon*, **2005**, *43*, 455.

34. A. Martinez, L. C. Vallribera, M. Cotet, L. Popovici, A. Martin, M. Roig, E. Moreno-Manas, E. Molins, *New Journal of Chemistry*, **2005**, *29*, 1342.

35. L. C. Cotet, M. Gich, A. Roig, I. C. Popescu, V. Cosoveanu, E. Molins, V. Danciu, *Journal of Non-Crystalline Solids*, **2006**, *352*, 2772.

36. S. Cacchi, C. L. Cotet, G. Fabrizi, G. Forte, A. Goggiamani, L. Martín, S. Martínez, E. Molins, M. Moreno-Mañas, F. Petrucci, A. Roig, A. Vallribera, *Tetrahedron,* **2007**, *63*, 2519.

37. T. F. Baumann, G. A. Fox, J. H. Satcher, N. Yoshizawa, R. Fu, M. S. Dresselhaus, *Langmuir*, **2002**, *18*, 7073.

38. Law 458/2002, 311/2004, 107/1996, 311/2004, 112/2006, HG 188/2002, HG 352/2005.

HEAVY METAL IONS REMOVAL FROM MODEL WASTEWATERS USING ORAŞUL NOU (TRANSILVANIA, ROMANIA) BENTONITE SAMPLE

ANDRADA MĂICĂNEANU[a]**, HOREA BEDELEAN**[b]**,
SILVIA BURCĂ**[a]**, MARIA STANCA**[a]

ABSTRACT. A bentonite sample from Oraşul Nou deposit, (Transilvania, Romania), was used to remove heavy metal ions (Zn^{2+}, Pb^{2+}, Cd^{2+}) from model monocomponent wastewaters. A representative sample of bentonite (ON) was characterised using, wet chemical analyses, XRD, BET and FTIR. The bentonite deposit from Oraşul Nou formed by alteration of rhyolites and perlites. Mineralogically, they contain clay minerals (montmorillonite, and subordinately kaolinite, illite), cristobalite, carbonates, zeolites (clinoptilolite), iron oxi-hydroxides and relics of primary minerals such as quartz and feldspar.The bentonite sample was used as powder, (d < 0.2 mm), without any chemical treatment. We studied the influence of the working regime, static and dynamic, concentration, and solid : liquid ratio over the process efficiency. We used monocomponent synthetic wastewaters containing zinc, lead and cadmium ions. The bentonite sample proved to be efficient for the removal of the considered heavy metal ions, removal efficiencies up to 100% (lead and zinc removal) were reached. First-order, pseudo- second-order and Elovich models were used to study the adsorption kinetic of zinc ions on the bentonite sample.

Keywords: bentonite, montmorillonite, zinc, lead, cadmium, removal

INTRODUCTION

Heavy metals such as Cd, Pb and Zn are usually found in Earth's crust mainly as minerals and are mobilised by soil erosion, volcanic activities and forest fires (natural sources). Heavy metals concentration in the environment increased drastically due to intense human activities (anthropogenic sources).

Cadmium, lead and zinc can be found in air (eroded particles), water (in ionic form, from wastewaters insufficient treated or mobilised from polluted soils) and soil (adsorbed on soil particles) in different combinations. Heavy metals exposure can take place by inhalation (contaminated air, cigarette

[a] *Universitatea Babeş-Bolyai, Facultatea de Chimie şi Inginerie Chimică, Str. Kogălniceanu Nr.1, RO-400084 Cluj-Napoca, România, andrada@chem.ubbcluj.ro*
[b] *Universitatea Babeş-Bolyai, Facultatea de Biologie şi Geologie, Str. Kogălniceanu Nr. 1, RO-400084 Cluj-Napoca, România, bedelean@bioge.ubbcluj.ro*

smoke, working exposure), ingestion (water and contaminated food) and dermal (contact with contaminated soil, heavy metal compounds) exposures. With exception of Zn, which in small quantities is nutritive elements, heavy metals are toxic to humans, animals and plants. Heavy metal ions have the tendency to accumulate in living organisms causing a variety of disorders [1-3].

Heavy metal ions can be removed from the environment using a variety of methods such as precipitation, solvent extraction, vacuum evaporation, membrane technologies, adsorption or ionic exchange, the selection of a method depending mainly upon the heavy metal ion concentration. Adsorption is used when concentration of heavy metal ions is small, but is higher that the allowable concentration according to environmental legislation.

Low-cost adsorbents such as natural zeolites, clay minerals (kaolinite, montmorillonite), chitosan, peat moss, fly ash, coal, natural oxides (aluminium oxide, ferric oxide), industrial waste (waste slurry, iron (III) hydroxide, lignin, furnace slag, sawdust, activated red mud, bagasse fly ash, brewery waste biomass), rice husk, coconut shell, agricultural waste, etc. were all considered as adsorbents for heavy metal ions (cadmium, chromium, cobalt, copper, iron, lead, manganese, nickel, zinc) removal from wastewaters [4,5]. Due to their availability and low costs, natural materials such as zeolites and clay minerals became object of many research papers in the last years.

In Romania, most studies related to the identification of new materials used in environmental protection, concerned natural zeolites (zeolitic volcanic tuffs), which were used in various applications based on their properties [6]. Clays, especially bentonite clays, are present in large amounts in Romania. Bentonite collected from Transilvanian deposits, Petreşti, Oraşul Nou and Valea Chioarului were considered for heavy metal ions (Petreşti), ammonium ions (Petreşti, Valea Chioarului, Oraşul Nou) and organics (Petreşti, Oraşul Nou) removal from wastewaters [7-9].

Clay minerals are aluminium hydrosilicates, crystallized in monoclinic system, characterized by planar reticular structures. Stratified structure of mineral clays is determined by the combination in one reticular plan (structural unit) of two cationic layers, one layer in which silicon is coordinated tetrahedric with $O^.OH$ (tetrahedric level Te) and one layer in which aluminium is coordinated octahedric with $O^.OH$ (octahedric level Oc). These layers are bonded between them with van der Waals bonds forming the structural unit. According to the numbers of Te and Oc layers, clay minerals are classified in 1Te:1Oc (e.g. kaolinite), 2Te:1Oc (e.g. montmorillonite) and 2Te:2Oc (e.g. chlorite). The layered structure of the clay minerals and presence of isomorphous replacement of Si^{4+} with Al^{3+} (negative charge compensated by Na^+, K^+, Ca^{2+} and/or Mg^{2+}) determines their main properties: swelling, water and organic compounds adsorption and ionic exchange capacity [4,10].

Bentonites are clay rocks formed by devitrification and chemical alteration of a glassy igneous material, usually a tuff or volcanic ash. Bentonites are composed mainly of smectite group minerals. This group includes dioctahedral minerals such as montmorillonite, beidellite and nontronite and trioctahedral minerals such as hectorite and saponite. The main mineral from smectite group is montmorillonite, a hydrated sodium calcium aluminum magnesium silicate hydroxide.

The purpose of this study was to characterise the bentonite from Oraşul Nou (ON) deposit, Satu Mare County, Romania and to evaluate its heavy metal ions (Zn^{2+}, Pb^{2+}, Cd^{2+}) removal capacity. Also, first, pseudo second and Elovich kinetic models were used to study the adsorption kinetics of zinc ions on the betonite sample.

RESULTS AND DISCUSSION

Bentonite characterization

The bentonite deposit from Oraşul Nou (Satu Mare County) is located about 30 km north-west of the city of Baia Mare, in the Oaş Basin, Maramureş Depression. The area consists of sedimentary rocks and volcanic rocks. Sedimentary formations are of marine origin (marls, fine sandstones) of Neogene age. Volcanic rocks outcrops are up to 300 m in thickness and consist of rhyolite and rhyolitic tuffs, andesitic tuffs, perlites, dacite and pyroclastic rocks. The bentonite deposit from Oraşul Nou formed by alteration of rhyolites and perlites.

Bentonite bodies are lens-like shaped, ranging between 3 and 8 m in thickness, 100 to 400 m in length and 50 to 250 m in width.

In Mujdeni area, from where we collected the samples used for our experiments, a rhyolite basement is covered by altered perlites gradually passing into bentonites. The bentonite layers are followed by unaltered perlites, clay and the soil. The bentonitization of perlites and rhyolites is a process connected to solutions' complex circulation favoured by the porosity of the rhyolites in the basement and by the small, concentric fissures within the perlites.

As a rule, bentonites are white in colour, fine grained or compact, the perlitic structure being more or less preserved.

Mineralogically, they contain clay minerals (montmorillonite, and subordinately kaolinite, illite), cristobalite, carbonates, zeolites (clinoptilolite), iron oxi-hydroxides and relics of primary minerals such as quartz and feldspar. The ratio between the montmorillonite and kaolinite-group minerals varies according to the degree of transformation of the original rock. Thus, the minerals from the kaolinite group are clearly dominant as compared to montmorillonite in the areas where bentonitization was not completed, while in the intervals with bentonite montmorillonite represents the major phase.

The chemical composition of the bentonites from Oraşul Nou is presented in the table 1. It is worthy to note the relatively high Al_2O_3 and relatively low Na_2O contents.

Semi-quantitative mineralogical composition of clay raw material realised by means of X-ray diffraction analysis, figure 1, indicated that in all bentonite samples, smectite (montmorillonite) is the most abundant clay mineral. Identified minerals were: smectite (montmorillonite), cristobalite, quartz, feldspars. The basal space was recorded at 15 Å, indicating the precence of Ca-montmorillonite [11].

The montmorillonite amount varies between 20-85%, according to the alteration degree of the rock; locally, it may even reach values of 95%.

Table 1. Chemical composition of the bentonite samples from Oraşul Nou (Satu-Mare County).

Oxides, [%]	SiO₂	Al₂O₃	Fe₂O₃	CaO	MgO	Na₂O	K₂O	TiO₂	L.O.I.
Oraşul Nou	60.62 -71.46	15.40 -23.55	0.84 -2.34	1.18 -1.86	0.54 -2.05	0.00 -0.30	0.25 -2.16	0.15 -0.36	8.69 -12.4
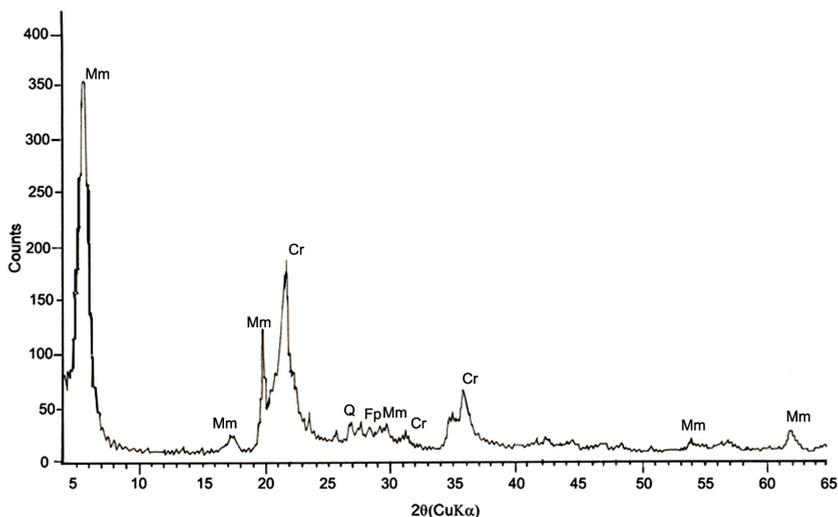
Figure 1. Powder X-ray diffractogram of the Oraşul Nou bentonite sample; Mm- montomorillonite, Cr-cristobalite, Q-quartz, Fp-feldspar.

Examination of IR spectra of the bentonite sample (figure 2), indicates the presence of specific 2:1 clay mineral peaks (montmorillonite) with peaks in 600-700 cm^{-1} region that could be attributed to illite, clinoptilolite or opal CT accompanying minerals [12-19]. The identified peaks can be attributed

as follows: 3631.30 cm^{-1} – stretching vibrations of isolate hydroxyls and OH less firmly bond to the tetrahedrical outer layer, 3448.10 cm^{-1} – stretching vibrations of the structural OH and also of the hydration water, 1639.20 cm^{-1} – angular deformation of hydroxyls from adsorbed water molecules (held in interlayers), 1095.37 and 1047.53 cm^{-1} – main bands corresponding to the stretching vibrations of Si,Al-O, 794.53 and a shoulder at 620.97cm^{-1} – weak bands corresponding to the stretching vibrations of Si,Al-O (there are not specific peaks for montmorillonite and could be attributed to the accompanying minerals), and 474.40 and 524.54 cm^{-1} bending vibrations of Si-O-M bonds (M can be Mg, Al, Fe).
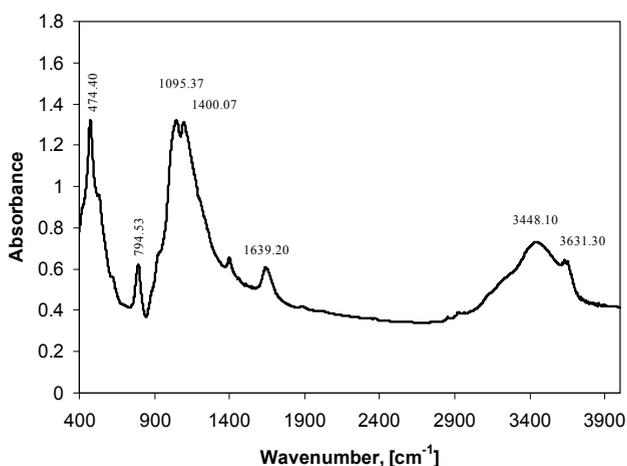
Figure 2. FTIR spectrum of the bentonite sample from Oraşul Nou deposit.

Heavy metal ions removal results

The results obtained in case of **zinc removal** from monocomponent model solutions are presented and discussed in terms of removal efficiency and adsorption capacity.

In figure 3, evolution of zinc removal efficiency in time is presented for the experiment conducted in _static regime_ (C_i = 125 mg Zn^{2+}/L, 2 g bentonite, 20 ml zinc solution). A closer inspection of this evolution led to the conclusion that in the first 24 hours, concentration of zinc ions drops significantly from the initial value to 1.68 mg Zn^{2+}/L, leading to high removal efficiency (98.71%). Equilibrium was reached in 48 hours, when concentration of zinc ions in solution drops to 0 (100% efficiency) and adsorption capacity increased up to 1.3003 mg Zn^{2+}/g bentonite.

The experiments realised in _dynamic regime_ (3D shaker) were conducted with the modification of the initial concentration of zinc in model solutions, and bentonite quantity. Results are presented in figures 4 to 7 in terms of removal efficiency and adsorption capacity.
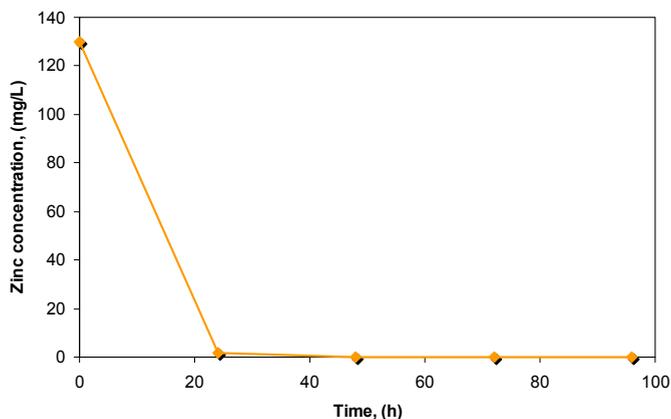
Figure 3. Removal efficiency evolution in time during zinc removal process on Oraşul Nou bentonite sample in static regime (C_i = 125 mg Zn^{2+}/L, 2 g bentonite).

From figure 4, where we presented the *influence of the initial zinc concentration* over the evolution of the removal efficiency it can be concluded that an increase of the initial concentration led to a decrease of the removal efficiency. Also in terms of time evolution of the removal efficiency, we observed that trends are similar. Equilibrium was reached after around 45 minutes. Maximum removal efficiencies were as follows 100, 83.48, and 71.65 for 125, 250, and 525 mg Zn^{2+}/L initial concentrations respectively. Adsorption capacities calculated for the three experiments are presented in figure 5. It is easy to observe, that with an increase in the initial concentration, zinc quantities retained on the bentonite sample increase. The highest adsorption capacity was calculated to be 3.8171 mg Zn^{2+}/g bentonite in case of the highest initial concentration (525 mg Zn^{2+}/L).

Influence of the *bentonite quantity* over the zinc removal efficiency is presented in figure 6 as evolution in time and in figure 7 as maximum values. If we follow the evolution of the removal efficiency in time we can observe that as the bentonite quantity increase the removal efficiency has higher values and equilibrium is reached faster. When we used 3 g of bentonite the equilibrium was reached in 15 minutes, with a maximum removal efficiency of 100%. In case of 2 g, equilibrium was reached in 45 minutes with 100% removal efficiency, while in case of 1 g, equilibrium was reached in 60 minutes with a removal efficiency of 98.71%.

At a closer inspection of the results obtained in case of the bentonite quantity influence we can conclude that an increase in the adsorbent quantity has to be implemented in an industrial scale process only after the realisation of the economic calculations, taking in account that an increase from 1 to 2 g of bentonite led to an increase of just 1.29 points (from 98.71 to 100%) of the removal efficiency, but with a decrease from 2.5671 to 1.3003 mg of the Zn^{2+} retained on the adsorbent unit (g).
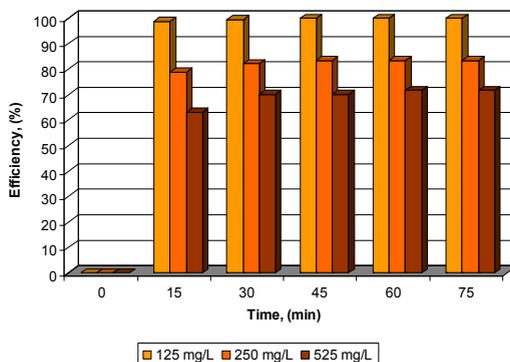
Figure 4. Influence of the initial zinc concentration over the removal efficiency evolution in time, during zinc removal process on 2 grams of Oraşul Nou bentonite sample in dynamic regime (3D shaker).
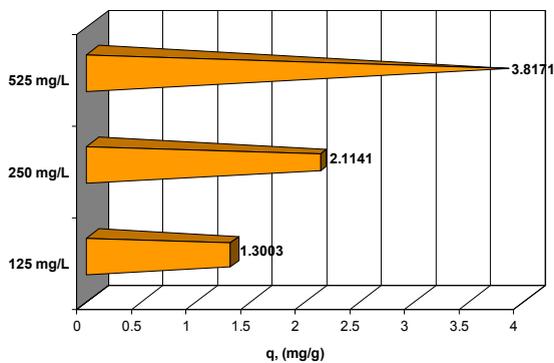
Figure 5. Influence of the initial zinc concentration over the adsorption capacity, in zinc removal process on 2 grams of Oraşul Nou bentonite sample in dynamic regime (3D shaker).
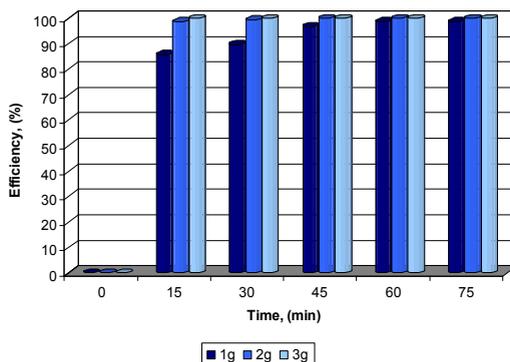
Figure 6. Influence of the bentonite quantity over the removal efficiency evolution in time, during zinc removal process on Oraşul Nou bentonite sample in dynamic regime (3D shaker), C_i = 125 mg Zn^{2+}/g.
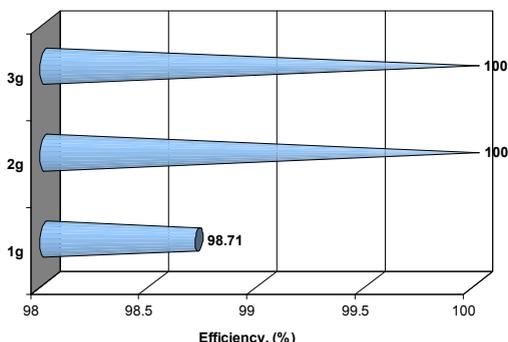
Figure 7. Influence of the bentonite quantity over the maximum removal efficiency, in zinc removal process on Oraşul Nou bentonite sample in dynamic regime (3D shaker), C_i = 125 mg Zn^{2+}/g.

In order to design and optimise a wastewater treatment process is also important to know the _adsorption kinetic models_, which can correlate the adsorbate up-take rate with the bulk concentration of the adsorbate. First-order (Lagergren), pseudo-second-order and Elovich models were used to study the adsorption kinetic of zinc ions on the bentonite sample [20]. Linear regression was used to determine the best fitting kinetic rate equation (correlation coefficients, R^2) [21].

Lagergren suggested a first-order equation for the adsorption of liquid/solid system based on solid capacity, which can be expressed as follows:

$$\frac{dq_t}{dt} = k_1(q_e - q_t) \tag{1}$$

Integrating eq. (1) from the boundary conditions t = 0 to t = t and q_t = 0 to $q_t = q_t$, gives:

$$\ln(q_e - q_t) = \ln q_e - k_1 t \tag{2}$$

where,

q_e and q_t are the amounts of zinc adsorbed (mg/g) at equilibrium and time t, respectively

k_1 is the rate constant of first-order adsorption (1/min).

In order to determine the rate constant and equilibrium zinc uptake, the straight line plots of $\ln(q_e - q_t)$ against t, eq. (2), were made at four different initial zinc concentrations. Correlation coefficients between 0.8080 and 0.9500 were obtained (figure not shown), therefore zinc adsorption on bentonite cannot be classified as first-order.

The pseudo-second-order kinetic model is derived on the basis of the adsorption capacity of the solid phase, expresses as:

$$\frac{dq_t}{dt} = k_2(q_e - q_t)^2 \tag{3}$$

Integrating eq. (3) from the boundary conditions $t = 0$ to $t = t$ and $q_t = 0$ to $q_t = q_t$, gives:

$$\frac{1}{(q_e - q_t)} = \frac{1}{q_e} + k_2 t \tag{4}$$

where,

q_e and q_t are the amounts of zinc adsorbed (mg/g) at equilibrium and time t, respectively

k_2 is the rate constant of first-order adsorption (g/mg·min).

Equation (4) can be rearranged in linear form, as follows:

$$\frac{t}{q_t} = \frac{1}{k_2 q_e^2} + \frac{t}{q_e} \tag{5}$$

In order to determine the rate constant and equilibrium zinc uptake, the straight line plots of t/q_t against t, eq. (5), were made at four different initial zinc concentrations. Correlation coefficients between 0.9867 and 1.0000 were obtained (figure 8 and table 1), therefore zinc adsorption on bentonite can be classified as pseudo-second-order.

Elovich equation that is widely used to describe the kinetics of chemisorption of gas and solids can also be applied to liquid/solid systems and can give information about the possibility that chemical adsorption or chemical adsorption involving valence forces through sharing or exchange of electrons between adsorbent and adsorbate to be rate determining step [20]. The Elovich equation was derived from the Elovich kinetic equation:

$$\frac{dq_t}{dt} = \alpha e^{-\beta q_t} \tag{6}$$

Integrating eq. (6) from the boundary conditions $t = 0$ to $t = t$ and $q_t = 0$ to $q_t = q_t$, gives:

$$q_t = \frac{1}{\beta} \ln(\alpha\beta) + \frac{1}{\beta} \ln(t + t_0) \tag{7}$$

where,

α and β are the parameters of the equations, and

$t_0 = 1/(\alpha\beta)$

α represents the rate of chemisorption at 0 coverage, (mg/g·min),

β is related to the extent of surface coverage and activation energy for chemisoprtion, (g/mg) [20].

When $t_0 \ll t$, then eq. (7) is replaced by:

$$q_t = \frac{1}{\beta} \ln(\alpha\beta) + \frac{1}{\beta} \ln(t) \tag{8}$$

In order to determine equations parameters, the straight line plots of q_t against $\ln(t)$, eq. (8), were made at four different initial zinc concentrations. Correlation coefficients between 0.8562 and 0.9188 were obtained (figure not shown), therefore zinc adsorption on bentonite cannot be classified as chemisorption.
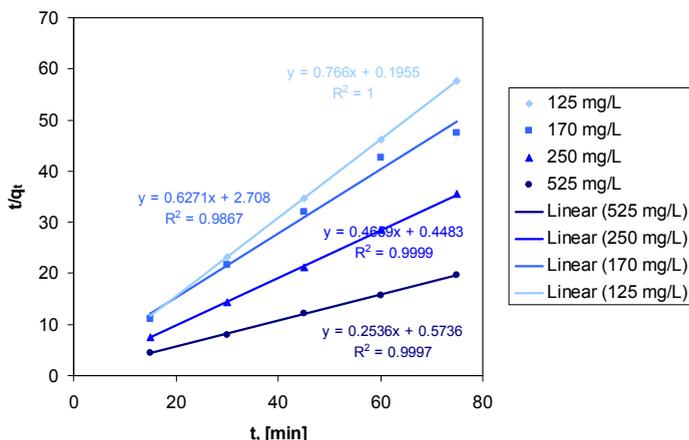
Figure 8. Plots of the second-order model, at different initial zinc concentrations (dynamic regime, 2 g bentonite, 20 ml zinc solution).

Table 1. Second order adsorption rate constants, and calculated and experimental q_e values for zinc adsorption using different initial concentrations.

C, (mg Zn^{2+}/L)	q_e (exp), (mg Zn^{2+}/g)	k_2, (g/mg·min)	q_e (calc), (mg Zn^{2+}/g)	R^2
125	1.3003	3.0013	1.3005	1.0000
170	1.5772	0.1452	1.5946	0.9867
250	2.1141	0.4842	2.1464	0.9999
525	3.8171	0.1121	3.9432	0.9997

The results obtained in case of **lead and cadmium removal** from monocomponent model solutions are also presented and discussed in terms of removal efficiency and adsorption capacity.

Lead removal process was realised in static and dynamic (3D shaker) regimes using 2 g of bentonite and 20 ml solution of 54 mg Pb^{2+}/L. In both static and dynamic regime the initial concentrations drops significantly in the first 24 h and 15 min, from the initial 54 to 3.73 and 0.01 mg Pb^{2+}/L, respectively, indicating a favourable diffusion process in case of dynamic conditions. Maximum efficiency reached 99.99% in both cases, while the adsorption capacity was calculated to be 0.5390 mg Pb^{2+}/g bentonite. Removal efficiency evolution in time during lead removal process on Oraşul Nou bentonite sample in dynamic regime is presented in figure 9. Equilibrium was reached in 72 h in static regime and 60 minutes in dynamic regime.

Cadmium removal process was realised in static regime using a 2150 mg Cd^{2+}/L model solution, 20 ml, and 2 g of bentonite. Maximum removal efficiency value was calculated to be 48.08% corresponding to an adsorption capacity of 10.3418 mg Cd^{2+}/g. Equilibrium was reached in 48 h. Evolution of removal efficiency in dynamic regime (C_i = 25 mg Cd^{2+}/L, 2 g bentonite, 20 ml solution) is presented in figure 10. Removal efficiency increases slowly in the first 60 minutes, until 62.37%, value obtained at equilibrium (60 min). At equilibrium, adsorption capacity was calculated to be 0.1589 mg Cd^{2+}/g. The adsorption capacity values obtained, ranging between 0.1589 and 10.3418 mg Cd^{2+}/g indicates that our bentonite sample has high adsorption capacities, therefore it can be used to remove cadmium ions from diluted as well as more concentrated solutions.
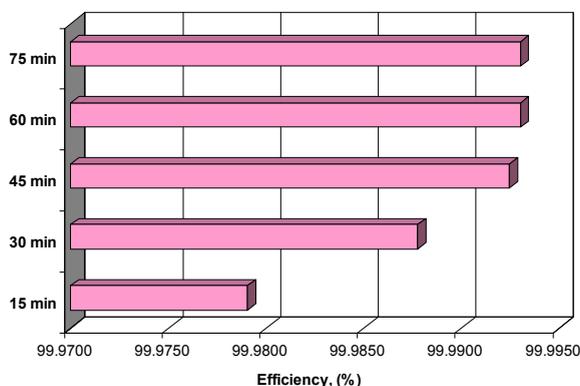
Figure 9. Removal efficiency evolution in time during lead removal process on Oraşul Nou bentonite sample in dynamic regime (3D shaker),
C_i = 54 mg Pb^{2+}/L, 2 g bentonite, 20 ml solution.
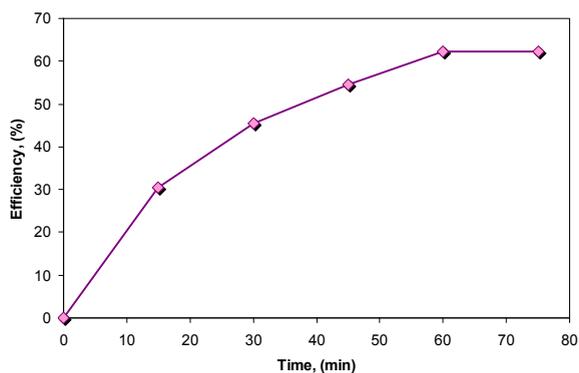
Figure 10. Removal efficiency evolution in time during cadmium removal process on Oraşul Nou bentonite sample in dynamic regime (3D shaker),
C_i = 25 mg Cd^{2+}/L, 2 g bentonite, 20 ml solution.

137

CONCLUSIONS

A bentonite sample from Oraşul Nou deposit, (Transilvania, Romania), was used to remove heavy metal ions (Zn^{2+}, Pb^{2+}, Cd^{2+}) from model monocomponent wastewaters.

Physico-chemical and mineralogical analyses of the bentonite from Oraşul Nou, Satu Mare County, Romania indicated that our sample is a smectitic clay mineral, containing Ca-montmorillonite (up to 85%).

The considered bentonite sample proved to be efficient in heavy metal ions removal process. Efficiencies up to 100% in case of Zn^{2+} (C_i = 125 Zn^{2+} mg/L), 99.99% in case of Pb^{2+} (C_i = 54 mg Pb^{2+}/L) and 62.37% in case of Cd^{2+} (C_i = 25 Cd^{2+} mg/L) in dynamic regime, were obtained.

First-order, pseudo-second-order and Elovich models were used to study the adsorption kinetic of zinc ions on the bentonite sample. We conclude that zinc adsorption on Oraşul Nou bentonite sample can be classified as pseudo-second-order.

EXPERIMENTAL SECTION

Bentonite compositional investigations

Representative bulk rock samples of bentonite were collected from open bentonite pits in Oraşul Nou area (Satu Mare County, Romania).

The analyses of whole-rock chemistry were performed at ICEI (Physico-Chemical Analises Center) Cluj-Napoca using usual analytical methods for silicate materials (wet chemistry).

X-ray diffraction analyses on random powders were performed using a Siemens Bruker unit with Cu Kα anticathode. The diffractograms were recorded from 10° to 70° 2θ. The analytic conditions are 40 A, 40 kV, step of 2 degrees. A semi-quantitative X-ray diffraction method to determine mineral composition was used.

Specific surface area of the bentonite sample was determined using Brunauer-Emmett-Teller (BET) method using a home made apparatus. BET specific surface area was determined to be 72 m^2/g.

FTIR spectrum of the bentonite sample was recorded using a Jasco 615 spectrophotometer, 400-4000 cm^{-1}, resolution 2 cm^{-1}.

Heavy metal ions removal procedure

Heavy metal ions (Zn^{2+}, Pb^{2+}, Cd^{2+}) removal was realised on a representative bentonite sample from Oraşul Nou (ON) deposit, Satu Mare County, Romania. The bentonite sample was used as powder, particles with grain size smaller than 0.2 mm, without any chemical treatment.

For the heavy metal ions removal study we used synthetic monocomponent solutions containing zinc ions (125-525 mg Zn^{2+}/L), lead ions (54 mg Pb^{2+}/L) and cadmium ions (25-2150 mg Cd^{2+}/L) prepared from $ZnSO_4 \cdot 7H_2O$, $(CH_3OO)_2Pb \cdot 3H_2O$ and $Cd(NO_3)_2 \cdot 4H_2O$ salts (analytical purity reagents). Cadmium and lead ions in solution were determined using an ion selective electrode and a pH meter (Jenway 3330), while in case of zinc ions we used a spectrophotometric method (potassium ferrocyanure, λ = 420 nm, Jenway 6305 spectrophotometer). Experiments were carried out without any modification of the temperature (the experiments were realised at room temperature, 20°C) and pH of the synthetic solutions.

Heavy metal ions removal process was realised in a batch reactor in static and dynamic (3D shaker) regimes, using 1, 2 and 3 grams of bentonite in contact with 20 ml heavy metal ion solution. In order to determine the exact concentration of heavy metal ions, water samples were taken every 24 hours in static regime and every 15 minutes in dynamic regime, until the equilibrium was reached.

We studied the influence of the working regime, static and dynamic (3D shaker), initial concentration and bentonite quantity (zinc) over the process efficiency and adsorption capacity.

Removal efficiencies (%) and adsorption capacities (mg M^{n+}/g) were calculated in order to establish the effectiveness of the considered bentonite sample in the heavy metal ions removal process (the calculated values of removal efficiencies and adsorption capacities should be regarded according to the precision of the determination methods we used).

First-order, pseudo-second-order and Elovich models were used to study the adsorption kinetic of zinc ions on the bentonite sample.

ACKNOWLEDGMENTS

REFERENCES

1. H. Abadin, A. Ashizawa, Y. W. Stevens, F. Llados, G. Diamond, G. Sage, M. Citra, A. Quinones, S. J. Bosch, S. G. Swarts, "Toxicological profile for lead", U.S. Department of Health and Human Services, Public Health Service Agency for Toxic Substances and Disease Registry, **2007**.

2. J. Taylor, R. DeWoskin, F. K. Ennever, "Toxicological profile for cadmium", U.S. Department of Health and Human Services, Public Health Service, Agency for Toxic Substances and Disease Registry, **1999**.

3. N. Roney, C. V. Smith, M. Williams, M. Osier, S. J. Paikoff, "Toxicological profile for zinc", U.S. Department of Health and Human Services, Public Health Service, Agency for Toxic Substances and Disease Registry, **2005**.

4. K. G. Bhattacharyya, S.S. Gupta, *Advances in Colloid and Interface Science*, **2008**, *140*, 114.

5. S. Babel, T. A. Kurniawan, *Journal of Hazardous Materials*, **2003**, *B97*, 219.

6. A. Măicăneanu, H. Bedelean, M. Stanca, "Zeoliții naturali. Caracterizare şi aplicaţii în protecţia mediului", Presa Universitară Clujeană, **2008**, Cluj-Napoca, chapter 1-3, 6.

7. H. Bedelean, A. Măicăneanu, S. Burcă, M. Stanca, *Clay Minerals*, **2009**, in press.

8. H. Bedelean, A. Măicăneanu, S. Burcă, M. Stanca, Sesiunea Ştiinţifică anuală GEO 2009 a Facultăţii de Geologie şi Geofizică, în parteneriat cu Societatea Geologică a României şi Societatea Română de Geofizică, **2009**, Bucureşti.

9. M. Stanca, A. Măicăneanu, S. Burcă, H. Bedelean, International Conference, Sustainable Development in the Balkan Area: Vision and Reality, **2007**, Alba-Iulia.

10. D. Rădulescu, N. Anastasiu, "Petrologia rocilor sedimentare", Editura Didactică şi Pedagogică, **1979**, Bucureşti, chapter 6.

11. N. Anastasiu, "Minerale şi roci sedimentare, Determinator, Editura Tehnică, **1977**, Bucureşti, chapter 3.

12. D. Haffad, A. Chambellan, J. C. Lavalley, *Catalysis Letter*, **1998**, *54*, 227.

13. A. Bakhti, Z. Derriche, A. Iddou, M. Larid, *European Journal of Soil Science*, **2001**, *52*, 683.

14. W. P. Gates, J. S. Anderson, M. D. Raven, G. J. Churchman, *Applied Clay Science*, **2002**, *20*, 189.

15. P. Komadel, *Clay Minerals*, **2003**, *38*, 127.

16. K. A. Carrado, (S.M. Auerbach, K.A. Carrado, P.K. Dutta, editors), in *Handbook of layered materials*, Marcel Dekker Inc., **2004**, New-York, chapter 1.

17. R. J. Hu, B. G. Li, *Catalysis Letter*, **2004**, *98*, 43.

18. A. Meunier, *Clays*, Springer-Verlag, **2005**, Berlin, chapter 1.

19. S. Ozcan, O. Gok, A. Ozcan, *Journal of Hazardous Materials*, **2009**, *161*, 499.

20. C. Namasivayam, D. Sangeetha, *Adsorption*, **2006**, *12*, 103.

21. J. Febrianto, A. N. Kosasih, J. Sunarsao, Y. Ja, N. Indraswati, S. Ismadji, *Journal of Hazardous Materials*, **2009**, *162*, 616.

PVC MATRX IONIC - SURFACTANT SELECTIVE ELECTRODES BASED ON THE IONIC PAIR TETRA ALKYL-AMMONIUM - LAURYLSULPHATE

CRISTINA MIHALI[a], GABRIELA OPREA[a], ELENA CICAL[a]

ABSTRACT. A series of all-solid-state electrodes sensible to the anionic surfactants were developed using silver pills coated with PVC membranes. We used cetyltrimethylammonium laurylsulfate (CTMA-LS) and tricapryl-methylammonium laurylsulfate (TCMA-LS) as electroactive matter (ionophore) and different plasticizers. The electrochemical properties of the electrodes were studied. The best electrochemical characteristics were obtained with TCMA-LS (dioctylsebaccate as plasticizer): nearnerstinan slope: 58,56 mV/pC; concentration range of linear response 10^{-3}-$2x10^{-6}$ M·L^{-1} of laurylsulfate anion. The selected membrane-electrode can be applied as equivalence point indicator to the potentiometric titration of anionic surfactants and to the determination of anionic surfactants in environmental samples.

Keywords: anionic surfactant-selective electrode; PVC - matrix membrane electrodes, sodium laurylsulfate

INTRODUCTION

The surfactants are compounds essential to the modern civilization and technology. Determination and monitorization of the surfactants concentration is necessary in the production of detergents, in the industrial processes where anionic surfactants are used, in quality control of products containing added surfactants and in environment surveillance activities, especially monitoring water quality.

In the last decades there have been created and improved numerous analytic methods for determination of anionic surfactants [1]. Among these, there are the potentiometric methods based on potentiometric sensors (electrodes sensible to anionic surfactants) .There are some review articles that presents the electrochemical or potentiometric measurement applied for the determination of surfactants [2-3]. Potentiometric sensors for anionic surfactants are very attractive tools due to their good precision, relatively

[a] *North University of Baia Mare, Sciences Faculty, 76 Victoriei, RO-430072, Baia Mare, Romania, cmihali@yahoo.com*

simple manufacturing, relatively low cost and their ability to determine the surfactants in the samples without previous separation steps [4-10]. Also some anionic surfactant ion-sensitive field effect transistors (anionic surfactant FET) were proposed [11-12].

In order to determine the concentration of the anionic surfactants potentiometric sensors with liquid membrane and polymeric membrane (especially PVC membrane) have been produced.

The polymeric membrane is made up of polyvinyl chloride (PVC) in most of the cases, with high relative molecular mass (100,000), a substance with plasticizer role and the organic ion exchanger (ionophore) that makes the electrode component. The plasticizer assures the mobility of the ion exchanger into the polymeric membrane; fixes the dielectric constant value of the membrane and confers it the corresponding mechanical properties. The proportion of the membrane components depends on the polymer type and on the ion exchanger used. It is chosen such that the electrode performances are optimum.

The electrodes with polymeric membrane are prepared in the classical way with internal reference solution, in the "coated wire" version [13] or in the constructive form of "all solid state" [14]. In the case of the last type of surfactant selective electrodes, the polymeric membrane is built on a graphite epoxy support. We realized in all solid-state electrode for anionic surfactants with the polymeric membrane attached by a metallic pill. These constructive forms was not presented in the literature devoted to the anionic surfactant polymeric electrodes and has as main advantages the robustness and an easier handling.

This layout of the electrode has the great advantage of a solid internal contact because it does not require internal reference electrode and internal electrolyte.

First, we wanted to produce electrodes sensible to anionic surfactants adopting this layout, using different compositions of the PVC membrane and to establish the functional characteristics of those electrodes. We used as ionophores CTMA-LS and TCMA-LS and different plasticizers: tricresylphosphate (TCF), *ortho*-nitrophenyloctylether (NPOE) and dioctylsebaccate (DOS).

Second, we wanted to use the electrodes with the best analytical performances to the determination of the anionic surfactants concentration from the environmental samples.

RESULTS AND DISCUSSION

The response function

In order to establish the electrode function we have used 10^{-7}- 5×10^{-2}M sodium laurysulphate solutions. We have worked in thermostatic regime at 25°C in magnetically stirred solutions. The sensors have been introduced successively

in laurysulphate solutions with increasing concentrations. The electrode potential has been registered after stabilizing its response. The potential values on different concentration levels are the average of three determinations.

We wanted to choose an optimum ionic strength adjustor in order to obtain a value of the slope as close as possible to the Nernstian one and an extended linear response range. In this purpose we tested the following solutions: Na_2SO_4 0.01 M (J=0.03), Na_2SO_4 0.1 M (J=0.3), NaCl 0.01M (J=0.01), NaCl 0.1 M (J=0.1).

The tests were performed using the CTMA-LS membrane electrode (plasticized with DOS). The results are presented in Table 1.

The electrode functions for the pure NaLS solutions and for those adjusted with Na_2SO_4 0.1 M and Na_2SO_4 0.01 M are exposed in Figure 1.

Table 1. Influence of ionic strength adjustor on the characteristics of the laurylsulphate sensible electrodes based on CTMA-LS (DOS plasticizer)

The nature and concentration of the ionic strength adjustor	Membrane characteristics	
	Slope, mV/conc. decade	Linear response range, M
Without ionic strength adjustor (pure NaLS solutions)	59.33	10^{-3}-4.33×10^{-6}
Na_2SO_4 0,1M, J=0.3	56.22	10^{-3}-4.29×10^{-6}
Na_2SO_4 0,01M, J=0.03	59.39	10^{-3}-3.93×10^{-6}
NaCl 0.1M, J=0.1	55.66	10^{-3}-2.94×10^{-6}
NaCl 0.01M, J=0.01	57.53	10^{-3}-3.99×10^{-6}
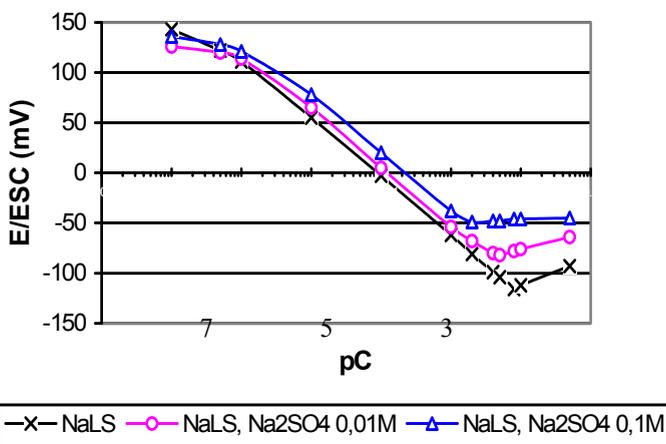
Figure 1. The influence of the ionic strength on the response functions of the laurylsulphate sensible electrode:
X **-** pure NaLS solutions; O **-** NaLS solutions with Na_2SO_4 0.01 M (J=0.03)
Δ**-** NaLS solutions with Na_2SO_4 0.1 M (J=0.3)

The best results, the slope 59.39 mV/decade and the linear response range 10^{-3}-3.93×10^{-6} M was obtained with Na_2SO_4 0.01 M (J=0.03) that was selected as optimum ionic strength adjustor.

We can observe that, in the case of pure NaLS solutions, the electrode function has a minimum at 8×10^{-3}M. This corresponds to the critical micellar concentration (CCM). For concentration values greater than CCM takes place the association on a large scale of the surfactant molecules and in these conditions, the number of the free laurylsulphate anions decreases. The sensor senses only the free laurylsulphate anions. CCM value depends on the presence and the nature of the ionic strength adjustor.

In the case of the ionic strength adjustor Na_2SO_4 0.01M, CCM takes the value 5×10^{-3} M and 2×10^{-3} M in the case of Na_2SO_4 0.1M respectively.

When we use NaCl as ionic strength adjustor, CCM is 6×10^{-3} M for NaCl 0.01M and 2×10^{-3} M for NaCl 0.1M. The CCM value determined this way corresponds to the value presented in the literature [15]. As the CCM value is a property related to industrial applications of the surfactants and it can be determined quickly with potentiometric sensors, they can be used to establish CCM value for surfactant solutions in presence of different inorganic electrolytes [16].

Comparing the electrodes prepared from the point of view of the linear response range and the slope (Table 2) we can notice that the best performances have been obtained with the CTMA-LS ionophore based electrode, plasticized with DOS (slope 59.39 mV/concentration decade, linear response range 10^{-3}-3.93×10^{-6}M) and the electrode with TCMA-LS ionophore and the same plasticizer (slope: 58.56 mV/concentration decade, linear response range 10^{-3}-2×10^{-6}). Nearer values have been obtained for membrane with TCMA-LS ionophore, plasticized with TCF (slope: 58.89 mV/decade and linear response range 10^{-3}-2.9×10^{-6} M).

Table 2. Influence of polymeric membrane composition on the electrode performances

Ionophore / Plasticizer		Membrane characteristics	
		Slope, mV/conc. decade	Linear response range, M
CTMA-LS	DOS	59.39	10^{-3}-3.93×10^{-6}
	TCF	58.19	10^{-3}-4.2×10^{-6}
	NPOE	56.08	10^{-3}-4.88×10^{-6}
TCMA-LS	DOS	58.56	10^{-3}-2×10^{-6}
	TCF	58.87	10^{-3}-2.9×10^{-6}
	NPOE	55.07	10^{-3}-3.5×10^{-6}

The performances of the prepared membranes are close to those of the membranes described in literature. Thus, the PVC membrane proposed by Gerlache [5] having as ionophore 1,3-didecyl-2-methyl-imidazolium laurylsulphate has the slope 58.9 mV/concentration decade and linear response range $2.5 \times 10^{-6} - 5 \times 10^{-3}$ M.

The pH function

We determined experimentally the pH functions of the laurylsulphate-sensible sensors with TCMA-LS membrane, plasticized with DOS, TCF and NPOE. The useful pH range where the electrode response is not influenced by the pH change depends on the nature of the plasticizer used and on the primary ion concentration (LS^-). In Table 3 there are shown the optimum pH ranges corresponding to different levels of NaLS concentration.

The useful pH is enough large allowing the utilization of the sensor to the determination of the anionic surfactants from water samples whose pH, generally does not exceed this domain.

Table 3. Influence of plasticizer nature
on the useful pH range for sensors with TCMA-LS membrane

NaLS conc., M	Plasticizer / useful pH range		
	DOS	**TCF**	**_o_-NPOE**
10^{-6}	3.5-9	4.5-9	4-9
10^{-5}	2.5-10	4-10.5	3.5-10
10^{-4}	2-11.5	3.5-11	3-11.5
10^{-3}	2-12	2.5-12	2.5-12

Interferences

The selectivity of the TCMA-LS laurylsulphate-sensible sensors to Cl^-, Br^-, I^-, NO_3^-, HCO_3^- anions was established using the mixed solutions method, by maintaining the primary ion (LS^-) concentration constant and varying the concentration of the interfering ion.

The Cl^-, Br^-, NO_3^- and HCO_3^- anions do not interfere, as their selectivity coefficients are less than 10^{-5}, but the I^- interferes and its response was influenced even for relatively great concentrations of NaLS (10^{-3} M). The selectivity with respect to other anionic surfactants like dodecylbenzenesulphonate (DBS^-) and ethoxylaurylsulphate ($Etoxi-LS^-$) was studied by applying the separate solutions method, by graphically valuing the concentrations corresponding to the same potential value. The values of selectivity coefficients of the sensors with TCMA-LS membrane are centralized in Table 4.

Table 4. Influence of plasticizer nature on the selectivity
of the membrane with TCMA-LS ionophore

Interfering ion, J^-	Selectivity coefficients K_{LS^-/J^-}^{pot} , Plasticizer		
	DOS	TCF	o-NPOE
I^-	3.2×10^{-1}	3.2×10^{-1}	8×10^{-2}
DBS^-	6.9×10^{-1}	1.86	1.77
Etoxi-LS$^-$	4.7×10^{-1}	1.2	5.9×10^{-1}

As a consequence it appears that these electrodes could be used in river or wastes waters without any interference from these ions except the I^- that, if it is present, interferes and must be removed from the sample.

Potentiometric titrations

In order to continue the study the electrode based on TCMA-LS ionophore and the DOS plasticizer was selected. This electrode has been used as indicating electrodes in potentiometric titration of anionic surfactants with cationic surfactants titrants. Several cationic surfactants were used, monitoring the accuracy of determinations, the potential jump around the equivalence point and the reproducibility.

The potential jump was considered the difference between the potential registered when the titrating ratio is 90% and 110% [18].

We have used the following cationic detergents:
- cetylpyridinium bromide (CPY-Br);
- cetyltrimethylammonium bromide (CTMA-Br);
- Hyamine 1622.

In order to select the optimal cationic agent we performed titrations of the sodium laurylsulphate (50 mL solution 10^{-3} M) with titrating agents mentioned above. Each titration was repeated three times after performing 1-2 titrations for conditioning the electrode with the new titrant.

The titration curves are shown in figure 3 and the results in Table 5.

Table 5. Statistical evaluation of potentiometric titrations of NaLS solutions,
performed with TCMA-LS (DOS plasticizer) membrane electrode
and different cationic surfactants

Cationic surfactant used as titrant	CTMA-Br	Hyamine 1622	CPY-Br
Equivalence volume, V_E, mean value [mL]	9,97	9,93	9,84
Mean square error s_{n-1} [mL]	0,107	0,134	0,114
Relative mean square error, s_{n-1} [%]	1,07	1,35	1,15
Potential jump ΔE 90/110%, mean value (mV)	185,33	110	170,33
Recovery %	99,67	99,27	98,40
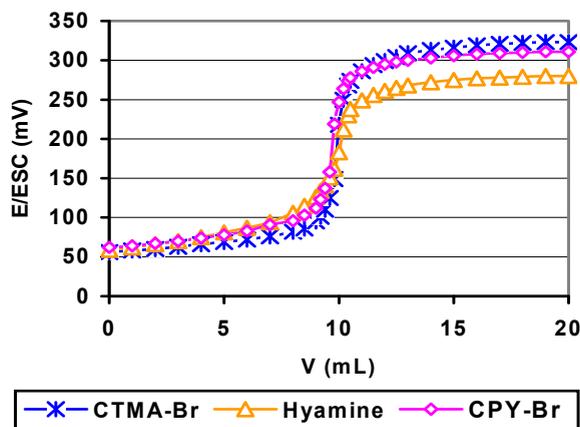
Figure 3. Influence of the titrating agent on the potentiometric titration curve
(titration of 50 mL NaLS 10^{-3} M with different cationic surfactants, 5×10^{-3}M)
Indicating electrode: TCMA-LS membrane plasticized with DOS

We obtained a good recovery in the case of titration with CTMA-Br and Hyamine. The potential jump around the equivalence point was high for CTMA-Br and CPY-Br. The best results were obtained for CTMA-Br.

We have carried out potentiometric titrations of other anionic surfactant species: sodium ethoxylated laurylsulphate and sodium dodecylbenzenesulphonate. We used CTMA-Br 5×10^{-3} M, and the indicating electrode was the one with TCMA-LS membrane plasticized with DOS. The titration curves are well contoured, the potential jump around the equivalence point is high, having values close to the value obtained in titrating of NaLS (203 mV for NaDBS, 167 mV for NaEtoxiLS, versus 217 mV for NaLS).

Measurement of anionic surfactants in river and waste waters

Samples from the river Săsar and from the waste water plant of Baia Mare were analyzed by potentiometric titration with CTMA-Br 10^{-5}M using the TCMA-LS electrode. The results compared with two-phase titration are presented in Table 6. A good correlation was obtained.

Table 6. Results of the determination of of anionic surfactants in
environmental samples

Sample	Anionic surfactant concentration, $c \times 10^6$ M	
	Potentiometric titration	**Two-phase titration**
Sasar River	2.86 (5.2%)[*]	2.88 (2.2%)
Waste water 1	7.60 (1.9%)	7.67 (0.13%)
Waste water 2	4.43 (2.8%)	4.4 (0.18%)

[*]RSD (relative standard deviation is indicated in the brackets);
Means values corresponds to measurements in fourfold.

CONCLUSIONS

Some series of polymeric membranes sensible to anionic surfactants based on plasticized PVC containing CTMA-LS or TCMA-LS ionophores were prepared. We elaborated the preparing methods for the ionic association compounds used as ionophores and we prepared electrodes with polymeric membranes formed directly on an adequate metallic plate, attached to the inferior side of the electrode body (internal solid contact).

We established the main functional characteristics of the electrodes: sensitivity (the slope of the electrode function mV/pC) and linear response range.

The sensor was utilized in the determination of anionic surfactants from the river and waste water samples. The results obtained results agree with the two-phase titration method.

EXPERIMENTAL SECTION

Reagents and apparatus

All the reagents used were of analytical grade. Aliquot 336 S (Fluka) and sodium laurylsulphate (Na-LS) form Merck were used to obtain the ionophore. The main component in Aliquat is tricaprylmethylammonium chloride (TCMA-Cl). High molecular weight polyvinyl chloride (PVC) (Fluka) was used as polymeric matrix of the sensitive membrane of anionic surfactants electrodes.

The following plasticizers have been used: tricresylphosphate (TCF) (BDH Chemicals), *orto*-nitrophenyoctylether (NPOE) (Fluka) and dioctylsebaccate (DOS) (Merck).

The pH/mVmeter Consort P 901 (Belgium) was used for the potential measurements. The reference electrode was a calomel saturated electrode (ESC). The potential measurements were made in stirred solutions at 25 °C (thermostat) using a magnetical stirrer. For pH measurements a pH-combination glass electrode was used.

Surfactant electrode preparation
Preparation of the ionophore

The ionic association compounds are made of a tensioactive anion and a bulky cation from a cationic surfactant. They are solid or viscous liquid substances. The technology for preparing the ionic association compounds is shortly described below:

We mixed equimolar solutions of anionic and cationic surfactants. The precipitation of the ionic association compound takes place. Their separation from the reaction mix is done with respect to its state (solid or liquid) by filtering or by extracting with organic solvent (chloroform).

We purified the ionic association compound by washing the precipitate with small amounts of water on the filter or by washing the extract in the organic solvent with distilled water several times (negative reaction with $AgNO_3$). The ionic association compound obtained may contain traces of water that can be removed by treating with anhydrous sodium sulfate, after dissolving in acetone.

CTMA-LS has been obtained based on the information found in literature regarding the preparation of ionic association compounds [17,19].

We mixed hot 10 mL of NaLS 0.05 M solution with the same volume of CTMA-Br 0.05 M solution, stirring continuously. A white precipitate of CTMA-LS was obtained, that was purified and desiccated according to the method presented above.

The ionic association between the laurylsulphate anion and the tricaprylmethylammonium cation was obtained by mixing together 50 mL NaLS 0.05 M solution with 50 mL TCMA-Cl equimolar solution.

The mixture of the two solutions was agitated for 15 minutes on water bath at 60°C. From the white emulsion obtained was extracted the TCMA-LS using chloroform and then it was purified and desiccated. The TCMA-LS obtained has a semisolid state.

Preparation of the membrane

From the point of view of the composition, the classical procedure has been used, with 1% ionophore, 33% PVC and 66% plasticizer [17,19-20].

We have used as ionophores: the ionic association compounds: CTMA-LS and TCMA-LS. As plasticizers we have used TCF, *o*-NPOE and DOS.

The polymeric membrane has been prepared by dissolving its components in tetrahydrofurane in the following order: ionophore, PVC and plasticizer. We poured a few drops of the resulting solution on the surface of the metallic plate of the electrode.

After the slow evaporation of the solvent (enclosed recipient) on the metallic surface remains the polymeric membrane sensible to anions, well attached to the PVC body of the electrode.

In order to raise the calibration curve, the electrodes were conditioned by maintaining them in a NaLS 10^{-2}M solution for 24 hours.

When not used, the electrodes should be stored dry, in dark places. They should be reconditioned by washing with HCl 5×10^{-3} M solution for 30 minutes and then by magnetic stirring in a NaLS 10^{-4} M solution before use.

Construction of the electrode

The technology for producing the "all solid state" sensors consists in forming the sensible PVC membrane directly on the metallic support, attaching it to the PVC electrode body.

The electrode is made of a PVC body with a copper or silver plate tightly attached at its bottom, which has attached the copper wire of the coaxial cable for coupling to the measuring device. On the plate surface there is the polymeric membrane which contains the ionophore and the plasticizer.

This layout of the electrode has the great advantage of a solid internal contact because it does not require internal reference electrode and internal electrolyte.

REFERENCES

1. D. O. Hummel, Analyse der Tenside, Carl Hansen Verlag, München, Wien, **1995**, chapters 4-5.

2. M. Gerlache, J. M. Kauffmann, G. Quarin, J. C. Vire, G. A. Bryant, J. M. Talbot, *Talanta*, **1996**, *43*, 507.

3. J. Sanchez, *Critical Reviews in Analytical Chemistry*, **2005**, *35*, 15.

4. P. Săp, D. F. Anghel, C. Luca, *Rev. Roum. Chim.*, **1983**, *28*, 883.

5. W. Szczepaniak, M. Ren, *Electroanalysis*, **1994**, *6*, 341.

6. L. Campanella, F. Mazzei, M. Tomassetti, R. Sbrilli, *Analyst*, **1988**, *113*, 327.

7. W. Szczepaniak, *Analyst*, **1990**, *115*, 1451.

8. J. Baró Romá, J. Sánchez, M, del Valle, J. Alonso, J. Bartroli, *Sensors and Actuators B*, **1993**, *15-16*, 179.

9. R. Matesic-Puac, B. Sak-Bosnar, M. Bilic, B.S. Grabaric, *Sensors and Actuators B*, **2005**, *106*, 221.

10. N. M. Mikhaleva, E. G Kulapina,. *Electroanalysis*, **2006**, *13-14*, 1389.

11. J. Sancez, M. del Valle, *Talanta*, **2001**, *54*, 893.

12. T. Masadome, S. Kugoh, M. Ishikawa, E. Kawano, S. Wakida, *Sensors and Actuators B*, **2005**, *108*, 888.

13. J. Vessel, K. Tulip, ″Analysis with ion-selective electrodes″, Ellis Horwood Ltd., Chichester, **1978**, chapter 2**.**

14. S. Alegret, J. Alonso, J. Bartroli, J. Baró-Romà, J. Sánchez, *Analyst*, **1994**, *119*, 2319.

15. E. Chifu, 2000, ″Chimia coloizilor şi a interfețelor (″The colloid and interfaces chemistry″), Ed. Presa Universitară Clujeană, Cluj-Napoca, **2000**, chapter 3.

16. D. Mihai, R. von Klitzing, D. F. Anghel, *11th Physical Chemistry Conference with International Participation ROMPHYSCHEM 11*, Timişoara, Romania, **2003**.

17. M. Gerlache, Z. Sentürk, J. C. Viré, J. M. Kauffmann, *Anal. Chim. Acta*, **1997**, *349*, 59.

18. N. Buschmann, H. Strap, *Tenside Surf. Det.*, **1997**, *34*, 84.

19. B. Kovács, B. Csóka, G. Nagy, A. Ivaska, *Anal. Chim. Acta*, **2001**, *437*, 6.

20. G. J. Moody, J. D. R. Thomas, ″Selective Ion Sensitive Electrodes″, Merrow, Watford, **1971**, chapter 3.

NEW LC/MS METHOD FOR DETERMINATION OF PROGESTERONE IN HUMAN PLASMA FOR THERAPEUTIC DRUG MONITORING IN PREGNANCY AND GYNECOLOGICAL DISORDERS

DAN MIHU[a], **LAURIAN VLASE**[a], **SILVIA IMRE**[b], **CARMEN M. MIHU**[a], **MARCELA ACHIM**[a], **DANIELA LUCIA MUNTEAN**[b]

ABSTRACT. A new simple, sensitive and selective liquid chromatography coupled with mass spectrometry (LC/MS) method for quantification of progesterone in human plasma was validated. The analyte was eluted in 1.9 minutes on a reversed phase column (Zorbax SB-C18, 100 mm x 3.0 mm I.D., 3.5 μm) under isocratic conditions using a mobile phase of a 20:80 (v/v) mixture of formic acid 0.1% (v/v) and methanol. The flow rate was 1 ml/min at the column temperature of 45 ºC. The detection of the analyte was in MS/MS mode using an atmospheric pressure chemical ionization source (APCI+, m/z 315.2 → m/z 279.2). The sample preparation was very simple and rapid and consisted in plasma protein precipitation from 0.2 ml plasma using 0.5 ml methanol. Calibration curves were generated over the range of 0.8-80 ng/ml with values for coefficient of determination greater than 0.995 and by using a weighted ($1/y^2$) linear regression. The values of precision (coefficient of variation %) and accuracy (relative error %) were less than 9.4% and 14.2%, respectively, both for within- and between-run analysis. The mean recovery of the analyte was 98.6%. The developed LC/MS/MS method could be applied for determination of progesterone in human plasma for therapeutic drug monitoring in pregnancy and gynecological disorders.

Keywords: progesterone, human plasma, LC/MS/MS, method validation

INTRODUCTION

Progesterone (PRG) is a steroid, secreted in large amounts by the corpus luteum and the placenta. It is an important intermediate in steroid biosynthesis in all tissues that secrete steroid hormones and small amounts enter the circulation from the adrenal cortex. It plays a key role in the female menstrual cycle (mainly produced after ovulation) and during pregnancy, when its production causes suppression of further ovulation and provides the correct environment for the developing embryo [1].

[a] *University of Medicine and Pharmacy "Iuliu Hatieganu", Emil Isac 13, RO-400023, Cluj-Napoca, Romania, vlaselaur@yahoo.com*
[b] *University of Medicine and Pharmacy Targu-Mures, Gheorghe Marinescu 38, RO-540139, Targu-Mures, Romania*

The analysis of steroid hormones in biological samples can be employed as a diagnostic tool in diseases promoted by disorders in the steroids profile. Progesterone is suitable to be monitored during treatment of infertility. Exogenous progestogens are administered in hormone replacement therapy and the modern, accurate and succesfully treatment involves hormon plasma level monitoring. This kind of therapeutic strategy has the problems of low concentration of steroids in plasma and the complexity of sample matrix, and demands for the development of highly selective and sensitive analysis methods. Progress in instrumental analytical chemistry and robust extraction techniques have enabled the detection of more compounds at lower concentrations, contributing to the success of different kind of therapies.

Liquid Chromatography coupled with Mass Spectrometry (LC–MS) has been commonly selected for the analysis of the steroids due to its advantages of high sensitivity and selectivity of MS and allows a very short analysis run-time. Many applications have been reported, regarding steroid hormons determinations, including, determinations in water [2-9], tissues [10-12], food [13], cosmetics [14] and only a few in urine, serum or blood [15-17].

In the present study, we attempted to develop a fast HPLC/MS/MS method able to quantify PRG in human plasma after a simple protein precipitation for both physiological and therapy levels monitoring of PRG. Then, the developed method was applied to monitor PRG level in pregnant women or with gynecological disorders under or without PRG treatment.

RESULTS AND DISCUSSION

No significant interference at the retention time of PRG (1.4 min) (Figure 1) was observed in different human male plasma blank samples chromatograms due to the specificity of selected signals (Figure 2).

Two ionization sources were tested, atmospheric pressure chemical ionization (APCI) and electrospray ionization (ESI), respectively. Finally, the APCI source was used due to the absence of pH-ionizable groups on progesterone molecule which determined a lower signal when electrospray ionization mode was applied. Different organic solvents were used for mobile phase: acetonitrile and methanol. At the same retention time for the analyte (obtained by using 72% acetonitrile with 28% formic acid 0.1% or 80% methanol with 20% formic acid 0.1%), the signal intensity of PRG was about 3 times higher in case of methanol and for this reason, this was selected for further investigation.

All the studied literature papers propose m/z 109.1 and/or 97.1 as daughter ions for monitoring. Our experiments demonstrated that, in this conditions, later eluting compounds interfere the determination (Figure 3, upper image), so a supplementary wash period is needed which extends the analysis with another six minutes. The selected monitoring ion m/z 279.2 alows a specific and sensitivie analysis in a very short run-time of 2 minutes (Figure 2 and Figure 3 lower image).
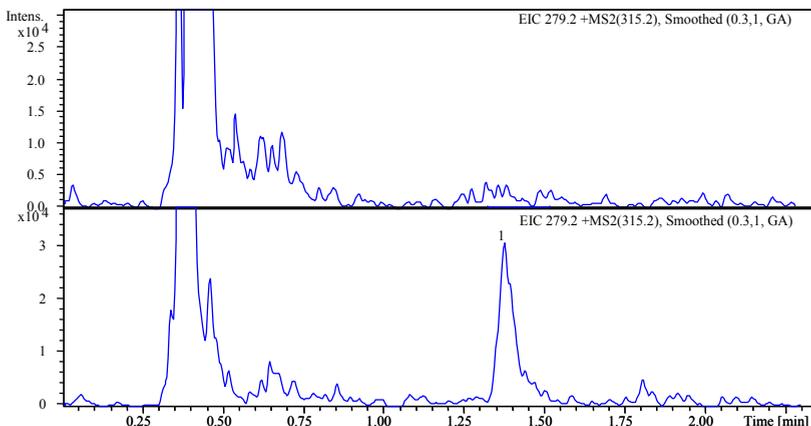
Figure 1. Chromatograms of a blank human male plasma (upper image) and a plasma standard sample of 0.8 ng/ml PRG (RT 1.4 min)(lower image)
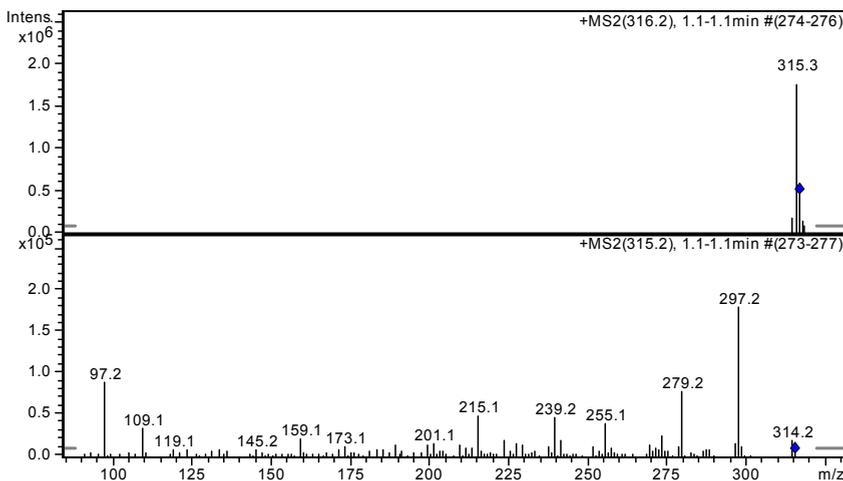
Figure 2. Mass spectra of progesterone: MS/MS non-reactive spectrum - isolation (upper image); MS/MS reactive spectrum - fragmentation (lower image)

The applied calibration curve model proved to be linear over the concentration range 0.8 - 80 ng/ml PRG, with a determination coefficient greater than 0.995. The mean calibration curve, $y = a (\pm SD) x + b (\pm SD)$ with SD standard deviation, was: $y = 18097.2 (\pm 1850.7) x – 1018.4 (\pm 538.3)$, N = 8 calibration points, n = 5 determinations for each calibration point. The residuals had no tendency of variation with concentration and were between ±15% values.
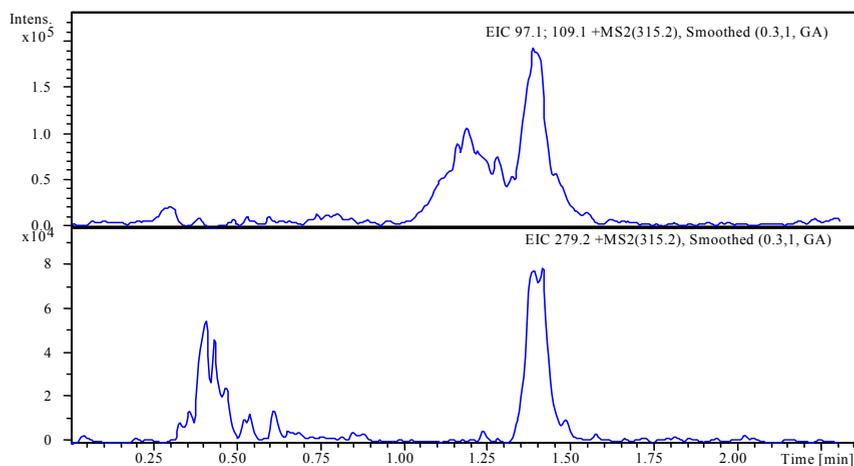
Figure 3. Chromatograms of the sample plasma with PRG (RT 1.4 min), different detection channels: transition 315.2>(97.1 + 109.1) (upper image) and transition 315.2> 279.2 (lower image)

The method had within- and between-run accuracy and precision (Tables 1 and 2), in agreement to international regulations regarding bioanalytical methods validation [18-20]. The lower limit of quantification was established at 0.8 ng/ml PRG, with accuracy and precision less than 20% (Tables 1 and 2).

The recovery was consistent and reproducible (Table 1 and 2).

The analyte proved its stability after sample preparation for at least 12 hours, the Bias% of found concentration being less than 15%, the maximum accepted value for method's accuracy.

Table 1. Within-run precision, accuracy and recovery for PRG (n = 5)

Nominal concentration ng/ml	Measured concentration ng/ml (± D.S.)		Precision %	Accuracy %	Recovery % (± D.S.)	
0.80	0.88	0.04	4.5	10.0	102.0	4.5
2.40	2.35	0.19	8.0	-2.0	101.6	4.8
16.00	15.87	1.50	9.4	-0.8	94.0	5.5
32.00	34.47	1.69	4.9	7.7	94.6	7.4

Table 2. Between-run precision, accuracy and recovery for PRG (n = 5)

Nominal concentration ng/ml	Measured concentration ng/ml (± D.S.)		Precision %	Accuracy %	Recovery % (± D.S.)	
0.80	0.92	0.07	7.4	14.2	98.6	8.4
2.40	2.54	0.05	2.1	5.7	100.8	3.7
16.00	16.61	0.76	4.5	3.8	98.8	7.6
32.00	33.62	2.50	7.4	5.1	98.2	7.6

In comparison with the studied chromatographic – mass spectrometry methods about PRG determination in human plasma, the sensitivity of the proposed method (LLOQ of 0.8 ng/ml PRG in plasma) is better [16,17]. But the main advantage, except the short run-time of 2 minutes, is the sample preparation by protein precipitation and besides its simplicity, that sample treatment allows obtaining a very good recovery of analyte. The current LC/MS method does not intend to be a competitor or to replace the immunoassays methods, and is focused as an analytical tool for therapeutic drug monitoring of progesterone. In Table 3 a critical comparison between determination of progesterone by LC/MS and immunoassay, focused on the main advantages of the former technique, is given.

Table 3. Comparison between determination of progesterone by
LC/MS and immunoassay

Parameter	Current LC/MS method	Immunoassay methods EIA, ELISA [18]	Observations
Selectivity	Highly selective	Less selective, possible overestimation due interference of compounds with very similar structure (cross-reaction)	LC/MS method is more selective than immunoassays methods
Sensitivity	0.8 ng/ml	Depends on method/ technique, usually between 0.02-0.2 ng/ml	Although immunoassay methods are more sensitive, the aim of our LC/MS method is therapeutic drug monitoring, and the expected levels of progesterone are in this case more than 10 ng/ml
Upper limit of quantification (ULOQ)	80 ng/ml	Depends on method / technique, usually between 5-50 ng/ml	If concentration is above ULOQ, sample dilution is required and re-analysis, increasing the total analysis time and costs
Matrix effects or interferences	Less susceptible to matrix effects	Highly susceptible to matrix effects due inter- and intra-individual differences in qualitative and quantitative serum composition; internal control required	LC/MS method is more robust due relatively less matrix effects
Analysis time / throughput	Less than 10 min per sample, including sample preparation and analysis	Usually 60-120 min per sample	LC/MS is high-throughput compared with immunoassays methods
Sample volume required	0.2 ml plasma	0.02-0.2 ml serum	Immunoassays methods usually require a smaller sample volume in comparison with LC/MS method
Reagents preparation and costs	In house-preparation and low cost of reagents	Special designed kits of reagents, about 10-50 folds higher costs as in case of LC/MS	LC/MS method is much cheaper regarding reagents costs compared with immunoassays methods
Shelf-life of reagents	The reagent is prepared in house as needed, from components with shelf life more than 3 years	Limited shelf-life of reagent kits, typically 3-18 months in case of un-opened recipient, less than 3 month after opening the reagent bottle	No problem with shelf-life of reagents in case of LC/MS method

Regarding method's applicability, as it can be seen from Table 4, the proposed analytical method demonstrated the increasing of the level of progesterone in human plasma in the luteal phase of menstrual cycle and it's decreasing in menopause. During the pregnancy and also during the treatments with Utrogestan 100 mg PRG, the level of progesterone in human plasma is increased.

Table 4. Levels of PRG in pregnant or in women with gynecological disorders with or without PRG treatment

Subject	Diagnostic	Observations	Treatment with PRG	PRG level found (ng/ml)
S01	Pelvic inflamatory disease	Age 22 years, The luteal phase of teh menstrual cycle, day 22	No	5.69
S02	Endocervical polyp	Age 52 years, Menopause from 5 years	No	<LOQ
S03	Pregnancy, Nausea and vomiting	Age 29 years, Pregnancy 6-WG	No	20.64
S04	Pregnancy Threatened abortion	Age 28 years, Pregnancy 22- WG	No	43.43
S05	Pregnancy Placenta previa with bleeding	Age 25 years, Pregnancy 25- WG	No	44.56
S06	Pregnancy Mild preeclamsia, Preterm birth	Age 22 years, Pregnancy 34- WG	No	85.24
S07	Pregnancy Threatened abortion	Age 31 years, Pregnancy 12- WG	Utrogestan, 2x1 cps/day, 3 weeks	23.77
S08	Pregnancy Threatened abortion	Age 26 years, Pregnancy 22- WG	Utrogestan, 2x1 cps/day, 14 weeks	32.15
S09	Pregnancy Threatened abortion	Age 28 years, Pregnancy 8- WG	Utrogestan, 2x1 cps/day, 2 weeks	20.20
S10	Pregnancy Cervical incompetence with cerclaj Preterm birth	Age 27 years, Pregnancy 32- WG	Utrogestan, 4x1 cps/day, 24 weeks	50.98
S11	Pregnancy Cervical incompetencewith cerclaj Threatened abortion	Age 34 years, Pregnancy 13- WG	Utrogestan, 2x1 cps/day, 10 days	25.5
S12	Abnormal uterine bleeding	Age 43 years	Utrogestan, 3x1 cps/day, 3 days	12.34

CONCLUSIONS

The proposed method provides accuracy and precision for quantitative determination of progesterone in human plasma for therapy of pregnant women or with gynecological disorders. The simple sample preparation by protein precipitation, the selected signal for monitoring and the short run-time allow a specific and efficient analysis of a large number of plasma samples, making the method more productive and thus more cost effective.

The proposed method allows evaluation of progesterone in human plasma in different phases of the menstrual cycle, menopause and also in the response of the progesterone replacement therapy, together to evaluation of pregnancies prognosis and the efficiency of Utrogestan therapy.

EXPERIMENTAL SECTION

Reagents

Progesterone (PRG) was reference standards from Sigma-Aldrich (St. Louis, MO, SUA). Methanol and formic acid were Merck products (Merck KgaA, Darmstadt, Germany). Distilled, deionised water was produced by a Direct Q-5 Millipore (Millipore SA, Molsheim, France) water system. The human blank plasma was obtained from male volunteers.

Standard solutions

A stock solution of PRG with concentration of 2 mg/ml was prepared by dissolving appropriate quantities of reference substance (weighed on an Analytical Plus balance from Ohaus, USA) in 10 ml methanol. A working solution of 8000 ng/ml was then obtained by diluting specific volume of stock solution with plasma and it was further diluted with plasma to 80 ng/ml. Then these working solutions were used to spike different volumes of plasma blank, providing finally eight plasma standards with the concentrations ranged between 0.8 and 80 ng/ml. Accuracy and precision of the method was verified using plasma standards with concentrations 0.8, 2.4, 16 and 32 ng/ml PRG. Quality control samples (QC) at 2.4 (QCA), 16 (QCB) and 32 (QCC) ng/ml analyte will be used during clinical samples analysis.

Chromatographic and mass spectrometry systems and conditions

The HPLC system was an 1100 series model (Agilent Technologies) consisted of a binary pump, an in-line degasser, an autosampler, a column thermostat, and an Ion Trap SL mass spectrometer detector (Brucker Daltonics GmbH, Germany). Chromatograms were processed using QuantAnalysis software. The detection of the analyte was in MS/MS mode using an atmospheric pressure chemical ionization source (APCI), positive ionization, by monitoring the transition m/z 315.2 → m/z 279.2). Other apparatus parameters: capillary 3500 V, vaporizer temperature 450 °C, nebulizer 60 psi, dry gas temperature 300 °C, dry gas flow 7.00 L/min. Chromatographic separation was performed at 45ºC on a Zorbax SB-C18 100 x 3 mm, 3.5 µm column (Agilent Technologies), protected by an in-line filter.

Mobile phase

The mobile phase consisted of a mixture of formic acid 0.1% (V/V) and methanol (20:80 v/v), each component being degassed, before elution, for 10 minutes in an Elma Transsonic 700/H (Singen, Germany) ultrasonic bath. The pump delivered the mobile phase at 1 ml/min.

Sample preparation

Standard and test plasma samples were prepared as follows in order to be chromatographically analyzed. In an Eppendorf tube, to 0.2 ml plasma, 0.5 ml methanol was added. The tube was vortex-mixed for 10 seconds and then centrifuged for 3 minutes at 10000 rpm. A volume of 150 µl supernatant was transferred in an autosampler vial and 30 µl were injected into the HPLC system.

Analytical performance of the method

The bio-analytical methods for utilization in pharmacokinetics-bioavailability studies and therapeutic drug monitoring are conducted in concordance with FDA, EMEA and laboratory's SOP regulations [19-26].

As a first step for the analytical performance determination of the method, specificity was verified using six different plasma blanks obtained from healthy human male volunteers. The progesterone level in men plasma not exceeds 0.1-0.4 ng/ml, however plasma with no detected PRG was used in order to obtain calibrators and quality control samples.

The concentration of analytes was determined automatically by the instrument data system using the external standard method. Calibration was performed using singlicate calibration standards on five different occasions. The calibration curve model was determined by the least squares analysis. The applied calibration model was a linear one: $y = ax + b$, $1/y^2$ weight, where y – peak area and x – concentration. Distribution of the residuals (% difference of the back-calculated concentration from the nominal concentration) was investigated. The calibration model was accepted, if the residuals were within ±20% at the lower limit of quantification (LLOQ) and within ±15% at all other calibration levels and at least 2/3 of the standards met this criterion, including highest and lowest calibration levels.

The lower limit of quantification was established as the lowest calibration standard with an accuracy and precision less than 20%.

The within- and between-run precision (expressed as coefficient of variation, CV%) and accuracy (expressed as relative difference between obtained and theoretical concentration, Bias%) of the assay procedure were determined by analysis on the same day of five different samples at each of the lower (2.4 ng/ml), medium (16 ng/ml), and higher (32 ng/ml) levels of the considered concentration range and one different sample of each on five different occasions, respectively.

The relative recoveries at each of the previously three levels of concentration and limit of quantification were measured by comparing the response of the treated plasma standards with the response of standards in solution with the same concentration of analytes as the prepared plasma sample.

The post-preparative stability (PPS) in the autosampler of the analytes in human plasma was investigated at lower (2.4 ng/ml) and higher concentration (32 ng/ml) for 12 hours, the expected longest storage times of the samples in autosampler before injection. The requirement for stable analytes was that the difference between mean concentrations of the tested samples in various conditions and nominal concentrations had to be in ±15% range.

Clinical application
The developed method was verified by analyzing different plasma samples obtained from pregnant women or with gynecological disorders, under treatment with vaginal capsules of PRG (Utrogestan 100 mg vaginal capsules) or without treatment.

REFERENCES

1. R. C. Tuckey, *Placenta*, **2005,** *26*, 273.
2. H. Chang, S. Wu, J. Hu, M. Asami, S. Kunikane, *J. Chromatogr. A.*, **2008**, *1195*, 44.
3. E. P. Kolodziej, J. L. Gray, D. L. Sedlak, *Environ. Toxicol. Chem.*, **2003**, 22, 2622.
4. E. P. Kolodziej, D. L. Sedlak, *Environ. Sci. Technol.*, **2007**, *41*, 3514.
5. M. Kuster, M. J. Lopez de Alda, M. D. Hernando, M. Petrovic, J. Martin-Alonso, D. Barcelo, *J. Hydrol.*, **2008**, *358*, 112.
6. M. J. Lopez de Alda, D. Barcelo, *J. Chromatogr. A*, **2000**, *892*, 391.
7. M. Sole, M. J. Lopez de Alda, M. Castillo, C. Porte, K. Ladegaard-Pedersen, D. Barcelo, *Environ. Sci. Technol.*, **2000**, *34*, 5076.
8. B. J. Vanderford, R. A. Pearson, D. J. Rexing, S. A. Snyder, *Anal. Chem.,* **2003**, *75*, 6265.
9. A. Yamamoto, N. Kakutani, K. Yamamoto, T. Kamiura, H. Miyakoda, *Environ. Sci. Technol.*, **2006**, *40*, 4132.
10. D. Caruso, S. Scurati, O. Maschi, L. De Angelis, I. Roglio, S. Giatti, *Neurochemistry International*, **2008**, *52*, 560.
11. T. Higashi, A. Nagahama, Y. Mukai, K. Shimada, *Biomed. Chromatogr.*, **2008**, *22*, 34.
12. P. E. Joos, M. V. Ryckeghem, *Anal. Chem.,* **1999**, *71*, 4701.
13. Y. Yang, B. Shao, J. Zhang, Y. Wu, J. Ying, *J. Chromatogr. B*, **2008**, *870*, 241.
14. D. De Orsi, M. Pellegrini, S. Pichini, D. Mattioli, E. Marchei, L. Gagliardi, *J. Pharm. Biomed. Anal.*, **2008**, *48*, 641.
15. B. Alvarez Sanchez, F. Priego Capote, J. Ruiz Jimenez, M. D. Luque de Castro, *J. Chromatogr. A*, **2008**, *1207*, 46.

16. N. Janzen, S. Sander, M. Terhardt, M. Peter, J. Sander, *J. Chromatogr. B*, **2008**; *861*, 117.

17. S. M. Zhang, S. R. Mada, S. Sharma, *J. Pharm. Biomed. Anal.*, **2008**, *48*, 1174.

18. http://www.biocompare.com/ProductListings/29520/Progesterone-ELISA-EIA-Kits.html

19. The European Agency for the Evaluation of Medicinal Products, Note for Guidance on the Investigation of Bioavailability and Bioequivalence, CPMP/EWP/QWP/1401/98, **2001**, London, UK, http://www.emea.europa.eu /pdfs/human/qwp/140198enfin.pdf

20. U. S. Department of Health and Human Services, Food and Drug Administration, Center for Drug Evaluation and Research. Guidance for Industry. Bioavailability and Bioequivalence studies for orally administered drug products - general considerations, **2003**, Rockville, USA, http://www.fda.gov/cder/guidance/5356fnl.pdf

21. U.S. Department of Health and Human Services, Food and Drug Administration, Guidance for Industry – Bioanalytical Method Validation, **2001**, http://www.fda.gov/cder/guidance/4252fnl.pdf

22. L. Vlase L, S. E. Leucuta, S. Imre, *Talanta*, **2008**, *75(4)*, 1104.

23. L. Vlase, A. Leucuta, D. Farcau D, M. Nanulescu, *Biopharmaceutics & Drug Disposition*, **2006**, *27(6)*, 285.

24. L. Vlase, S. Imre, D. Muntean, S. E. Leucuta, *Journal Of Pharmaceutical And Biomedical Analysis*, **2007**, *44(3)*, 652.

25. L. Vlase, D. Muntean, S. E. Leucuta, I. Baldea, *Studia Universitatis Babes-Bolyai Chemia*, **2009**, *54(2)*, 43.

26. A. Butnariu, D. S. Popa, L. Vlase, M. Andreica, D. Muntean, S. E. Leucuta, *Revista Romana de Medicina de Laborator*, **2009**, *15(2)*, 7.

PHOTO-CATALYSTS BASED ON GOLD - TITANIA COMPOSITES

ANCA PETER[a], MONICA BAIA[b], FELICIA TODERAS[b], MIHAELA LAZAR[c], LUCIAN BARBU TUDORAN[d], VIRGINIA DANCIU[e]

ABSTRACT. Porous TiO_2 aerogels with different Au colloidal particles concentrations were synthesized and their functionality to decontaminate the water was evaluated using model pollutants. It was showed that the decrease of noble metal concentration determines a decrease of the composites pore size and specific surface area and of the photo-degradation apparent rate constant. The morphological (porosity, surface area, TEM and TGA) particularities of the synthesized porous composites were also briefly discussed from the perspective of the photo-catalytic results. Since the photodecomposition rate depends on the $[OH]_{surface}$ adsorbed on the surface, additional measurements have been performed.

Keywords: Au -TiO_2 composite, porosity, TEM microscopy, photo-catalysis, salicylic acid

INTRODUCTION

TiO_2 photo-catalysis has been improved by numerous investigations in recent years, particularly owing to its application for the complete mineralization of almost all organic contaminants to carbon dioxide, water and inorganic constituents [1, 2]. The advantages of using TiO_2 are its non-toxic nature and stability, but it is also significant that the low rate of electron transfer to oxygen and the high recombination rate of electron-hole pairs limit the rate of organic compounds photo-oxidation on the catalyst surface [3]. Many investigations have reported that the addition transition metals to TiO_2 are two ways to enhance the photo-catalytic reaction rate [3-9]. The noble metals as gold [4, 5], platinum [6, 7] and silver [9] were usually

[a] *North University, Faculty of Science, Department of Chemistry-Biology, 430083, Baia Mare, Romania, peteranca@yahoo.com*
[b] *Babes-Bolyai University, Faculty of Physics, 400084, Cluj-Napoca, Romania*
[c] *National Institute for Research and Development of Isotopic and Molecular Technologies, Donath 71 – 103, RO-400293, Cluj-Napoca, Romania*
[d] *Faculty of Biology and Geology, Electron Microscopy Center, Babes-Bolyai University, 5-7 Clinicilor Str., 400006, Cluj-Napoca, Romania*
[e] *Babes-Bolyai University, Faculty of Chemistry and Chemical Engineering, 400028, Cluj-Napoca, Romania*

used to produce the highest Schottky barriers among the metals, in order to facilitate the electron capture. Moreover, the research studies [10, 11] have demonstrated that the gold particles interact with TiO_2 surface oxygen vacancies (note that on an oxygen vacancy site, two neighbouring Ti atoms are reduced from Ti^{4+} to Ti^{3+}), thus reducing the surface defects.

Due to their very low density, high surface area, translucency or transparency to the visible light and to their microstructure, the TiO_2 aerogels are the preferred materials as supports for noble metals. On the other hand, the photo-catalytic activity of Au-TiO_2 composites has been described as strongly influenced by morphological and structural parameters, such as their structure, surface area, porosity, gold particle size and surface hydroxyl group density [12, 13].

In this paper, we study the photo-catalytic behaviour of a series of Au - TiO_2 composites in the aqueous salicylic acid (SA) oxidation. The goal of this study was to investigate the influence of the Au loading on the photo-catalytic activity of the Au –TiO_2 composites.

RESULTS AND DISSCUTION

Morphology and Structure of the Composites

The morpho-structural characteristics of the Au – TiO_2 composites are presented in Table 1. In columns 2 and 3 of the Table 1 are indicated the gold colloid volumes used to the TiO_2 gels impregnation and gold content, respectively. One observes an increase of the Au content as the colloid volume increases from 20 to 75 ml. By using a volume higher than 75 ml Au colloid, the Au content slowly decreases, probably due to the saturation of the TiO_2 surface with Au particles (Figure 1).

The pore size distribution of the obtained composites is presented in Figure 2 A (a-e). The Au -TiO_2 composites have a porous structure containing pores ranging from 8 to 55 Å, while TiO_2 aerogel contains pores ranging from 20 to 80 Å. So, the Au presence in the composites reduces the composite's porosity. This behaviour was attributed to the insertion of a small amount of gold nano-particles into the pores. This insertion occurs without damaging the pore structure. Similar changes have been reported in the surface structure of porous titania with the insertion / deposition of ruthenium and platinum nano-particles by the sono-chemical method [14, 15]. The decrease of porosity by Au deposition can be observed also by analyzing the pore volume values from Table 1. It is interesting to notice that the porosity decreases with the decrease of Au content (Figure 2B). The B1Au and B2Au composites with similar Au content (0.395 % and 0.397%, respectively) have the major pore size ranging from 35 to 40 Å while B4Au composite with 0.131% Au, which contains predominantly 15 A pores. At low Au concentrations, pores with 20 Å diameters are dominant, whereas composites with high Au content (samples B1Au and B2Au) contain pores with diameters higher than 20 Å.

Table 1. Morpho-structural particularities and photo-catalytic behavior of the studied Au-TiO$_2$ composites

u - TiO$_2$ ID	V$_{Au\ coll.\ sol.}$ (ml)	[Au] (% mol)	S$_{BET}$ (m^2/g)	V$_{pore}$ (cm^3/g)	[OH]$_{surf}$ (mmol/g)	k$_{ads}$ x 10^3 (min^{-1})	k$_{photo}$ x 10^3 (min^{-1})	X (%)
B1 Au	150	0.395	477	0.86	0.56	0.23	10.9	63
B2 Au	75	0.397	450	0.44	0.61	0.24	11	59
B3 Au	40	0.373	332	0.38	0.52	0.12	10.6	52
B4 Au	25	0.131	337	0.95	0.57	0.04	8.1	50
TiO$_2$	-	-	340	1.08	0.6	0.09	10.1	60
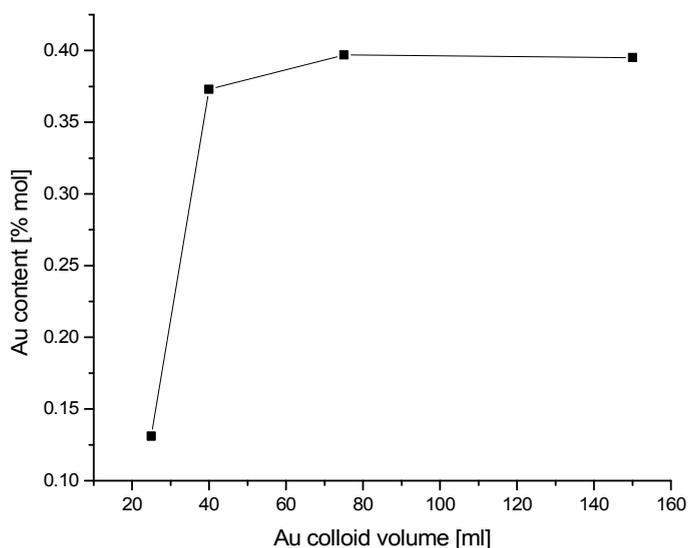
Figure 1. Dependence of Au content on the Au colloid volume used inTiO$_2$ gel impregnation

The specific surface area BET of the obtained composites increases with Au content (Table 1). These effects have been previously reported for gold supported on MCM-41 and MCM-48 zeolites [16] and for gold supported on alumina and ceria [17], and are explained through the expansion of the porous structure of the support due to of the introduction of gold nano-particles [18].
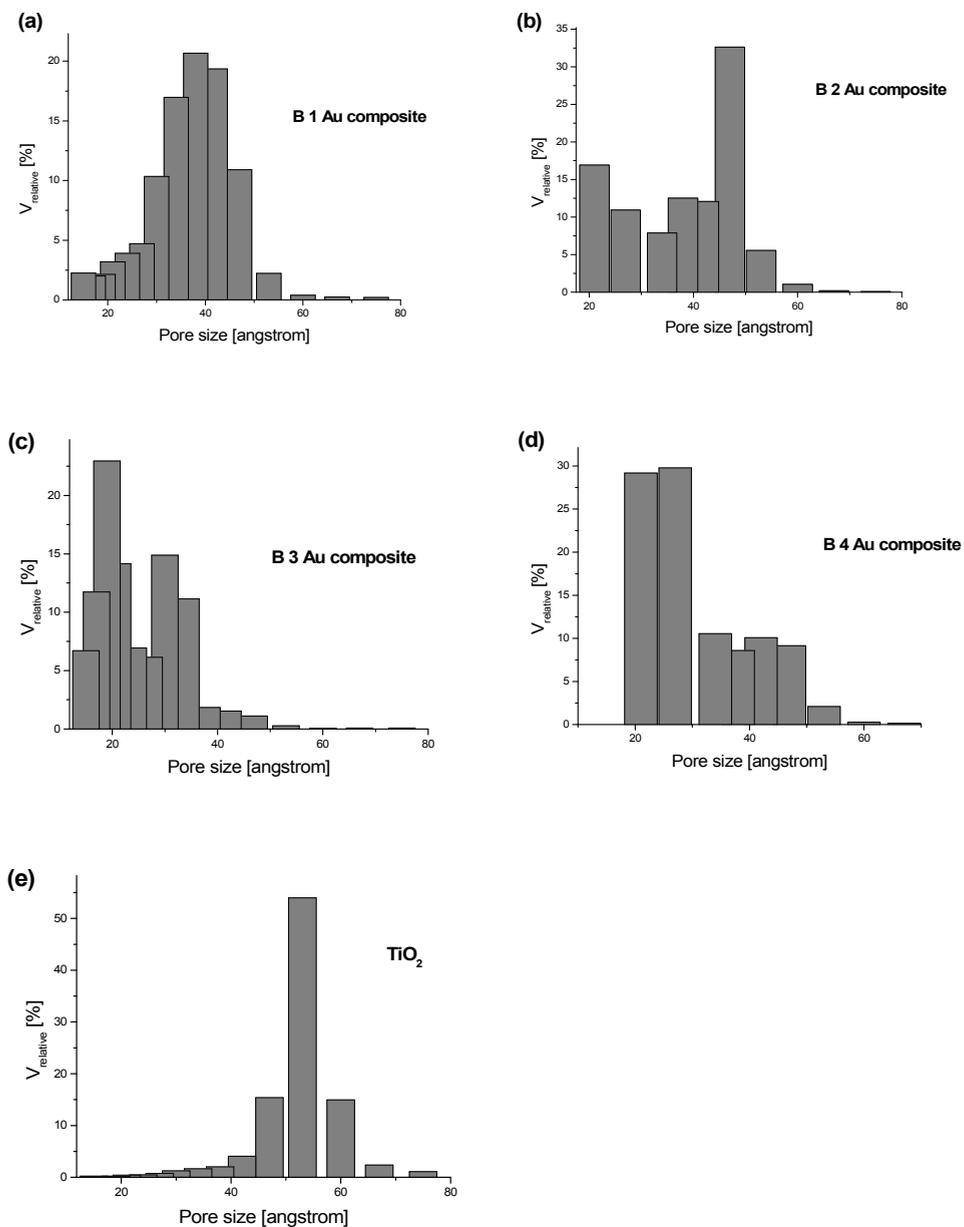
Figure 2A. Influence of the Au loading on the composites pore structure.
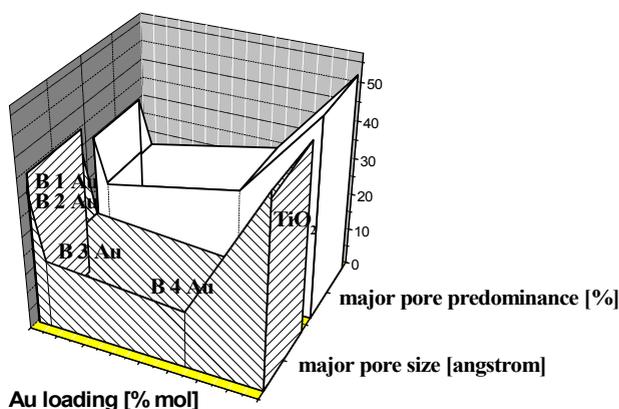
Figure 2B. Variation of major pore size and major pore predominance with Au loadings.

According to TEM pictures analysis, the composite B1Au (Figure 3) has an amorphous TiO_2 structure. The Au particles (dark points) are heterogeneously dispersed on the TiO_2 surface. In some areas, the Au colloidal particles were agglomerate into clusters (indicated by the arrow from Figure 3), while in other regions individual Au particles with a 15 nm diameter (determined from TEM analyses) were detected. The association of Au nano-particles in large clusters reduced the TiO_2 photo-excitation, due to the fact that all its active centres are occupied with Au particles. This behaviour will, subsequently, cause a decrease of the SA photo-degradation rate.
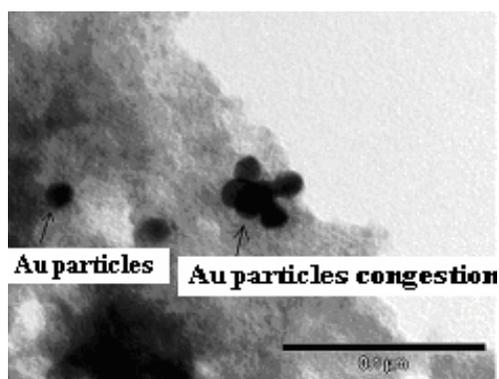
Figure 3. TEM image of the B1Au composite (bar 100 nm).

In Figure 4 presents the Au -TiO$_2$ composites weight decrease after heat treatment at temperatures increasing from 25 to 500^{0}C.

The weight loss at t < 200^{0}C is due to the first dehydration step, resulted from physically adsorbed water, and the elimination of the ethanol traces [19]. It can be observed that the mass loss increases with decrease of the Au content. This is explained by the fact that the Au nano-particles from TiO$_2$ surface inhibit the network shrinkage in thermal treatment. At 250-300^{0}C, a second dehydration step resulted from structural / ligand water and thermal decomposition of the un-reacted titania precursors, takes place. Again, at this stage, the mass loss increases with decrease of the Au content. This is explained by the fact that the higher number of Au nano-particles from TiO$_2$ surface stabilize the aerogel network, by forming a metal skeleton around the TiO$_2$ structure. Moreover, at temperatures higher than 300^{0}C, the aerogel begins to become crystalline. By comparing the weight loss of the TiO$_2$ and Au -TiO$_2$ composites, one observes that the TiO$_2$ network is more stable than the composites network. The weight loss in the case of TiO$_2$ aerogels is lower than that observed for the composites.
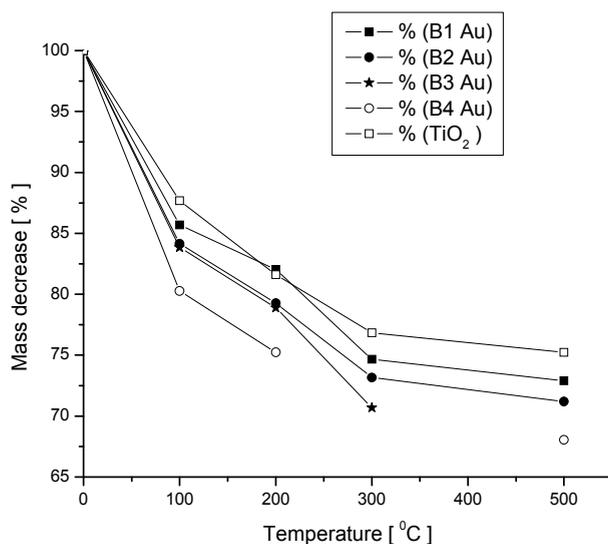
Figure 4. Influence of the Au loading on the thermal behavior of the Au-TiO$_2$ composites.

Catalytic Activity

In Table 1, there are presented some catalytic parameters (salicylic acid adsorption and photo-degradation apparent rate constants and photo-degradation efficiency) which are determinated for the SA photo-decomposition process. The adsorption constants were calculated from the slope of the plot

ln (Q_t) *vs.* time $(Q_t$ – current adsorbed quantity) after applying a linear fit [20]. The photodecomposition rate constants were obtained from the slope of the plot ln (C_0/C) *vs.* time after applying a linear fit [21, 22]. The photo-degradation efficiency was calculated with the following equation:

$$X (\%) = (C_0 - C) / C_0 \times 100 \qquad (1)$$

where: C_0 – SA initial concentration, C– SA concentration after 150 minutes iradiation [23].

The more intense adsorption of SA occurs on B1Au and B2Au composites with the highest Au content (Table 1 and Figure 5). The adsorption rate constants decrease with decrease of the Au loading, in the same manner as the specific surface area and pore volume. Moreover, the $[OH]_{surface}$ is relatively high for those two composites, except for the B4Au sample which has the highest $[OH]_{surface}$. Even if the pore volume and $[OH]_{surface}$ of B4Au composite are highest than those of the other composites, the adsorption rate constant is very low. This is explained by the fact that the B4Au composite contains, in the major preponderance, pores smaller than 20 Å diameter (micro-porous structure) which do not permit the penetration of the SA molecules having a higher surface area (35.52 Å^2), due to the steric impediment [24]. So, in this case SA adsorption and photo-decomposition take place only on geometric surface and not in the real surface. This observation is available also for the TiO_2 aerogel and shows that the adsorption intensity is deeply influenced by the specific surface area and pore size.

The SA photo-degradation rate constants vary with Au loading in the same manner as the adsorption constants (Table 1 and Figure 5). The SA photo-degradation on B1Au, B2Au and B3Au composites occurs with a higher rate, due to the fact that SA adsorption on these composites was more intense. The SA photo-degradation apparent rate constants increase with the specific surface area, pore size and $[OH]_{surface}$. In B1Au and B2Au composites, pores of about 40 Å are predominant, thus the SA molecules may easily get into the composite network, increasing the SA photo-degradation rate.

By comparing the relationship between Au loading and photo-degradation rate constant in the case of B2Au and B4Au composites, one observes that whereas the Au content increase by almost three times, the photo-degradation rate constant increase by 1.35 times. This indicates a non-linear dependence of photo-degradation rate on Au loading on the composites and challenges to new researches in order to establish that this dependence is kept up for Au loadings higher than 0.397%.

The photo-degradation efficiency (Table 1) decreases with the decrease of the adsorption and photo-degradation rate constants and is influenced also by the specific surface area, pore size and $[OH]_{surface}$, which, subsequently, are induced by the Au loading.
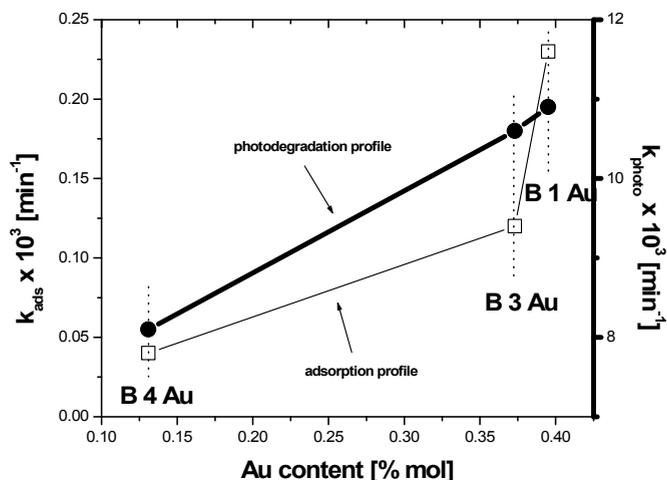
Figure 5. Influence of Au loading on SA adsorption and photo-degradation rate constants (B 1 Au – 0.395% Au, B 3 Au – 0.373% Au, B 4 Au – 0.131% Au)

CONCLUSIONS

Au – TiO_2 composites with different Au loadings were prepared and characterized by nitrogen adsorption-desorption method, TEM microscopy and thermo-gravimetric analyses. Additionally, the OH group's concentration was measured. The catalytic activity of the obtained composites was tested in the SA photo-degradation process.

- The pores size varies inversely proportionate with the Au loading.
- The specific surface area, SA adsorption and photo-degradation rate constants vary proportionate with Au loading.
- The SA adsorption and photo-degradation rates are deeply influenced by the pore size and specific surface area of the Au-TiO_2 composites.

EXPERIMENTAL SECTION

Composites preparation

At first, the TiO_2 gels were prepared by sol-gel method. The TiO_2 sols were obtained by mixing titanium-isopropoxide (IV) (Merck, 99.9%), with anhydrous ethanol (Fluka, 99.8%), ultra pure water and nitric acid reagent (Merck, 65%) as catalyst. The molar ratio of reactants was: $[Ti(OC_3H_7)_4]:[H_2O]:[C_2H_5OH]:[HNO_3] = 1:3.675:21:0.08$.

The transparent TiO_2 gels were kept for 3 days in a gold colloidal solution, obtained by $HAuCl_4$ 10^{-3} M (Merck, 99.8%) reduction with sodium citrate 38,8 x 10^{-3} M (Merck). The colloidal solution volumes used for TiO_2 gel impregnation were between 25-150 ml (Table 1).

The obtained Au – TiO_2 gels were supercritically dried using liquid CO_2 in a SAMDRI – 790 A (Tousimis) dryer (T = 40 ^{0}C and p = 1400 psi). The composite aerogels were transparent, with a violet nuance. The gold contents for the obtained composites are presented in Table 1.

Characterisation Techniques

The surface area and the pore volume of the as-prepared composites were determined by the Brunauer-Emmett-Teller (BET) method. A Sorptomatic, Thermo Electron Corporation system coupled with a Flatron L 1718S computer system was used. The partial pressure range for surface area calculation was $0.05 < P/P_0 < 0.3$. The nitrogen adsorption was carried out at 77 K. Before each measurement, the composites were degassed at p = 0.5 Pa and T = 333 K for 2 h.

A transmission electron microscope (TEM) Jeol JEM 1010 operating at an accelerating voltage of 100 kV was employed to obtain bright field images. Au particle sizes were measured from images using SIS software after calibration. 400 mesh cooper grid covered with a plain carbon film, obtained by vacuum evaporation on freshly cleaved mica, were used to support a drop of ultrasonic dispersed composite powder in distilled water. The TEM images were recorded with a MegaView III CCD camera.

The thermo-gravimetric analyses were performed using a Thermal Analysis System Mettler Toledo with a thermo-gravimetric cell TGA / SDTA 851 (heating rate 5^0C / min, in nitrogen flow) and a thermal analysis cell DSC 822.

The $[OH]_{surface}$ on the TiO_2 aerogels was determined by spectro-photometrical evaluation of the Fe (III) acetyl-acetonate concentration in toluene solution after its partial coupling with $[OH]_{surface}$ (reaction 1) [25].

$$(3-x)(S– OH) + Fe(acac)_3 \rightarrow (S – O)_{3-x}Fe(acac)_x + y(Ti_S – OH) + (3-x)Hacac \quad (1)$$
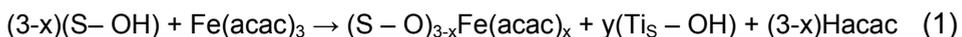
where: S - aerogel surface, Hacac- pentane-2,4-dione, solvent – toluene.

The concentration of gold in all composites was determinated using an FAAS 800 Flame Atomic Adsorption Spectrometer. The sample preparation consists in the chemical treatment with 5 ml of acid mixture (HNO_3 37%: HF = 4:1 volume proportion). The mixture was homogenized and brought to 25 ml volumetric flask with distilled water and than filtered

Catalytic Activity

The adsorption properties and the photocatalytic activity of the Au -TiO_2 composites was established from the adsorption and photo-oxidation rate of salicylic acid used as a standard pollutant molecule [26]. In all adsorption and photo-oxidation processes 0.05 g composite was used. The decrease in

salicylic acid concentration (C_0 = 5.25 x 10^{-4} M for all investigated composites) was monitored by UV-Vis spectroscopy (λ = 297 nm). The composites immersed in salicylic acid solution were irradiated with a medium pressure Hg lamp HBO OSRAM (500 W). A Teflon photochemical cell with quartz window (S = 12 cm^2) and a volume of 8 ml was also used. The distance between the photochemical cell and the lamp was about 30 cm. The working temperature was of 20-22^{0}C and the solution pH was 5.3. Before the UV irradiation as well as before the UV-Vis measurements, the cell with the SA solution and composite was kept in dark for 30 min in order to achieve the equilibrium of the SA adsorption-desorption process [15]. One should emphasize that throughout the photodecomposition process no shift of the UV band located at 297 nm was observed and no other new absorption band occurred.

ACKNOWLEDGMENTS

REFERENCES

1. F.B. Li, X.Z. Li, *Appl. Catal. A: General* , **2002**, *228,* 15.
2. M.R. Hoffmann, S.T. Martin, W.Y. Choi, *Chem. Rev*., **1995**, *95*, 69.
3. A. Linsebigler, G. Lu, J.T. Yates, *Chem. Rev.,* **1995**, *95,* 735.
4. C.Y. Yang, C.Y. Liu, J. Chen, *J. Colloid. Interf. Sci.,* **1997**, *191*, 464.
5. C.Y. Yang, C.Y. Liu, X. Zheng, *Colloid. Surf. A*, **1998**, *131*, 271.
6. A. Sclafani, L. Palmisana, G. Marci, *Sol. En. Mater. Sol C*, **1998**, *51*, 203.
7. J.C. Yang, Y.C. Kim, Y.G. Shul, *Appl. Surf. Sci*., **1997**, *121/122*, 525.
8. W. Choi, A. Termin, M.R. Hoffmann, *J. Phys. Chem.,* **1998**, *98,* 13669.
9. P. Falaras, I.M. Arabatzis, T. Stergiopoulos, M.C. Bernard, *Intern. J. Photoen.,* **2003**, *5*, 123.
10. M.S. Chen, D.W. Goodmann, *Topics in Catal.*, **2007**, *44, 1-2,* 41.
11. A. Kolmakov, D.W. Goodmann, *Catal. Lett.*, **2000**, *70,* 93.
12. X. Chen, S.S. Mao, *Chem. Rev*., **2007**, *107,* 2891.
13. S. Sakthivel, M.C. Hidalgo, D.W. Bahnemann, S-U Geissen, V. Muguresan, A. Vogelpohl, *Appl. Catal. B*, **2006**, *63*, 31.
14. N. Perkas, Z. Zhong, L. Chen, M. Besson, A. Gedanken, *Catal. Lett.*, **2005**, *103*, 9.
15. N. Perkas, D. Minh Pham, P. Gallezot, A. Gedanken, M. Bessot, *Appl. Catal. B,* **2005**, *59*, 121.

16. Z. Kónya, V.F. Puntes, I. Kiricsi, J. Zhu, J.W. Ager, M.K. Ko, H. Frei, P. Alivisatos, G.A. Somorjai, *Chem. Mater*, **2003**, *15*, 1242.

17. M.I. Dominguez, M. Sanchez, M.A. Centeno, M. Montes, J.A. Odriozola, *Appl. Catal. A,* **2006**, *302*, 96.

18. M.A. Centeno, M.C. Hidalgo, M.I. Dominguez, J.A. Navió, J.A. Odriozola, *Catal. Lett.,* **2008**, *123*, 198.

19. S.A. Selim, Ch.A.Philip, S. Hanafi, H.P. Boehm, *J. Mat. Sci.*, **1990**, *25 (11),* 4678.

20. S.M. Ould-Mame, O. Zahraa, M. Bouchy, *Inter. J. Photoen.*, **2000**, *2*, 59.

21. W. Lee, H-S. Shen, K. Dwight, A. Wold, *J. Sol. State Chem.,* **1993**, *106 (2)*, 288.

22. J. Papp, H. S. Shen, R. Kershaw, K. Dwight, and A. Wold, *Chem. Mater.,* **1993**, *5(3)*, 284.

23. N.A. Laoufi, D. Tassalit, F. Bentahar, *Global Nest Journal,* **2008**, *10(3)*, 404.

24. http://www.chemspider.com/331#suppinfo.

25. J.A. Rob van Veen, F.T.G. Veltmaat, G. Jonkers, *J. Chem. Soc.*, *Chem.Commun.*, **1985**, 1656.

26. M. Tomkiewicz, *Catal. Today,* **2000**, *58*, 115.

BIOSORPTION OF PHENOL FROM AQUEOUS SOLUTIONS BY FUNGAL BIOMASS OF *PHANEROCHAETE CHRYSOSPORIUM*

TÍMEA PERNYESZI[a], KRISZTINA HONFI[a], BORBALA BOROS[a], KATALIN TÁLOS[a], FERENC KILÁR[a], CORNELIA MAJDIK[b]

ABSTRACT. The biosorption of phenol from aqueous solution on non-living mycelial pellets of *Phanerochaete chrysosporium* was studied using batch technique with respect to pH, initial concentration and biomass dosage. *Ph. chrysosporium* was grown in a liquid medium with a simple constitution. The phenol biosorption studies on fungal biomass was carried out at an initial pH of 5. Adsorption kinetics was characterized at an initial concentration of 12.5, 25 and 50 mg/L in a suspension concentration of 5.0 g/L. The sorption process followed the second-order kinetics. Phenol adsorption isotherms were determinated on fungal biomass at biomass concentration of 1.0 and 5.0 g/L and initial pH of 5. The adsorption equilibrium of phenol from aqueous solutions by mycelial pellets could be well described with Freundlich equation. The adsorption capacity of phenol and the Freundlich constant decreased with increasing biomass concentration.

Keywords: phenol, biosorption, Phanerochaete chrysosporium biomass, adsorption isotherm, adsorption kinetics, water treatment

INTRODUCTION

Wastewaters containing phenolic compounds present a serious problem. Wastewaters containing phenol cannot be discharged in surface waters without prior treatment due to the phenol toxicity. The toxic and hazardous nature of phenols and their associated derivatives, and their increasing amounts in industrial wastewaters have been documented. They are known human carcinogens. Phenolic compounds are present in the wastewaters generated by paint, solvent, petroleum, coal-conversion, pharmaceutical, wood preserving chemicals, plastic, rubber-proofing, pesticide, iron-steel, paper and pulp industries.

Traditionally, adsorption on activated carbon and polymer based adsorbents is the most widely used technique for the removal of phenols. The high cost of activated carbon and polymer has stimulated interest to use cheaper

[a] *University of Pécs, Faculty of Science, Department of Analytical and Environmetal Chemistry, 6 Ifjúság, H-7624 Pécs, Hungary*
[b] *University Babeş-Bolyai; Faculty of Chemistry and Chemical Engineering, 11 Arany J., RO-400293 Cluj-Napoca, Romania*

raw environmental-friendly materials as adsorbents. Recently, microorganisms have been considered as one of the most promising adsorbents [1-12]. However, information on fungal interacting with toxic phenolic compounds is still limited. In the concept of biosorption, several chemical processes may be involved, such as adsorption, ion exchange, and covalent binding. The biosorptive sites on the microorganisms are carboxyl, hydroxyl, sulphuryl, amino and phosphate groups [4,5]. Fungal cell walls and their components have a major role in biosorption. Aksu and Yener evaluated the biosorption of phenol and monochlorinated phenols on the dried activated sludge [6]. Ning et al. reported that anaerobic biosorption of 2,4-dichlorophenol was mainly a physicochemical process. They studied the equilibrium sorption isotherms and sorption kinetics of 2,4-DCP on live and chemically inactivated anaerobic biomass [7]. Rao and Viraraghavan have used nonviable pretreated cells of *Aspergillus niger* to remove phenol from an aqueous solution, and observed that maximum removal of phenol occurred at an initial pH of 5.1 [8]. Other workers investigated the biosorption capacity of dead and live fungal biomass, and they found, that better removal was achieved with dead fungal biomass than with live one [9-11].

Wu and Yu have used *Phanerochaete chrysosporium* biomass as a sorbent material for removal of phenol and chlorophenols [12,13]. They found that the sorption capacity on mycelial pellets increased in order: phenol < 2-CP < 4-CP < 2,4-CP. The adsorption increased with decreasing water solubility and increasing octanol-water partitioning coefficients. The presence of 2-CP or 4-CP and the initial concentration of 2-CP and 4-CP had no significant effect on the sorption of 2,4-DCP on fungal mycelial pellets. These suggests that partitioning was largely involved in biosorption mechnisms, and that hydrophobicity might govern the biosorption of phenolic compounds by mycelial pellets [4,12,13].

The objectives of this study were:

1. to test the biomass of *Phanerochaete chrysosporium* grown in a medium having simple constitution for phenol biosorption,
2. to evaluate the influences of different experimental parameters on biosorption such as initial pH, sorption time and initial phenol concentration using batch technique,
2. to model phenol biosorption kinetics by mycelial pellets using pseudo-first-order and second-order kinetic equations,
3. to determine adsorption isotherms using batch technique and analyse the adsorption equilibrium using Freundlich-equation,
4. to investigate the effect of biomass concentration on biosorption process.

174

RESULTS AND DISCUSSION

Factors influencing biosorption of phenol by mycelial pellets

Effect of initial pH on phenol biosorption on *Phanerochaete chrysosporium* in aqueous suspension

The effect of initial pH on the equilibrium uptake capacity of phenol by mycelial pellets of *P. chrysosporium* at pH values between 3.0 and 10.0 and 22.5 ± 2 °C is shown in Figure 1. The biosorption of fungi was influenced by pH in a range of 3.0 – 10.0. The initial concentration of phenol was 25 mg/L and the biomass concentration was 0.5 g/L. The maximal adsorbed phenol amount was $q_{max} = 0.073$ mg/g at pH 4. In the natural state of phenol solution, pH 5.0, without pH adjustment, the adsorption was slightly reduced, the adsorbed amount of phenol was 0.065 mg/g. The adsorption was reduced in an alkaline medium and slightly reduces in an acidic medium. The effect of pH on the adsorption of phenol was not significant at pH 3.0 – 6.0, and the uptake of phenol in the same pH interval was larger than that observed at other pH values. Further biosorption experiments were carried out at the natural state of pH 5 in the biomass suspensions.
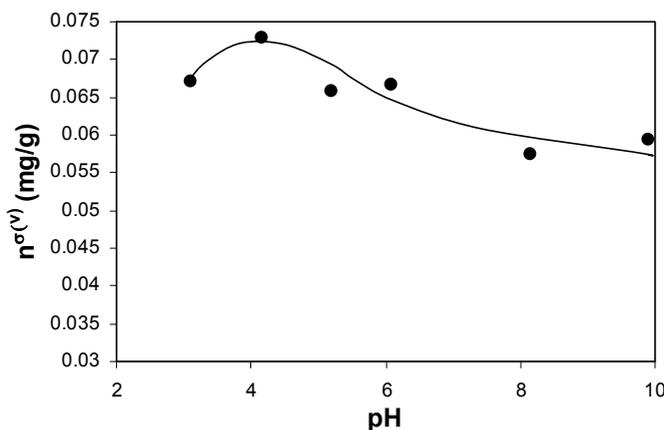
Figure 1. The pH effect over the phenol biosorption on *Phanerochaete chrysosporium* biomass. The biomass concentration is 0.5 g/L and the initial phenol concentration is 25 mg/L.

Phenol is weakly acidic, and pH has a significant effect on the degree of ionization of phenol and the cell surface properties. The amount of adsorbed phenol seemed to be related to the dissociation constant (pK_a), which is 9.9 for phenol [14]. The ionic fraction of phenolate ion increases which increasing pH, and phenol could be expected to become more negatively charged as pH increases. The surface charge on fungal biomass

is predominately negative at pH 3.0 – 10.0 [8, 13]. At pH < 3.0, the overall surface charge on fungal cells become positive. Thus, phenol can be adsorbed to a lesser extent at pH $\geq$ pK$_a$, due to the repulsive forces prevailing at higher pH values. A lower pH value resulted in a higher undissociated fraction of phenol and led to a decrease in phenol uptake by the mycelium pellets.

Adsorption kinetics of phenol on *Phanerochaete chrysosporium* biomass in aqueous suspension

The phenol adsorption kinetics was investigated on the biomass at a suspension concentration of 0.5 g/L. The initial phenol concentrations were of 12.5; 25 and 50 mg/L. In the figure 2 the adsorbed phenol amounts are presented against the adsorption time. The results show that adsorption equilibrium was reached during sixty minutes. The adsorption rate was higher in the first thirty minutes, but decreased until the equilibrium was reached. Similar trends were found by other workers [2, 12, 13, 15]. It should be noticed that the adsorption of phenol increased with an increas of the sorption time.

In the adsorption equilibrium at initial phenol concentration of 12.5 mg/L the maximal adsorbed phenol amount is q_{max} = 0.09 mg/g, at initial phenol concentration of 25.0 mg/L the maximal adsorbed phenol amount is q_{max} = 0.10 mg/g, and at initial phenol concentration of 50.0 mg/L the maximal adsorbed phenol amount is q_{max} = 0.19 mg/g.

To evaluate the biosorption kinetics of phenol, two kinetic models were used to fit the experimental data at different initial concentrations at pH 5.0.
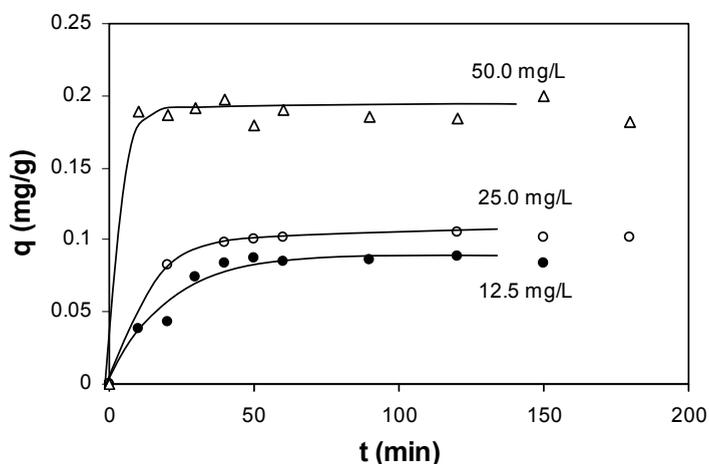
Figure 2. The effect of initial concentration on the sorption kinetics of phenol by mycelial pellets of *Phanerochaete chrysosporium*, initial concentration: 12.5; 25.0; 50.0 mg/L, temperature: 22.5 ^{o}C, biomass concentration: 5 g/L.

Pseud-first-order Lagergren model

The pseudo first-order rate expression of Lagergren model [16] is generally expressed as follows:

$$\frac{dq}{dt} = k_{1,ad}(q_{eq} - q) \tag{2}$$

where,

q_{eq} and q have their usual meanings and

$k_{1,ad}$ is the rate constant of first-order biosorption (min^{-1}).

The integrated form of equation (2) is:

$$\log(q_{eq} - q) = \log q_{eq} - k_{1,ad}\frac{t}{2.303} \tag{3}$$

However, to fit equation (3) to experimental data, the value of q_{eq} (equilibrium sorption capacity) must be pre-estimated by extrapolating the experimental data to t = ∞. In addition, in most cases the first-order rate equation is usually applicable over the initial 30 − 50 minutes of the sorption [13, 17, 18]. The plots of log(q_{eq} − q) as a function of sorption time are shown in Figure 3a. The linear relationships were observed only for the initial 60 minutes of sorption and the experimental data considerably deviated from the theoretical ones (not shown in the figure) after this period. The rate constants $k_{1,ad}$ and theoretical values of q_{eq} calculated from the slope and intercept of the linear plots are summarized in table 1 along with the corresponding correlation coefficients. The first-order rate constants $k_{1,ad}$ and the equilibrium sorption capacities $q_{eq,cal}$ ($q_{eq,cal}$ = 0.103 mg/g for the initial concentration of 12.5 mg/L, $q_{eq,cal}$ = 0.104 mg/g for 50.0 mg/L) have almost the same values for both initial concentration of 12.5 and 25.0 mg/L. In the case of initial concentration of 50.0 mg/L acceptable calculated results were not received using the first-order Lagergren model.

Pseudo- second-order kinetic model

If the sorption rate is second-order, the pseudo second-order kinetic rate equation is expressed as [18]:

$$\frac{dq}{dt} = k_{2,ad}(q_{eq} - q)^2 \tag{4}$$

where,

$k_{2,ad}$ is the rate constant of second-order biosorption (g/mg min) After integration, the following equation is obtained:

$$\frac{t}{q} = \frac{1}{k_{2,ad}q_{eq}^2} + \frac{t}{q_{eq}} \tag{5}$$

It should be noticed that for the utilization of this model, the experimental value of q_{eq} is not necessary to be pre-estimated. By plotting t/q against t for the initial concentrations (12.5, 25.0, 50.0 mg/L), straight lines were obtained as shown in Figure 3b. The second-order rate constants $k_{2,ad}$ and q_{eq} values are presented in table 1 were determined from the slopes and intercepts of the plots. The results show that the second-order rate constants $k_{2,ad}$ increased with an increase in initial phenol concentration. The biosorption of 2,4-dichlorophenol from aqueous solution on non-living pellets of *Phanerochaete chrysosporium* grown by Kirk et al [20] was also studied by Wu and Yu [12,13]. On the basis of their experiments they also found that the biosorption process to biomass followed pseudo second-order kinetics. The pseudo-second-order kinetic constants decreased with an increase in initial concentration for 2,4-dichlorophenol biosorption [13].

The correlation cefficients for the second-order kinetic model were close to 1.0, and the theoretical values of q_{eq} also agreed well with the experimental data. On the other hand, the correlation coefficients for the pseudo-first-order kinetics were lower than those for the pseudo-second-order one. Using pseudo-first-order model the theoretical q_{eq} values did not give reasonable values. This can be explained that the sorption of phenol on mycelial pellets follow the second-order kinetics. The second-order kinetic parameters can be used to determine the equilibrium sorption capacity, percent of the removal of phenol, rate constants and initial sorption rate for a bioreactor design.
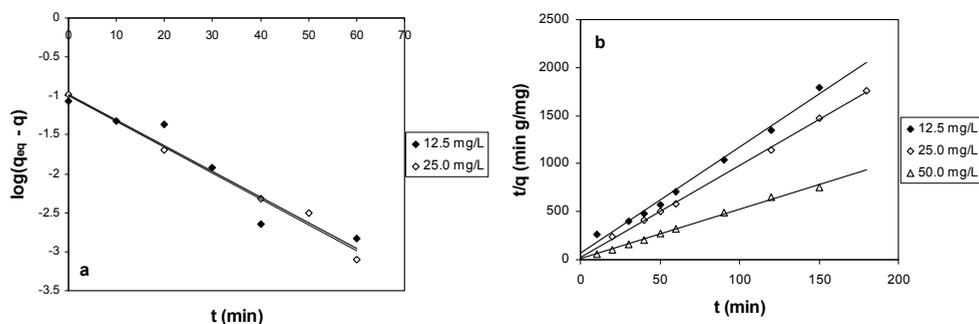
Figure 3. **(a)** Linearized pseudo-first-order kinetic model for phenol by mycelial pellets of *Phanerochaete chrysosporium* at different initial concentrations, initial concentrations: 12.5 and 25.0 mg/L, temperature: 22.5 $^\circ$C, biomass concentration: 5 g/L.
(b) Linearized pseudo-second-order kinetic model for phenol by mycelialpellets of *Phanerochaete chrysosporium* at different initial concentrations, initial concentrations: 12.5, 25.0, 50.0 mg/L, temperature: 22.5 °C, biomass concentration: 5 g/L.

Table 1. The first-order and secon- order adsorption rate constants of phenol for different initial concentrations, at pH 5.0, temperature: 22.5 °C, biomass concentration: 5 g/L

c_0 (mg/L)	k_{1,ad_1} (min^{-1})	$q_{eq,cal}$ (mg/g)	R^2	$k_{2,ad}$ (g/mg min)	$q_{eq,cal}$ (mg/g)	R^2	$q_{eq,exp}$ (mg/g)
12.5	0.076	0.104	0.918	1.861	0.090	0.991	0.086
25.0	0.077	0.103	0.985	3.475	0.105	0.999	0.103
50.0	-	-	-	4.172	0.193	0.997	0.189

Adsorption isotherms of phenol by *Phanerochaete chrysosporium* biomass in aqueous suspension

The biosorption isotherms of phenol by mycelium pellets were evaluated in the initial concentration range of 10 – 100 mg/L by varying biomass dosage. The biomass concentrations were 1.0 and 5.0 g/L. It is observed from Figure 4a that the uptake of phenol by biomass increases with the decrease of the biosorbent dosage and also increases with an increase of the initial concentration of phenol in solution. When suspension concentration was 5 g/L the maximal adsorbed amount was about 0.3 mg/g, while in the suspension of concentration of 1 g/L it was about 0.9 mg/g.

Analysis of equilibrium is important for developing a model that can be used for the design of biosorption systems. Two classical adsorption models, Langmuir and Freundlich isotherms, are mostly frequently employed.

Freundlich isotherm

The Freundlich equation based on sorption on a heterogeneous surface is given below as equation (6):

$$q_{eq} = K_F C_{eq}^{1/n} \qquad (5)$$

where,

K_F and n are the Freundlich constants, which are indicators of adsorption capacity and adsorption intensity of the sorbents [6, 7, 21]. Equation (5) can be linearized in logarithmic form as follows:

$$\log q_{eq} = \log K_F + \frac{1}{n} \log C_{eq} \qquad (6)$$

The values of K_F and n can be estimated respectively from the intercept and slope of a linear plot of experimental data of log q_{eq} versus log C_{eq}.

The linearized Freundlich adsorption isotherms of phenol obtained using different biomass dosages are shown in figure 4.b. The values of K_F and n calculated from the plot are also given in table 2. along with the regression correlation coefficients. The parameter K_F related to the sorption capacity increased with decreasing biomass concentration and thus increasing

maximal adsorbed amount of phenol. In table 2, n is less than unity, indicating that phenol is slightly linearly adsorbed by mycelial pellets in the equilibrated concentration range of $10 - 90$ mg/L at temperature of $22.5\ ^{\circ}$C, and then the monolayer is saturated. Adsorption equilibriums of organic pollutants, such es phenol and chlorophenols, followed the Freundlich isotherm better than the Langmuir one [13, 15, 21].
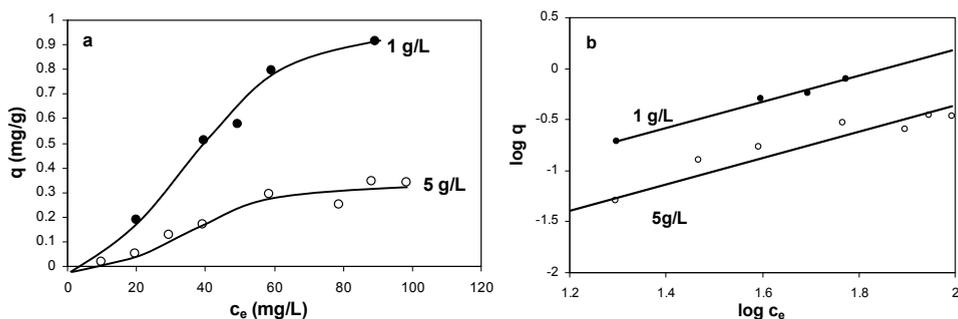
Figure 4. (a) Phenol adsorption isotherms by mycelial pellets of *Phanerochaete chrysosporium* from aqueous solutions at the biomass concentrations of 1 g/L and 5 g/L in the initial concentration range of 10 – 100 mg/L.
(b) Linearized adsorption isotherms of Freundlich.

Table 2. The Freundlich isotherm constants of phenol on micelial pellets in the initial concentration range of $10 -100$ mg/L, at different biomass concentrations, at pH of 5.0

biomass dosage (g/L)	q_{eq} (mg/g)	K_F (mg/g)(mg/L)^n	n	R^2
1.0	0.9	0.004	0.78	0.989
5.0	0.3	0.001	0.76	0.942

CONCLUSIONS

The potential of non-living mycelial pellets of *Phanerochaete chrysosporium* grown in a medium of simple constitution to adsorb phenol molecules from aqueous solution was demonstrated in this study. The sorption capacity increased with an increase in initial phenol concentration and decreased with increasing biomass concentration. The biosorption of phenol by *Ph. chrysosporium* followed pseudo-second-order kinetics. The second-order kinetic constants increased with increasing initial concentration. The Freundlich model exhibited a good fit to the adsorption data of phenol.

In the studied concentration range of 10 – 100 mg/L phenol was adsorbed almost linearly by the fungal biomass and then the monolayer coverage was reached. Increasing biomass concentration, the maximal adsorbed amount of phenol decreased, and thus the calculated Freundlich constant decreased as well.

EXPERIMENTAL SECTION

Microorganism and its growth conditions

Phanerochaete chrysosporium a white-rot fungus, obtained from the Institute of Microbiology, University of Pécs, was maintained by subculturing on potato dextrose agar slants. Hyphal suspensions were prepared from 7-day old cultures, grown on potato dextrose agar slants at $35 \pm 2\,°C$. *Ph. chrysosporium* was grown in a liquid medium containing (g/L) D-glucose, 10.0; KH_2PO_4, 2.0; $MgSO_4·7H_2O$, 0.5; NH_4Cl, 0.12; $CaCl_2·H_2O$, 0.1; thiamine, 0.001. The medium pH was adjusted to 4.5 with 1.0 mol/L HCl and 1.0 mol/L NaOH. The incubation was carried out at $39\,°C$ in an orbital shaker incubator at 150 rpm for 5 days [1].

Preparation of the biosorbent

After 5 days, the mycelial pellets were harvested through filtering. The biomass was then washed thoroughly with distilled water to remove the growth medium adhering on its surface. In order to exclude the possibility of biodegradation of phenol by living mycelia, the mycelial pellets used in the all adsorption experiments were inactivated at $120\,°C$ and 104 kPa for 20 min. The biosorbent used in this study was in the form of mycelium pellets without homogenization. Therefore, term particle size reffers to the diameter of the mycelial pellet.

Chemicals

Phenol (>99 % purity) was purchased from Sigma-Aldrich Ltd (Hungary) and was used without further purification. All other inorganic chemicals were of analytical grade. Stock solutions were prepared by dissolving 0.1 g of phenol in 1.0 L of distilled water. The test solutions containing phenol were prepared by diluting 100 mg/L of stock solutions of phenol to the desired concentrations. The phenol concentrations of prepared solutions varied between 10 – 100 mg/L in the sorption experiments. The pH value of the solutions in this study (2.0 – 11.0) was adjusted to the required value by using NaOH or HCl solutions. All solutions were stored in the dark at $4\,°C$ prior to use.

Batch experiments

Biosorption experiments were carried out in batch mode. The biomass concentration was 5.0 g/L, (0.25 g dry mycelial pellets mixed with 50 mL of solution containing a pre-determined concentration of phenol). Mycelial pellets and phenol solution were placed in a test-tube, which was subsequently

covered to prevent photodegradation. All adsorption experiments were conducted in the dark to avoid formation of photodegradation products. Tubes were agitated on a shaker at 150 rpm and a constant temperature ($22.5 \pm 2\,°C$). Samples were taken at given time intervals, and then centrifuged at 10 000 rpm for 10 min. The supernatant was used for analysis of the residual phenol. The amount of phenol adsorbed at equilibrium, q (mg/g), was obtained as follows:

$$q = \frac{(c_0 - c_e)V}{m} \tag{1}$$

where,

   c_0 and c_e are the initial and equilibrium liquid phase concentrations (mg/L)
   V is the volume of the solution (L) and
   m is the weight of the dry biomass used (g).

Analysis

Phenol concentration in supernatant was determined by HPLC. The HPLC system containes a liquid chromatograph (LC-10 AD$_{VP}$, Shimadzu), a micro vacuum degasser (DGU-14 A, Shimadzu), a system controller (SCL-10 A*VP*, Shimadzu), a diode array detector (SPD-M 10 A*VP,* Shimadzu) and an injector (7725i, Rheodyne). The LCMS solution software was applied on the HPLC system. The measurements were performed on the UV/VIS-photo diode array detector with detection at 270 nm. Chromatographic separations were performed on a Phenomenex C18 column (150×4.6 mm i.d., 5 μm, Phenomenex, USA). For separations the mobile phase A, water and mobile phase B, methanol and gradient system (0.03 min 42 % B eluent, 8.00 min 60 % B eluent, 8.10 min 42 % B eluent and 11.00 min 42 % B eluent) were used. Operating conditions were as follows: flow rate 1.0 mL/min, column temperature ambient and injection volumes 20 μL of the standard and samples. Calibration curve of the standard was made by diluting stock solution of standard in water to yield 10-100 mg/L.

ACKNOWLEDGEMENT

182

REFERENCES

1. M. Iqbal, A. Saeed, *Process Biochemistry*, **2007**, *42*, 1160.

2. N. Calace, E. Nardi, B.M. Petronio, M. Pietronio, M. Pietroletti, *Environ. Pollut*., **2002**, 118(3), 315.

3. G. Bülbül, Z. Aksu, *Turkish J. Eng. Envir. Sci.*, **1997**, *21*, 175.

4. A. Denizli, N. Cihangir, A.Y. Rad, M. Taner, G. Alsancak, *Process Biochemistry*, **2004**, *39*, 2025.

5. H. Volesky, Z.R. Holan, *Biotechnol. Prog*., **1995**, *11*, 239.

6. Z. Aksu, J. Yener, *Process Biochem*., **1998**, *33*, 649.

7. Z. Ning, K.J. Kennedy, L. Fernandes, *Water Res*., **1996**, *30*(9), 2039.

8. I.R. Rao, T. Viraraghavan, *Bioresour. Technol*., **2002**, *85*(2), 165.

9. J.L. Wang, Y. Qian, N. Horan, E. Stentiford, *Bioresourcs Technol*., **2002**, *65*, 165.

10. M. Tsezos, J.P. Bell., *Water Res*. **1989**, *23*, 561.

11. O. Yesilda, K. Fiskin, E. Yesilda, *Envir. Techn*., **1995**, *16*, 95.

12. J. Wu, H-Q. Yu, *Process Biochemistry*, **2006**, *41*, 44.

13. J. Wu, H-Q. Yu, Journal of *Haradous Materials B*., **2006**, *137*, 498.

14. C.G. Silva, J.L.Faria, *J. of Molecular Catalysis*, **2009**, *305*, 147.

15. P. Benoit, E. Barriuso, R. Calvet, *Chemosphere*, **1998**, *37*(7), 1271.

16. S. Lagergren, Zur theorie der sogenannten adsorption geloster stoffe: Kungliga Svenska vetenskapsakademiens, *Handlingar* **1998**, *24*, 1.

17. D. Batabyal, A. Sabu, S.K. Chaudhuri, *Separations Technol.*, **1995**, *5(4),* 179.

18. Z. Aksu, S. Tezer, *Process Biochemistry*, **2000**, *36(5),* 431.

19. G. Mckay, Y.S. Ho, *Process Biochem.*, **1999**, *34*, 451.

20. T.K. Kirk, E. Schultz,cW.J. Connors, *Arch Microbiol*., **1978**, *117*, 227.

21. B. Antizar-Ladislao, N.J. Galil, *Water Res*., **2004**, *38(2),* 267.

ISOCONVERSIONAL LINEAR INTEGRAL KINETICS OF THE NON-ISOTHERMAL EVAPORATION OF 4-[(4-chlorobenzyl)oxy]-4'-trifluoromethyl-azobenzene

ANDREI ROTARU[a]**, MIHAI GOŞA**[b,c]**, EUGEN SEGAL**[d]

ABSTRACT. The activation energy of the linear non-isothermal evaporation of 4-[(4-chlorobenzyl)oxy]-4'-trifluoromethyl-azobenzene has been determined by various linear integral isoconversional methods. Activation energy may be evaluated using several isoconversional methods as the well-known Tang *et al.* method, Generalized KAS method, but also by means of two so-called "local linear integral" (Tang & Chen) and "average linear integral" (Ortega) isoconversional methods. A comparison study has been carried out in order to understand how the activation energy values are affected when using different approaches.

Keywords: azomonoether dyes, non-isothermal kinetics, linear integral, local linear integral and average linear integral isoconversional methods.

INTRODUCTION

Dyes from the category of azoic aromatics have been intensively studied since they are of large interest from the point of view of possible applications [1-4]. Thermal characterizations and stability studies are usually required before choosing them to be part of composite materials, moreover since they are used in thermal-controlled devices. Kinetic studies are required for predicting their behaviour in other conditions than in those that are accessible for normal runs [5-9].

This paper aims to present a isoconversional kinetic study of the linear non-isothermal evaporation of 4-[(4-chlorobenzyl)oxy]-4'-trifluoromethyl-azobenzene liquid crystal that has been previously investigated [7] only by KAS (Kissinger-Akahira-Sunose) [10,11] and FWO (Flynn-Wall-Ozawa) [12,13]

[a] *INFLPR – National Institute for Laser, Plasma and Radiation Physics, Laser Department, Bvd. Atomistilor, Nr. 409, PO Box MG-16, RO-077125 Magurele, Bucharest, Romania, andrei.rotaru@inflpr.ro*

[b] *University of Craiova, Faculty of Automatics, Computers and Electronics, Bvd. Decebal, Nr. 107, Craiova, Romania*

[c] *KineTAx, Str. Ştefan cel Mare, nr. 3, bl. L, sc. B, ap. 1, 200137 Craiova, Romania, mihai.gosa@kinetax.com*

[d] *University of Bucharest, Faculty of Chemistry, Bvd. Regina Elisabeta Nr. 4-12, Bucharest, Romania, esegal@gw-chimie.math.unibuc.ro*

isoconversional methods. Since for our early papers we have used regular calculations, we were able to report results only for a few methods and conversions. The new software package TKS-SP [14,15] for kinetic analysis allows the rapid evaluation of the activation energy by means of isoconversional methods (integral and differential), as well as by other more complex procedures.

With the increasing number of papers dealing with the approximation of the temperature integral, its evaluation improved [16-22] and led to the general opinion that other methods should be used instead of those consecrated ones [10-13]. The method of Tang *et al.* [16] and the generalized KAS [17, 18] methods have been used here, together with the new "local linear isoconversional" of Tang & Chen [19] and "average linear integral"of Ortega [20] methods as well.

RESULTS AND DISCUSSION

Thermal behaviour of 4-[(4-chlorobenzyl)oxy]-4'-trifluoromethyl-azobenzene was investigated in a previous paper [7], together with a couple of other liquid crystals from the same category of aromatic azomonoethers. Before evaporating in the temperature range of 190-310 ^{o}C (endothermic effect), at 155 ^{o}C the compound melts. The FTIR spectrum of the evolved gases perfectly matches to the FTIR spectrum of the solid compound. No influence of the gas atmosphere (air or inert flow) was found.

The complexity of a physical or chemical process can be expressed from the activation energy dependence on the conversion degree. Usually, "model-free" kinetic methods are the most popular. Such applications require the use of isoconversional methods for the evaluation of the activation energy.

1) Regular linear integral methods (Tang et al. and Generalized KAS)
Here we made use of several isoconversional methods: The methods of Tang *et al.* [16] (very close to KAS method) and Generalized KAS [17,18]; are the isoconversional integral linear ones, based on the following integral form of the reaction rate:

$$g(\alpha) = \int_{0}^{\alpha} \frac{d\alpha}{f(\alpha)} = \frac{A}{\beta} \int_{0}^{T_\alpha} e^{-\frac{E}{RT}} dT = \frac{A}{\beta} I(E_\alpha, T_\alpha) \qquad (1)$$

where β is the heating rate, R is the universal gas constant, $g(\alpha)$ is the integral conversion function and $I(E_\alpha, T_\alpha)$ represents the temperature integral. Substitution of $I(E_\alpha, T_\alpha)$ in the equation (1) by various approximation mathematical expressions, provides various equations – therefore a multitude of isoconversional methods.

In the case of Tang *et al.* method [16], for *α=const.*, the plot *ln(β/T^1.894661)* *vs. (1/T)*, obtained from the experimental thermogravimetric curves recorded for several constant-heating rates, should be a straight line whose slope could be used for the activation energy evaluation (E [kJ·mol^{-1}]= – slope·R/1001.45033). In the case of Generalized KAS method [17,18], for *α=const.*, several plots of *ln(β/T^{n+m}) vs. (1/T)*, obtained from the experimental thermogravimetric curves recorded for several constant-heating rates, should gave straight lines whose slopes could be used for the activation energy evaluation (E [kJ·mol^{-1}]= – slope·R/1000). For KAS method, n=2, m=0.

Figure 1 shows the kinetic results of the non-isothermal evaporation of the investigated compound, obtained using Tang *et al.* and Generalized KAS (m=0.5, 1 and 2) methods, as values of the activation energy for various conversion degrees from 0.2 to 0.9 with a step of 0.01, using TKS software (SP 1.0 and SP2.0) [14,15].
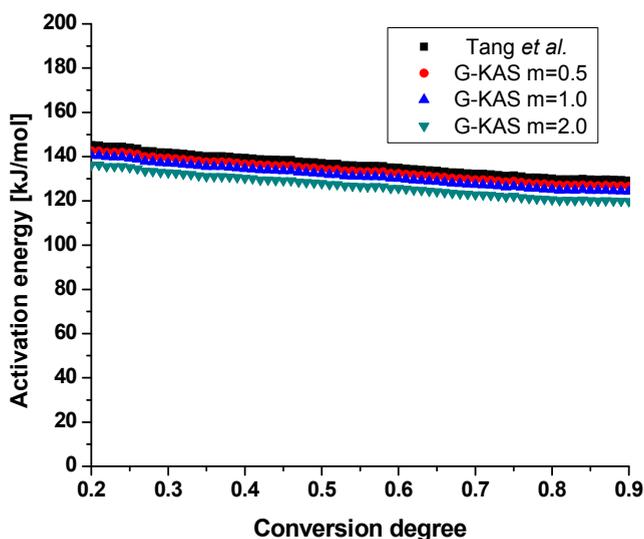
Figure 1. Isoconversional activation energy of the non-isothermal evaporation of 4-[(4-chlorobenzyl)oxy]-4'-trifluoromethyl-azobenzene (by Tang *et al.* and G-KAS methods)

All employed regular linear integral isoconversional methods exhibit a similar trend of the activation energy; for all of them, the activation energy decreases with about 10% in the conversion range of 0.2-0.9. Table 1 contains a statistic of the activation energy values:

Table 1. Statistics of the activation energy values by means of
regular linear integral isoconversional methods

Method	Max. activation energy kJ/mol	Min. activation energy kJ/mol	Average activation energy kJ/mol
Tang *et al.*	145.2	129.3	136.2±4.8
G-KAS (m=0.5)	142.7	126.5	133.5±4.9
G-KAS (m=1.0)	140.6	124.3	131.3±4.9
G-KAS (m=2.0)	136.3	119.7	126.9±5.0

The differences between the results of the employed methods are due to the exponents (*n* and *m*) of the temperature that are used. With increasing the temperature exponent, the activation energy decreases, but the shape of the isoconversional evaluation remains the same. Although the absolute value is not determined, its trend is the same.

Figure 2. Correlation coefficients for the isoconversional activation energy of the non-isothermal evaporation of 4-[(4-chlorobenzyl)oxy]-4'-trifluoromethyl-azobenzene (by Tang *et al.* and G-KAS methods)

During the evaporation process, the activation energy may be however considered to remain practically constant; the accuracy in determining the activation energy is very high – correlation coefficients over 0.99650 (Figure 2). Since this compound is a liquid crystal, it may be used in specific devices; knowing the dependence of the activation energy behaviour with the consumption of the

evaporation, it may help manufacturers when designing their products and establish the limits the devices may be used. It can be easily noticed that with increasing value of the temperature's exponent *m*, the activation energy is evaluated with higher accuracy.

2) Local linear (Tang & Chen) and Average linear (Ortega) integral isoconversional methods

In 2005 Tang & Chen [19] have proposed an integral isoconversional procedure that they have called "local linear" method. This method is basically the linear version of Vyazovkin's "advanced integral isoconversional" method [21], called by Tang & Chen: "modified integral non-linear isoconversional procedure".

Equation 2 was derived by the authors and used for Δα→0; however it was concluded that integration over very small segments provides activation energy values close to those obtained using Friedmann [23] method.

$$ln\frac{\beta\,[\,1/(1+\alpha\,)]}{T_{\alpha+\Delta\alpha}-T_{\alpha-\Delta\alpha}}=ln\,A_{\alpha}-ln[\,g(\alpha+\Delta\alpha\,)-g(\alpha-\Delta\alpha\,)]-\frac{E}{RT_{\alpha}}\qquad(2)$$

For very small intervals of conversion, this method is no more an integral one, but rather a differential isoconversional method. Here we made use of Δα=0.2, which is quite a high value, therefore the method being no more a differential one (Figure 3).
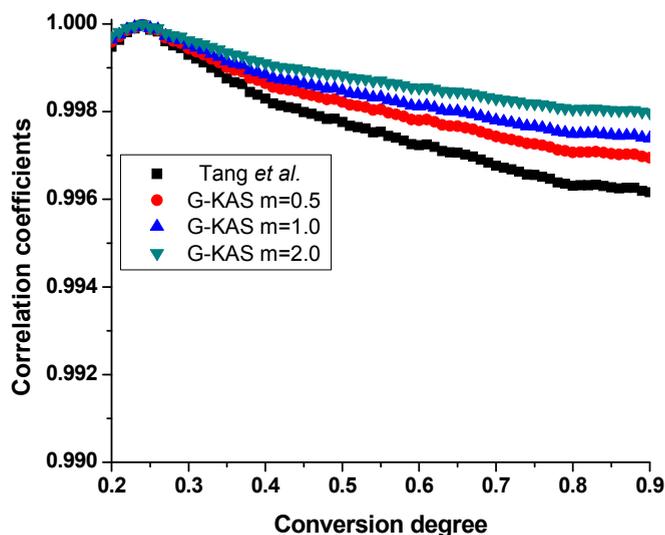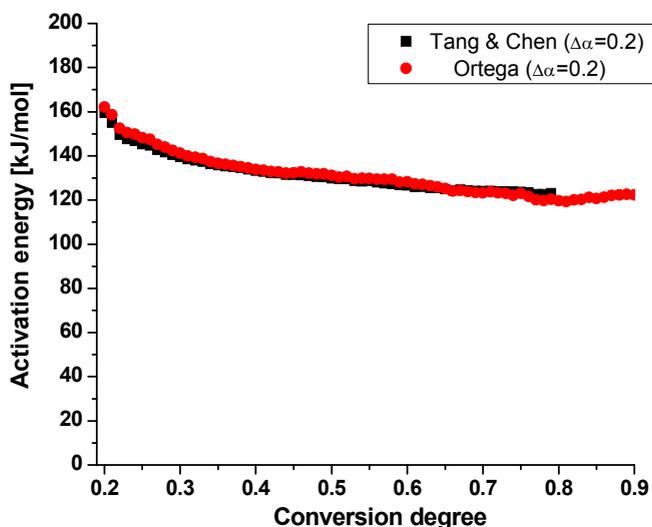

Figure 3. Isoconversional activation energy of the non-isothermal evaporation of 4-[(4-chlorobenzyl)oxy]-4'-trifluoromethyl-azobenzene (by Tang&Chen and Ortega methods)

The same judgement was used when applying Ortega [20] method (recently published in 2008). Ortega method, or Average linear (Ortega) integral isoconversional method uses equation 3. This method takes into account the history of the process as well.

$$ln\frac{\beta}{T_{\alpha} - T_{\alpha - \Delta\alpha}} = ln\,A_{\alpha} - ln[\,g(\alpha + \Delta\alpha\,) - g(\alpha - \Delta\alpha\,)] - \frac{E}{RT_{\alpha}} \qquad (3)$$

From Figure 3 it can be seen that these two methods provide similar results.

Even if the correlation coefficients (Figure 4) are higher for Tang & Chen method, Ortega method permits the evaluation until a higher conversion degree.
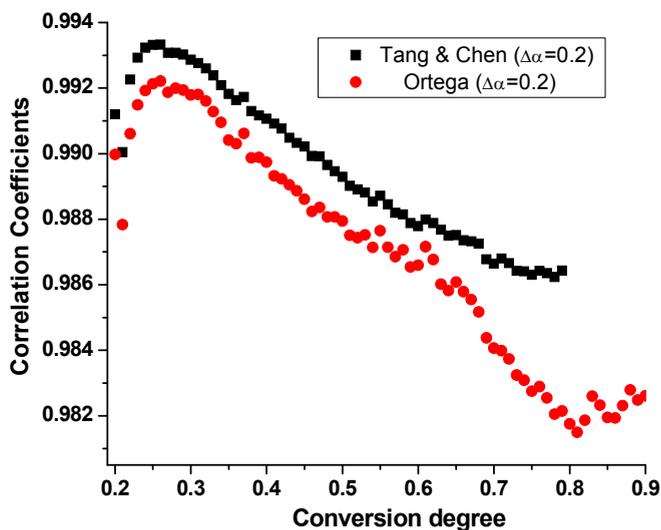
Figure 4. Correlation coefficients for the isoconversional activation energy of the non-isothermal evaporation of 4-[(4-chlorobenzyl)oxy]-4'-trifluoromethyl-azobenzene (by Tang&Chen and Ortega methods)

These two methods that strongly depend on the history and future of the process, provide in this case however similar results to the results of regular isoconversional ones. In the conversion degree range of 0.25-0.75, for Tang & Chen method the activation energy decreases from 145 to 123 kJ·mol^{-1}, while in the conversion degree range of 0.25-0.75, for Ortega method the activation energy decreases from 148 to 120 kJ·mol^{-1}.

CONCLUSIONS

The non-isothermal evaporation of 4-[(4-chlorobenzyl)oxy]-4'-trifluoromethyl-azobenzene has been investigated by several isoconversional methods; regular integral methods provided different, but symmetric trends of the isoconversional activation energy, that are strongly dependent on the temperature exponents (n and m). New methods like Tang & Chen and Ortega methods have been derived by using two other concepts and have to be still used until they will be completely understood. An imposed range of conversion confidence $\Delta\alpha=0.2$ should overcome the problem of differential approach; however, these methods induce a higher inaccuracy in the evaluation of activation energy. It is not clear how this $\Delta\alpha$ interval should be chosen, but it is obvious that the same value of it provides the same activation energy values for both methods.

EXPERIMENTAL SECTION

Aromatic azomonoethers were obtained by the condensation of some(phenyl-azo)phenols with chloromethylated derivatives of chlorobenzene in alkaline medium (Williamson ether synthesis) [24]. Thermal stability (TG, DTG and DSC) measurements of 4-[(4-chlorobenzyl)oxy]-4'-trifluoromethyl-azobenzene were carried out in air flow (150 mL·min^{-1}) in a horizontal Diamond Differential/Thermogravimetric Analyzer from Perkin-Elmer Instruments [7]. Samples from 0.8 to 1 mg, contained in Al_2O_3 crucibles, were heated from room temperature to 800 ^{o}C, with the heating rates of: 2, 4, 6 and 8 K·min^{-1}.

REFERENCES

1. A. Rotaru, C. Constantinescu, P. Rotaru, A. Moanta, M. Dumitru, M. Socaciu, M. Dinescu, E. Segal, *J. Therm. Anal. Cal.*, **2008**, *92*, 279.

2. T.-Y. Chao, H.-L. Chang, W.-C. Su, J.-Y. Wu, R.-J. Jeng, *Dyes Pigments*, **2008**, *77*, 515.

3. H. Dincalp, F. Toker, J. Durucasu, N. Avcibasi, S. Icli, *Dyes Pigments*, **2007**, *75*, 11.

4. M. Gűr, H. Kocaokutgen, M. Taş, *Dyes Pigments*, **2007**, *72*, 101.

5. A. Rotaru, A. Moanţă, I. Sălăgeanu, P. Budrugeac, E. Segal, *J. Therm. Anal. Cal.*, **2007**, *87*, 395.

6. A. Rotaru, B. Jurca, A. Moanta, I. Salageanu, E. Segal, *Rev. Roum. Chim.*, **2006**, *51*, 373.

7. A. Rotaru, A. Kropidłowska, A. Moanţă, P. Rotaru, E. Segal, *J. Therm. Anal. Cal.*, **2008**, *92,* 233.

8. A. Rotaru, A. Moanta, P. Rotaru, E. Segal, *J. Therm. Anal. Cal.*, **2009**, *95*, 161.

9. A. Rotaru, G. Bratulescu, P. Rotaru, *Thermochim. Acta*, **2009**, *489*, 63.

10. H. E. Kissinger, *Anal. Chem.*, **1957**, *29*, 1702.

11. T. Akahira, T. Sunose, *Res. Report Chiba Inst. Technol*., **1971**, *16*, 22.

12. J. H. Flynn, L. A. Wall, *J. Res. Natl. Bur. Stand., A. Phys. Chem.*, **1966**, *70*, 487.

13. T. Ozawa, *Bull. Chem. Soc. Jpn.*, **1965**, *38*, 1881.

14. A. Rotaru, M. Gosa, P. Rotaru, *J. Therm. Anal. Cal.*, **2008**, *94*, 367.

15. A. Rotaru, M. Gosa, *J. Therm. Anal. Cal.*, **2009**, *96*, x.

16. W. Tang, Y. Liu, H. Zhang, C. Wang, *Thermochim. Acta*, **2003**, *408*, 39.

17. H. X. Chen, N. A. Liu, *J. Therm. Anal. Cal.*, **2007**, *90*, 449.

18. H. X. Chen, N. A. Liu, *J. Therm. Anal. Cal.*, **2008**, *92*, 573.

19. W. Tang, D. Chen, *Thermochim. Acta*, **2005**, *433*, 72.

20. A. Ortega, *Thermochim. Acta*, **2008**, *474*, 81.

21. S. Vyazovkin, *J. Comput. Chem.*, **2001**, 22, 178.

22. P. Budrugeac, *J. Therm. Anal. Cal.*, **2002**, *68*, 131.

23. H. L. Friedmann, *J. Polym. Sci. C*, **1963**, *6*, 183.

24. S. Radu, C. Sarpe-Tudoran, A. Jianu, G. Rau, *Rev. Roumaine. Chim.*, **1998**, *43*, 735

OVERALL KINETICS FOR THE CATALYTIC IGNITION OF ETHANE-AIR MIXTURES ON PLATINUM

OCTAVIAN STAICU[a], VALENTIN MUNTEANU[a], DUMITRU OANCEA[a]

ABSTRACT. The overall kinetics of the catalytic ignition of a stoichiometric ethane/air mixture on an isothermally heated platinum wire is studied. The isothermal regime, achieved in an original experimental set-up, allows the direct measurement of the reaction rate in various operational conditions and the determination of the overall activation energy and reaction order on the basis of a previously reported kinetic model. The results are discussed and compared with other data obtained using different experimental techniques and models.

Keywords: catalytic combustion, ignition, ethane/air mixture, isothermal, kinetics

INTRODUCTION

The catalytic combustion of alkanes represents one of the most important ways to reduce the pollutant emissions which unavoidably accompany the conversion of chemical energy stored in fuels into other forms of energy. The high temperature combustion of alkanes in air, within the specific flammable ranges, between the lower flammability limit and the stoichiometric concentration, promotes the NO_x formation with unwanted consequences on the environment. The heterogeneous catalytic combustion of the same fuels, occurring at much lower temperatures, leads to a drastic reduction of NO_x formation. Moreover, the catalytic combustion on solid catalysts allows the process to occur for fuel concentrations much lower than the lower flammability limits. The catalytic combustion has consequently a valuable potential in many applications like the radiant heaters, catalytic combustors for power production, removal of hazardous air pollutants etc. [1]. The phenomenological description of this process advanced considerably during the last decades. Less information is available for the kinetics and mechanism of the interconnected steps including mass and heat transport, fluid flow and heterogeneous chemical reactions [2]. Additionally, at higher temperatures, the simultaneous homogeneous combustion induced by

---

[a] *Department of Physical Chemistry, University of Bucharest, 4-12 Bd. Elisabeta, 030018 Bucharest, Romania, doan@gw-chimie.math.unibuc.ro*

the heterogeneous catalytic reaction plays a significant role. One of the most known difficulties associated with the kinetic studies of the combustion reactions is related to its exothermicity, which leads to catalyst heating at temperatures significantly higher than the surrounding fluid. The catalyst heating can be diminished either by working at very low reactant concentrations or at very high fluid recirculation rate. Both procedures add new difficulties for these studies. This well-known phenomenon can explain the differences reported by various researchers. For platinum wires, frequently utilized in kinetic studies [3-5], we recently described an efficient method able to maintain a constant temperature during the catalytic reaction of different fuel/air mixtures [7-10]. The results obtained for *n*-butane/air, *iso*-butane/air and propane/air mixtures demonstrated the potentialities of the proposed method. A similar analysis is presented in this paper for the stoichiometric ethane/air mixture. A quasi-step temperature perturbation of a platinum catalytic wire immersed in a fuel/air mixture is applied and the corresponding reaction heat flow rate, $dQ_r/dt = F_r$, is measured in time until the process becomes stationary. The heterogeneous catalytic reaction exhibits an induction period, τ_i, which can be measured as a function of wire temperature, T_w, total pressure, p_0 and gas composition. The analytical form of this dependence, $\tau_i = f(T_w, p_0)$, allows the determination of the overall kinetic parameters through linear regression analysis [10].

RESULTS AND DISCUSSION

The experimentally recorded reaction heat flow rate, F_r, as a function of time can be easily converted in the more relevant catalytic reaction rate, r_R, in time through:

$$r_R = (dQ_r/dt)\big/(\Delta^c H_T^0 \cdot S) \tag{1}$$

where $\Delta^c H_T^0$ is the standard heat of combustion at the wire temperature, and S is the surface of the platinum wire ($\Delta^c H_T^0 = \Delta^c H_{298}^0 = 1{,}428.61$ kJ/mole and $S = 1.41 \times 10^{-5}$ m^2). A typical result is given in Figure 1.

Two properties are available from such a plot: the length of the induction period, τ_i, and the diffusion controlled reaction heat flow rate, F_r, or the corresponding reaction rate, r_R. These properties were measured for the stoichiometric ethane-air mixture at various wire temperatures and gas pressures. Their physical significances were discussed in several previous papers. The induction period is given by [10]:

$$\tau_i = \beta \cdot (p_0/p^*)^{-n} \cdot e^{E_a/RT_w} \tag{2}$$

where β is a proportionality constant including the pre-exponential factor and a critical amount, ΔC^*, of a reactant required to initiate the ignition ($r_R = \Delta C^*/\Delta t = \Delta C^*/\tau_i$), p^* is the standard pressure (≈ 101 kPa), n and E_a are the overall reaction order and activation energy, respectively, and R is the universal gas constant.

On the other hand, the diffusion controlled reaction heat flow rate can be rationalized according to an Arrhenius type equation [8]:

$$dQ_r/dt = F_r = A_0 \cdot (p_0/p^*)^n \cdot e^{-E_a/RT_w} \tag{3}$$
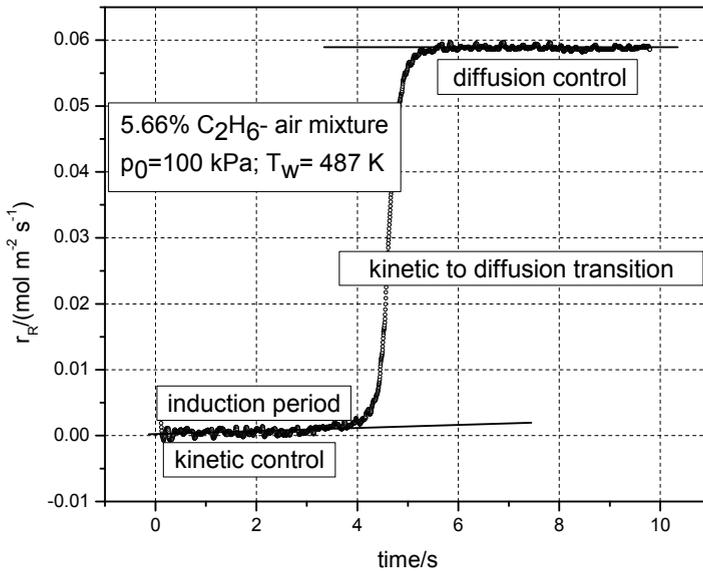
Figure 1. Variation of the surface reaction rate in time indicating the existence of an induction period and of the transition from kinetic to diffusion control

Equations (2) and (3) are used to evaluate the parameters n and E_a. It can be observed that equation (2) refers to the kinetic control, while equation (3) refers to the diffusion control.

Activation energy evaluation. A typical plot for the kinetic control is given in Figure 2 resulted from the linear regression $\ln(\tau_i)$ versus $1/T_w$ of equation (2) at constant pressure. Similar plots, $\ln(F_r)$ versus $1/T_w$, were obtained also for the diffusion control from equation (3) at constant pressure.

Table 1. Kinetic and diffusion overall activation energies

p_0/kPa	E_a/(kJ/mol) $\ln(\tau_i)$ vs $1/T_w$	E_a/(kJ/mol) $\ln(F_r)$ vs $1/T_w$
100	97.6 ± 3.2	11.5 ± 0.35
70	84.9 ± 8.5	11.54 ± 0.01
50	87.1±3.1	10.71 ± 0.37
30	74.4 ± 6.2	10.61 ± 0.36
10	75.6 ± 11.5	9.08 ± 2.43
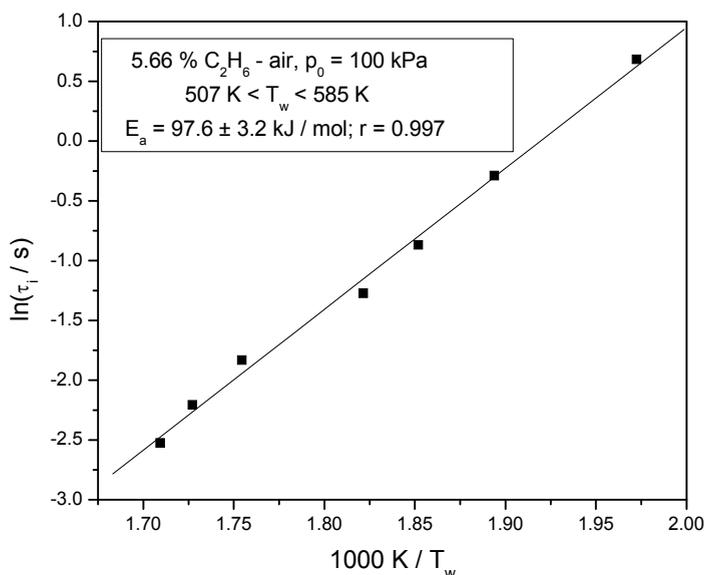
Figure 2. Evaluation of the overall activation energy for the kinetic control

The results obtained at various initial pressures for both kinetic and diffusion controls are given in Table 1. Within the limits of experimental errors no significant variation of activation energies can be detected using this method. The activation energies for the kinetic control are in good agreement with other data reported in literature: 114 kJ/mol on platinum wire from ignition temperature measurements [11], or on platinum foil in a recirculating batch reactor with mass spectrometry detection [12]; 95 kJ/mol on platinum foil in a stagnation point flow [13]; 57 kJ/mol on platinum wire from ignition temperature measurements [14]; 109 kJ/mol on platinum wires in a flow reactor [15]. When the reaction occurs on platinum dispersed on different supports the activation energy varies from 29.7 to 143 kJ/mol [16].

The activation energies for the diffusion control are within the limits accepted for these reactions.

Reaction rate and related properties evaluation. The measurement of the reaction rate for the diffusion regime offers the possibility to compare the experimental results with several relevant properties like the turnover frequency, *TOF*, the collision frequency of fuel molecules with the catalytic surface, v_F and the ratio r_R/v_F. The turnover frequency was calculated as $TOF=r_R/\Gamma_{Pt}$, using the literature data for the atomic surface density of platinum exposed atoms ($\Gamma_{Pt}=2.49 \times 10^{-5}$ mol m^{-2} [12]). The collision frequency of fuel molecules with the catalytic surface was calculated for the stoichiometric ethane-air mixture as [8]:

$$v_F = p_F \big/ (2\pi M_F RT_w)^{1/2} \qquad (4)$$

where p_F is the partial pressure of the fuel and M_F its molar mass.

The results are given in Table 2.

Table 2. Reaction rates and associated properties for diffusion control at T_w = 549 K

p_0 kPa	r_R (mol m^{-2} s^{-1})	$10^{-3} \times TOF$ (s^{-1})	v_F (mol m^{-2} s^{-1})	$10^4 \times (r_R/v_F)$
100	0.0765	3.07	193	3.96
70	0.0720	2.89	135	5.33
50	0.0660	2.65	96.5	6.84
30	0.0591	2.37	57.9	10.2
10	0.0348	1.40	19.3	18.0

The *TOF* values are very large compared with other literature data [8, 10]. A possible explanation is based on the observation that the platinum wire exhibits significant catalytic activity only after heating at temperatures higher than 800 K, when the initially smooth surface becomes coarse with an increased atomic surface density. The ratio r_R/v_F has very low values, (4-18) $\times 10^{-4}$, indicating a reduced efficiency of fuel collisions with the catalyst surface. If these values are corrected for the activation energy factor (of the order 9.6×10^{-2}), very small sticking coefficients are obtained. The data given in Table 2 indicate that the method and the measurements give realistic results for a typical heterogeneous catalytic reaction of combustion.

Reaction order evaluation. The measurements at constant temperature of the reaction heat flow rates for a diffusion controlled process and of the induction periods for a kinetically controlled process can be used to evaluate the overall reaction orders using the linear regression analysis of equations (3) and (2). The results are given in Table 3. It can be observed that the overall reaction orders have an approximately constant value of 0.34, without a significant trend. These figures are in agreement with the frequently reported

order $n_F=1$ for alkane-air catalytic combustion and with the recognized inhibitory effect of oxygen in these reactions ($n_{ox}<0$), giving $n=n_F+n_{ox}<1$. The inhibitory effect of oxygen in alkane-air catalytic combustion has been attributed to its preferential adsorption on platinum surface, even at lower temperatures. The fraction of catalyst surface available for fuel adsorption is consequently very small, lowering the reaction rate for a mechanism of competitive adsorption of fuel and oxygen.

Table 3. Overall reaction orders, n, at different temperatures

T_w/K	$\ln(\tau_i)$ vs $\ln(p_0/p^*)$	$\ln(F_r)$ vs $\ln(p_0/p^*)$
564	0.25 ± 0.05	0.31 ± 0.04
549	0.35 ± 0.03	0.34 ± 0.04
534	0.36 ± 0.04	0.37 ± 0.04
525	0.39 ± 0.02	0.33 ± 0.01

Critical ignition temperatures measurement and analysis. Many kinetic studies concerning the catalytic combustion of fuel-air mixtures rely upon the ignition temperature measurement for different fuel content. Starting from the assumption that the ignition is triggered when the catalyst temperature attains a critical value which ensures the transition from the kinetic control to the diffusion control, a simple relationship was proposed, allowing the evaluation of the activation energy [11]:

$$C_F\big/(T_{ign}-T_0)^2 = \alpha_1 \cdot e^{E_a/RT_{ign}} \qquad (5)$$

where C_F is the bulk concentration of reactant and α_1 is a proportionality constant.
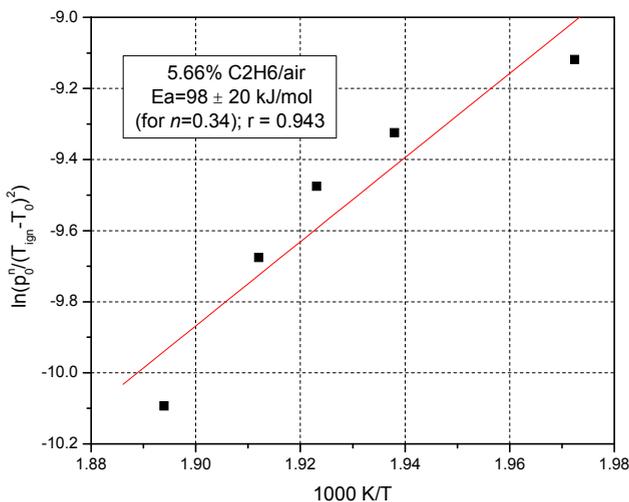
Figure 3. Evaluation of activation energy according to equation (7)

198

It was also assumed that the surface reaction is of first order in hydrocarbon and zero order in oxygen concentration (for large excess of oxygen). This relationship has been subsequently generalized [2] for a *n* order reaction in the form:

$$C_F^n \big/ (T_{ign} - T_0)^2 = \alpha_1 \cdot e^{E_a/RT_{ign}} \tag{6}$$

Since our experimental technique allows the measurement of the ignition temperature at various total pressures, we recently proposed an alternative procedure for the determination of the activation energy [10] as long as $C_F^n \propto p_0^n$ for constant T_0 and fuel molar fraction:

$$p_0^n \big/ (T_{ign} - T_0)^2 = \alpha_2 \cdot e^{E_a/RT_{ign}} \tag{7}$$

where α_2 is a proportionality constant.

A representative result is given in Figure 3. The measured activation energy is in good agreement with the results given in Table 1 for the kinetically controlled process.

CONCLUSIONS

The catalytic combustion of the stoichiometric ethane-air mixture on a platinum wire heated in isothermal conditions allows a deeper understanding of the kinetics of this heterogeneous reaction. Since the wire temperature is constant during the ignition and subsequent combustion, the self-acceleration of the reaction rate cannot be explained on the basis of the thermal ignition, which assumes a continuous increase of the catalyst temperature. From the measurement of the induction periods of the catalytic ignition at various temperatures and total pressures, the overall kinetic parameters – activation energy and reaction order – can be evaluated. The obtained results are in good agreement with those obtained using other experimental approaches. The analysis of the ignition temperature variation with the total pressure using a new model allows an alternative method for the determination of activation energy. All these results validate the proposed method and recommend it as a valuable alternative for kinetic studies concerning the heterogeneous catalytic combustion reactions.

EXPERIMENTAL SECTION

The experimental measurements were carried out using the equipment and procedure described in details previously [7-10] and given schematically in Figure 4. A platinum wire of 0.1 mm diameter and 45 mm length (99.99% from Aldrich), connected through brass conductors in a heating circuit, is immersed in the center of a cylindrical test cell of 9 cm diameter and height, containing either air or fuel/air mixture at a prescribed pressure. It is heated according to a quasi-rectangular profile, with a rise time of 1 – 2 ms using the discharge of a capacitor C followed by a controlled feeding system designed to maintain a constant wire temperature. A standard resistor R_{std}, connected in series with the wire of resistance R_w, forms a Wheatstone bridge with the potentiometer P and allows the measurement of the input power, recording the variation of the voltage drop U_{std} during the test. Any unbalance of the bridge is detected by the integrated circuit IC which readjusts the voltage applied across R_w through the series transistor T in order to maintain its resistance constant. The diagram U_{std} versus time contains the information necessary for the kinetic study. To evaluate the heat flow rate dQ_r/dt due to the catalytic reaction occurring on the wire it is necessary to eliminate the power dissipated through the heat transfer from the hot wire to the surroundings.

The kinetically relevant quantity dQ_r/dt can be obtained from the diagrams recorded in air and in a fuel/air mixture in similar conditions as:

$$dQ_r/dt = (R_w/R_{std}^2)\left[(U_{std}^2)_{air} - (U_{std}^2)_{mixture}\right] \tag{8}$$
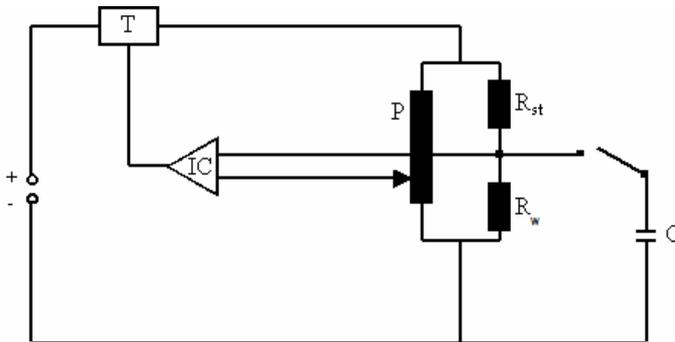
Figure 4. Schematic representation of the electrical circuit able to heat the platinum wire according to a quasi-rectangular profile

A typical recording of U_{std} is given in Figure 5.
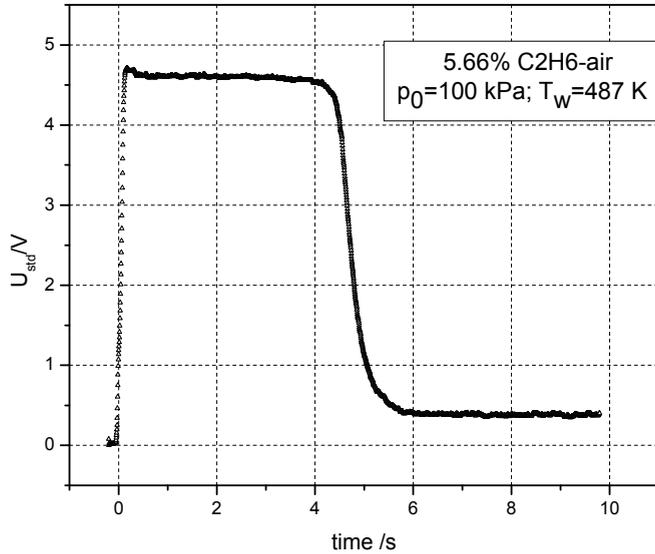
Figure 5. Recorded U_{std} versus *time* diagram

Using equation (8) and the similar diagram recorded in air (without fuel) at the same wire temperature and total pressure, a kinetic diagram given in Figure 1 can be obtained. The wire temperature is calculated according to literature recommendations as [17]:

$$T_w = 273.15 + D_0 + \sum_{i=1}^{9} D_i \cdot [\frac{x - 2.64}{1.64}]^i \qquad (9)$$

where x is the ratio between the wire resistance at temperature T_w and at 273.15 K and D_0, D_j are constants given in literature [17]. All the other details were given elsewhere [7-10].

ACKNOWLEDGMENTS

REFERENCES

1. J. Saint-Just, J. der Kinderen, *Catalysis Today*, **1996**, *29*, 387.
2. A. Schwartz, L. Holbrook and H. Wise, *Journal of Catalysis*, **1971**, *21*, 199.
3. C. G. Rader and S. W. Weller, *American Institute of Chemical Engineering Journal*, **1974**, *20*, 515.
4. S. W. Weller and C. G. Rader, *American Institute of Chemical Engineering Journal*, **1975**, *21*, 176.
5. P. Cho and C.K. Law, *Combustion and Flame*, **1986**, *66*, 159.
6. M. A. A. Cardoso and D. Luss, *Chemical Engineering Science*, **1969**, *24*, 1699.
7. D. Oancea, D. Razus, M. Mitu and S. Constantinescu, *Revue Roumaine Chimie*, **2002**, *47*, 91.
8. D. Oancea, O. Staicu, V. Munteanu, and D. Razus, *Catalysis Letters*, **2008**, *121*, 247.
9. O. Staicu, V. Munteanu, D. Oancea, *Catalysis Letters*, **2009**, *129*, 124.
10. O. Staicu, D. Razus, V. Munteanu, D. Oancea, *Central European Journal of Chemistry*, **2009**, *7*, 478.
11. L. Hiam, H. Wise, S. Chaikin, *Journal of Catalysis*, **1968**, *9-10*, 272.
12. M. Aryafar and F. Zaera, *Catalysis Letters*, **1997**, *48*, 173.
13. G. Veser and L.D. Schmidt, *American Institute of Chemical Engineering Journal*, **1996**, *42*, 1077.
14. T. A. Griffin, L. D. Pfefferle, *American Institute of Chemical Engineering Journal*, **1990**, *36,* 861.
15. Y.-F. Yu Yao, *Industrial and Engineering Chemistry, Product Research and Development*, **1980**, *19*, 293.
16. T. F. Garetto, E. Rincon, C. R. Apesteguia, *Applied Catalysis B: Environmental*, **2007**, *73*, 65.
17. H. Preston-Thomson, *Metrologia*, **1990**, *27*, 3.

GROWTH AND CHARACTERISATION OF ZINC-CADMIUM SULPHIDE THIN FILMS WITH SPECIAL OPTICAL PROPERTIES

MARIA ŞTEFAN[a, b]**, IOAN BÂLDEA**[b]**, RODICA GRECU**[a]**, EMIL INDREA**[c]**, ELISABETH-JEANNE POPOVICI**[a]

ABSTRACT. Nanostructured ZnCdS thin films with variable thickness and high transparency were deposited under variable growth parameters on optical glass platelets, using chemical bath deposition. UV-VIS absorption/reflection spectroscopy, X-ray diffraction, fluorescence spectroscopy, electron microscopy investigations (SEM, EDX) were used to investigate the effect of growth and annealing regime on the films morphology and optical properties. The luminescence properties of copper activated ZnCdS thin films were also investigated. The deposition conditions (medium pH, reagent molar ratio, deposition time) and the presence of the doping ions (copper) influence the morpho-structural properties and optical characteristics of the nanocrystalline zinc-cadmium sulfide thin films.

Keywords: thin films; chemical synthesis; optical properties; luminescence

INTRODUCTION

Zinc sulfide (ZnS), cadmium sulfide (CdS) and their solid solution zinc-cadmium sulfide ($Zn_{1-x}Cd_xS$ or ZnCdS) are interesting wide band gap semiconductors, which attract much attention because of their interesting optoelectronic properties [1-4].

Due to their special optical and electrical properties, metal chalcogenide thin films have been used in various optoelectronic devices, such as solar energy absorbers, photodetectors and electroluminescent displays [5-7]. Different methods could be used for metal chalcogenide thin films preparation including sputtering [8], MOCVD (metal organic chemical vapor deposition) [9], SILAR (successive ionic layer adsorbtion and reaction) [10], pulsed laser deposition [11], chemical bath deposition (CBD) [12] or electrodeposition [13]. Among them,

[a] *Raluca Ripan" Institute for Research in Chemistry, "Babes-Bolyai" University, 30 Fantanele, 400294, Cluj-Napoca, Romania; marialadar@yahoo.com*
[b] *Faculty of Chemistry and Chemical Engineering, "Babes-Bolyai" University, 400028 Cluj-Napoca, Romania*
[c] *National Institute for R & D of Isotopic and Molecular Technology, 71 Donath, 103,400293 Cluj-Napoca, Romania*

CBD is a simple and inexpensive method to produce uniform and adherent films onto a variety of substrates. There are few literature data referring to the chemical bath deposition of ZnCdS thin films with optical properties illustrating that the characteristic films properties strongly depend on chemical bath deposition conditions [14,15]. In order to control the quality of ZnCdS thin films, supplementary studies aiming at the optimization of CBD parameters are needed.

The paper presents our results on the growth and characterization of some reproducible ZnCdS thin films prepared by chemical bath deposition. The effect of cadmium ions addition into the chemical deposition bath on the quality of metal chalcogenide thin films is investigated. Moreover, attempts were made to prepare ZnCdS thin films with luminescent properties using a special doping procedure, not mentioned in the literature.

RESULTS AND DISCUSSION

The preparation of ZnCdS thin films by CBD was based on the reaction, in alkaline medium (NH_3), between zinc acetate, $Zn(CH_3COO)_2$ and cadmium acetate, $Cd(CH_3COO)_2$ as metal sources and thiourea $(NH_2)_2CS$, as chalcogen source. The main chemical process for zinc-cadmium sulphide thin films formation is described by the following equation:

$$M (CH_3COO)_2 + (NH_2)_2 CS + 2OH^- \rightarrow MS + H_2CN_2 + 2H_2O + 2CH_3COO^-$$
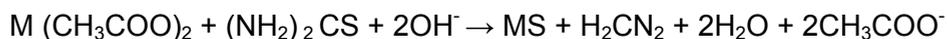
where M=Zn and Cd

The formation of thin films takes place either in the bulk of the solution due to the spontaneous precipitation of ZnS and CdS (homogeneous reaction) or at the surfaces of the substrate leading to the film formation (by heterogeneous reaction).

Our previously studies on chemical bath deposited ZnS thin films [16] pointed out the importance of sodium citrate [Cyt] as complexing agent. Based on our results, the standard chemical deposition bath corresponds to the following reagent ratio: $[Zn^{2+}]$: $[Cyt^{3-}]$: $[NH_3]$: [thiourea] =1:3:20:10. Starting from this bath, ZnCdS /glass/ ZnCdS hetero-structures were prepared by replacing $5 \div 100$ mol % of zinc acetate with cadmium acetate.

Zinc-cadmium sulfide thin films were grown by multilayer technique. Four consecutive layers were deposited on glass platelets to give ZnCdS /glass/ ZnCdS heterostructures. For the same deposition time, addition of cadmium acetate into the standard chemical bath used for ZnS-film deposition does not deteriorate the film quality. The as obtained ZnCdS thin films possess good adherence to the substrate, are transparent and show colors varying from white-yellowish to orange-yellowish, depending on the Cd^{2+} - amount from the chemical deposition bath.

According to the literature data [17], the deposition of ternary materials by chemical bath methods is a problem due to the different hydrolytic stabilities of the two metals. This is illustrated with the fact that, ZnCdS films obtained by CBD show properties that vary non-linearly with the bath composition.

The packing density of ZnCdS thin films varies non-monotonically with Cd^{2+} - concentration, thus suggesting the existence of more different competitive deposition processes with consequences on the film homogeneity (Fig. 1).
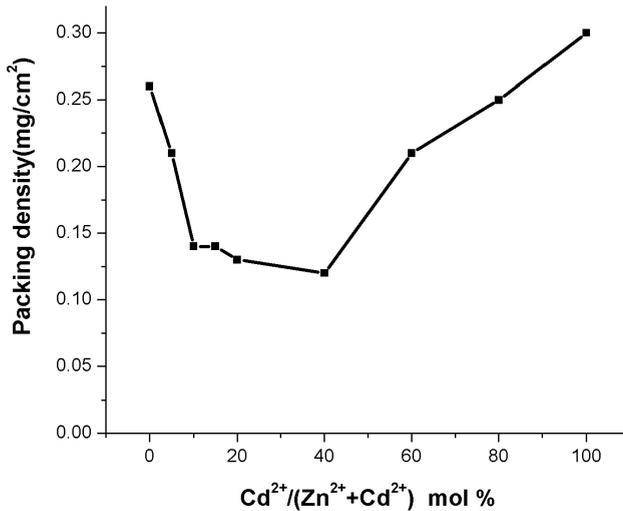
Figure 1. Packing density of ZnCdS *versus* Cd^{2+}-concentration from the chemical deposition bath

The optical properties of ZnCdS thin films are strongly influenced by the deposition technique and CBD bath composition. The transmittance spectra of ZnCdS thin films obtained from chemical bath with different Cd^{2+} amounts are depicted in figure 2.

UV-Vis transmittance spectra illustrate the non-monotonous variation of film transparency with Cd^{2+} content. Films obtained from bath containing 5-10 mol% Cd^{2+} are the most transparent and optical homogeneous. The absorption edge (Fig. 3) shifts non-linearly from UV domain (~ 300 nm for 0 mol% Cd^{2+}) to blue domain (~455 nm for 100 mol% Cd^{2+}). Evaluation is based on the wavelength corresponding to 0.1 % transmittance values.

UV-Vis reflectance spectra (Fig. 4) illustrate that the behavior of ZnCdS films is very different in respect with their specular reflectivity. The reflection peak shifts non-monotonically from ultraviolet (0 mol% Cd^{2+}) to red domain (100 mol% Cd^{2+}). The most light reflecting films are obtained in bath containing $5 \div 20$ mol % Cd^{2+}.
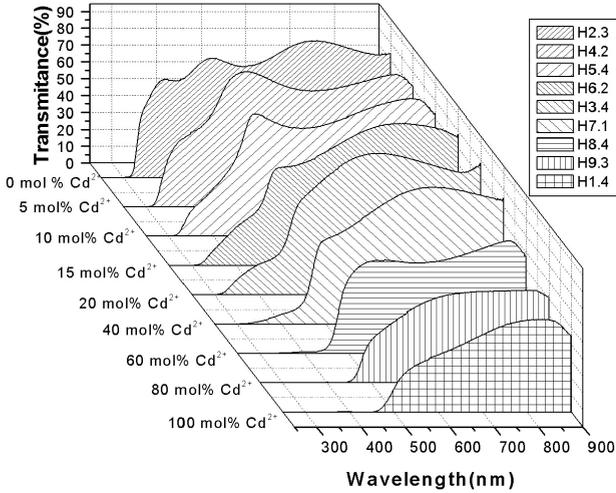
Figure 2. Transmittance spectra of ZnCdS thin films obtained from chemical bath with different Cd^{2+} amounts
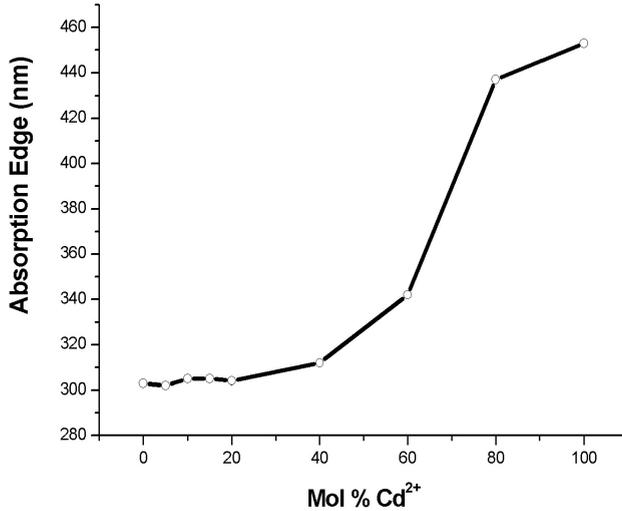
Figure 3. Variation of absorption edge position of ZnCdS thin films with Cd^{2+}-amount from chemical bath

The specular reflectance was evaluated as difference between total reflectance (measured at 8° incidence) and diffuse reflectance (measured at 0° incidence).
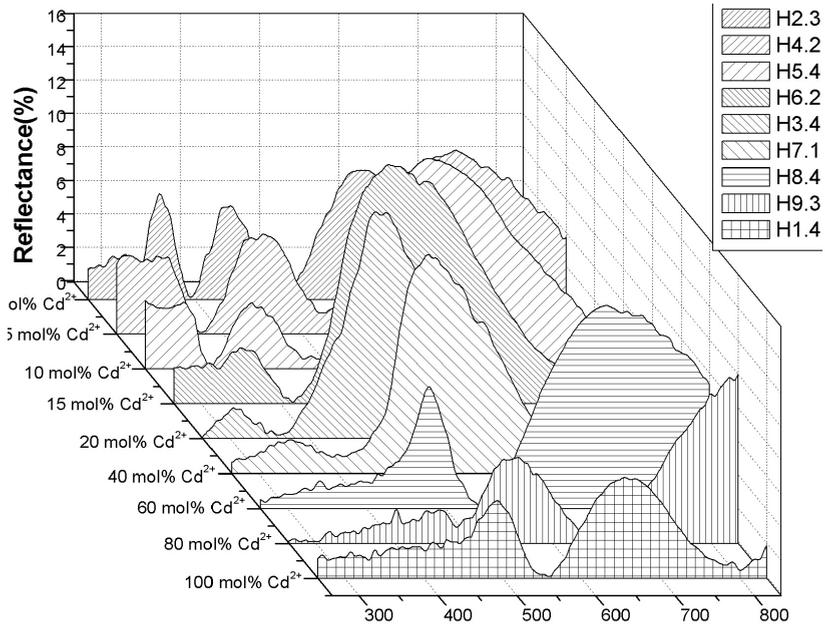
Figure 4. Specular reflectance spectra of ZnCdS thin films obtained from chemical bath with different Cd^{2+} amounts

Morphology of ZnCdS films was investigated by scanning electronic microscopy (Fig. 5). SEM images put in evidence that the surface of films deposited from bath with different Cd^{2+} amounts, is variable. The most structured/particulate film is obtained from bath containing only cadmium acetate.
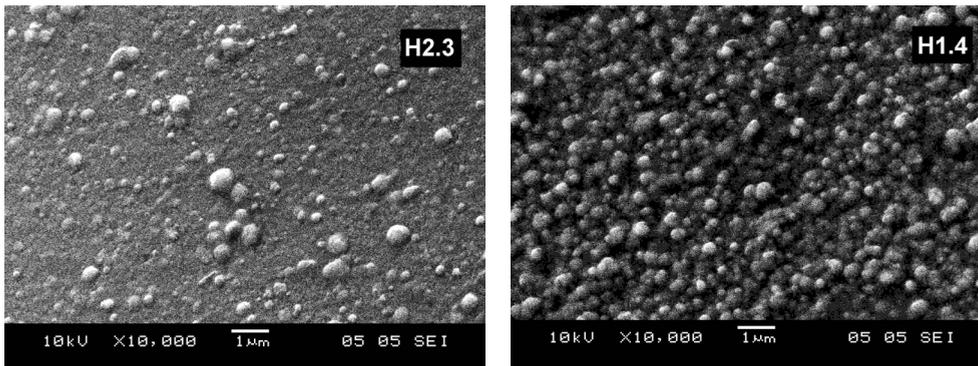
Figure 5. SEM images of ZnS film (H2.3) and CdS film (H 1.4)

EDX investigations proved that film composition is different of that one of the chemical bath, as already suggested by the UV-Vis spectroscopic investigations (Table 1). For instance, the composition of film H7.2 obtained from bath with 40 mol% Cd^{2+} contains about 75 mol% Cd^{2+}. One notes also that the ZnCdS are usually thinner than the pure ZnS or CdS films). As expected, the preferential precipitation of cadmium sulfide is observed and Cd-rich ZnCdS films are usually growth in our CBD conditions.

One can also note that, according to the EDX data, the heterostructure contains Zn, Cd and S from the chalcogenide films and Si, O, Ca, Na, Mg and Al from the glass substrate (the electron beam penetrates the thin ZnCdS film and enters into the glass substrate, see table 1).

Table 1. Composition of the ZnCdS/glass/ZnCdS films heterostructures obtained from chemical bath with different compositions (where others = Na, Mg, Al, K, Ca, O)

Code	Zn/Cd in bath	Heterostructure composition (mol %)					Zn/Cd in film	Packing density (mg/cm^2)
		Si	Others	Zn	Cd	S		
H2.1	1:0	10.70	72.51	11.25	0	5.54	1:0	0.26
H3.2	1:0.25	62.89	29.79	1.23	1.56	4.53	1:1.27	0.13
H7.2	1:0.66	29.89	67.03	0.29	1.05	1.74	1:3.62	0.12
H9.2	1:4.00	29.76	62.54	0.19	3.27	4.24	1:17.21	0.25
H1.5	0:1	29.65	56.00	0	6.53	7.82	0:1	0.30

The crystalline structure of ZnCdS thin films has been investigated by the X-ray diffraction technique (Fig. 6). All films deposited on glass substrate are amorphous, as illustrated by the X-ray scattering curves; an organization tendency of CdS containing layers in comparison with ZnS films can be observed.
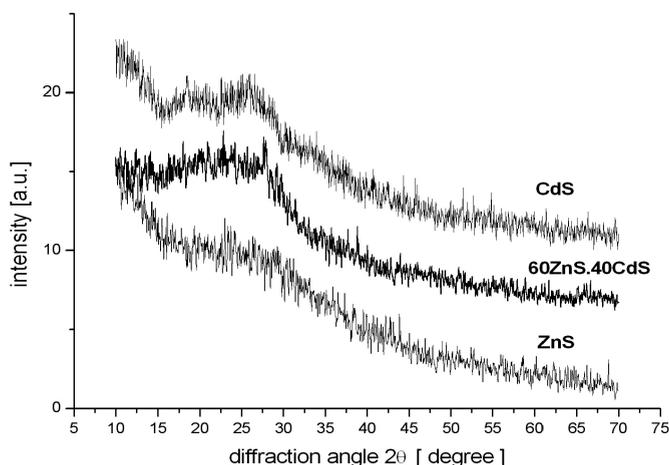
Figure 6. X-ray scattering curves of some ZnCdS films (MoK$_\alpha$)

The light emitting properties of metal chalcogenide thin films are highly sensitive to the annealing regime as well as to the doping conditions [16]. In order to develop photoluminescent properties, ZnCdS /glass/ ZnCdS heterostructures were activated with copper ions, using indirect doping technique [16]. Emission spectra of Cu doped heterostructures obtained from chemical bath with different Cd^{2+} amounts are presented in figure 7.
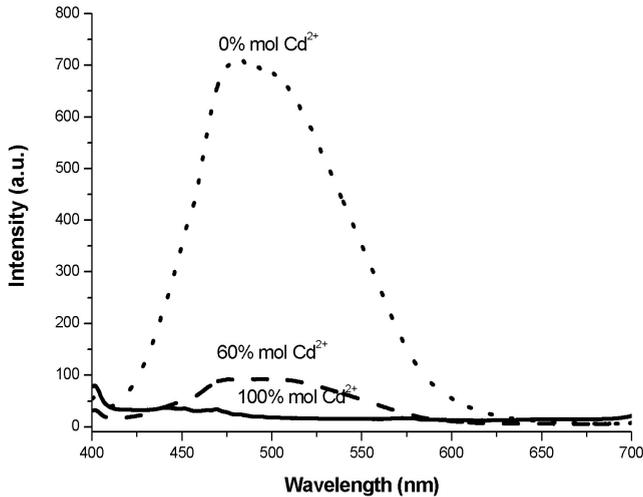
Figure 7. Emission spectra of ZnCdS: Cu films obtained from chemical bath with different Cd^{2+} amounts

ZnS:Cu film show intense green luminescence, with maxima at 483 nm and 500-510 nm. The addition of cadmium into the bath produces a dramatic decrease of the photoluminescent emission and a small shift of the emission peak toward higher wavelengths.

CONCLUSIONS

High quality zinc-cadmium sulfide thin films with special optical properties were prepared by chemical bath deposition onto optical glass platelets using zinc acetate- cadmium acetate– sodium citrate - ammonia – thiourea system. The deposition from chemical bath with variable cadmium amounts leads to ZnCdS /glass/ ZnCdS heterostructures with very different morpho-structural and optical (transmittance/reflectance) characteristics.

Photoluminescence measurements performed on some Cu-doped ZnCdS films illustrate that CBD grown metal chalcogenide films can be activated with different cations, using the indirect doping technique. Further investigations are needed in order to obtain more performing luminescent ZnCdS layers.

EXPERIMENTAL SECTION

ZnCdS thin films have been grown on 3 x 4.5 x 1 cm^3 optical glass substrates by CBD using the multilayer technique already employed. The deposition of ZnCdS thin films was carried out using the method employed for the chemical bath deposition of ZnS and CdS, respectively. The starting point was the chemical bath used for ZnS film deposition, as follows: [zinc acetate] = 0.015 M; [sodium citrate] = 0.045 M; [ammonia] = 0.3 M; [thiourea] = 0.15 M. ZnCdS thin films were deposited from chemical bath obtained by replacing 5÷100 mol % of the zinc acetate from the standard chemical bath with cadmium acetate. The glass substrates have been previously ultrasonically cleaned in acetone-ethanol mixture. During the deposition, the bath temperature was maintained at 82-86°C and the solution pH at 9.5-10.5. Luminescent ZnCdS thin films were prepared using indirect doping technique. In this purpose, ZnCdS /glass/ ZnCdS heterostructures were introduced into a Cu-containing doping mixture based on high-purity ZnS powder and annealed at 550°C. The details of the experimental technique and conditions have been described in our previous works [16, 18-20]

Chemical bath deposited ZnCdS /glass/ ZnCdS structures have been analysed as grown or after annealing. Packing density was determined by the micro-weighing method. An UNICAM Spectrometer UV4 has been used for optical investigations of ZnCdS thin films and a Perkin Elmer 204 Fluorescence Spectrophotometer was used to investigate photoluminescence characteristics. The structural properties of the films were studied with a standard DRON-3M Diffractometer using the filtered Kα emission of molybdenum (λ=0.70932 Å). Morphology of the films was studied with a JEOL-JSM 5510LV Electron Microscop. Chemical composition of the films was detected by Energy Dispersive X-ray Analysis (EDX) in a JSM 5510LV Scanning Electron Microscop atached with an Oxford Instruments, Inca 200 analytical system.

ACKNOWLEDGEMENTS

REFERENCES

1. I. O. Oladeji, L. Chow, *Thin Solid Films*, **1999**, *399*, 148.
2. T. B. Nasr, N. Kamoun, M. Kanzari, R. Benaceur, *Thin Solid Films*, **2006**, *500*, 4.
3. J. Lee, *Applied Surface Science,* **2005**, *252*, 1398.
4. K. Sambhu, C. O. Larry, *Thin Solid Films*, **2005**, *471*, 298.

5. Z. Khefaca, M. Mnari, M. Dachraoui, *Physical&Chemical News*, **2003**, *14(1)*, 77.

6. T. B. Nasr, N. Kamoun, C. Guasch, *Applied Surface Science,* **2008**, *254*, 5039.

7. R.S. Mane, C.D. Lochande, *Materials Chemistry Physics*, **2000**, *65*, 1.

8. L.X. Shao, K.H. Chang, H.L.Hwang, *Applied Surface Science*, **2003**, *212-213*, 305.

9. C.T. Hsu, *Thin Solid Films*, **1998**, *335*, 284.

10. M. P. Valkonen, S. Lindroos, T. Kanniainen, M. Leskalä, U. Tapper, E. Kauppinen, *Applied Surface Science*, **1997**, *120*, 58.

11. S.Yano, R.Schroeder, B.Ullrich, H. Sakai, *Thin Solid Films*, **2003**, *423*, 273.

12. L. Zhou, Y. Xue, J. Li, *Journal of Environmental Sciences Supplement*, **2009,** S76.

13. M. Ichimura, T. Furukawa, K. Shirai, F. Goto, *Materials Letters,* **1997**, *33*, 51.

14. J. M. Dona, J. Herrero, *Thin Solid Films,* **1995**, *268*, 5.

15. I. O. Oladeji, L. Chow, *Thin Solid Films ,* **2005**, *474*, 77.

16. M. Lădar, E.J. Popovici, I. Baldea, R. Grecu, E. Indrea, *Journal of Alloys and Compounds,* **2007**, *434-435*, 697.

17. D. S. Boyle, O. Robbe, D. P. Halliday, M. R. Heinrich, A. Bayer, P. O'Brien, D. J. Otway, M. D. G. Potter, *Journal of Materials Chemistry*, **2000**,*10*, 2439.

18. M. Lădar, E- J. Popovici, L Pascu, R. Grecu, I.C. Popescu, E. Indrea, *Studia Universitatis Babes-Bolyai, seria Physica*, **2003**, *2, XLVIII*, 469.

19. R. Grecu, E. J. Popovici, M. Lădar, L. Silaghi-Dumitrescu, E. Indrea, *Studia Universitatis Babes-Bolyai, seria Physica*, **2003**, *2, XLVIII*, 472.

20. R. Grecu, E. J. Popovici, M. Lădar, L. Pascu, E. Indrea, *Journal of Optoelectronics and Advanced Materials*, **2004**, *6*, 127.

EQUILIBRIUM STUDY ON ADSORPTION PROCESSES OF 4-NITROPHENOL AND 2, 6-DINITROPHENOL ONTO GRANULAR ACTIVATED CARBON

MIHAELA-CLAUDIA TERTIŞ[a], FLORINA IONESCU[a], MARIA JITARU[a]

ABSTRACT. Adsorption of 4-nitrophenol and 2, 6-dinitrophenol onto granular activated carbon has been studied. Adsorption experiments were carried out in a batch system and were followed by UV-Visible spectroscopy over a period of 120 min. Adsorption isotherms were derived at $25^{o}C$ and the isotherm data were treated according to Langmuir, Freundlich and Tempkin isotherm equations. The fitting of experimental data was tested and the parameters of these equations were determined. Based on the correlation coefficients both Langmuir and Freundlich models are suitable for the study (the squares of correlation coefficients are all > 0.97). Based on the values of normalized percent deviation P, the Freundlich model is suitable for 4-NP and the Langmuir model is suitable 2,6-DNP adsorption onto granular activated carbon type NORIT GAC 1240W (value of P less than 5). The calculated adsorption capacity values (q_{max}) are: 277.77 mg g^{-1} for 4-NP, respective 41.15 mg g^{-1} for 2, 6-DNP.

Keywords: adsorption, nitrophenols, isotherm, activated carbon

INTRODUCTION

Among the environmentally concerned substances, nitrophenols represent one of the most common groups of highly toxic water pollutants. The monosubstituted 4-nitrophenol is found in wastewaters discharged from various industrial activities such as pulp and paper industries, textile mills, steel plants, oil refineries, etc. [1]. This compound is also associated with agricultural activities as an intermediate for the production of pesticides, herbicides and insecticides [2].

Phenol and some of its derivatives are considered priority pollutants with a permissible limit of 0.1 mg mL^{-1} in wastewater [3-6] and must be removed from industrial effluents before discharge into environment. Particular attention has been given to 4-nitrophenol which presents some undesired effects and has a permissible limit of 0.06 mg mL^{-1} [3, 6].

[a] *Research Centre LAF-INT-ECOL, Faculty of Chemistry and Chemical Engineering, "Babes-Bolyai" University, 11 Arany Janos Street, 400028*

Attempts have been made to remove mononitrophenols from wastewater by a number of methods: oxidation with strong oxidizing agents as H_2O_2 [7], biodegradation [8], biosorption [9], photo catalytic degradation [10], etc.

Adsorption is an efficient, simple and inexpensive method for the removal of organic pollutants. As adsorbents, activated carbons, polymeric resins, silica, fly ash, zeolites were commonly used. Activated carbons are preferred adsorbents in industrial processes even they had poor mechanical properties and difficult regeneration processes [11].

Phenolic compounds in aqueous solutions can exist as phenolate ions, depending on the pH of the solution. Conversion of phenol and nitrophenol derivatives to phenolate anions is negligible in water solutions considering its small acidic dissociation constants [12, 13].

RESULTS AND DISCUSSION

The equilibrium nitrophenols solutions concentrations were determined by the aid of the calibration curves equations, obtained from spectrophotometric measurements (UV-Visible spectrophotometer UNICAM HELIOS and DR2800 HACH-LANGE).

The equilibrium adsorption capacities of the adsorbent were calculated using equation (1).

$$q_e = \frac{V(C_0 - C_e)}{m} \qquad (1)$$

where q_e is the adsorption capacity of adsorbent material (mg nitrophenol/g of adsorbent); C_0 is the initial concentration of nitrophenol (mg L^{-1}); C_e is the equilibrium concentration of nitrophenol (mg L^{-1}); V is the volume of nitrophenol solution (L) and m is the mass of the adsorbent (g).

Adsorption characteristics and calibration data for nitrophenol derivatives

In water and acid solution, nitrophenols derivatives are in neutral form, with inessential amount of ionisation products [12, 13]. The spectral and calibration data for the studied compounds are given in Table 1.

It can be observed that both for 4-NP and 2, 6-DNP the UV-Visible spectra present two adsorption bands having significantly different values for the wavelength of maximum absorption (λ_{max}: 223 and 317nm in the case of 4-nitrophenol respective 222 and 430nm in the case of 2, 6-dinitrophenol). Although the calibration data were derived at both λ_{max} values for each compound, only one of them was utilized in this experiment due to the higher intensities of adsorption bands (ε = 9330 at 317nm for 4-NP respectively ε = 6280 at 430nm for 2,6-DNP).

Table 1. Spectral and calibration data for treated nitrophenol derivatives in water

Nitro phenol	λ_{max} (nm)	ε (M^{-1}cm^{-1})	Equation for calibration curve*	Standard deviation for A(%)	Regression coefficient (R^2)
4-NP HO—⬡—NO$_2$	317	9330	$C_{4-NP} = \dfrac{A}{0.2793}$	± 0.3÷1.4	R^2 = 0.9902
2,6-DNP O$_2$N HO—⬡ O$_2$N	430	6280	$C_{2,6-DNP} = \dfrac{A}{0.0194}$	± 0.4÷13	R^2 = 0.9989
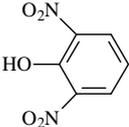
* 7 calibration points for 4-NP; 14 calibration points for 2, 6-DNP; 3 different determinations for each calibration point.

The use of the data corresponding to the other two wavelengths of maximum adsorption, which have smaller values for ε, will affect the quantitative determination. On the other hand, due to the difference of about 100 nm between λ_{max} the method can be used for determination of both nitro phenols derivatives in water.

Adsorption isotherms

Adsorption isotherms at 25°C, derived for 4-nitrophenol and 2, 6-dinitrophenol in water, are shown in Figures 1(a) and 1(b). All the measurements were three times repeated and the values used represent the arithmetical mean of the correspondent three values.

The isotherm data were analyzed according to three well known isotherm equations: Langmuir, Freundlich and Tempkin, whose liniarized forms are given in equations (2)-(4) respectively [14-16].

- The liniarized form for Langmuir isotherm equation:

$$\frac{C_e}{q_e} = \frac{C_e}{q_{max}} + \frac{1}{bq_{max}} \tag{2}$$

- The liniarized form for Freundlich isotherm equation:

$$\ln q_e = \ln K_F + \left(\frac{1}{n}\right)\ln C_e \tag{3}$$

- The liniarized form for F Tempkin isotherm equation:

$$q_e = k_1 \ln k_2 + k_1 \ln C_e \tag{4}$$

215

where q_e is the amount of adsorbate adsorbed per unit mass of adsorbent at equilibrium (mg nitrophenol g^{-1} NORIT GAC 1240W); C_e is the final concentration at equilibrium (mg L^{-1}); q_{max} is the maximum adsorption at monolayer coverage of surface (mg nitrophenol g^{-1} NORIT GAC 1240W); b is the adsorption equilibrium constant related to the energy of adsorption (L mg^{-1}); K_F is a Freundlich constant representing the adsorption capacity (mg g^{-1})(L mg^{-1})$^{1/n}$; n is a constant depicting the adsorption intensity; k_1 the Tempkin isotherm energy constant (L mg^{-1}) and k_2 the Tempkin isotherm constant. The main difference between these three isotherm models is in the variation of heat of adsorption with the surface coverage. Langmuir model assumes uniformity, Freundlich model assumes logarithmic decrease and Tempkin model assumes linear decrease in heat of adsorption with surface coverage.
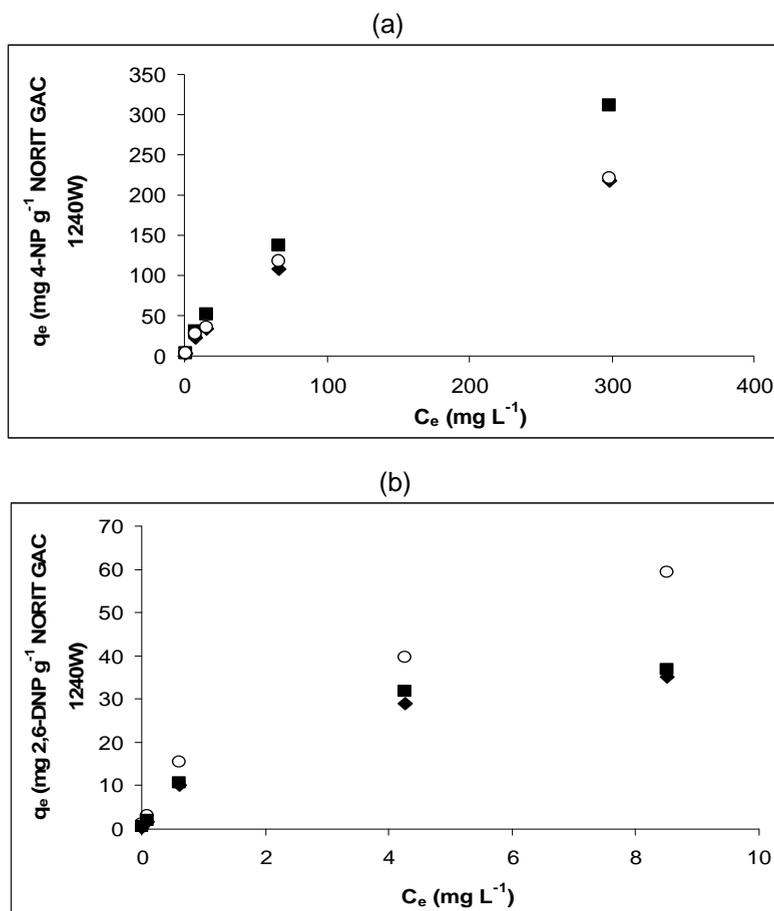
Figure 1. The fit of experimental data (♦) to Langmuir (■) and Freundlich (○) models at 25^{0}C for: (a) 4-nitrophenol and (b) 2, 6-dinitrophenol in water.

The Langmuir equation is valid for monolayer adsorption of adsorbate onto adsorbent surface and assumes there are a definite and energetically equivalent number of adsorption sites. The bonding to adsorption sites can either be chemical or physical, but it must be sufficiently strong to prevent displacement of adsorbed molecules along the surface. This model also presumes that molecules adsorbed on neighbouring sites do not interact each other [11, 17].

(a)

(b)
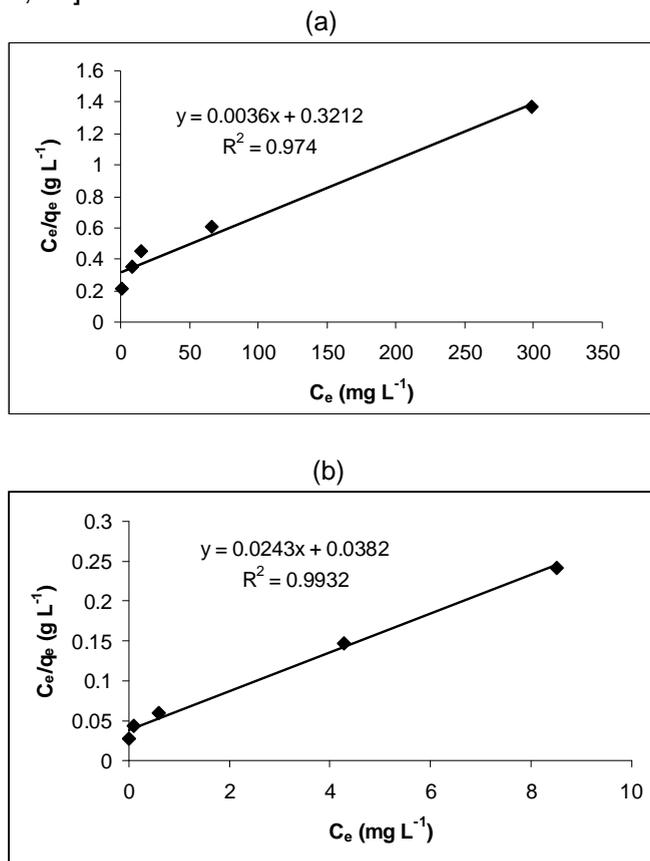
Figure 2. Linear form of Langmuir adsorption isotherm for: (a) 4-NP and (b) 2, 6-DNP adsorption on granular activated carbon type NORIT GAC1240W, at 25°C.

The liniarized forms of Langmuir, Freundlich and Tempkin isotherm equations are given in equations (2)-(4), which describe these models. Figures 2-4 present the obtained results, and the parameters of these equations are given in Table 2.

Table 2. The equations parameters of Langmuir, Freundlich and Tempkin adsorption isotherm for nitrophenolic compounds at 25°C.

Nitro phenol	Langmuir parameters		Freundlich parameters		Tempkin parameters	
	q_{max} (mg g^{-1})	b (L mg^{-1})	K_F (mg g^{-1}) (L mg^{-1})$^{1/n}$	$1/n$	k_1 (L mg^{-1})	k_2
4-NP	277.77	86.44	2.04	1.52	33.6	0.59
2,6-DNP	41.15	0.63	2.01	2.30	5.4	36.39

(a)   (b)

Figure 3. Linear form of Freundlich adsorption isotherm for: (a) 4-NP and (b) 2, 6-DNP adsorption on granular activated carbon type NORIT GAC1240W, at 25°C.
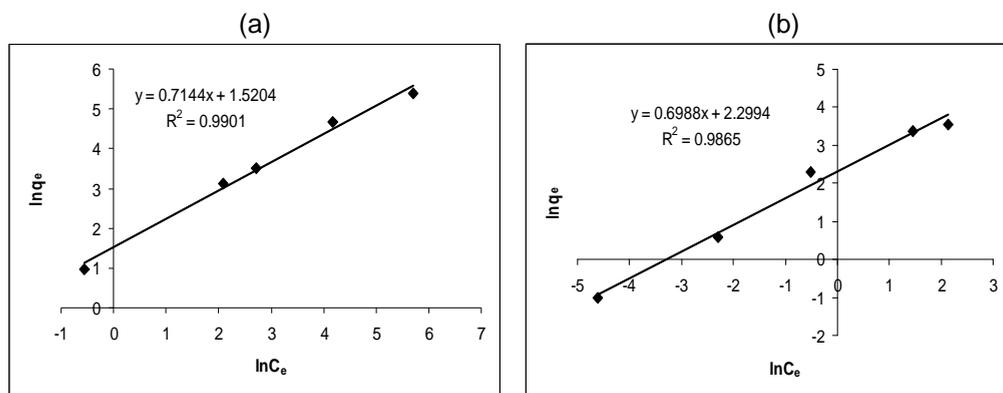
(a)   (b)

Figure 4. Linear form of Tempkin adsorption isotherm for: (a) 4-NP and (b) 2, 6-DNP adsorption on granular activated carbon type NORIT GAC1240W, at 25°C.
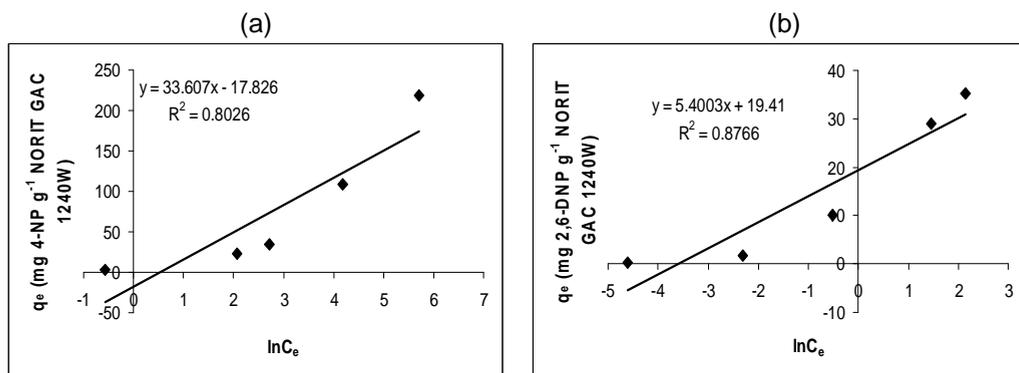
A better criterion to test the correlation between experimental data to one of the three isotherm equations (Langmuir, Freundlich and Tempkin), is a parameter known as normalized percent deviation [14], or percent relative deviation modulus, P, [15, 16], given by the equation (5):

$$P = \left(\frac{100}{N}\right) \Sigma \left(\frac{\left|q_{e(\exp)} - q_{e(pred)}\right|}{q_{e(\exp)}}\right)$$

(5)

where $q_{e(exp)}$ is the experimental q_e at any C_e; $q_{e(pred)}$ is corresponding predicted q_e according to the equation under study with best fitted parameters; N is the number of measurements (5 in our case). It is generally accepted that when the P value is less than 5, the fit is considered to be good [15]. The values for percent relative deviation modules, P, calculated for all three models and both nitrophenol derivatives are presented in Table 3. It can be seen that, in the case of 4-nitrophenol the value of P is less than 5 only for Freundlich model (P=0.9), and in the case of 2, 6-dinitrophenols for Langmuir model (P=2).

Table 3. Values of normalized percent deviations (P) for Langmuir, Freundlich and Tempkin models for nitrophenolic derivatives, at 25°C.

Nitro phenol	P Langmuir model	P Freundlich model	P Tempkin model
4-NP	10.99	0.90	26.60
2,6-DNP	2.00	26.20	80.00

The efficiency of adsorption process can be predicted by the dimensionless equilibrium parameter R_L, which is defined by the equation (6):

$$R_L = \frac{1}{1 + b \cdot C_0}$$

(6)

where b is the Langmuir constant (L mg^{-1}); C_0 the initial concentration of nitrophenolic compound (mg L^{-1}). Isotherm is considered to be unfavourable when $R_L > 1$, linear when $R_L = 1$, favourable when $0 < R_L < 1$ and irreversible when $R_L = 0$ [16, 18, 19].

The R_L calculated values are given in Table 4.

Table 4. Values of equilibrium parameter R_L for Langmuir, Freundlich and
Tempkin models for nitrophenolic derivatives, at 25°C.

Nitro phenol	C_0 (mg L^{-1})	R_L
4-NP	13.91	0.46
	69.55	0.15
	139.11	0.08
	695.55	0.02
	1391.10	0.01
2,6-DNP	1.84	8.30×10^{-4}
	9.20	1.60×10^{-4}
	18.41	8.30×10^{-5}
	92.04	1.60×10^{-5}
	184.11	8.30×10^{-6}

Since all the R_L values calculated for treated nitrophenols are between 0 and 1, the adsorption processes are favorable in all cases.

CONCLUSIONS

In this study granular activated carbon type NORIT GAC1240W was used as adsorbent for 4-nitrophenol and 2, 6-dinitrophenol, to evaluate the applicability to remove these nitrophenols from water solutions. The experiments were conducted in a batch mode at constant working conditions. The equilibrium adsorption data were described by the Langmuir, Freundlich and Tempkin mathematical models. The values of the constants and correlation coefficients in all three models were calculated. Based on the correlation coefficients both Langmuir and Freundlich models are suitable for the study (the squares of correlation coefficients are all > 0.97).

According to the analysis of the results, and the values of normalized percent deviation P, the experimental data for 4-NP adsorption onto granular activated carbon type NORIT GAC1240W were correlated reasonably by the Freundlich model, unlike those for 2, 6-DNP adsorption which were correlated by the Langmuir model.

From the liniarized Langmuir equation, the calculated adsorption capacity values (q_{max}) are: 277.77 mg g^{-1} for 4-NP, respective 41.15 mg g^{-1} for 2, 6-DNP adsorption on granular activated carbon type NORIT GAC 1240W.

Because the equilibrium parameter R_L values are close to 0 ($10^{-5} \div 10^{-6}$) for 2, 6-dinitrophenol at higher concentrations ($5 \times 10^{-4} \div 10^{-3}$ mol L^{-1}), it is possible to presume that, in this condition, adsorption is irreversible. Future experiments are necessary to study the reversibility of the nitrophenol compounds adsorption onto activated carbon.

EXPERIMENTAL SECTION

Materials and methods

4-NP with purity greater than 98% (Merk, Germany), and 2, 6-DNP with purity greater than 95% (calculated based on dry substance), moistened with 20% H_2O (ALDRICH, Switzerland) were used to prepare the solutions, with desirable concentration, for the experiments in this study. Distilled water was used to prepare the aqueous solutions. All the reagents were analytical grade and used without further purification.

The activated carbon used in the present work was NORIT GAC 1240W, obtained from NORIT (Netherlands), having the following characteristics: micropores volume: 0.38 cm^3 g^{-1}; specific area: 1062 m^2 g^{-1}; mesopores volume: 0.45 cm^3 g^{-1}; apparent density: 495 kg m^{-3} [20].

Before use carbon was dried at 105^0C for 12 h and stored in desiccators at room temperature.

In adsorption experiments, the concentration of nonadsorbed 4-nitrophenol and/or 2, 6-dinitrophenol was determined from the absorbance of the species obtained spectrophotometrically at a wavelength of 316 nm for 4-nitrophenol and 430 nm for 2, 6-dinitrophenol. A Unicam Helios B spectrophotometer with the specific software VISION 32, and a quartz vat of 2 ml, with optical route of 1 cm, and a Direct Reading Spectrophotometer type DR/2800 HACH-LANGE with a quartz vat of 2 ml and with optical route of 1 cm were used to measure the adsorption intensities of the species.

The amount of the adsorbed nitrophenol was calculated from the equations which express the connection between the nitrophenols absorbance and concentration.

Batch adsorption experiments

Adsorption experiments were carried out using the conventional batch technique. Nitrophenol solutions were prepared by dissolving required amount of solid nitrophenol in distilled water. The initial concentrations of nitrophenolic compounds (between 13.91 and 1391.10 mg L^{-1} for 4-NP, respective 1.84 and 184.11 mg L^{-1} for 2, 6-DNP); the amount of activated carbon (1 g activated carbon to 0.2 L of nitrophenolic solution) and the temperature $(25\pm2)^0C$ were kept constant during the adsorption experiments.

Isotherm tests

For adsorption isotherms tests, granular activated carbon was weighed and transferred to several glass containers. A known concentration of adsorbate solution was added and the containers were sealed and placed onto a TERMOMIX GRANT LTD6G thermostat where they were maintained at constant temperature of 25^oC for 48 h to ensure that equilibrium was reached. The adsorption experiments occurred under mechanical stirring (350 rpm) with an AGITUVAR 10W stirrer.

REFERENCES

1. Spectrum Laboratories, Chemical Fact Sheet – CAS # 100027; (http://www.speclab.com).

2. The International Programme on Chemical Safety (IPCS), Cincise, International Chemical Assessment Document 20 (CICAD), Mononitrophenols.

3. USEPA, Technical support document for water quality based toxics control, U.S. Environmental Protection Agency, Washington DC, USA, **1991**.

4. S.E. Manahan, "Fundamentals of Environmental Chemistry", CRC Press, Boca Raton, **2000**.

5. P.M. Alvarez, J.F. Garcia-Araya, F.J. Beltran, F.J. Masa, F. Medina, *Journal of Colloid and Interface Science*, **2005**, *283*, 503.

6. B. Pan, X. Chen, W. Zhang, X. Zhang, Q. Zhang, *Journal of Hazardous Materials*, **2006**, *137*, 1236.

7. Y.S. Li, Y.H. You, E.T. Lien, *Archives of Environmental Contamination and Toxicology*, **1999**, *4*, 427.

8. J-P. Arcangeli, E. Arvin, *Water Science and Technology*, **1995**, *31*, 117.

9. B. Koumanova, Z. Kircheva, *Journal of the University of Chemical Technology and Metallurgy (Sofia)*, **2003**, *38 (1),* 71.

10. M. Salaices, B. Serrano, H.I. de Lasa, *Chemical Engineering Science*, **2004**, *59*, 3.

11. M. Erdem, E. Yuksel, T. Tay, Y. Cimen, H. Turk, *Journal of Colloid Interface Science*, **2009**, *article in press,* doi: 10.1016/j.jcis.2009.01.014.

12. E. Ayranci, O. Duman, *Journal of Hazardous Materials B*, **2005**, *124*, 125.

13. J.B. Lambert, H.F. Shurvell, D. Lightner, R.G. Cooks, „Introduction to Organic Spectroscopy", Macmillan Publishers, New York, **1987**.

14. R-S. Juang, R-L. Tseng, F-C. Wu, S-H. Lee, *Separation Science and Technology*, **1991**, *26*, 661.

15. C.J. Lamauro, A.S. Bakshi, T.B. Labuza, *Lebensm-Wiss Technology*, **1985**, *18*, 111.

16. E. Ayranci, O. Duman, *Journal of Food Engineering*, **2005**, *70*, 83.

17. W.S. Wan Ngah, S. Fatinathan, *Colloids and Surfaces A: Physicochemical and Engineering Aspects,* **2006**, *277*, 214.

18. K. Kadirvelu, C. Namasivayam, *Advances in Environmental Research***, 2003**, *7*, 471.

19. R. Sivaraj, C. Namasivayam, K. Kadirvelu, *Waste Management*, **2001**, *21*, 105.

20. I. M. Gullon, R. Font, *Water Research*, **2001**, *35*, 516.

STRATEGIES OF HEAVY METAL UPTAKE BY *PHASEOLUS VULGARIS* SEEDS GROWING IN METALLIFEROUS AND NON-METALLIFEROUS AREAS

CAMELIA VARGA[a]**, MONICA MARIAN**[a]**, ANCA PETER**[a*]**, DELIA BOLTEA**[a]**, LEONARD MIHALY-COZMUTA**[a]**, EUGEN NOUR**[b]

ABSTRACT. This study focuses on the accumulation of metal ions (Pb^{2+}, Zn^{2+}, Cu^{2+}, Fe^{2+}) in *Phaseolus vulgaris* seeds (*Fabaceae* family) collected from metalliferrous / non- metalliferrous areas in Maramures County. By "metalliferous areas" we will understand following in this research paper only areas displaying such pollution, as opposite to the other areas, consequently labeled as "non-metalliferous". Four different concentrations of metal ions were used and their imbibition's degree into the seeds was investigated. The accumulation of metal ions in the seeds of *P. vulgaris* increases as the initial concentration of metal ions is higher. Even more, the seeds growing in non-metalliferous areas display a higher absorption of all metal ions, except the Fe^{2+}, than the seeds growing in metalliferous areas. From an anatomical point of view, we have observed that regardless of concentration, the metal ions were able to penetrate the seed through the hilum, up to the coat.

Keywords: *Phaseolus vulgaris, lead, copper, iron, zinc, heavy metal accumulation, atomic absorption spectrometry, optical microscopy*

INTRODUCTION

Plants usually show the ability to accumulate large amounts of metals without visible changes in their appearance or yield. In many plants, the level of metal accumulation can exceed even several hundred times the maximum level permissible for human beings, without having any negative effect on their growth or yield [1]. Therefore, it seems that plants can endure a level of environmental pollution that might be even several times higher than the level observed nowadays.

The persistence of metallic pollutants in soil is the most difficult issue. The presence of metals accumulated in soil will span hundreds of years, impacting to a lesser or greater extent plants grown on such sites [2]. The plants

---

[a] *Universitatea de Nord Baia Mare, Faculty of Science, Department of Chemistry-Biology, 430083, Baia Mare, Romania*

[*] *coresponding author: Anca Peter, e-mail peteranca@yahoo.com*

[b] *Inspectorate of Emergency Situation, Maramures, Romania*

growing in metalliferous habitats probably have the ability to inactivate the heavy metal by binding the excess metal ions and/or by changing the chemical composition and physical organization of their cell membranes [3]. There are numerous investigations [4, 5] on the influence of heavy metals on the plants metabolism, but data remains scarce about the accumulation of heavy metals in the reproductive organs of plants [6, 7]. Stefanov *et. al.* [3], which studied the accumulation of lead, zinc and cadmium in different plants seeds, showed that plants accumulate selectively heavy metal ions in their seeds. Peanut and corn seeds accumulate mainly lead, pea seeds accumulate mainly cadmium and wheat seeds accumulate mainly zinc. On the other hand, *Lane and Martin* [8] showed that the seed coats of *Raphanus sativus* were a strong barrier to lead and helped prevent contamination of embryos until the seed coat was torn apart by the germinating embryonic root. There are reports on the inhibitory effect of lead on the germination of seeds of the following species *Lupinus luteus* [9]*, Oryza sativa* [10] and *Sinapis alba* [11]*.* The fact that a method of measuring the tolerance of plants to metals entails sowing the seeds of tolerant and sensitive species on metal-contaminated soil points to a significant effect of heavy metals on germination [12]. The above studies, unlike those by Lane and Martin [8], point to the significant influence of lead on seed germination. In this situation it seems probable that the effect of lead on germination depends on interspecies differences in seed structure-in particular, on differences in the structure of seed coats. As it is well known, the role of the seed coat is to protect the embryo from harmful external factors. But seed coats have a wide range of anatomic forms that exist in no other plant organ or tissue [13]. *Wierzbicka et. al* [1] showed that from all plants families tested, the *Fabaceae* family is very susceptibile to the higher concentration of metal ions.

The aims of this study were to evidence the role playing the seeds coat of bean, but also the vulnerability of these seeds to the heavy metals presence. The role of the seed coats as heavy metal barriers is often bypassed by the high concentration of these chemical species, this fact generating a risk of these seeds consumption. We present a selection of research data on the accumulation of heavy metals (Pb^{2+}, Zn^{2+}, Cu^{2+}, Fe^{2+}) in *P. vulgaris* seeds growing in metalliferous and non-metalliferous areas in Maramures county. Investigating how the initial concentration of metal ions impacts the imbibition capacity of seeds and, on the other hand, establishing the degree to which those ions have penetrated the seeds were our key research goals. We have also researched how the imbibition capacity of seeds varies depending on their area of origin (metalliferous or not).

RESULTS AND DISCUSSION

Figure 1 displays the *P. vulgaris* seeds, as a whole and split, impregnated with different ions in different concentrations and originating from metallic and non – metallic areas. All images reveal the imbibition of metal ions into the

seeds as taking place starting with the hilum and going up to the cotyledon, as the colored zones on the seeds split demonstrate. Moreover, as substantiated in all images by the change in color of the tegument of seeds in whole, the penetration of metal ions takes place up to the tegument of the seed. On the other hand, the analysis of images of seeds impregnated with the same metal ion (Figures 1(a)-(b), 1(c)-(d), 1(e)-(f) and 1(g)-(h) respectively) reveals that the intensity of color inside the seed increases as the concentration of metal ions is higher (namely green for Fe^{2+}, red-brown for Zn^{2+}, red for Cu^{2+} and yellow for Pb^{2+}). The optical microscopic analyses confirm this observation (see below).

The macroscopic views of seeds as illustrated in Figures 1 (h) and (i) reveal that seeds impregnated with Pb^{2+} ions, at the same concentration (10. 000 mg/L), display different colors depending on the source of each seed (coming either form a metalliferous area – Ferneziu, in our particular case, or from a non–metalliferous one – Oarta de Jos, in our case). The images demonstrate that in seeds originating in a metalliferous area (as in Figure 1 (i)) Pb^{2+} has prevalently accumulated in the tegument and in the superior part of the cotyledons, while the accumulation in seeds originating from a non–metalliferous area take place in the whole cotyledons and tegument.

Thus, the absorption capacity of seeds originating from non–metalliferous areas exceeds the absorption capacity of those from metalliferous ground. This happens as plants growing in metalliferous sites have the ability to inactivate the excess of metal ions and/or to alter the chemical composition and/or physical layout of membranes of their cells [3].

At the lowest concentration in Fe^{2+} we have tested (see Figure 2 (a)) no presence of the Fe^{2+} ions into seed structures was microscopically observed. In opposition to this, at 50 mg/L in concentration (see Figure 2 (b)) the penetration of Fe^{2+} into the cotyledon and going up to the tegument can be noticed, to stabilize in the area between tegument and cotyledon. A more or less homogeneous distribution of metal ions in the cotyledon is obvious in Figure 2(d). The green color of the cotyledon at the highest concentration of Fe^{2+}, as in Figure 2(d), is clearly more intense than the color displayed at lower concentration of Fe^{2+}, as in Figure 2(c). The imbibition's degree trends up, as the concentration in Fe^{2+} increases. The analysis of Fe^{2+} ions in terms of their imbibition capacity depending on the origin of the seeds (as in Figures 2(a) and (b)), has led us to conclude that the seeds originating from a non-metalliferous area have a higher capacity to absorb Fe^{2+} ions than those originating from a metalliferous area. In particular, Fe^{2+} ions penetrate the seeds originating from a non-metalliferous area up to the cotyledon, to a smaller extent the tegument and agglomerate in the area between the tegument and the cotyledon (the green layer). We have remarked no Fe^{2+} ions penetration at all, however, in seeds originating from a metalliferous area.

(a)

(b)

(c)

(d)

(e)

(f)

(g)

(h)

(i)
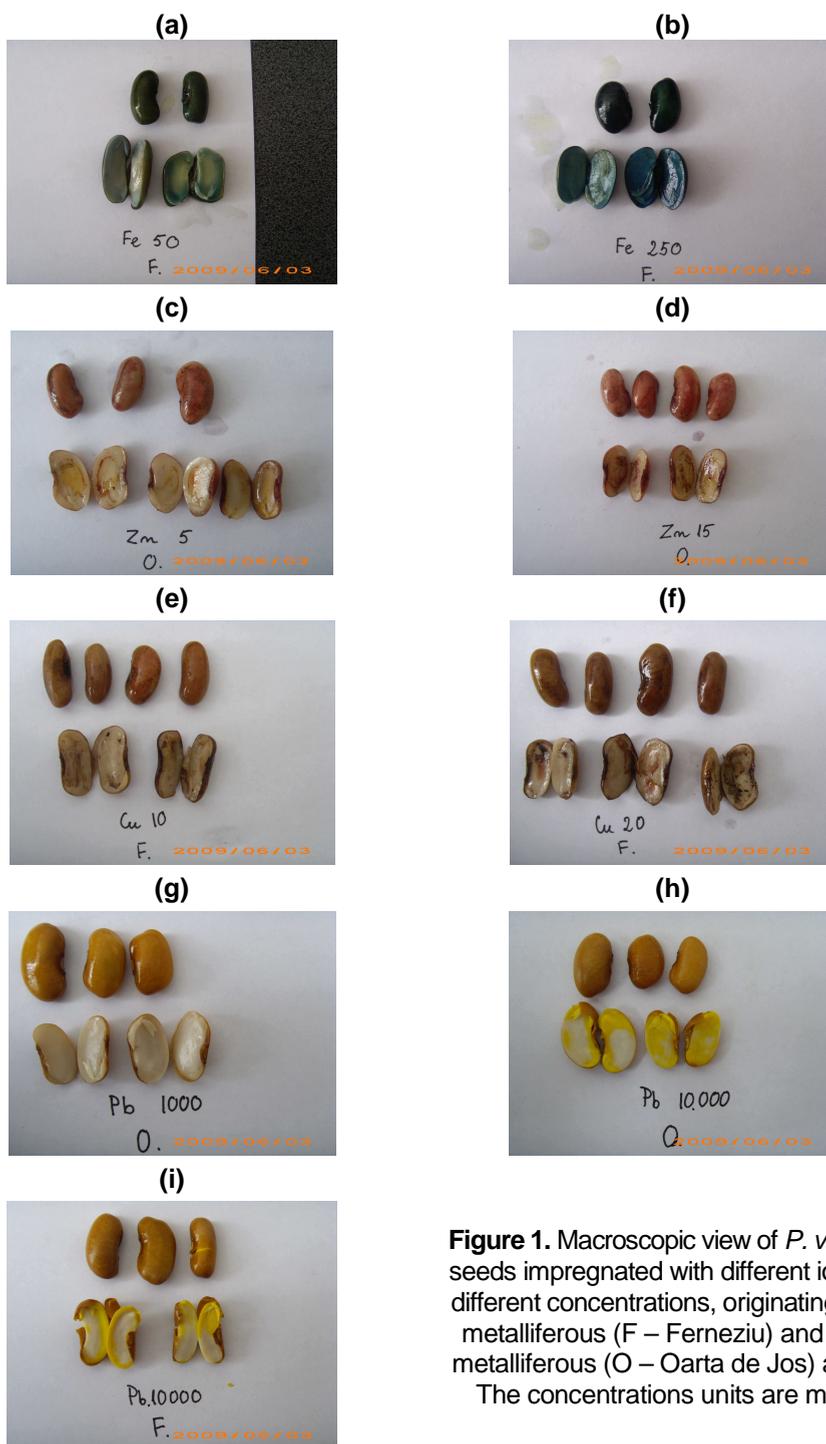
Figure 1. Macroscopic view of *P. vulgaris* seeds impregnated with different ions, at different concentrations, originating from metalliferous (F – Ferneziu) and non-metalliferous (O – Oarta de Jos) areas. The concentrations units are mg/L.

This behavior is explained by the fact that the iron (known as essential trace element for plants [14]) diminish the toxic effect of the other metals by compete with these for binding sites on the cell membranes, followed by penetration and accumulation into the cells [15, 16, 17]. This ionic exchange process is part of the plant strategy to survive on soils strongly polluted with heavy metals.

(a) - Fe 10 F

(b) - Fe 10 O

(c) - Fe 50 F

(d) - Fe 250 F

(e) - Cu 10 O

(f) - Cu 20 F

(g) - Zn 15 F

(h) - Zn 15 O
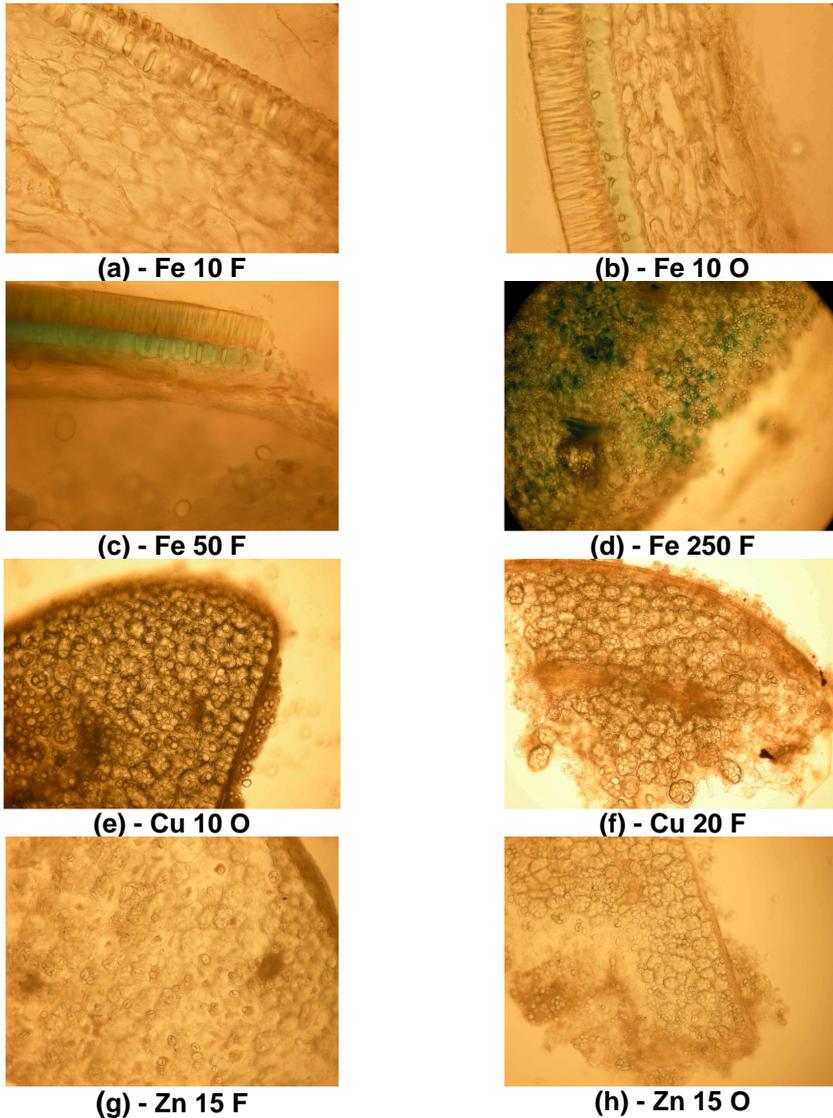
Figure 2. *P. vulgaris* seed – cross sections as captured in optical microscope images at 10 X magnification to detect how the concentration of metal ions impacts the imbibition degree.

As we have monitored the process of imbibition of seeds with Cu^{2+} ions (see Figures 2(e) and (f)) we have noticed the trend of these ions to agglomerate on the cellular wall [3, 5, 18] (red lines between cells) and in the tegument, regardless of the concentration and origination of seeds.

We have conducted the microscopic analysis of seeds impregnated with Zn^{2+} ions (see Figures 2(g) and (h)) and Pb^{2+} ions (not shown) exactly as we did to research the imbibition process with Cu^{2+} ions. We have in this case noticed that regardless of concentration and origination of seeds, the ions agglomerate on the cellular wall (brown lines between cells, for Zn^{2+}) and on the tegument.

Table 1 gives the range of concentrations we have used for the metal ions. We have concluded, as outcome valid for all the metal ions, that the higher their initial concentration was (as in Figure 3), the higher the concentration of metal in seeds is.

We have prepared our initial solutions with the pH ranging between 3,99 and 5. 41 (as revealed in Table 1) and with weak acidity. The process by which *Pistacia vera* L. removes Pb^{2+} ions from aqueous solutions takes place with maximum efficiency (ca. 93,8–95,1%) at a pH ranging from 3,5 to 5,5, as demonstrated by Yetilmezsoy *et. al.* [19]. The absorption of metal ions into seeds subsides at low pH (namely at high concentrations of hydrogen), as hydrogen ions compete with those of metals in the attempt to penetrate the plant [20]. As the pH grows above 7, a decline in mobility of the metal ions in aqueous solutions translates into those ions lower probability to reach and penetrate the seed. [21].

The influence of *P. vulgaris* seeds provenience on the Cu content in seeds is illustrated in Figure 4. Seeds originating in non-metalliferous area (Oarta de Jos) display a higher concentration in copper than seeds in metalliferous area (Ferneziu). Zinc and lead displays a behavior comparable to copper, as confirmed during our optical microscopic analyses. The ability of plants to inactivate the heavy metal by binding the excess and/or by changing the chemical composition and physical organization of their cell membranes [3] stands as explanation for this outcome. Moreover, the plants growing on polluted areas develop, in time, some mechanisms to survive in drastically ecologic conditions. The selection of this kind of resistant plants constitutes during the time a particularly ecotype.

Iron makes the exception to the above – mentioned behavior. Figure 5 reveals how the origin of seeds has an influence on the Fe content. Seeds originating in non-metalliferous areas (Oarta de Jos) display a lower Fe concentration than the seeds from metalliferous sites (Ferneziu).

Table 1. Particularities of the metal ions investigated in *P. vulgaris* seeds.

| Sample ID	Seed Prove-nience	[Metal ion]$^{2+}_{initial}$/pH (mg / L)	[Metal ion]$^{2+}_{soil}$ (mg / Kg)	[Metal ion]$^{2+}_{seed}$ (mg/Kg)	RSD (%)[*]
Fe–10 F	Ferneziu	10 / 4,46	15 287,5	40,4	1,9
Fe-50 F		50 / 3. 99		138,2	7,3
Fe-250 F		250 / 3,51		979,2	1,8
Reference		-		30,5	4,7
Cu-10 F		10 / 4,62	153,2	36,9	1,6
Cu-20 F		20 / 4,58		37,6	0,2
Cu-25 F		25 / 4,65		115,5	0,2
Reference		-		0	0
Zn-5 F		5 / 5,07	93,64	63,6	6,5
Zn-10 F		10 / 5,41		93,3	1,8
Zn-15 F		15 / 4,7		150,4	0,8
Reference		-		29,4	0,2
Pb-100 F		100 / 4,84	357,89	5. 067,4	7,3
Pb-1. 000 F		1. 000 / 4,68		13. 793,4	0,3
Pb-10. 000 F		10. 000 / 4,33		92. 247, 1	1,4
Reference		-		8,1	14,5
Fe-10 O	Oarta de Jos	10 / 4,46	11 952,52	56,1	3,4
Fe-50 O		50 / 3. 99		60,5	16,1
Fe-250 O		250 / 3,51		454,5	4,0
Reference		-		29,5	4,0
Cu-10 O		10 / 4,62	14,61	72,4	1,2
Cu-20 O		20 / 4,58		104,3	0,3
Cu-25 O		25 / 4,65		151,2	0,01
Reference		-		0	0
Zn-5 O		5 / 5,07	40,41	86,9	3,1
Zn-10 O		10 / 5,41		102,5	1,0
Zn-15 O		15 / 4,7		172,7	1,3
Reference		-		23,4	0,5
Pb-100 O		100 / 4,84	40,13	3. 989,4	2,4
Pb-1. 000 O		1. 000 / 4,68		18. 396,1	0,9
Pb-10. 000 O		10. 000 / 4,33		87. 442,1	0,9
Reference		-		8,2	21,3

[*] RSD was determined from three parallel measurements.
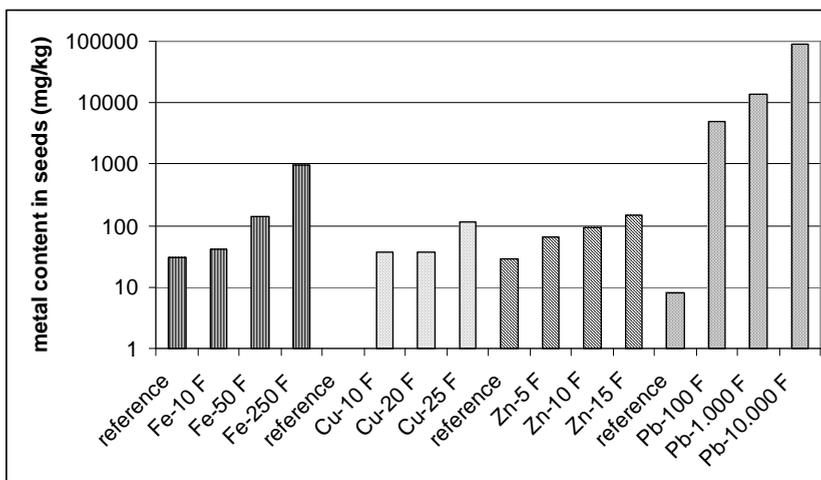
Figure 3. Influence of the initial concentration on the metal contents in
P. vulgaris seeds originating in Ferneziu
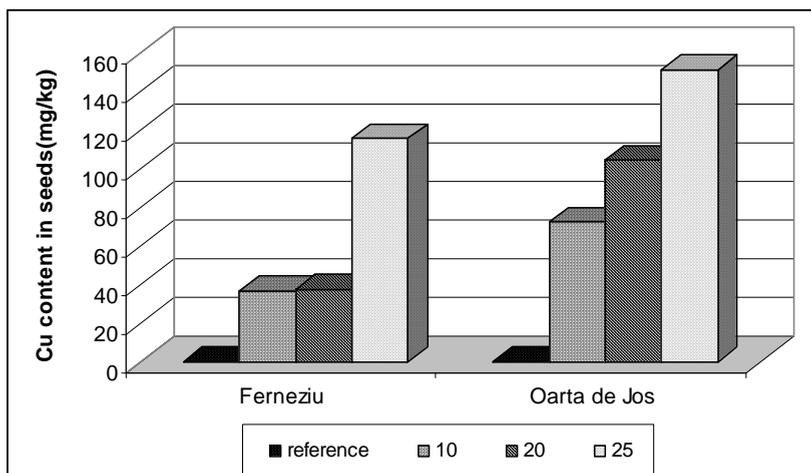
Figure 4. Influence of provenience of the *P. vulgaris* seeds
on the Cu content in seeds

Various levels of concentration in Fe ions could generate on a plant substantially different outcomes. In small concentrations, Fe ions play a beneficial role, as they are essential to the well-being of the plant. In higher concentrations, however, Fe ions become a source of stress, as at sub-cellular level the concentration of metabolic compounds that react with oxygen goes up [22].

230
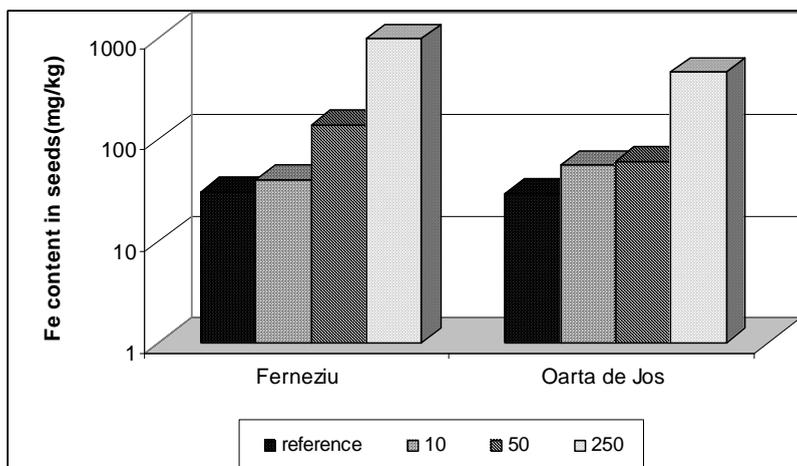
Figure 5. Dependence of the Fe content in seeds on the origin of *P. vulgaris* seeds

CONCLUSIONS

The accumulation of metal ions (Pb^{2+}, Zn^{2+}, Cu^{2+}, Fe^{2+}) in *Phaseolus vulgaris* seeds (Fabacea family) collected from metalliferous and non-metalliferous areas in Maramures County is the key focus of this study. In this respect, we have used four different concentrations of metal ions and we have investigated their respective degree of imbibition into the seeds.

♦ The intensity of color of the seed (green for Fe^{2+}, red-brown for Zn^{2+}, red for Cu^{2+} and yellow for Pb^{2+}) grows as the concentration of metal ions increases.
♦ Seeds originating in non-metalliferous areas display a higher adsorption capacity of metal ions (except iron) than seeds from metalliferous areas
♦ The plants growing on polluted areas develop during the time, mechanisms to survive in drastically ecologic conditions, following a selection process, thus resulting a particularly ecotype.

## EXPERIMENTAL SECTION

Seed Material

Ferneziu is a neighborhood of Baia Mare and also a metalliferous area due to the mining and ore processing activity. The soils originating from this area is very polluted, containing heavy metals (Table 1) and toxic anions which influence the vegetation and fauna growing and propagation. Oarta de Jos is located at aproximatively 50 km away from Baia Mare, in the

south–east of the Maramures County (see the map in Figure 6) and is a non-metalliferous area due to the fact that there is no any mining and industrial activity. Moreover, the village is at aproximatively 10 km away from the main road, which is also considered a source of pollution. The concentrations of the reference metal ions in soil are presented in Table 1.

We have collected *P. vulgaris* seeds out of the crop harvested in Ferneziu and respectively in Oarta de Jos, in the fall of 2008.
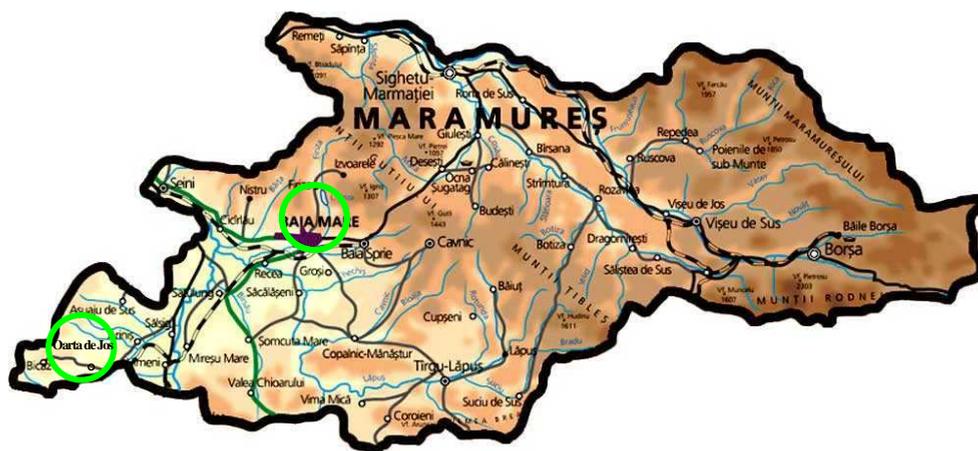
Figure 6. Map of Maramures County. Green circles identify the locations from where we have collected the seeds of *P. vulgaris* for the research interests of this paper.

Series of fifty seeds, collected in the above-mentioned areas, were washed three times with distilled water and immersed in solutions with different concentrations of heavy metal ions. The solutions containing the mentioned metal ions were prepared using $FeSO_4$, $Pb(NO_3)_2$, $CuSO_4$, $ZnSO_4$ salts. The initial concentrations of those solutions were established having in view the same metal ions concentration in soil and are presented in Table 1.

Analyses on heavy metals

After 7 days of immersion at 22^0C in the solution with ions of heavy metals, we have washed three times the seeds with distilled water before initiating our analyses, conducted in two ways.

1. We have relied on a German – made Krúss Optronic binocular microscope in order to investigate the degree of imbibition by optical microscopy. This method has entailed the use of a special reagent to color each category of metal ions under scrutiny. Table 2 gives the color assigned to each metal ion and corresponding to each reagent.

Table 2. The chemical reagents used to identify the iron, copper,
zinc and lead ions and the colors obtained

Heavy metal	Reagent	Color
Fe	$K_3[Fe(CN)_6]$ 5%	Green
Cu	Ditizone 0,12% in $CHCl_3$	Red
Zn	Ditizone 0,12% in $CHCl_3$	Brown
Pb	KI 5%	Yellow

We have maintained the seeds for 10 minutes immersed in reagent, and have dried them up for another 10 minutes in open air. A manual MIC – 500 – type microtome has allowed us to produce mono-cellular microscopic sections. In order to use the microtome efficiently, before sectioning we have immersed the seeds in a paraffin bath, to get them fastened.

2. A Perkin Elmer AAS 800 Spectrometer has allowed us to apply a spectrometric method in order to measure the concentration of metals in seeds. The drying process, in air at 1200^oC for 2 hours, took place in a US-made Binder drying oven. A German – made Retsch RM 100 grinding machine has completed the next step in the process. The mineralization of the powder of seeds (m_{powder} = 5 g), thus produced has entailed the chemical treatment with 28 ml of acid mixture (HNO_3 65%, d=1,4 kg/L (Lach-Ner): HCl 37%, d=1,19 kg/L (Merck) = 1 : 3, volume proportion). We have ensured the adequate homogeneity of the mixture after a half an hour process and we have brought to 100 ml volumetric flask with distilled water the mix that we have finally filtered.

ACKNOWLEDGEMENTS

REFERENCES

1. M. Wierzbicka, J. Obidzińska, *Plant Sci.,* **1998**, *137,* 155.
2. A. Piechalak, B. Tomaszewska, D. Baralkiewicz, A. Malecka, Phyt*ochem.,* **2002**, *60,* 153.
3. K. Stefanov, K. Seizova, N. Yanishlieva, E. Marinova, S. Popov, *Food Chem.,* **1995**, *54*, 311.
4. A. J. M. Baiker, *New Phytol.,* **1987**, *106,* 93.
5. W. H. O. Ernst, J. A. C. Verkleij, H. Schat, *Acta Bot Neerl,* **1992**, *41*, 229.

6. W. H. O. Ernst, Schwerzmetalpflanzen: *Pflanzenokologie und Mineralstoffwechsel,* **1982**, 472.

7. K. B. Searcy, D. C. Mulcahy, *Am. J. Bot.,* **1985**, *72*, 1695.

8. S. B. Lane, E. S. Martin, *New Phytol.*, **1977**, *79*, 281.

9. A. Woźny, B Zatorska, F. Młodzianowski, *Acta. Soc. Bot. Pol.*, **1982**, *51*, 345.

10. R. Mukherji, P. Maitra, *Pflanzenphysiol.,* **1977**, *81*, 26.

11. A. Fargašová, *Bull. Environ. Contam. Toxicol.,* **1994**, *52*, 452.

12. A. J. M. Baker, P. L. Walker, *Bioavailability*, **1989**, *1*, 7.

13. S. Grzesiuk, K. Kulka, "Pan´stwowe Wydawnictwo Rolnicze i Les´ne", Warsaw, **1981**, chapter 3.

14. A. E. Mohamed, M. N. Rashed, A. Mofty, *Ecotoxicol. Environ. Safety*, **2003**, *55*, 251.

15. C. J. Engleman Jr, W. F. McDiffett, *Environmental Pollution,* **1996**, *94*, 67.

16. S. O. King, C. E. Match, P. L. Brezonik, *Environ. Pollut.,* **1992**, *78*, 9.

17. J. W. Moore, "Inorganic Contaminants of Surface Water Research and Monitoring Priorities", Springer-Verlag, New York, USA, **1991**.

18. H. Nishizono, K. Kubota, S. Suzuki, F. Ishii, *Plant Cell. Physiol.,* **1989**, *30,* 595.

19. K. Yetilmezsoy, S. Demirel, *J. Hazard. Mat.,* **2008**, *153,* 1288.

20. D. Demirel, *MSc Thesis, Department of Environmental Science, The Graduate School of Natural and Applied Sciences of Harran University, Sanliurfa,* **2002**.

21. H. Chen, A. Wang, *J. Colloid. Interface Sci.,* **2007**, *307,* 309.

22. S. Sinha, R. Saxena, *Chemosphere*, **2006**, *62,* 1340.

CORROSION INHIBITION OF BRONZE BY AMINO ACIDS IN AQUEOUS ACIDIC SOLUTIONS

SIMONA VARVARA[a], **MARIA POPA**[a], **LIANA MARIA MURESAN**[b]

ABSTRACT. The electrochemical behavior of bronze in an aerated solution of 0.2 g/L Na_2SO_4 + 0.2 g/L $NaHCO_3$ (pH=5), in the absence and in the presence of different amino acids was studied using open-circuit potential and electrochemical impedance spectroscopy measurements. The investigated amino acids were: glutamic acid (Glu), arginine (Arg), histidine (His), methionine (Met) and cysteine (Cys).

      The impedance measurements revealed that the bronze interface in the presence of the amino acids could be suitably represented by a 3RC equivalent electrical circuit. The magnitude of polarization resistance, determined from the impedance spectra, and the efficiency of corrosion inhibition were found to significantly depend on the structure of amino acids. The protection efficiencies of the investigated compounds decrease in the order: Cys > Glu > Met > Arg > His.

Keywords: *bronze, corrosion, amino acids, electrochemical impedance spectroscopy*

INTRODUCTION

      One of the most efficient methods for protecting metals from degradation is the use of corrosion inhibitors. Various types of organic compounds, especially nitrogen, sulphur and oxygen containing substances have been widely used as corrosion inhibitors in various aggressive media [1-11]. The effectiveness of heterocyclic molecules as corrosion inhibitors is based on their ability to adsorb on the metallic surface and to form an organic layer which protects the metal from corrosion [5-12]. The adsorption of inhibitors takes place through the heteroatoms (nitrogen, oxygen and sulfur), aromatic rings or triple bounds. Generally, the inhibition efficiency increases in the following order: O < N < S [12].

      In spite of their effectiveness, most of the heterocyclic compounds used as corrosion inhibitors are highly toxic and their replacement by "green" inhibitors is desirable [13-14].

---

[a] *"1 Decembrie 1918" University, Science Faculty, Str. Nicolae Iorga, Nr. 11-13, RO-510009 Alba Iulia, Romania, svarvara@uab.ro*
[b] *"Babes-Bolyai" University, Faculty of Chemistry and Chemical Engineering, Str. Kogalniceanu, Nr. 1, RO-400084 Cluj-Napoca, limur@chem.ubbcluj.ro*

Among the organic compounds tested as environmental friendly corrosion inhibitors, amino acids have been reported as promising alternatives to the toxic inhibitors. They are innoxious, biodegradable, soluble in aqueous media, relatively cheap and easy to produce at high purity [12]. These properties would justify the use of amino acids as corrosion inhibitors.

In the last years, various works focused on the investigation of the anticorrosive properties of different amino acids on aluminium [15], steel [16-19], vanadium [20], lead [21], and alloys [12] corrosion in various aggressive media.

Inhibition of copper corrosion by amino acids has also aroused interests. The investigations revealed that cysteine (Cys) is the most efficient corrosion inhibitors of copper in neutral and acidic chloride solutions, due to its physical adsorption on the metallic surface *via* the mercapto- group in its molecular structure.

K. Ismail [13] reported that Cys acts as cathodic-type inhibitor for copper corrosion and its maximum inhibition efficiency (84%) was achieved at concentrations of about 16 mM in 0.6 M NaCl and at 18 mM in 1 M HCl, respectively. The presence of Cu^{2+} ions increases the inhibition efficiency of Cys up to 90%. The adsorption of Cys on the copper surface in neutral and acidic chloride solutions obeys the Langmuir adsorption isotherm. Matos *et al.* [22] found that Cys inhibits the anodic dissolution of copper in sulphuric acid media at low polarisation due to formation of the cysteine–Cu (I) intermediate. At high overpotentials, Cys has no influence on anodic process.

Zang *et al.* [23] studied the inhibiting effect of serine (Ser), threonine (Thr) and glutamic acid (Glu) on copper corrosion in an aerated 0.5 M HCl solution. They reported that the amino acids act as cathodic inhibitors due to their adsorption on the metallic surface through both nitrogen and oxygen atoms, which forms a blocking barrier to copper dissolution. The inhibition action of the above-mentioned amino acids decrease in the order: Glu > Thr > Ser.

A limited inhibiting effect on copper corrosion in 0.5 M HCl was also noticed in the presence of aspartic acid (Asp), asparagine (Asn), glutamine (Gln) and glutamic acid (Glu) [24]. The efficiency of these inhibitors depends on their chemical structure and decreases in the following order: Gln > Asn > Glu > Asp. The results obtained from the potentiodynamic polarisation indicate that the four amino acids are mixed-type inhibitors and their protection efficiency increases with increasing their concentration up to 0.1 M.

Zang *et al.* [25] also showed that alanine (Ala) and cysteine (Cys) at a concentration of 10^{-5} M act as anodic inhibitors against copper corrosion in 0.5 M HCl. The maximum protection efficiency was obtained in the presence of Cys (58.7%). The inhibition efficiencies of Ala and Cys were found to be higher than the one of the benzotriazole (BTA), which is widely known as the most efficient corrosion inhibitor of copper and its alloys.

Methionine (Met) has shown limited inhibiting properties for copper corrosion in 0.5 M HCl. The presence of Zn^{2+} ions in the corrosive solution increases the inhibition efficiency up to 92% [26].

Barouni *et al.* [27] measured the effect of valine (Val), glycine (Gly), lysine (Lys), arginine (Arg) and Cys on the copper corrosion in aerated nitric acid solution. They reported that some amino acids (Arg, Cys, Lys) were able to decrease the dissolution rate, while others, such as, Val and Gly actually seems to accelerate the corrosion phenomenon. The inhibition efficiencies determined from polarisation measurements vary in the order: Val (-15%) < Gly (-4%) < Arg (38%) < Lys (54%) < Cys (61%).

Furthermore, in a recent paper we have reported the beneficial effect exerted by Cys and Ala on bronze corrosion in an aerated electrolyte containing Na_2SO_4 and $NaHCO_3$ at pH=5. The electrochemical investigations showed that the two innoxious amino acids have fairly good inhibiting properties for bronze corrosion, the best anticorrosive protection being obtained in the presence of 0.1 mM Cys (90%) [28].

In the present study, four environmentally safe amino acids were tested as inhibitors on bronze corrosion in an aerated solution of 0.2 g/L Na_2SO_4 + 0.2 g/L NaHCO3 (pH=5). The compounds examined were: glutamic acid (Glu), methionine (Met), histidine (His) and arginine (Arg). Some of our previous results obtained using cysteine (Cys) as bronze corrosion inhibitors will also be mentioned for comparison sake.

In order to establish some correlation between the molecular structure of the amino acids and their inhibiting efficiency, as well as the optimum concentration of each amino acid as bronze corrosion inhibitor, conventional electrochemical techniques, such as open-circuit potential (ocp) and electrochemical impedance spectroscopy (EIS) measurements were used.

RESULTS AND DISCUSSION

Open-circuit potential measurements

The evolution of the open-circuit potential (ocp) for bronze over 60 minutes immersion in the corrosive solution in the absence and presence of different concentration of amino acids is illustrated in Figure 1.

As it can be seen in Figure 1, the open-circuit potential shows the same trend in most of the investigated solutions. Thus, it gets more negative with time until it reaches a steady state value.

Generally, the steady state potential (E_{ss}) was reached within less than 30 minutes after the electrode immersion in the corrosive media.

The value of the steady-state potential of bronze in blank solution was + 48.70 mV *vs.* SCE.
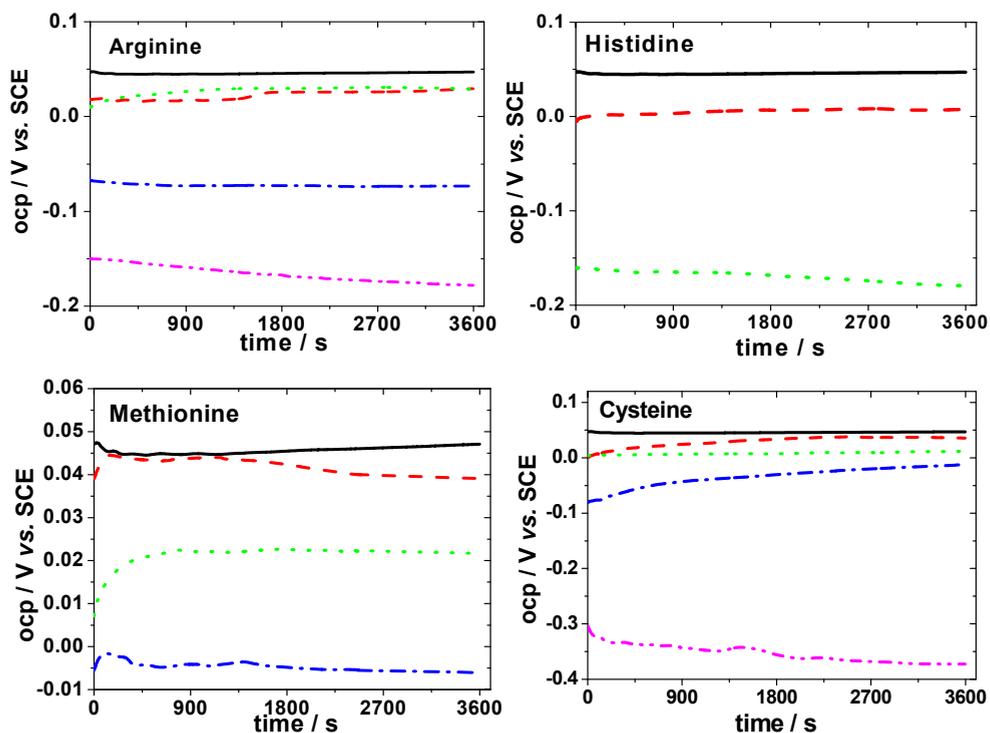
Figure 1. Variation of the open-circuit potential in time for bronze electrode after immersion in the corrosive media in the absence and in the presence of amino acids at different concentrations of amino acids (mM):
(—) 0; (— —) 0.01; (·····); 0.1; (—·—) 1; (—··—) 10.

The values of E_{ss} obtained in the presence of different concentrations of amino acids are presented in Table 1.

Table 1. The values of the steady-state potential of bronze in electrolytes containing different concentrations of amino acids

Amino acids conc. (mM)	E_{ss} / mV *vs.* SCE				
	Glu	His	Arg	Met	Cys
0.01	+47.11	-	+32.71	+40.10	+35.93
0.1	+45.48	+19.78	+28.54	+22.17	-11.77
1	+26.72	+ 7.56	-73.43	- 5.33	-13.33
10	-	-17.95	-177.51	-	-327.60

The value of the shift in the E_{ss} is related to the structure of the amino acid and its concentration in the electrolyte. Thus, for Cys and Arg the maximum negative shifts occur at concentrations of 1 mM and 10 mM, respectively.

238

Addition of Glu, Met and His at concentrations of 1 mM has a less pronounced effect on the E_{ss} value.

Generally, the potential shift can be attributed to the adsorption of the amino acids molecules on the active sites and/or the deposition of corrosion products on the electrode surface [steel, Pb, carbon steel].

A precise categorization of a compound as an anodic or cathodic inhibitor requires an E_{ss} displacement of up to 85 mV with respect to the blank corrosive solution [16]. The magnitude of the E_{ss} displacements suggests that at low concentrations (0.01-0.1 mM) the amino acids simultaneously affect the cathodic and anodic reactions, while at higher concentrations (1 and 10 mM) they predominantly influence the cathodic reduction, probably acting as barriers to the diffusion of oxygen molecules from the solution to the bronze surface.

Electrochemical impedance spectroscopy measurements

In order to provide insight into the characteristics and kinetics of bronze corrosion in the presence of amino acids, the electrochemical process occurring at the open-circuit potential was examined by electrochemical impedance spectroscopy.

As it is well-know [29], the most important advance of the electrochemical impedance spectroscopy is the fact that it enables the fitting of the experimental impedance data to theoretical values according to equivalent circuit models allowing the understanding of the corrosion inhibition mechanism and the suggestion of the suitable electrical model that explains the behaviour of the metal under different conditions.

Nyquist plots collected after 60 minutes immersion of the bronze in solutions without and with various concentrations of amino acids are presented in Figure 2.

The impedance spectra obtained in the absence and in the presence of amino acids display a capacitive behaviour in the whole frequency domain and the low frequency limit of the impedance significantly increases by addition of various concentrations of organic compounds in the corrosive solution.

In order to calculate the numerical values of the parameters that describe the electrochemical system and to verify the mechanistic model of bronze corrosion in the presence of the amino acids, the impedance spectra were appropriately analyzed by fitting the experimental data to the electrical equivalent circuits presented in Figure 3.

We have recently reported and discussed [5, 28] that the impedance spectra obtained for bronze corrosion in the absence of any inhibitor could be suitable described by two R-C ladder circuits, while in the presence of some inhibitors (*i.e.* Cys and Ala), three capacitive loops, though badly separated each other, were necessary for computer fitting of experimental data with an electrical equivalent circuit.
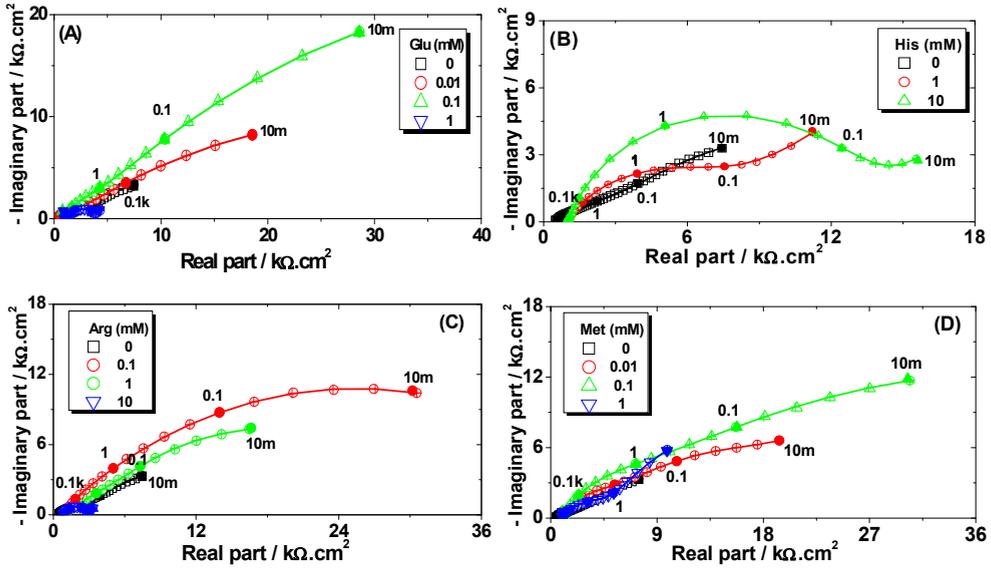
Figure 2. Nyquist plots of bronze electrode in 0.2 g/L Na_2SO_4 + 0.2 g/L $NaHCO_3$ (pH=5) solution, in the absence and in the presence of different amino acids: (A) glutamic acid; (B) histidine; (C) arginine; (D) methionine. The symbol (—+—) corresponds to the simulated spectra. Frequencies are expressed in Hz.
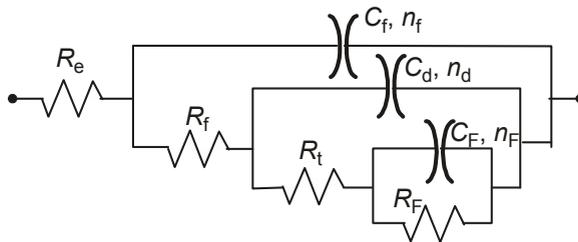
Figure 3. Equivalent electrical circuit used for computer fitting of experimental data

In the present work, the (3RC) electrical circuit was also adopted for carrying out a non-linear regression calculation of the impedance data obtained in the presence of the amino acids (Glu, His, Arg, Met) using a Simplex method.

The origin of the various variables used in the equivalent circuit from Figure 3 were ascribed as follows [5, 28]: R_e-electrolyte resistance; R_f - resistance representing the ionic leakage through pores of a dielectric thin film formed on the surface that is reinforced in the presence of the inhibitors and by the ionic conduction through its pore; C_f - capacitance due to the dielectric nature of the surface film (corrosion products); R_t - charge transfer resistance; C_d - double layer capacitance at the bronze|electrolyte interface;

R_F - faradic resistance of the corrosion products layer accumulated at the interface; C_F - faradic capacitance due to a redox process taking place at the electrode surface, probable involving the corrosion products; n_d, n_f, and n_F: are coefficients representing the depressed characteristic of the capacitive loops in the Nyquist diagrams.

A capacitive loop was calculated according to the following equation:

$$Z = \frac{R}{1 + (j \cdot \omega \cdot R \cdot C)^n} \tag{1}$$

C has the dimension of F cm^{-2}, and corresponds to the value at the frequency of the apex in Nyquist diagram ($\omega RC = 1$) [5].

Table 2 summarises the results of the regression calculations with the electrical circuits from Figure 3. For comparison, the values of the impedance parameters previously obtained in the absence and in the presence of the optimum concentration of Cys (0.1 mM) [28] were included in the Table 2, as well.

The fine overlap between the experimental and the calculated data (cross symbols) observed in Figure 2 proves that the chosen equivalent electrical circuits properly reproduce the experimental data obtained in the absence and in the presence of different concentrations of amino acids, respectively.

In presence of oxidation–reduction process at the electrode surface, the polarization resistance R_p is the parameter the most closely related to the corrosion rate [5].

The values of the polarisation resistance, R_p were determined as the sum ($R_f + R_t + R_F$) from the resistances values determined by regression calculation (Table 2).

In most cases, the addition of the amino acids in the corrosive solution decreases the bronze corrosion rate, as attested by the increase of the polarization resistance values. This indicates that amino acids inhibit the bronze corrosion process, probably due to their ability to adsorb and to form a protective layer on the metallic surface. The highest values of the R_p were obtained in the presence of: 0.1 mM Glu; 0.1 mM Arg; 10 mM His and 0.1 mM Met.

In order to evaluate the anticorrosive effectiveness of the amino acids, their inhibition efficiency (IE) was calculated using the polarization resistance values, according to the following equation:

$$IE(\%) = 100 \cdot \frac{R_p^0 - R_p}{R_p} \tag{2}$$

where R_p and R_p^0 are the polarisation resistances in electrolytes with and without amino acids, respectively.

Table 2. The results of non-linear regression of the impedance spectra presented in Figure 2
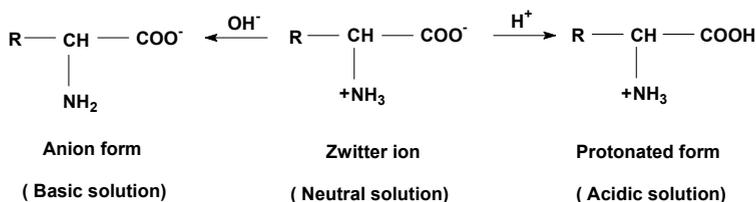
Amino acids conc. (mM)	R_e (kΩcm²)	R_f (kΩcm²)	C_f (µF/cm²)	R_t (kΩcm²)	C_d (µF/cm²)	R_F (kΩcm²)	C_F (mF/cm²)	R_p (kΩcm²)	IE (%)
0	0.46	-	-	3.34	36.84	12.66	1.65	16.01	-
Glu									
0.01	1.04	0.56	0.13	4.14	62.68	38.22	0.36	42.92	62.70
0.1	9.84.	3.94	0.14	15.28	85.99	79.23	0.038	98.45	**83.74**
1	9.77	0.55	0.18	2.68	108.74	1.63	19.32	4.86	-
His									
1	0.99	0.16	5.33	10.62	15.06	9.80	5.45	20.58	2.19
10	1.01	0.34	5.53	17.74	3.05	10.04	3.82	28.12	**43.06**
Arg									
0.01	0.89	2.65	3.28	4.17	13.35	10.49	1.82	17.31	7.51
0.1	0.97	5.31	10.73	9.42	61.20	30.10	3.20	44.83	**64.28**
1	0.79	0.085	4.21	5.20	19.69	24.00	1.30	29.29	45.34
10	0.82	0.051	2.09	2.21	7.54	3.64	35.75	5.90	-
Met									
0.01	1.01	5.71	9.69	20.90	29.87	15.00	6.14	41.61	61.52
0.1	1.02	3.96	3.83	33.82	1.67	53.89	0.2	91.67	**82.54**
1	0.99	3.47	27.50	5.63	57.85	13.68	0.49	22.78	29.73
Cys 0.1	1.08	1.53	0.94	42.55	1.95	126.71	0.031	170.79	**90.63**

$^*R_p = R_f + R_t + R_F$

As it can be seen from the last column of table 2, the anticorrosive protection offered by the investigated amino acids on bronze is relatively weak at low concentrations. As the amino acid concentration increases, their inhibition efficiencies increase and reach a maximum value in the presence of optimum concentration of the inhibitors. Nevertheless, a further increases of the amino acids concentration leads to a decrease of their protective effectiveness. This phenomenon could be probably attributed to the saturation of the bronze surface with inhibitor molecules at a certain concentration [13].

As previously mentioned [30], the effectiveness of the corrosion organic inhibitors is related to the extent to which they absorb and cover the metallic surface. The adsorption process mainly depends on the number of adsorption sites in the inhibitors molecule and their charge density, molecular size and interaction mode with the metallic surface [24].

In general, the amino acid molecule occurs in its protonated form in acidic solution according to the following equilibrium [13, 20]:

R — CH — COO⁻ ←(OH⁻)— R — CH — COO⁻ —(H⁺)→ R — CH — COOH

| NH₂ | +NH₃ | +NH₃ |

Anion form   **Zwitter ion**   **Protonated form**

(Basic solution)   (Neutral solution)   (Acidic solution)

In acidic solutions, the amino acid molecules could be adsorbed on the electrodic surface through the nitrogen, the oxygen or sulphur atoms, which form a blocking barrier to metallic surface and decrease the corrosion rate [20].

In the investigated experimental conditions, the inhibition efficiency of the amino acids as bronze corrosion inhibitors decreases in the order: Cys > Glu > Met > Arg > His.

As expected, among the studied amino acids, Cys exhibits the best inhibition efficiency compared with the five others, probably because its adsorption on bronze as bidentate ligand in which surface coordination is taking place through both the amino group and the –S– moiety [5, 13, 17].

The relatively good anticorrosive protection of Glu on bronze corrosion could be explained if we take into consideration that the molecule has a smaller net positive charge of N atom and a more net negative charge of O atoms [23], which can contribute to its adsorption on the bronze surface. Consequently, the improved inhibition of glutamic acid could be due to the stabilization of its adsorption on the metallic surface by the oxygen atoms in its structure.

In the case of metionine, the electron-donor group (–CH₃) attached to the S atom could exert a steric hindrance [17] which probably affects the adsorption of the organic molecule on bronze surface. Therefore, the inhibition efficiency of Met slightly decreases as compared to Glu.

Although Arg has a radical which contains 3 nitrogen atoms, its effectiveness is lower probably due to the existence of a tautomeric and steric hindrance at the N atoms [15]. The lower inhibition efficiency of His compared to Arg could be due to the fact that His contains a cyclic imidazole group which probably give a smaller surface coverage than the straight chain structure of the radical in Arg. Moreover, the adsorption of His on the metallic surface is probably taking place through only one -N atom in the secondary amine group [15].

CONCLUSIONS

Our study reports the effects of several amino acids (glutamic acid, arginine, histidine, methionine and cysteine) on bronze corrosion in an aerated solution of 0.2 g/L Na₂SO₄ + 0.2 g/L NaHCO₃ at pH 5 using open-circuit potential measurements and electrochemical impedance spectroscopy.

The electrochemical measurements showed that all investigated amino acids present inhibition properties on bronze corrosion.

The molecular structure of amino acids significantly influences the magnitude of R_p values and, consequently, their inhibition efficiency.

The order of anticorrosive effectiveness of the inhibitors was Cys > Glu > Met > Arg > His. The variation of the inhibition efficiency with the structure of the amino acids was interpreted taking into consideration the number of adsorption active centres in the molecule, the adsorption mode and the molecular size of the compounds.

In the investigated experimental conditions, the optimum concentration of each amino acids was relatively low (0.1 mM), except for the case of His, when a concentration of 10 mM was necessary to attain its maximum inhibition efficiency.

EXPERIMENTAL SECTION

Reagents

The corrosive medium was an aqueous aerated solution of 0.2 g/L Na_2SO_4 + 0.2 g/L $NaHCO_3$, acidified to pH=5 by addition of dilute H_2SO_4. This electrolyte corresponds to an acidic rain in an urban environment. The solutions used in this study were prepared using analytical grade reagents (Merk, Darmstadt, Germany) and ion-exchanged water.

The amino acids were dissolved in the electrolyte solution to the concentration of 0.01-10 mM. They were purchased from Sigma-Aldrich and used as received.

The amino acids used in the electrochemical investigations are:
1. Acidic amino acids: glutamic acid.
2. Basic amino acids: histidine and arginine.
3. Sulphur-containing amino acids: methionine and cysteine.

The molecular structures of the amino acids are shown in scheme 1.

glutamic acid (**Glu**)   arginine (**Arg**)

histidine (**His**)   methionine (**Met**)   cysteine (**Cys**)
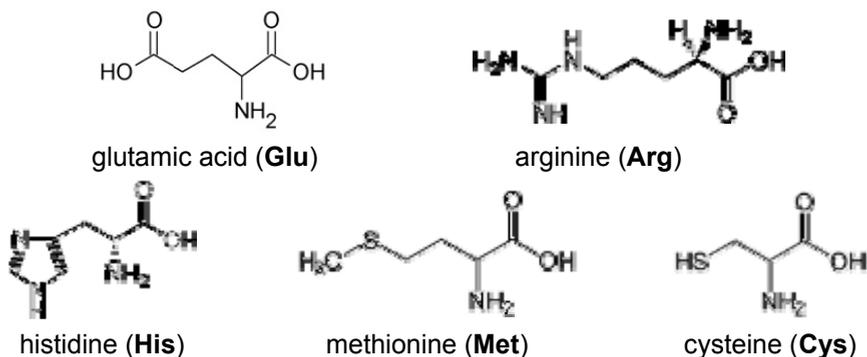
Scheme 1. Molecular structure of the investigated amino acids

Electrochemical measurements

The investigation of the inhibiting properties of the amino acids on bronze corrosion was performed by open-circuit potential measurements and electrochemical impedance spectroscopy.

An electrochemical cell with a three-electrode configuration was used; a large platinum grid and a saturated calomel electrode (SCE) were used as counter and reference electrodes, respectively. To avoid the electrolyte infiltration, the working electrode was made of a bronze cylinder rod which was first covered with cataphoretic paint layer (PGG; W742 and P962), and cured at 150°C for 15 minutes. Then, the bronze cylinder was embedded into an epoxy resin leaving only a circular cross section (0.38 cm^2) in contact with the corrosive solution. The composition of the working electrode is presented in Table 3.

Table 3. Weight composition (%) of the bronze working electrode

Cu	Sn	Pb	Zn	Sb	Ni	Fe	Mn	As	S	P, Si
87.975	6.014	4.02	1.172	0.299	0.181	0.11	0.002	0.033	0.19	0.004

Prior to use, the bronze surface was mechanically polished using grit paper of 600 and 1200 and then rinsed thoroughly with distilled water.

Electrochemical experiments were performed using a PAR model 2273 potentiostat controlled by a PC computer.

Electrochemical impedance measurements were carried out at the open circuit potential after 60 minutes immersion of the bronze electrode in the corrosive medium. The impedance spectra were acquired in the frequency range 100 kHz to 10 mHz at 10 points per hertz decade with an AC voltage amplitude of ± 10 mV. The impedance data were then analyzed with software based on a Simplex parameter regression.

ACKNOWLEDGMENTS

REFERENCES

1. H. Otmacic, E. Stupnisek-Lisac, *Electrochimica Acta*, **2003**, *48,* 985.
2. K. Es-Salah, M. Keddam, K. Rahmouni, A. Srhiri, H. Takenouti, *Electrochimica Acta*, **2004**, *49*, 2771.
3. A. Dermaj, N. Hajjaji, S. Joiret, K. Rahmouni, A. Srhiri, H. Takenouti, V. Vivier, *Electrochimica Acta*, **2007**, *52*, 4654.
4. K. Rahmouni, N. Hajjaji, M. Keddam, A. Srhiri, H. Takenouti, *Electrochimica Acta*, **2007**, *52* 7519.

5. L. Muresan, S. Varvara, E. Stupnisek-Lisac, H. Otmacic, K. Marusic, S. Horvat Kurbegovic, L. Robbiola, K. Rahmouni, H. Takenouti, *Electrochimica Acta*, **2007**, *52*, 7770.

6. H. Ma, S. Chen, L. Niu, S. Zhao, S. Li, D. Li, *Journal of Applied Electrochemistry*, **2002**, *32*, 65.

7. J.B. Matos, L.P. Pereira, S.M.L. Agostinho, O.E. Barcia, G.G.O. Cordeiro, E. D' Elia, *Journal of Electroanalytical Chemistry*, **2004**, *570*, 91.

8. S.A. Abd El-Maksoud, *Electrochimica Acta*, **2004**, *49*, 4205.

9. K.F. Khaled, *Materials Chemistry and Physics*, **2008**, *112*, 104.

10. D. Zhang, L. Gao, G. Zhou, K.Y. Lee*, Journal of Applied Electrochemistry*, **2008**, *38*, 71.

11. S.M. Milic, M.M. Antonijevic*, Corrosion Science*, **2009**, *51*, 28.

12. M.A. Kiani, M.F. Mousavi, S. Ghasemi, M. Shamsipur, S.H. Kazemi, *Corrosion Science,* **2008**, *50*, 1035.

13. K. M. Ismail, *Electrochimica Acta*, **2007**, *52*, 7811.

14. E. Stupnisek-Lisac, A. Gazivoda, M. Madzarac, *Electrochimica Acta*, **2002**, *47*, 4189.

15. A.A. E.Shafei, M.N.H. Moussa, A.A. ElFar, *Journal of Applied Electrochemistry*, **1997**, *27* 1075.

16. E. Oguzie, Y. Li, F.H. Wang*, Electrochimica Acta*, **2007**, *53*, 909.

17. M. S. Morad, *Journal of Applied Electrochemistry*, **2008**, *38*, 1509.

18. A.B. Silva, S.M.L. Agostinho, O.E. Barcia, G.G.O. Cordeiro, E.D'Elia, *Corrosion Science*, **2006**, *48*, 3668.

19. P. Singh, K. Bhrara, G. Singh, *Applied Surface Science*, **2008**, *254*, 5927.

20. M.M. El-Rabiee, N.H. Helal, Gh.M. A. El-Hafez, W.A. Badawy, *Journal of Alloys and Compounds*, **2008**, *459*, 466.

21. N.H. Helal, M.M. El-Rabiee, Gh.M. Abd El-Hafez, W.A. Badawy, *Journal of Alloys and Compounds*, **2008**, *456*, 372.

22. J.B. Matos, L.P. Pereira, S.M.L. Agostinho, O.E. Barcia, G.G.O. Cordeiro, E. Delia, *Journal of Electroanalytical Chemistry*, **2004**, *570*, 91.

23. D.-Q. Zhang, Q.-R. Cai, L.-X. Gao, K.Y. Lee, *Corrosion Science*, **2008**, *50*, 3615.

24. D.-Q. Zhang, Q.-R. Cai, X.-M. He, L.-X. Gao, G.-D. Zhou, *Materials Chemistry and Physics*, **2008**, *112*, 353.

25. D.-Q. Zhang, L.-X. Gao, G.-D. Zhou, *Journal of Applied Electrochemistry*, **2005** *35*, 1081.

26. D.-Q. Zhang, Q.-R. Cai, X.-M. He, L.-X. Gao, G.S. Kim, *Materials Chemistry and Physics*, **2009**, *114*, 612.

27. K. Bauroni, L. Bazzi, R. Saghi, M. Mihit, B. Hammouti, A. Albourine, S. E. Issami, *Materials Letters*, **2008**, *62*, 3325.

28. S. Varvara, M. Popa, G. Rustoiu, R. Bostan, L. Muresan, *Studia Universitatis Babes-Bolyai, Chemia,* **2009**, in press.

29. A. J. Bard, L. R. Faulkner, "Electrochemical methods. Fundamentals and Applications" (2nd Edition), John Wiley & Sons Publisher, New York, **2001**, chapter 10.

30. E. Stupnisek-Lisac, A. Gazivoda, M. Madzarac, *Electrochimica Acta*, **2002**, *47*, 4189.

# POTASSIUM-SELECTIVE ELECTRODE BASED ON A CALIX[6]ARENIC ESTER (C6Es6)

LIDIA VARVARI[a], SORIN-AUREL DORNEANU[a], IONEL CĂTĂLIN POPESCU[a]*

ABSTRACT. An ion-selective electrode (ISE) was elaborated based on a calyx[6]arenic ester (C6Es6) as ionophore and PVC as polymer matrix. Potentiometric measurements were performed in standard solutions of Ca^{2+}, Mg^{2+}, Na^+, K^+, NH_4^+ and Li^+. The best response was observed for K^+: slope 52 mV/ΔpK; linear range from 0.1 mM up to 0.1 M; detection limit of 0.02 mM; potentiometric selectivity coefficients of 0.06 and 0.16 for Na^+ and NH_4^+, respectively.

Keywords: calyx[6]arenic ester, PVC-based ISE, potassium ISE

INTRODUCTION

Ion-selective electrodes (ISE) are of great importance due to their wide applications mainly in clinical, food and environmental chemistry [1]. For example, it was estimated that, all over the world, over a billion of clinical analyses are performed annually using ISE [2].
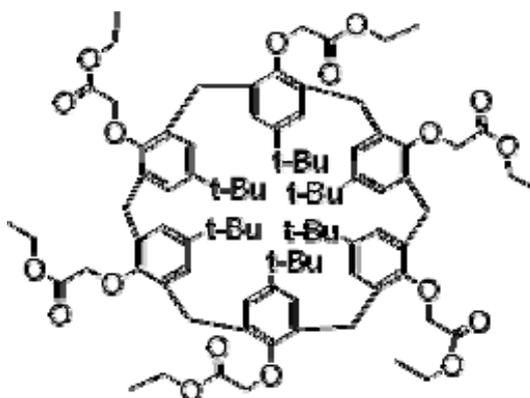
Figure 1. The structure of C6Es6 ester

[a] *Department of Physical Chemistry, Babes-Bolyai University, 400028 Cluj-Napoca, Romania, *e-mail address: cpopescu@chem.ubbcluj.ro*

The ion selective membrane of an ISE is usually made of a polymer matrix (such as PVC) incorporating an ionophore. Most often, ionophores are macrocyclic compounds, which selectively bind different ions by entrapping them in their cavity. Consequently, the selectivity of the membrane strongly depends on the size match between the ion and the host cavity, but also on the ion charge. Many calixarenic compounds have been successfully used as ionophores [3- 10].

The aim of this paper was to evaluate the ionophore abilities of a calyx[6]arenic ester synthesized at ICCRR (Cluj-Napoca) using a new chemical route. The structure of this compound, named 4-tert-butylcalix [6]arene-hexaacetic acid hexaethyl ester (C6Es6), is shown in Figure 1. The study was focused on the determination of the main analytical parameters (sensitivity, detection limit, selectivity) of C6Es6-based ISE for various alkaline and alkaline-earth cations.

RESULTS AND DISCUSSION

I. Calibration curves for Ca^{2+}, Mg^{2+}, Na^+, K^+, NH_4^+ and Li^+

As the ionophore properties of the C6Es6, synthesized using a new chemical route, were unpredictable, our study started with the evaluation of the sensitivity (S) and detection limit (DL) towards several cations of biotechnological and medical interest: Ca^{2+}, Mg^{2+}, Na^+, K^+, NH_4^+ and Li^+. All measurements were performed in "batch", using the known addition method for the preparation of standard solutions. Figure 2 shows the calibration curves obtained in presence of K^+ and Na^+, at variable ionic strength. The calculated values of the corresponding S and DL parameters are presented in Table 1. All values represent the average of two successive measurements, carried out with four electrodes, under the same experimental conditions.

The best S values were obtained for Na^+, K^+ and NH_4^+, being quasi-nernstian in the limit of experimental errors. For all other investigated cations the S values were significantly under-nernstian. A low interelectrode reproducibility was observed for S value calculated in the presence of Ca^{2+}.
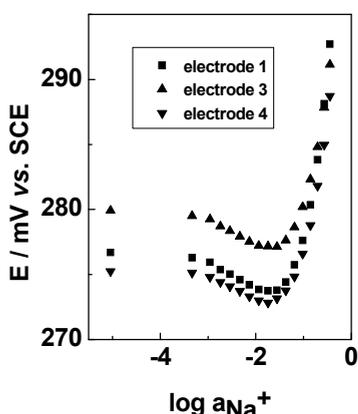
DL values around 10^{-5} M were observed for K^+ and NH_4^+. All other DL values were at least 10 times higher than for K^+ and NH_4^+.

Table 1. Values of S and DL for C6Es6-based ISE in presence of different cations

Ion	Ca^{2+}	Mg^{2+}	Na^+	K^+	NH_4^+	Li^+
S (mV/Δp_i)	14-26	12	55	52	56	5
DL (mM)	$2.2*10^{-3}$	$5.4*10^{-4}$	$1.4*10^{-4}$	$2.0*10^{-5}$	$8.6*10^{-5}$	$1.1*10^{-3}$
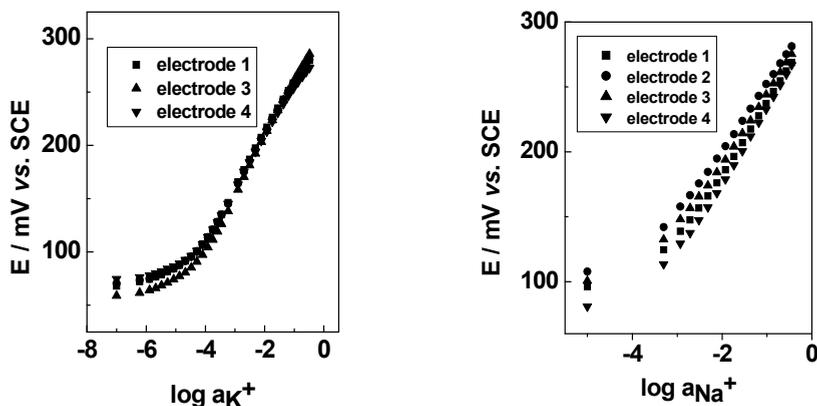
Figure 2. Calibration curves recorded for C6Es6-based ISE
in presence of K^+ and Na^+

Figure 3. Potentiometric response
recorded at C6Es6-based ISE in
presence of constant concentration of
K^+ and variable concentrations of Na^+

II. Study of the ionic interference

Based on the calibration curves obtained for the investigated cations, K^+ was chosen as primary ion (best S and DL values). During the whole interference study the K^+ concentration was kept at 10^{-2} M for two main reasons: (i) this value corresponds to the middle of the linear range on the K^+ calibration curve; (ii) the K^+ concentration in common biologic fluids (blood, plasma) is close to this value. A rigorous evaluation of the potentio-metric selectivity coefficients requi-res a quasi-nernstian response for the interfering cations, too. For this reason the selectivity study was restricted only to Na^+ and NH_4^+ ions.

Figure 3 presents an example of potentiometric response obtained from the interference study carried out in presence of variable Na^+ concentration. The average values of the potentiometric selectivity coefficients estimated for Na^+ and NH_4^+ were 0.06 and 0.16, respectively.

Obviously, the selectivity study can be extended for different concentrations of the primary ion. Taking into account that the selectivity coefficients are a complex function on the primary and interfering ion concentration, the level of the primary ion concentration should be established in direct correlation with the specific application of the investigated ISE.

III. Study of repeatability

Based on experimental results obtained from calibration curves recorded in presence of Na^+ and K^+, studies of inter-measurement and inter-electrode repeatability were also performed.

As can be seen from Figure 4, an excellent repeatability was observed both between two successive measurements and between four similar electrodes. The data dispersion observed in the domain of low concentrations could be due to the absence of the supporting electrolyte.
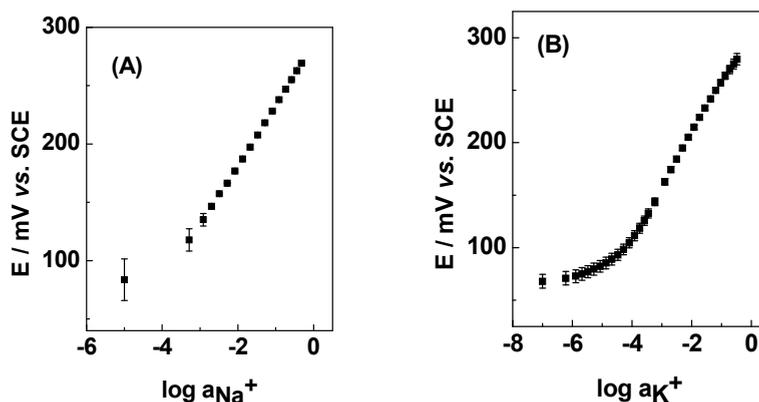
Figure 4. Mean values and standard deviations for: (A) two measurements performed successively, using the same electrode for Na^+ ion; (B) measurements performed in parallel, using four electrodes for K^+ ion

CONCLUSIONS

The aim of the present study was to evaluate the main analytical parameters of ISE based on a PVC membrane containing the ionophore C6Es6, synthesized by a new chemical route. Measurements were performed in separate solutions of Ca^{2+}, Mg^{2+}, Na^+, K^+, NH_4^+ and Li^+. Quasi-nernstian slopes were obtained for K^+ (52 mV), Na^+ (55 mV) and NH_4^+ (56 mV).). For all the other ions, the sensor showed undernernstian sensitivities. The lowest detection limit was obtained in the case of K^+ ($2.0*10^{-5}$ M). A very good repeatability was observed both for inter-measurement and inter-electrode tests.

Based on these main electroanalytical parameters, it can be concluded that the newly prepared calix[6]arenic ester may be used as an ionophore for obtaining K^+-selective electrodes, good enough to replace the consecrated but expensive valinomycin. Further studies are in progress in order to optimize the PVC membrane composition.

EXPERIMENTAL SECTION

I. Materials

The C6Es6 ionophore was provided by dr. Elisabeth-Jeanne Popovici from "Raluca Ripan" Chemistry Research Institute, Cluj-Napoca (Romania).

All reagents used were of analytical grade. Calcium chloride, lithium acetate, lithium chloride, ammonium chloride, 2-nitrophenyloctylether (NPOE), high molecular weight polyvinyl chloride (PVC) and tetrahydrofurane (THF) were purchased from Fluka (Darmstadt, Germany). Potassium chloride was from Riedel-deHaën (Darmstadt, Germany), magnesium chloride was purchased from Chimopar (Bucharest, Romania) and sodium chloride was from Merck (Darmstadt, Germany).

II. Membrane preparation

The ISE membrane was prepared from 1% (w/w) ionophore (C6Es6), 33% (w/w) polymer matrix (PVC), and 66% (w/w) plasticizer (NPOE); the mixture had a total weight of 0.3 g. The components were successively dissolved in THF, under stirring, in the following order: ionophore, polymeric matrix, and plasticizer. After complete dissolution, the mixture was poured into a glass cylinder and covered by a glass recipient, under which a THF-impregnated paper was placed, in order to avoid pores formation. When dried, the membrane was placed for one day in a dark place, in open air.

III. Experimental setup

All the measurements were performed using a PC-controlled setup [11]; its scheme is presented in Figure 5. This device is composed of: the electrochemical cell; a personal computer; two interfaces for communication between the computer and other components; an unit for controlling the solution stirring; a magnetic stirrer; a peristaltic pump allowing automatic exponential additions of standard solution.

The system control as well as data acquisition were performed using the LabView 5.1 software. Data processing was done by using the Origin 5.0 software.

EIS were prepared by fixing an 8 mm diameter disc membrane at the bottom end of a plastic syringe body. As internal reference, a Ag/AgCl system was used. The inner electrolytes contained the same ion as the test solution, at a concentration of 5 mM. Four similar electrodes were tested in parallel, and each measurement was repeated three times under same experimental conditions. A double-junction saturated calomel electrode was used as external reference. The external liquid junction was filled with CH_3COOLi 0.1 M.
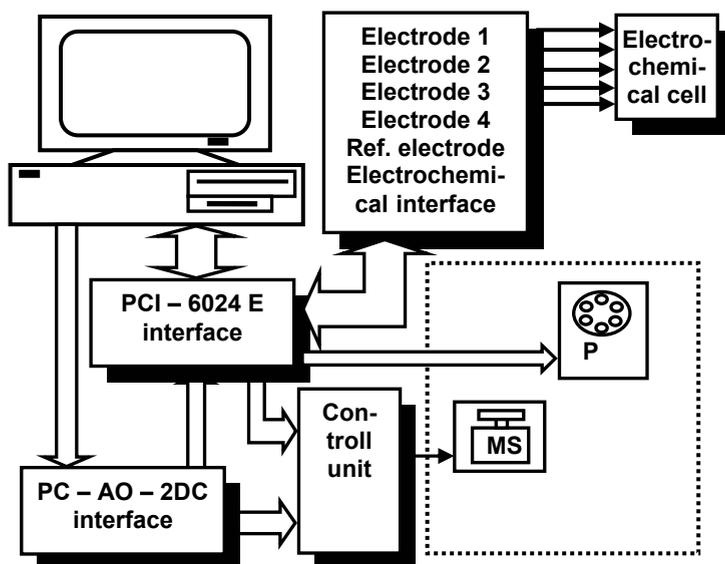
Figure 5. The scheme of the computer-controlled device
used for the ISE potentiometric measurements;
MS – magnetic stirrer; P – peristaltic pump

IV. Experimental procedure

Before use, all electrodes were conditioned for at least 24 hours in the solution containing the cation to be determined.

The experimental procedure consisted in two main parts: in the first one, the potentiometric response of the prepared membranes was recorded for Ca^{2+}, Mg^{2+}, Na^+, K^+, NH_4^+ and Li^+ using separate solutions, and the corresponding calibration curves were recorded. In the second part, the ionic interference between K^+ and different common cations was examined. All potentiometric measurements were performed in batch mode, using the standard addition method for the preparation of standard solutions.

For the interference study, the method of fixed primary ion concentration was used: the primary ion concentration was kept constant, while the concentrations of the interfering ions were increased.

ACKNOWLEDGMENTS

REFERENCES

1. E. Bakker, D. Diamond, A. Lewenstam, E. Pretsch, *Anal. Chim. Acta,* **1999**, *393,* 11.

2. E. Bakker, P. Buhlmann, E. Pretsch, *Chem. Rev.*, **1997**, *97*, 3083.

3. P. Buhlmann, E. Pretsch, E. Bakker, *Chem. Rev.*, **1998**, *98*, 1593.

4. V. Arora, H. M. Chawla, S. P. Singh, *ARKIVOC,* **2007**, *2*, 172.

5. R. Ludwig, N. T. K. Dzung, *Sensors*, **2002**, *2*, 397.

6. K. Belhamel, R. Ludwig, M. Benamor, *Microchimica Acta,* **2005**, *149*, 145.

7. T. D. Chung, H. Kim, *Journal of Inclusion Phenomena and Molecular Recognition in Chemistry*, **1998**, *32*, 179.

8. V. S. Bhat, V. S. Ijeri, A. K. Srivastava, *Sensors and Actuators B,* **2004**, *99,* 98.

9. V.K. Gupta, R. N. Goyal, M. Al Khayat, P. Kumarc, N. Bachheti, *Talanta,* **2006**, *69*, 1149.

10. A.K. Jain, V.K. Gupta, L. P. Singh, J. R. Raisoni, *Electrochimica Acta,* **2006***, 51,* 2547.

11. S. A. Dorneanu, V. Coman, I. C. Popescu, P. Fabry, *Sensors and Actuators B*, **2005**, *105,* 521.

COMPARATIVE STUDY OF CARBON PASTE ELECTRODES MODIFIED WITH METHYLENE BLUE AND METHYLENE GREEN ADSORBED ON ZEOLITE AS AMPEROMETRIC SENSORS FOR H_2O_2 DETECTION

CODRUTA VARODI[a], DELIA GLIGOR[b], LEVENTE ABODI[a], LIANA MARIA MURESAN[a]*

ABSTRACT. Methylene Blue (MB) and Methylene Green (MG) adsorbed on a synthetic zeolite (13X) and incorporated in carbon paste resulted in modified electrodes (MB-13X-CPEs and MG-13X-CPEs) with electrocatalytic activity for H_2O_2 reduction. Using the treatment proposed by Laviron, the heterogeneous electron transfer rate constant (k_s) was estimated, and values between 2.9 and 6.6 s^{-1} were found. The electrocatalytic ability of the modified electrodes towards H_2O_2 electroreduction depends mainly on the formal potential of mediator. The MB-13X-CPEs and MG-13X-CPEs respond to H_2O_2 in the linear range from ~10^{-4} to 10^{-1} M. The best performances were attained with MB-13X-CPEs in phosphate buffer (pH 6): detection limit 0.13 mM, at a signal to noise ratio equal to 3; sensitivity 0.94 mA/M, calculated as the ratio I_{max}/K_M.

Keywords: carbon paste electrodes; Methylene Blue; Methylene Green; Zeolite; Hydrogen peroxide.

INTRODUCTION

Zeolites ability to immobilize large amounts of redox dyes, with significant solubility in specific experimental conditions recommend them as attractive matrices for the preparation of composite electrode materials [1-4]. Methylene Blue (MB) and Methylene Green (MG) are water-soluble cationic dyes with the redox potential close to the optimal potential window for amperometric detection of ascorbic acid, NADH or H_2O_2. Electrodes incorporating zeolites modified with MB and MG were realized for amperometric detection of ascorbic acid [2,5,6], NADH [5,7] or H_2O_2 [8-11].

Continuing our preoccupation in obtaining modified electrodes by immobilization of different dyes onto zeolites [6,7,9-11], in the present paper, the electrochemical behavior and the electrocatalytic properties of carbon paste

---

[a] *Facultatea de Chimie şi Inginerie Chimică, Str. Kogălniceanu, Nr. 1, RO-400084 Cluj-Napoca*
[b] *Facultatea de Ştiinţa Mediului, Universitatea Babeş-Bolyai, Str. Kogălniceanu, Nr. 1, RO-400084 Cluj-Napoca, Romania, limur@chem.ubbcluj.ro*

electrodes incorporating a synthetic zeolite (molecular sieves 13X, Aldrich) modified with Methylene Blue (MB-13X-CPEs) or Methylene Green (MG-13X-CPEs) are assessed comparatively and the influence of some experimental parameters (pH, and potential scan rate) on the voltammetric response of these electrodes were investigated.

The electrochemical parameters for the heterogeneous electron transfer process corresponding to the surface immobilized mediators were determined from voltammetric measurements. All observed differences were used to put on evidence the influence of the mediator structure on the redox response. The modified electrodes were tested for electrocatalytic mediated reduction of H_2O_2 at MB-13X-CPES and MG-13X-CPEs, using cyclic voltammetry (CV) and the calibration of modified electrodes were realized by using amperometry.

RESULTS AND DISCUSSION

Cyclic voltammetric experiments were carried out using MB-13X-CPEs and MG-13X-CPEs. In Figures 1A and 1B, a pair of well-defined redox waves in the case of both electrodes, can be observed. This peak pair was assigned to the oxidation and reduction of MB and MG adsorbed on the 13X zeolite.
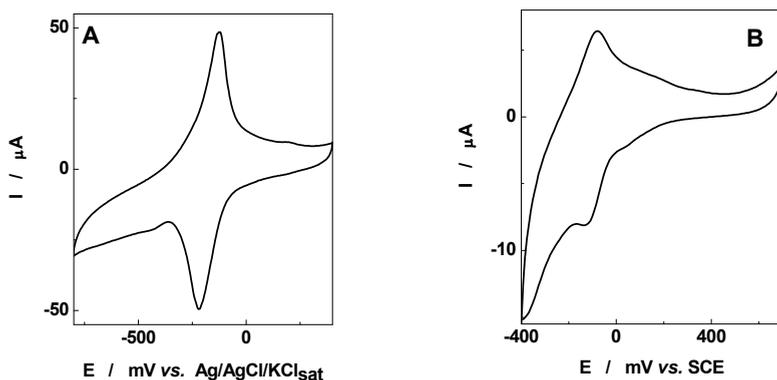
Figure 1. Cyclic voltammograms for MB-13X-CPEs (A) and MG-13X-CPEs (B). Experimental conditions: starting potential, -650 mV *vs.* Ag|AgCl/KCl_sat (A) and -400 mV *vs.* SCE (B); potential scan rate, 10 mV s^{-1}; supporting electrolyte, 0.1 M phosphate buffer, pH 7.

$E^{0'}$ value for MG-13X-CPEs is more positive (see Table 1) than the $E^{0'}$ value for MB-13X-CPEs, suggesting that MG is more difficult to oxidize than MB. This behavior could be explained by the presence of a nitro-group at the 4-position, in the MG structure. The nitro-group is a strong electron acceptor group and it enhances the stability of the compound, making its oxidation more difficult.

Table 1. Electrochemical parameters corresponding to MB-13X-CPEs and MG-13X-CPEs modified electrodes. Experimental conditions: as in Figure 1.

| Electrode	E_{pa}*	E_{pc}*	$E^{0'}$*	ΔE_p	Γ (mol cm^{-2})
MB-13X-CPEs	-130	-220	-175	90	$1.40 \cdot 10^{-8}$
MG-13X-CPEs	-35	-81	-58	46	$1.03 \cdot 10^{-8}$

* mV *vs*. Ag|AgCl/KCl$_{sat}$

The peak separation ΔE_p ($\Delta E_p = E_{pa} - E_{pc}$) for MB-13X-CPEs and MG-13X-CPEs was found to be 90 mV and 46 mV, respectively, in phosphate buffer, pH 7 (10 mV s^{-1}), indicating a quasi-reversible redox process. The peaks split are larger than that reported for MG adsorbed on graphite (~ 20 mV) [12], indicating a diffusion behavior of the mediator.

As can be observed from Figure 2, for MG-13X-CPEs, the slope of $E^{0'}$ *vs.* pH dependence (pH 4-7) was 0.034 V/pH, indicating a e$^-$/H$^+$ ratio equal to 2 corresponding to the reaction:

$$MGH \rightarrow MG^+ + 2e^- + H^+.$$

The $E^{0'}$ *vs.* pH dependence could be mainly explained by the steric impediments which hinder the entrance of the MG molecules in the channels and pores of the zeolite and make them sensitive to the external solution pH change.

Contrarily, for MB-13X-CPEs, $E^{0'}$ does not change significantly with pH. This result is remarkable and can be due to the absence of NO_2 group from MB structure. Due to its smaller size, MB is entrapped in the holes of the 13X type zeolite (host matrix) where it is strongly hold by electrostatic interactions being not affected by the external solution pH change [11].
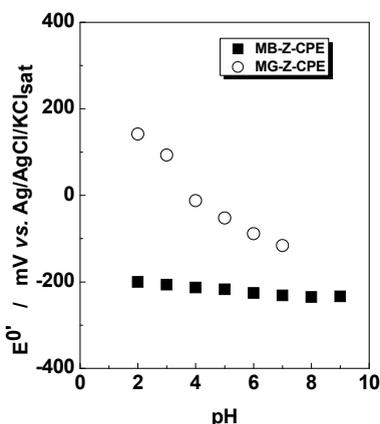
Figure 2. Variation of $E^{0'}$ with pH for MB-13X-CPEs and MG-13X-CPEs. Experimental conditions: potential scan rate, 50 mV s^{-1}; for other conditions, see Figure 1.

Moreover, the slope of the log I -log v dependence (see Table 2) confirms that MB is stronger adsorbed than MG on the zeolite surface.

Table 2. Parameters of the log-log linear regression corresponding to the peak current dependence on the potential scan rate for MB-13X-CPEs and MG-13X-CPEs. Experimental conditions: as in Figure 3.

Electrode	pH	Slope		R / N	
		oxidation	reduction	oxidation	reduction
MB-13X-CPEs	3	0.80	0.92	0.992 / 12	0.996 / 12
	5	0.81	0.95	0.999 / 12	0.997 / 12
	6	0.82	0.96	0.999 / 12	0.997 / 12
	7	0.82	0.95	0.998 / 12	0.995 / 12
	8	0.78	1.01	0.999 / 8	0.998 / 8
	9	0.81	0.96	0.999 / 12	0.998 / 12
MG-13X-CPEs	5	0.67	0.64	0.996 / 11	0.996 / 11
	6	0.62	0.73	0.997 / 12	0.984 / 9
	7	0.57	0.60	0.998 / 10	0.993 / 8

Using the treatment proposed by Laviron [13], the heterogeneous electron transfer rate constant (k_s) and the transfer coefficients (α) were determined (Figure 3 and Table 3). At pH values greater than 5, MB-13X-CPEs present relatively higher k_s values than MG-13X-CPEs, but the differences are not important. The k_s values in the case of MB-13X-CPEs and MG-13X-CPEs are in accordance with the better adsorption of MB and MG on the zeolite and suggest a faster electron transfer rate. It should be mentioned that the values of k_s calculated for MG-13X-CPEs are higher than those obtained using a NaX type synthetic zeolite from Bayer [10], suggesting a stronger interaction between MG and 13X type zeolite than between MG and NaX type zeolite. This confirms that the type of adsorbent is very important for the modified electrode electrochemical behavior.

The differences occurring between the transfer coefficients values, α, corresponding to the two electrodes suggest a different electron transfer mechanism in the two cases and a possible change of the reaction path with increasing pH. Probably, in the case of MB-13X-CPEs the charges are transferred mainly *via* a mechanism involving an ion exchange process between the immobilized positively charged MB species and the supporting electrolyte cations, followed by an electron transfer process occurring between the free MB species and the graphite particles from the carbon paste, while in the case of a MG-13X-CPEs the charge transfer mechanism is partially based on a surface-mediated electron transfer. Moreover, the α values indicate that the redox processes are not fully reversible.
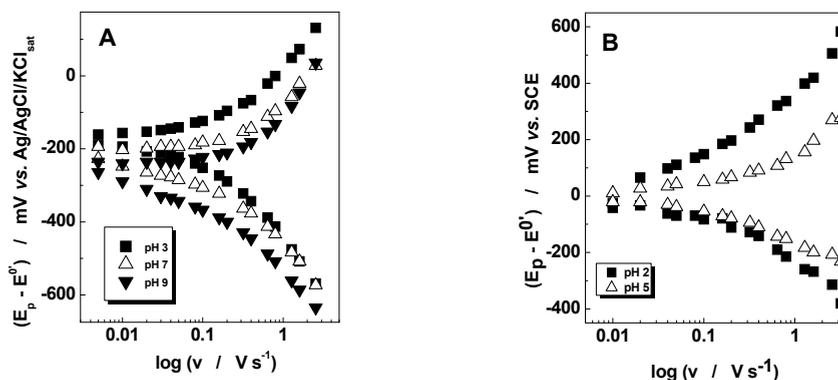
Figure 3. Experimental dependence of $(E_p - E^{o'})$ *vs.* logarithm of the scan rate for MB-13X-CPEs (A) and MG-13X-CPEs (B). Experimental conditions: as in Figure 1.

Table 3. Kinetic parameters for the heterogeneous electron transfer at MB-13X-CPEs and MG-13X-CPEs modified electrodes. Experimental conditions: as in Figure 3.

Electrode	pH	k_s (s^{-1})	α	R/N	
				oxidation	reduction
MB-13X-CPEs	3	5.6	0.55	0.998 / 5	0.999 / 5
	5	5.4	0.61	0.998 / 5	0.998 / 6
	7	5.5	0.69	0.992 / 5	0.993 / 6
	8	5.5	0.72	0.996 / 5	0.999 / 5
	9	4.9	0.79	0.989 / 5	0.999 / 5
MG-13X-CPEs	3	6.6	0.82	0.986 / 5	0.978 / 7
	5	3.5	0.90	0.991 / 5	0.990 / 7
	6	2.9	0.80	0.993 / 6	0.986 / 8

Hydrogen peroxide electroreduction studies were performed by cyclic voltammetry on MB-13X-CPEs and MG-13X-CPEs immersed in H_2O_2 solutions of different concentrations (phosphate buffer, pH 7) (see Figure 4 for MB-13X-CPEs). In the presence of H_2O_2 an enhancement of the cathodic currents and a small peak potential shift towards negative direction with the increase of H_2O_2 concentration were observed. The electrocatalytic efficiency, estimated as the ratio, at an applied potential of -400 mV *vs.* Ag|AgCl/KCl$_{sat}$, in phosphate buffer pH 7, was 0.55 for MG-13X-CPEs and 0.10 for MB-13X-CPEs.

$$\frac{(I_{peak})_{[H_2O_2]=3mM} - (I_{peak})_{[H_2O_2]=0}}{(I_{peak})_{[H_2O_2]=0}}$$

The slight difference between the electrocatalytic activity of the two electrodes suggests that the acceptor group -NO_2 existing in the MG molecule enhances the electrocatalytic efficiency of this mediator.

Batch amperometric measurements at constant applied potential (-400 mV *vs.* Ag|AgCl/KCl$_{sat}$) proved that both MB-13X-CPEs and MG-13X-CPEs work well as H_2O_2 amperometric sensors (Figure 5), as suggested by the analytical parameters presented in Table 4.
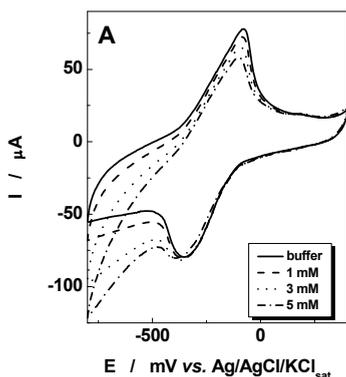
Figure 4. Cyclic voltammograms obtained at MB-13X-CPEs, in the absence and in the presence of H_2O_2. Experimental conditions: potential scan rate, 10 mV s^{-1}; starting potential, -800 mV *vs.* Ag|AgCl/KCl$_{sat}$; supporting electrolyte, 0.1 M phosphate buffer, pH 7.0.
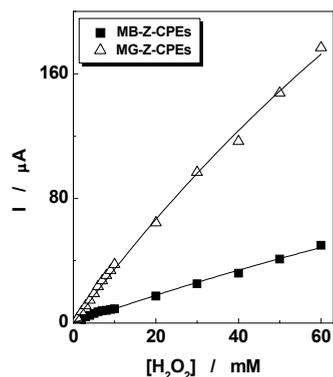
Figure 5. Calibration curves for H_2O_2 at MB-Z-CPEs and MG-13X-CPEs. Experimental conditions: applied potential, -400 mV *vs.* Ag|AgCl/KCl$_{sat}$; supporting electrolyte, 0.1 M phosphate buffer, pH 6.0.

Table 4. Electroanalytical parameters corresponding to MB-13X-CPEs and MG-13X-CPEs modified electrodes. Experimental conditions: as in Figure 5.

Electrode	pH	Detection limit (mM)	Linear domain (M)	Sensitivity* (mA/M)	R / N
MB-13X-CPEs	6	0.13	$10^{-4} - 3 \cdot 10^{-1}$	1.20	0.991 / 8
	7	0.79	$8 \cdot 10^{-4} - 10^{-1}$	1.80	0.986 / 15
MG-13X-CPEs	6	0.42	$4 \cdot 10^{-4} - 2 \cdot 10^{-1}$	3.90	0.999 / 17
	7	0.60	$6 \cdot 10^{-4} - 1$	2.00	0.995 / 20

*calculated as the slope of calibration curve

The best detection limit (for a signal to noise ratio of 3) was obtained for MB-13X-CPEs in phosphate buffer pH 6 and that obtained for MG-13X-CPEs is better than that already reported by using a natural zeolitic volcanic tuff (natural X type mesoporous clinoptilolyte) [10]. In all cases the response time < 20 s.

The higher sensitivity of MG-13X-CPEs as compared with that of MB-13X-CPEs for H_2O_2 detection is in accordance with the better electrocatalytic effect of the MG-13X-CPEs, even if they exhibit smaller k_s values than MB-13X-CPEs.

CONCLUSIONS

Modified electrodes with electrocatalytic activity toward H_2O_2 reduction were obtained by Methylene Blue and Methylene Green adsorption on a synthetic zeolite (molecular sieves 13X, Aldrich), followed by their incorporation in carbon paste. The characteristics of the voltammetric response of MB-13X-CPEs and MG-13X-CPES (ΔEp of 90 and 46 mV, respectively and I_{pa}/I_{pc} of ~ 1) pointed out to a quasi-reversible, surface confined redox process in both cases.

The observed differences between the electrochemical behavior of MB-13X-CPEs and MG-13X-CPEs (the standard formal potentials, the effect of pH on $E^{0'}$ and the magnitude of the rate constants for heterogeneous electron transfer) as well as the electrocatalytic activity for H_2O_2 reduction can be explained in terms of mediator structure. The MG-13X-CPEs present a better sensitivity and electrocatalytic efficiency, but its $E^{0'}$ is not pH independent as in the case of MB-13X-CPEs.

Concluding, both investigated modified electrodes showed moderate catalytic efficiency towards H_2O_2 reduction and a relatively low limit of detection (0.13 mM for MB-13X-CPEs and 0.42 mM for MG-13X-CPEs, pH 6).

EXPERIMENTAL SECTION

Chemicals

Methylene Blue (MB) and Methylene Green (MG) (Schemes 1 and 2), graphite powder and paraffin oil were purchased from Fluka (Buchs, Switzerland).

The 13X type zeolite, $1Na_2O:1Al_2O_3:2.8\pm0.2\ SiO_2 \times H_2O$ (particle size, 3-5μ; pore diameter, 10 Å; specific surface area 548.69 m^2/g; bulk density 480.55 kg/m^3; Si/Al ratio 1.5) was purchased from Aldrich (Germany).

Hydrogen peroxide, $K_2HPO_4 \cdot 2H_2O$ and $KH_2PO_4 \cdot H_2O$ were purchased from Merck (Darmstadt, Germany). All other reagents were of analytical grade and used as received.

The supporting electrolyte was a 0.1 M phosphate buffer solution. The pH was adjusted in the interval 1-9 using appropriate H_3PO_4 or NaOH solutions.
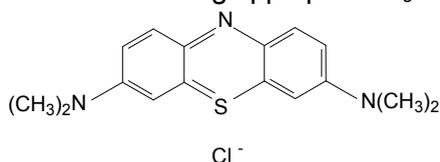
Scheme 1
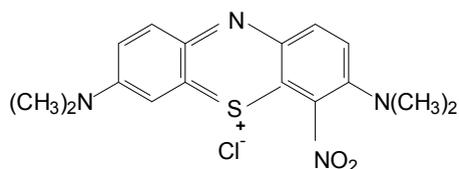
Scheme 2

Electrode preparation

50 ml of a 0.001 % (w/v) MB or MG solution in water were shaken (3 days) with 50 mg zeolite. The modified zeolite was filtered, washed and dried. 25 mg of the modified zeolite were mixed with 25 mg graphite powder and 10 µl paraffin oil in order to obtain the modified carbon paste electrodes (MB-13X-CPEs and MG-13X-CPEs).

The preparation of MB-13X-CPEs and MG-13X-CPEs was reproducible when the experimental conditions and variables were maintained constant during the preparation period. The current response of the electrodes did not change significantly by storing them in air for several months.

Electrochemical measurements

Electrochemical experiments were carried out using a typical three-electrode electrochemical cell. The modified carbon paste electrode was used as working electrode, a platinum ring as counter electrode and an Ag|AgCl/KCl$_{sat}$ or SCE as reference electrodes.

Cyclic voltammetry experiments were performed on a PC-controlled electrochemical analyzer (Autolab-PGSTAT 10, EcoChemie, Utrecht, The Netherlands).

Batch amperometric measurements at different H_2O_2 concentrations were carried out at an applied potential of -400 mV *vs.* Ag|AgCl/KCl$_{sat}$, under magnetic stirring, using 0.1 M phosphate buffer solution (pH 7) as supporting electrolyte. The current-time data were collected using the above-mentioned electrochemical analyzer.

For each electrode, the surface coverage (Γ, mol cm^{-2}) was estimated from the under peak areas, recorded during the cyclic voltammetry (CV) measurements at low potential scan rate (v ≤ 10 mV s^{-1}) [14] and considering the number of transferred electrons equal to 2 [15,16].

The experimental results are the average of at least 3 identically prepared electrodes, if not otherwise mentioned.

ACKNOWLEDGMENTS

REFERENCES

1. A. Walcarius, *Anal. Chim. Acta*, **1999**, *384*, 1.
2. M. Arvand, Sh. Sohrabnezhad, M. F. Mousavi, *Anal. Chim. Acta*, **2003**, *491*, 193.
3. A. Walcarius, *Electroanalysis*, **2008**, *20*, 711.
4. I. Svancara, K. Vytras, K. Kalcher, A. Walcarius, J. Wang, *Electroanalysis*, **2009**, *21*, 7.
5. J. Kulys, G. Gleixner, W. Schuhmann, H.-L. Schmidt, *Electroanalysis*, **1993**, *5*, 201.
6. C. Varodi, D. Gligor, L. M. Muresan, *Stud. Univ.Babes-Bolyai, Chemia*, **2007**, *1*, 109.
7. C. Varodi, D. Gligor, A. Maicaneanu, L. M. Muresan, *Rev. Chim.*, **2007**, *58*, 890.
8. H. Yao, N. Li, S. Xu, J.-Z. Xu, J.-J. Zhu, H.-Y. Chen, *Biosen. Bioelectron.*, **2005**, *21*, 372.
9. D. Gligor, L. Muresan, I.C. Popescu, *Acta Univ. Cibiniensis, Seria F Chemia*, **2004**, *7*, 29.
10. D. Gligor, L. M. Muresan, A. Dumitru, I. C. Popescu, *J. Appl. Electrochem.*, **2007**, *37*, 261.
11. C. Varodi, D. Gligor, L. M. Muresan, *Rev. Roum. Chim.*, **2007**, *52*, 81.
12. Q. Chi, S. Dong, *Anal. Chim. Acta*, **1994**, *285*, 125.
13. E. Laviron, *J. Electroanal. Chem.*, **1979**, *101*, 19.
14. H. Huck, *Phys. Chem. Chem. Phys.*, **1999**, *1*, 855.
15. C. Lei, Z. Zhang, H. Liu, J. Kong, J. Deng, *Anal. Chim. Acta*, **1996**, *332*, 73.
16. B. Liu, Z. Liu, D. Chen, J. Kong, J. Deng, *Fresenius J. Anal. Chem.*, **2000**, *367*, 539.

PHARMACOKINETIC INTERACTION BETWEEN IVABRADINE AND CIPROFLOXACINE IN HEALTHY VOLUNTEERS

LAURIAN VLASE[a], **DANA MUNTEAN**[a, b], **ADINA POPA**[a], **MARIA NEAG**[a], **IOAN BÂLDEA**[b], **MARCELA ACHIM**[a], **SORIN E. LEUCUȚA**[a]

ABSTRACT. The pharmacokinetic interaction of ivabradine with ciprofloxacin in healthy volunteers was evaluated. A dose of 5 mg ivabradine in combination with 500 mg ciprofloxacin was administered to 18 healthy male volunteers in a two treatment study design, separated by 6 days in which the ciprofloxacin alone was administrated as a single p.o. dose daily. Plasma concentrations of ivabradine were determined during a 12 hours period following drug administration. Ivabradine plasma concentrations were determined by a validated LC/MS method. Pharmacokinetic parameters of ivabradine were calculated using non-compartmental and compartmental analysis. In the two periods of treatments, the mean peak plasma concentrations (C_{max}) were 8.52 ng/ml (ivabradine alone) and 8.40 ng/ml (ivabradine after pre-treatment with ciprofloxacin). The times taken to reach C_{max}, t_{max}, were 0.86 hr and 1.52 hr respectively and the total areas under the curve ($AUC_{0-\infty}$) were 27.9 ng.hr/ml and 28.1 ng.hr/ml, respectively. The absorption rate constants (k_a) of ivabradine were 10.8 hr^{-1} and 5.27 hr^{-1}, respectively. Statistically significant differences have been observed for both t_{max} and k_a of ivabradine when administered alone or with ciprofloxacin, whereas for C_{max} and $AUC_{0-\infty}$ the differences were non-significant. The experimental data demonstrate the pharmacokinetic interaction between ciprofloxacin and ivabradine, however, the observed interaction may not be clinically significant.

Keywords: ivabradine, ciprofloxacin, pharmacokinetics, drug interaction

INTRODUCTION

Ivabradine (3-(3-{[((7S)-3,4-dimethoxi-bicyclo[4.2.0]octa-1,3,5-trien-7-yl) methyl]methylamino}propyl)-1,3,4,5-tetrahydro-7,8-dimethoxy-2H-3-benzazepin-2-one, hydrochloride) (Figure 1a) is a novel heart rate–lowering agent that selectively and specifically inhibits the depolarizing cardiac pacemaker I*f* current in the sinus node. Its activity provides pure heart rate reduction at rest and

[a] *University of Medicine and Pharmacy "Iuliu Hațieganu", Faculty of Pharmacy, Emil Isac 13, RO-400023, Cluj-Napoca, Romania, vlaselaur@yahoo.com*
[b] *"Babeş-Bolyai" University, Faculty of Chemistry and Chemical Engineering, Arany Janos 11, RO-400028, Cluj-Napoca, Romania*

during exercise, which improves myocardial oxygen balance and increases coronary perfusion, without any relevant influence on conduction, contractility, ventricular repolarization or blood pressure. The anti-ischemic efficacy and the safety of ivabradine have been demonstrated in patients with stable angina pectoris [1-5].

Despite its therapeutical benefit, ivabradine has some important side effects, including bradycardia, AV block, ventricular extrasystoles and luminous phenomena [1,3,5]. Due to high potential of ivabradine to give adverse reactions on overdosing, but also lack of therapeutic effect on under-dosing, is important to know the way in some other substances modify the ivabradine pharmacokinetics.

After oral administration, the metabolic clearance of ivabradine accounts for about 80% of its total clearance, with the other 20% corresponding to renal clearance. Only CYP3A4 is involved in invabradine's metabolism, so numerous potential interactions can therefore arise with CYP3A4 inhibitors and inducers [6-8].

Ciprofloxacin (1-cyclopropyl- 6-fluoro- 4-oxo- 7-piperazin- 1-yl- quinoline-3-carboxylic acid) (Figure 1b) is a fluoroquinolone used for treating severe bacterial infections. Ciprofloxacin is a potent inhibitor of CYP1A2 and medium inhibitor of CYP3A4 [9-11], thus it can interfere with metabolism of ivabradine.

The aim of our study is to determine if a potentially harmful pharmacokinetic interaction occurs between ivabradine and ciprofloxacin, when administered together.

(a)   (b)
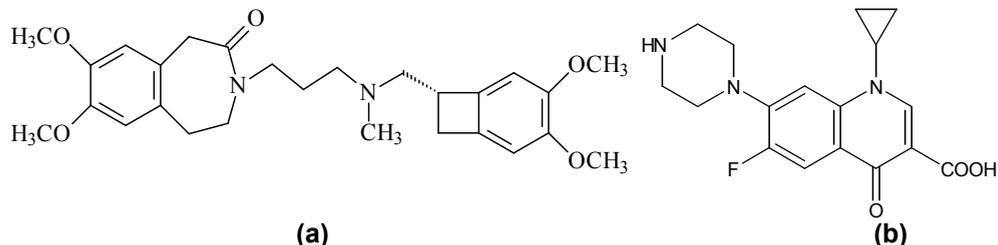
Figure 1. Molecular structure of ivabradine (a) and ciprofloxacin (b)

RESULTS AND DISCUSSION

The mean plasma concentrations of ivabradine when administered alone or in combination with ciprofloxacin after 5 days treatment with ciprofloxacin are shown in Figure 2. The bi-phasic plot describes absorption and elimination consecutive processes (see eq. in section Pharmacokinetic analysis).

The mean pharmacokinetic parameters of ivabradine administered alone or in combination with ciprofloxacin, as well as the statistical significance following their comparison are given in Table 1.
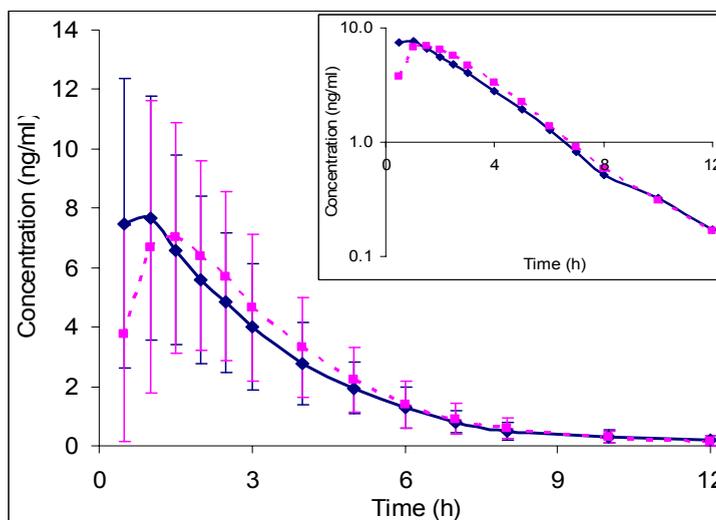
Figure 2. Mean (±SD) plasma levels of ivabradine (5 mg p.o.) given alone
(continuous line) or in combination with ciprofloxacin (500 mg, p.o.)
after treatment with ciprofloxacin for 6 days (500 mg p.o.) (dotted line),
n=18; in insert: semilogaritmic presentation.

Table1. Pharmacokinetic parameters of ivabradine administered alone or
after treatment with ciprofloxacin and the result of statistical t test
used for comparison

Pharmacokinetic parameter (±SD)	Ivabradine alone	Ivabradine + ciprofloxacin	p* value, t-test
C_{max} (ng/ml)	8.52(4.37)	8.40(4.67)	0.78
t_{max} (hr)	0.86(0.41)	1.52(0.52)	* 0.0014
$AUC_{0-\infty}$ (ng.hr/ml)	27.92(13.59)	28.15(13.74)	0.85
k_{el} (1/hr)	0.35(0.10)	0.37(0.08)	0.36
k_a (1/hr)	10.8(6.8)	5.27(6.71)	* 0.025
$t_{1/2}$ (hr)	2.10(0.60)	1.93(0.44)	0.28

* significance for $p<0.05$

Peak plasma concentrations (C_{max}) of ivabradine before and after
the ciprofloxacin multiple doses treatment (8.52 ng/ml vs. 8.40) were not
significantly different between the two treatments. The same was found
when comparing $AUC_{0-\infty}$, k_{el} and $t_{1/2}$ parameters. However, the time to reach
the peak plasma concentration (t_{max}) and the absorption rate constant k_a
were significantly different between treatments (p=0.0014 and 0.025 hr^{-1},
respectively).

The pharmacokinetic parameters C_{max}, t_{max} and $AUC_{0-\infty}$, were also used for bioequivalence evaluation of ivabradine administered in Test and Reference period respectively. The parametric 90% confidence interval for the ratio Test/Reference period of the mean pharmacokinetic parameters C_{max} and $AUC_{0-\infty}$ (log transformed) of ivabradine and the significance of the difference of t_{max} are shown in Table 2.

Table 2. Bioequivalence evaluation of pharmacokinetic parameters of ivabradine administered alone or after treatment with ciprofloxacin.

Pharmacokinetic parameter	90% Confidence intervals
$AUC_{0-\infty}$ (ng.h/ml)	0.93-1.08 (ANOVA, NS)
C_{max} (ng/ml)	0.89-1.07 (ANOVA, NS)
t_{max} (hr)	χ^2=3.841 (Friedman, S)

The 90% confidence intervals for geometric mean of ivabradine in Test/Reference individual ratios for C_{max} and $AUC_{0-\infty}$ were in the acceptable limits of bioequivalence (0.8-1.25). However, the difference between mean t_{max} values of the test and reference formulations was statistically significant.

The present study shows that the treatment with ciprofloxacin influences the pharmacokinetics of ivabradine. No systemic metabolic drug-drug interaction was observed, as time the half-life is not changing between treatments and the drug exposure (C_{max} and $AUC_{0-\infty}$) is about the same. However, the ciprofloxacin has a negative effect of absorption rate of ivabradine, because the related pharmacokinetic parameters (t_{max} and k_a) are significantly changing between treatments. Despite those observed differences, since the drug exposure related pharmacokinetic parameters (C_{max} and $AUC_{0-\infty}$) were in bioequivalence interval, the observed pharmacokinetic interaction may not have clinical significance.

CONCLUSIONS

A pretreatment with ciprofloxacin until achieving the steady state plasma concentrations influences the pharmacokinetics of ivabradine co-administered as a single oral dose in healthy volunteers.

EXPERIMENTAL SECTION

Subjects

Eighteen, non-smoking males, aged 22-27 years took part in the study. The study was conducted according to the principles of Declaration of Helsinki (1964) and its amendments (Tokyo 1975, Venice 1983, Hong Kong 1989) and Good Clinical Practice (GCP) rules. The clinical protocol was reviewed and approved by the Ethics Committee of the University of Medicine and Pharmacy "Iuliu Hatieganu", Cluj-Napoca, Romania. All volunteers gave their written informed consent prior to study inclusion. The volunteers were healthy according to history, physical examination and laboratory tests, had no history of alcohol or drug abuse and did not take any regular medication.

Study design

The study consisted of 2 periods: Period 1 (Reference), when each volunteer received a single dose of 5 mg ivabradine and Period 2 (Test), when each volunteer received a single dose of 5 mg ivabradine and 500 mg ciprofloxacin. Between the two periods, the subjects were treated for 6 days with a single daily dose of 500 mg ciprofloxacin. All the drugs were administered in the morning, in fasted state. The pharmaceutical products used were Corlentor (5 mg tablets, producer Les Laboratoires Servier, France) and Ciprolen (500 mg tablets, producer AC Helcor, Romania). Venous blood (5 ml) was drawn into heparinized tubes, in the first and in the last day of the study, before drug administration as well as at 0.5, 1, 1.5, 2, 2.5, 3, 4, 5, 6, 7, 8, 10 and 12 hours after drug administration and the separated plasma was stored frozen (-20°C) until analysis.

Analysis of plasma samples

Ivabradine plasma concentrations were determined by a validated LC/MS method. [12]

Pharmacokinetic analysis

The noncompartmental and compartmental pharmacokinetic analysis method was employed to determine the pharmacokinetic parameters of ivabradine given alone or in combination with ciprofloxacin. The maximal plasma concentration (C_{max}, ng/ml) and the time to reach the peak concentration (t_{max}, hr) were obtained directly by the visual inspection of each subject's plasma concentration-time profile. The area under the concentration-time curve (AUC_{0-t}) has been estimated by integration using trapezoildal rule from time zero to the last measurable concentration at time t. The area was extrapolated to infinity ($AUC_{0-\infty}$) by addition of C_t/ k_{el} to AUC_{0-t} where C_t is the last quantifiable drug concentration and k_{el} is the elimination rate constant.

The elimination rate constant k_{el} was estimated by the least-square regression of plasma concentration-time data points lying in the terminal region by using semilogarithmic dependence that corresponds to a first-order kinetics. The half-life ($t_{\frac{1}{2}}$) was calculated as $0.693/k_{el}$. The absorption constant rate of ivabradine (k_a) was calculated using a mono-compartmental pharmacokinetic model by fitting the data using the equation:

$$Q = D \frac{k_a}{k_a - k_{el}} (e^{-kelt} - e^{-kat})$$

where Q is the quantity of ivabradine in the body at time "t" after oral administration, D is the doze and k_a and k_{el} are the absorption and elimination rate constants in hr^{-1}.

The pharmacokinetic analysis was performed using Kinetica 4.0.2 (Thermo Labsystems, U.S.A.) [13].

Statistical analysis

The *t*-test for paired values was used to compare the calculated pharmacokinetic parameters of ivabradine for the two periods. In order to evaluate a possible clinical significance of the pharmacokinetic interaction, an analysis of variance (ANOVA) was performed on the pharmacokinetic parameters C_{max} and $AUC_{0-\infty}$ using general linear model procedures, in which sources of variation were subject and period. Then the 90% confidence intervals of the test/reference period ratios for C_{max} and $AUC_{0-\infty}$ (log transformed) were determined by the Schuirmann's two one-sided t test [14]. The bioequivalence between ivabradine in Test and Reference period can be concluded when the 90% confidence intervals for these pharmacokinetic parameters of two products are found within an acceptable range of 0.8-1.25 [15-18]. Regarding analysis of t_{max}, the limit for bioequivalence range was expressed as untransformed data, the significance of the difference of t_{max} (Test-Reference) being established by a nonparametric test (Friedman test). All the statistical analysis was performed using Kinetica 4.0.2 software [13].

ACKNOWLEDGMENTS

REFERENCES

1. U.K. Prasad, D. Gray, H. Purcell, *Advances In Therapy*, **2009**, *26(2)*, 127.

2. M.Z. Khawaja, D.M. Walker, *International Journal Of Clinical Practice,* **2009**, *63(4)*, 542

3. J. C. Tardif, P. Ponikowski, T. Kahan, *European Heart Journal*, **2009**, *30(5)*, 540

4. P. Milliez, S. Messaoudi, J. Nehme, C. Rodriguez, J. L. Samuel, C. Delcayre, *American Journal Of Physiology-Heart And Circulatory Physiology,* **2009**, *296(2)*, H435

5. G. Riccioni, N. Vitulano, N. D'Orazio, *Advances In Therapy*, **2009**, *26(1)*, 12

6. A. Portoles, A. Calvo, A. Terleira, L. Laredo, G. Resplandy, C. Gorostiaga, A. Moreno, *Journal of Clinical Pharmacology*, **2006**, *46*, 1195.

7. A. Portoles, A. Terleira, A. Calvo, *Journal Of Clinical Pharmacology,* **2006**, *46(10)*, 1188

8. A. Portoles, A. Calvo, A. Terleira, L. Laredo, G. Resplandy, G. Gorostiaga, A. Moreno, *Journal Of Clinical Pharmacology,* **2006**, *46(10)*, 1195

9. Z. Iqbal, A. Khan, A. Naz, J. A. Khan, G. S. Khan, *Clinical Drug Investigation*, **2009**, *29(4)*, 275

10. H. S. Abou-Auda, A. A. Mustafa, M. S. Al-Humayyd, *Biopharmaceutics & Drug Disposition*, **2008**, *29(1)*, 29

11. K. Herrlin, M. Segerdahl, L. L. Gustafsson, E. Kalso, *Lancet*, **2000** *356(9247),* 2069.

12. L. Vlase, D. Muntean, S. E. Leucuta, I. Baldea, *Studia Universitatis Babes-Bolyai Chemia*, **2009**, *54(2)*, 43

13. http://www.thermo.com/eThermo/CMA/PDFs/Product/productPDF_27347.pdf

14. D. J. Schuirmann, *J Pharmacokinet Biopharm* **1987**, *15(6)*, 657

15. U. S. Department of Health and Human Services, Food and Drug Administration, Center for Drug Evaluation and Research. Guidance for Industry. Bioavailability and Bioequivalence Studies for Orally Administrated Drug Products – General Considerations, Rockville, USA, **2003**, *http://www.fda.gov/cder/guidance/index.htm*

16. The European Agency for the Evaluation of Medicinal Products. Note for Guidance on the Investigation of Bioavailability and Bioequivalence, London, UK, **2001** (CPMP/EWP/QWP/1401/98).

17. L. Vlase, A. Leucuta, D. Farcau D, M. Nanulescu, *Biopharmaceutics & Drug Disposition*, **2006**, *27(6)*, 285

18. L. Vlase, B. Bodiu B, S.E. Leucuta, *Arzneimittel-Forschung-Drug Research*, **2005**, *55(11)*, 664